

Control of the emission wavelength of gallium nitride-based nanowire light-emitting diodes

DISSERTATION

zur Erlangung des akademischen Grades

Doctor rerum naturalium (Dr. rer. nat.)
im Fach Physik

eingereicht an der
Mathematisch-Naturwissenschaftlichen Fakultät I
Humboldt-Universität zu Berlin

von
Dipl.-Phys. Martin Wölz

Präsident der Humboldt-Universität zu Berlin:
Prof. Dr. Jan-Hendrik Olbertz

Dekan der Mathematisch-Naturwissenschaftlichen Fakultät I:
Prof. Dr. Stefan Hecht

Gutachter:

1. Prof. Dr. Henning Riechert
2. Prof. Dr. W. Ted Masselink
3. Dr. Bruno Daudin

Tag der mündlichen Prüfung: 15. Mai 2013

Abstract

Semiconductor nanowires are investigated as a building block for light-emitting diodes (LEDs). Conventional gallium nitride (GaN) LEDs contain several crystal films grown on single crystal substrates, and their performance is limited by strain-induced piezoelectric fields and defects arising from lattice mismatch.

GaN nanowires can be obtained free of defects on foreign substrates. In nanowire heterostructures, the strain arising from lattice mismatch can relax elastically at the free surface. Crystal defects and piezoelectric fields can thus be reduced.

In this thesis, GaN nanowires are synthesized in the self-induced way by molecular beam epitaxy. A proof-of-concept study for the growth of semiconductor nanowires on metal shows that GaN nanowires grow epitaxially on titanium films. GaN of high crystal quality is obtained without a single crystal substrate.

Quantitative models for the growth of axial (In,Ga)N/GaN nanowire heterostructures are developed. The successful fabrication of nanowire LED devices on silicon wafers proves that these models provide control over the emission wavelength.

In the (In,Ga)N/GaN nanowire heterostructures, strain is non-uniform due to elastic relaxation at the sidewalls. Additionally, the self-induced growth leads to statistical fluctuations in the diameter and length of the GaN nanowires, and in the thickness of the axial (In,Ga)N segments. The (In,Ga)N crystal composition and lattice strain are analyzed by x-ray diffraction and resonant Raman spectroscopy. Due to the non-uniformity in strain, detailed numerical simulations are required to interpret these measurements.

A simple approximation for the average strain in the nanowire segments is derived from the detailed numerical calculation. Strain engineering is possible by defining the nanowire segment lengths. Simulations of resonant Raman spectra deliver the experimental strain of (In,Ga)N segments in GaN nanowires, and give a proof of this universal concept.

Key words: gallium nitride, GaN, nanowires, light-emitting diodes, molecular beam epitaxy, x-ray diffraction, Raman spectroscopy

Zusammenfassung

Halbleiter-Nanosäulen (auch -Nanodrähte) werden als Baustein für Leuchtdioden (LEDs) untersucht. Herkömmliche LEDs aus Galliumnitrid (GaN) bestehen aus mehreren Kristallschichten auf einkristallinen Substraten. Ihr Leistungsvermögen wird durch Gitterfehlpassung und dadurch hervorgerufene Verspannung, piezoelektrische Felder und Kristallfehler beschränkt.

GaN-Nanosäulen können ohne Kristallfehler auf Fremdsubstraten gezüchtet werden. Verspannung wird in Nanosäulen elastisch an der Oberfläche abgebaut, dadurch werden Kristallfehler und piezoelektrische Felder reduziert.

In dieser Arbeit wurden GaN-Nanosäulen durch Molekularstrahlepitaxie katalysatorfrei gezüchtet. Eine Machbarkeitsstudie über das Kristallwachstum von Halbleiter-Nanosäulen auf Metall zeigt, dass GaN-Nanosäulen in hoher Kristallqualität ohne einkristallines Substrat epitaktisch auf Titanschichten gezüchtet werden können.

Für das Wachstum axialer (In,Ga)N/GaN Heterostrukturen in Nanosäulen wurden quantitative Modelle entwickelt. Die erfolgreiche Herstellung von Nanosäulen-LEDs auf Silizium-Wafern zeigt, dass dadurch eine Kontrolle der Emissionswellenlänge erreicht wird.

Die Gitterverspannung der Heterostrukturen in Nanosäulen ist ungleichmäßig aufgrund des Spannungsabbaus an den Seitenwänden. Das katalysatorfreie Zuchtverfahren führt zu weiteren statistischen Schwankungen der Nanosäulendurchmesser und der Abschnittlängen. Die entstandene Zusammensetzung und Verspannung des (In,Ga)N-Mischkristalls wird durch Röntgenbeugung und resonant angeregte Raman-spektroskopie ermittelt. Infolge der Ungleichmäßigkeiten erfordert die Auswertung genaue Simulationsrechnungen.

Eine einfache Näherung der mittleren Verspannung einzelner Abschnitte kann aus den genauen Rechnungen abgeleitet werden. Gezielte Verspannungseinstellung erfolgt durch die Wahl der Abschnittlängen. Die Wirksamkeit dieses allgemeingültigen Verfahrens wird durch die Bestimmung der Verspannung von (In,Ga)N-Abschnitten in GaN-Nanosäulen gezeigt.

Schlagworte: Galliumnitrid, GaN, Nanosäulen, Nanodrähte, Leuchtdioden, Molekularstrahlepitaxie, Röntgenbeugung, Raman-Spektroskopie

Abbreviations

CBED	Convergent beam electron diffraction
CL	Cathodoluminescence
DAP	Donor-acceptor pair
EELS	Electron energy loss spectroscopy
EL	Electroluminescence
f.c.c.	face-centered cubic
FWHM	Full width at half maximum
FX	Free exciton
GPA	Geometric phase analysis
h.c.p.	hexagonal close-packed
HAADF	High-angle annular dark field
HRTEM	High-resolution transmission electron microscopy
HVPE	Hydride vapor phase epitaxy
LED	Light-emitting diode
LO	Longitudinal optical
MC	Monte Carlo (algorithm)
MBE	Molecular beam epitaxy
MOVPE	Metal-organic vapor phase epitaxy
MQW	Multi quantum well
NW	Nanowire
PAMBE	Plasma-assisted molecular beam epitaxy
PID	proportional-integral-derivative
PL	Photoluminescence
QCSE	Quantum-confined Stark effect
QMS	Quadrupole mass spectrometer
QW	Quantum well
RF	Radio frequency
RHEED	Reflection high-energy electron diffraction
SAG	Selective area growth
SEM	Scanning electron microscopy
SF	Stacking fault
SL	Superlattice
STEM	Scanning transmission electron microscopy
T/C	Thermocouple
TEM	Transmission electron microscopy
TRPL	Time-resolved photoluminescence
XRD	X-ray diffraction

Contents

1	Introduction	1
2	The GaN-InN material system for solid-state lighting	5
2.1	Light-emitting diodes (LEDs)	5
2.2	Properties of III-nitrides	9
2.2.1	Crystal structure	10
2.2.2	Light emission from $\text{In}_x\text{Ga}_{1-x}\text{N}$ quantum wells	12
2.3	Nanowires as an alternative to planar LED device geometry	14
2.4	Integration of a nanowire LED device	16
3	Growth and in-situ analysis of group-III-nitride nanowires	19
3.1	Molecular beam epitaxy	19
3.2	In-situ analytical methods in molecular beam epitaxy	20
3.2.1	Reflection high-energy electron diffraction	21
3.2.2	Line-of-sight quadrupole mass spectrometry	24
3.2.3	<i>In-situ</i> metrology example: substrate temperature	25
3.3	Growth of GaN nanowires by molecular beam epitaxy	26
3.3.1	GaN nucleation	28
3.3.2	Thermodynamically driven faceting	30
3.3.3	Nanowire elongation	30
3.4	Growth of GaN nanowires on amorphous substrates with metal interlayer	32
3.4.1	Epitaxial growth of GaN on Ti interlayer	33
3.4.2	GaN nucleation on Ti interlayer	39
3.4.3	Perspectives of Ti as an alternative substrate	41
4	Analytical tools for the structural investigation of nanowire ensembles	43
4.1	Statistical fluctuation of self-induced nanowire morphology	43
4.2	Simulation of x-ray diffraction profiles for fluctuating layer thicknesses	45
4.3	Elastic strain relaxation in axial nanowire heterostructures	49
4.3.1	Strain states in mismatched heterostructures	50
4.3.2	Lateral relaxation approximation	51
4.3.3	Average out-of-plane lattice constant	55
4.4	Resonant Raman spectroscopy	56
4.4.1	Strain- and composition dependence of LO phonon frequency	58
4.4.2	Simulation of Raman spectra for non-uniform strain in nanowire heterostructures	59
4.5	Conclusion	62

5	Growth of $\text{In}_x\text{Ga}_{1-x}\text{N}/\text{GaN}$ nanowire heterostructures	63
5.1	Previous studies of $\text{In}_x\text{Ga}_{1-x}\text{N}/\text{GaN}$ nanowire heterostructure growth . . .	63
5.2	Experimental procedure	64
5.3	Morphology of $\text{In}_x\text{Ga}_{1-x}\text{N}$ nanowire segments	67
5.3.1	Microstructure of the $\text{In}_x\text{Ga}_{1-x}\text{N}$ insertion	68
5.3.2	Polytype of the $\text{In}_x\text{Ga}_{1-x}\text{N}$ insertion	71
5.3.3	$\text{In}_x\text{Ga}_{1-x}\text{N}$ nanowire segment growth direction	73
5.3.4	Best practice: V/III, In/Ga, axial growth rate	77
5.4	Active region growth rate	78
5.4.1	Graphical estimation of quantum well thickness and composition .	79
5.4.2	Structural parameters from x-ray diffraction profile simulation . .	83
5.4.3	Surface diffusion during quantum well growth	83
5.5	Quantum well composition analysis	86
5.5.1	X-ray diffraction and transmission electron microscopy	86
5.5.2	Raman spectroscopy	89
5.5.3	Compositional fluctuations	90
5.6	In incorporation in $\text{In}_x\text{Ga}_{1-x}\text{N}$ nanowire segments	93
5.6.1	Processes during ternary $\text{In}_x\text{Ga}_{1-x}\text{N}$ alloy formation	93
5.6.2	<i>In-situ</i> growth control by line-of-sight quadrupole mass spectrometry	95
5.6.3	Quantification of In loss	97
5.6.4	<i>Ex-situ</i> verification of the growth model for $\text{In}_x\text{Ga}_{1-x}\text{N}$ nanowires .	98
5.7	Conclusion	101
6	Properties of $\text{In}_x\text{Ga}_{1-x}\text{N}/\text{GaN}$ nanowire heterostructures	103
6.1	Previous studies of $\text{In}_x\text{Ga}_{1-x}\text{N}/\text{GaN}$ nanowire properties	103
6.2	Design options: $\text{In}_x\text{Ga}_{1-x}\text{N}$ segment composition, thickness and strain . .	105
6.3	Luminescence	107
6.3.1	Distinction of single emission centers in nanowire ensembles . . .	107
6.3.2	Photoluminescence of $\text{In}_x\text{Ga}_{1-x}\text{N}/\text{GaN}$ nanowire ensembles with different composition	111
6.3.3	Calculation of transition energies	112
6.3.4	Limitation of 1d-model and suggested carrier localization	112
6.4	Impact of composition on $\text{In}_x\text{Ga}_{1-x}\text{N}$ nanowire LEDs	114
6.5	Strain engineering in nanowire heterostructures	115
6.5.1	Evidence for strain relaxation in $\text{In}_x\text{Ga}_{1-x}\text{N}/\text{GaN}$ nanowires from resonant Raman spectroscopy	116
6.5.2	Relaxation in strain-engineered nanowire heterostructures	118
6.6	Conclusion	120
7	Conclusions and Outlook	123
A	Sample list	127
B	Statistical fluctuation of self-induced GaN nanowire morphology	133
C	Calibration of material supply rates in molecular beam epitaxy	137
	Bibliography	139

1 Introduction

Semiconductors are the technological base of electronic switches, amplifiers, memory, sensors, and much more. These devices are small, reliable, and cheap. Many everyday applications are not thinkable now without semiconductors, just to name rectifiers and computers. Energy-efficient light sources have become another field of application, and semiconductors now bring the mass market of general lighting under revolution. Light-emitting diodes (LEDs) can be designed to emit only light in the visible spectrum. Therefore, the light generation principle is more efficient than in other light sources: it incurs no conversion losses from ultra-violet light, as do gas discharge lamps, and no waste heat is generated by broad infrared emission, in contrast to incandescent lamps. Red and yellow-green LEDs of low intensity were produced in the 1960s,^[1] but compared to classical semiconductor applications, solid-state lighting has matured only recently.

In the development of semiconductors, there are two key factors to innovation. First, the semiconducting material has to be produced in large volumes with high perfection. To this end, silicon (Si) single crystals are well developed and form the base of the semiconductor devices that are produced in the largest mass today. LEDs and other optoelectronic devices, as well as high-power and high-speed switches, however, require compound semiconductor materials such as gallium arsenide (GaAs) and gallium nitride (GaN). The key to white light generation based on electroluminescence was the successful synthesis of gallium nitride (GaN) films of high crystal quality in the mid-1990s.^[2,3] The second source of innovation in semiconductor development is the ever-increasing integration density, which largely defines the cost, and hence the usefulness, of a semiconductor device. At present, the lateral structure size in silicon-based integrated circuits approaches physical limits, and fundamentally new device geometries are being explored. New solutions are expected from material and device physicists.

One way to achieve high-quality material and to depart from building devices on the planar wafer surface is to use semiconductor crystals in the shape of nanowires. The growth of filamentary crystals, with diameters in order of 10 nm to 100 nm and lengths in the order of μm , was reported in the 1960s,^[4] but nanowires were not envisaged as building blocks for devices until the 1990s.^[5] The high surface-to-volume ratio, the possibility of self-assembly, and the unique quantum-mechanical and electrostatic properties of nanowires can be exploited in new device concepts. Nanowires have been proposed for low-power electronics (tunnel FET),^[6] biological and chemical sensors,^[7] LEDs,^[8] and more.

GaN-based LEDs are made by growing thin films of GaN and (Al,Ga,In)N alloys onto foreign substrates such as silicon carbide, sapphire, or silicon. These LEDs possess a comparatively simple device structure, and their development and commercialization has largely been tied to progress in material synthesis. GaN, which is difficult to obtain free of crystal defects in planar films, can be grown in the shape of nanowires with excellent crystal quality.^[9] GaN nanowires can be obtained on a range of substrate materials, including amorphous silicon oxide.^[10] The promise of a high crystal quality is the first motivation for LEDs based on nanowires. Thin film LEDs are made of different crystals grown coherently onto each other. Lattice-mismatch of two crystals in a heterostruc-

1 Introduction

ture induces strain, and the crystal quality is often compromised by imperfections at the interface. Another benefit of nanowires is expected from the elastic relaxation of lattice-mismatch strain. While strain relaxation in heterostructures can in principle be obtained in top-down nanostructuring, better results are obtained from the self-assembly of nanowires without introducing dislocations. Defect-free heterointerfaces were reported in bottom-up grown nanowires.^[11]

It is particularly motivating to conduct scientific research when a technological benefit from the scientific results is conceivable. In this sense, GaN nanowire-based devices are a rewarding object of study, because the two key factors of technological innovation in the field of semiconductors are addressed: material synthesis and nanostructuring. The guideline of this thesis is the synthesis of $\text{In}_x\text{Ga}_{1-x}\text{N}/\text{GaN}$ nanowire heterostructures as a building block for a nanowire LED device. This study has multiple interests: First, physical models are developed for this specific crystal growth. Second, the elastic and optical properties of the heterostructures are analyzed, and methods are derived to control these properties by designing the crystal growth process. The results of these two study efforts on growth and properties of $\text{In}_x\text{Ga}_{1-x}\text{N}/\text{GaN}$ nanowires are universal, in the sense that they are not application-specific. In addition to that, the simple device structure of an LED allows to test the practical implications of nanowire heterostructure design: A third aspect of this research is the feasibility of $\text{In}_x\text{Ga}_{1-x}\text{N}/\text{GaN}$ nanowire LEDs with a controlled emission color.

As a starting point, a simple LED is described in Ch. 2, and the $\text{In}_x\text{Ga}_{1-x}\text{N}$ properties are discussed which directly impact the luminescence. Advantages of the nanowire geometry for LEDs are explained, and the method of manufacturing a nanowire LED in the laboratory is outlined.^[12] In the following chapters of this thesis, the LED device will be withdrawn from the center of attention, in favor of the analysis and physical modelling of the $\text{In}_x\text{Ga}_{1-x}\text{N}/\text{GaN}$ nanowire crystal growth and optical properties.

In principle, substrates accessible to GaN nanowire growth include metals, ceramics and glass, which may allow savings in production cost even compared to silicon. The experimental growth technique, and the criteria for the choice of alternative substrates, are introduced in Ch. 3. Experimental results will be reported from GaN nanowire growth on titanium, which is shown in this thesis for the first time.

The self-induced nanowire ensembles under study here exhibit characteristic statistical fluctuations. Complexity is added by the inherent non-uniformity of the elastic strain in mismatched nanowire heterostructures, which is detailed in Ch. 4. Conventional semiconductor characterization techniques cannot be directly applied to the structure studied here, and new methods of interpreting x-ray diffraction and Raman spectroscopy were developed in the course of this work. Chapter 4 describes these methods, and credits especially the contributions made by Vladimir M. Kaganer and Manfred Ramsteiner at the *Paul-Drude-Institut für Festkörperelektronik* (PDI).

Control over the emission wavelength of an LED requires the predictable growth of the In-containing active region. At the starting point of this thesis, very little was known about the underlying growth mechanisms. Chapter 5 develops the main objective of this thesis, the controlled growth of axial $\text{In}_x\text{Ga}_{1-x}\text{N}$ quantum wells in GaN nanowires. Series of growth experiments are described that permit to study the impact of the temperature and the material supply rates on the growth of $\text{In}_x\text{Ga}_{1-x}\text{N}$ segments in GaN nanowires. The indium (In) incorporation into the crystal is limited by desorption of In during the crystal growth. A growth model is formulated that allows to predict the alloy composition from a quantitative *in-situ* measurement of the In desorption. The change in

composition between samples of one series is confirmed *ex situ* with the newly developed statistical methods.

With the knowledge gained from the growth analysis, the structure of the $\text{In}_x\text{Ga}_{1-x}\text{N}$ quantum wells was systematically varied in series of experiments. Chapter 6 reveals that a controlled shift of the emission color was obtained in nanowire LED demonstrator devices. A detailed comparison with the behavior of a planar active region indicates that for an understanding of the light emission mechanism in nanowire LEDs, the radial distribution of electronic states has to be taken into account. In this chapter, too, a general approach to strain engineering in nanowire heterostructures is discussed. Simple design rules are derived from detailed numerical calculations. Values for the average strain in $\text{In}_x\text{Ga}_{1-x}\text{N}$ quantum wells in nanowires are obtained from the simulation of resonant Raman spectra, in order to prove the applicability of the design criteria.

Chapter 7 will conclude the findings and the open questions, and provide an outlook for future research.

2 The GaN-InN material system for solid-state lighting

General concepts of semiconductor physics and the operating principle of GaN-based LEDs will be introduced in the following. The purpose of this chapter is to highlight which structural parameters influence the behaviour of an LED, and why $\text{In}_x\text{Ga}_{1-x}\text{N}$ /GaN NWs are a promising alternative to planar films. The presentation relies to a large extent on the introductory LED book by E. F. Schubert,^[1] to which the reader is also directed for a deeper discussion of the device physics. Information specific to nitride semiconductors can be found in the handbook by H. Morkoç.^[13] The method of NW LED device integration used here was developed in the doctoral thesis of F. Limbach^[12] and is explained briefly at the end of the chapter.

2.1 Light-emitting diodes (LEDs)

Light can be emitted from a solid when an electron changes its quantum mechanical state from a higher to a lower energy. The behavior of an electron is described by the Schrödinger equation, which is fulfilled by wavefunctions with the wavevector \mathbf{k} . The energy state of the electron corresponds to the eigenvalue $E(\mathbf{k})$. In a solid, the electrons are subject to the electrostatic potential of atoms which are so close together that the electron wavefunctions overlap. It was shown by Felix Bloch in 1928 that, as a consequence, the electron states form continuous energy bands, as opposed to free electrons with quantized energy states.^[14] In the special class of semiconducting materials, the allowed energy bands are separated by a bandgap: at very low temperatures, practically all electrons on the outer shell occupy the valence band up to the energy E_V , and the material is insulating. Electrons can, however, be thermally excited into the conduction band above the energy E_C . They become charge carriers, and the material is now conductive. (The density of states in the conduction band is analogous to free electrons, and the occupation is governed by the Fermi distribution function.) An electron state can return to the valence band by emitting a photon with an energy close to the bandgap $E_g = E_C - E_V$. In other words, the wavelength λ of the light emitted by a band-to-band transition is given by $\lambda \approx hc/E_g$. ($hc \approx 1240 \text{ nm eV}$)

For the light emission process to occur, according to the Pauli principle, an occupied state in the conduction band and an unoccupied state in the valence band must be present. In a picture made popular by William Shockley around 1950,^[15] unoccupied states in the valence band can be described as holes. By exchanging the ionization between two atoms, holes can move in the valence band, and can therefore be described analogously to electrons in the conduction band. This picture is sketched in Fig. 2.1. Emission of a photon can occur if the electrons and holes recombine. The arrows in the figure indicate another condition for radiative recombination: the electron and hole must be close to each other, i. e. their wavefunctions must overlap spatially.

The band structure of a semiconductor determines if radiative recombination of elec-

2 The GaN-InN material system for solid-state lighting

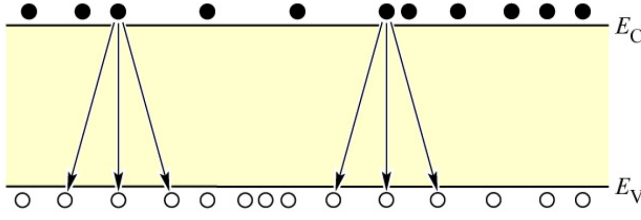


Figure 2.1: Illustration of electrons in the conduction band and holes in the valence band of a semiconductor. The arrows indicate electron-hole recombinations in real space. From Ref. 1.

trons and holes is likely to occur. Similar to a free electron, the dispersion relation of electrons and holes is parabolic, as shown in Fig. 2.2. Electrons will thermalize to the valence band minimum, and holes to the conduction band maximum. Since the momentum of the emitted photon is negligible, momentum conservation requires that both have a common k . Materials with such a band structure, so-called direct bandgap semiconductors, include many compound semiconductors. Silicon, however, possesses an indirect bandgap, and photon emission occurs at a negligible rate and only accompanied by momentum transfer to the crystal lattice.

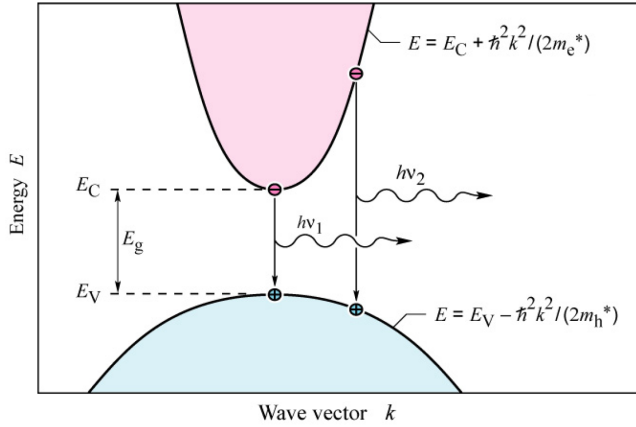


Figure 2.2: Illustration of electron and hole dispersion relations for a direct-bandgap semiconductor, and recombination in momentum space. From Ref. 1.

Electron-hole pairs can be created by photoexciting the semiconductor. This is done in photoluminescence spectroscopy (PL), which is used as a characterization tool in this thesis. LEDs, however, are electrically driven (electroluminescence, EL) and employ a p-n junction. The following will explain how a p-n junction can electrically inject electrons and holes into the active region of an LED device.

If foreign atoms of higher valence replace a native atom in the crystal lattice, for example Si at a Ga-site in GaN, the surplus electron is only loosely attached. The Si atom is a donor with an electronic state E_D close to the conduction band. (The ionization energy $E_C - E_D$ is much smaller than the bandgap.) The material is said to be ‘n-doped’. The donors are ionized at room temperature, freeing electrons into the conduction band and increasing the electron concentration n .^[16] At room temperature, the conduction electrons from donor ionizations dominate over intrinsic conduction electrons, and the Fermi level E_F is shifted from the center of the bandgap towards the conduction band. Conversely, a foreign atom of lower valence, such as Mg at a Ga-site, is an acceptor, and shifts the Fermi level to the valence band. Ionization of the acceptors creates holes in the valence band, increasing the hole concentration p .

A p-n junction is formed by bringing regions of both types in contact. The band diagram and occupation under zero bias are shown in Fig. 2.3(a). Particles can travel between the p- and the n-side. Thus, a band bending occurs to align the respective Fermi

2.1 Light-emitting diodes (LEDs)

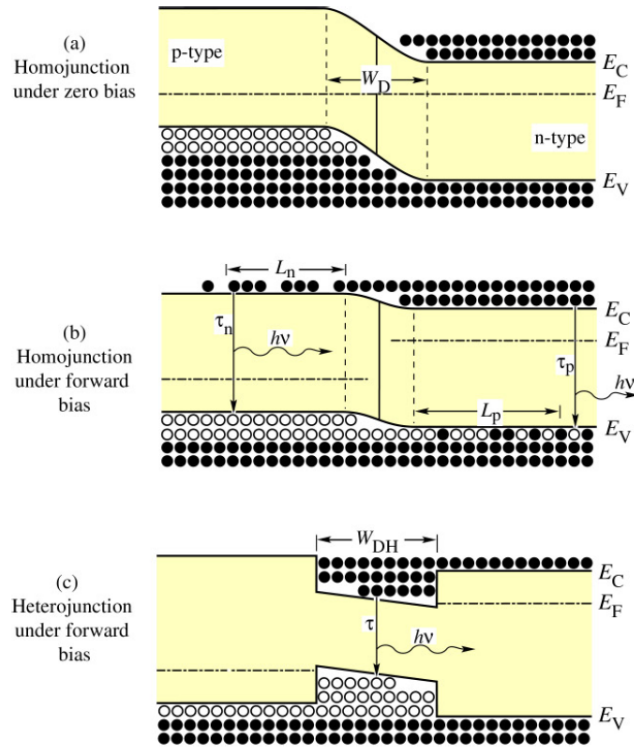


Figure 2.3: Illustration of LED active regions embedded in a p-n junction. (a) The p-n junction is depleted under zero bias, no recombination occurs. (b) Forward bias promotes diffusion current of electrons and holes, providing minority carriers and allowing recombination and luminescence. (c) A double heterostructure active region can form a quantum well (QW). The QW can act as a diffusion barrier and drastically increase the carrier density and the recombination efficiency. From Ref. 1.

levels. The potential gradient makes electrons in the n-type region and holes in the p-type region drift away from the junction. A depletion region of the width W_D is created, which is kept in equilibrium by the oppositely directed diffusion currents of electrons and holes. No luminescence occurs. Figure 2.3(b) shows a p-n junction under forward bias. The externally applied voltage promotes diffusion current of both carrier types. Electroluminescence can occur by recombination of electrons and holes, which are now brought together. In this homojunction, however, electrons diffuse over L_n and holes over L_p , which limits the concentrations n and p at any given location. Significantly higher EL intensity is obtained in LEDs possessing a quantum well (QW) in the active region. The QW is formed by introducing a material of lower bandgap. (In a GaN-based LED, the QW is typically $\text{In}_x\text{Ga}_{1-x}\text{N}$.) The double heterostructure creates potential barriers for the diffusion current, as shown in Figure 2.3(c). The width W_{DH} can be made much lower than the diffusion lengths, thereby increasing the carrier concentrations in the active region, and hence the recombination rate R , since $R \propto np$ (bimolecular recombination rate, cf. Ref. 1).

The efficiency of light creation in the active region depends on the carrier capture in the QW. Figure 2.4 indicates that the carrier distribution onto the conduction band states in the QW can extend to energies high enough for carrier escape. In typical LED devices, this is counteracted by an electron blocking layer (EBL). The EBL is a thin layer of a material of higher bandgap ($\text{p-Al}_x\text{Ga}_{1-x}\text{N}$), located at the p-side of the active region, and aligned at the valence band edge by p-doping.

The layers of different materials that constitute the elements of an LED device have to be obtained by successive epitaxial crystal growth. This is fundamentally different from silicon electronics, where a p-n heterostructure can be obtained, for example, by diffusion or implantation. Established methods for the growth of crystal heterostructures are metal-organic vapor phase epitaxy (MOVPE) and molecular beam epitaxy (MBE, see

2 The GaN-InN material system for solid-state lighting

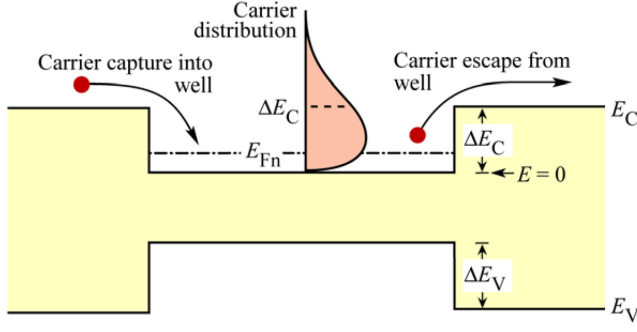


Figure 2.4: The band profile of a QW and the distribution of electrons on energy states in the conduction band are symbolized. The effectiveness of carrier capture in the QW depends on the barrier height ΔE_C . From Ref. 1.

Sec. 3.1). With an active region as simple as the structure discussed so far, commercial green GaN-based LED devices were grown by MOVPE, starting in 1994.^[3,17] Figure 2.5 shows a sketch of the complete LED device, with the n-type GaN grown on a sapphire substrate. The substrate is insulating, and therefore a groove has to be etched for the n-electrode. The inset shows the band alignment of the EBL made from p-Al_xGa_{1-x}N.

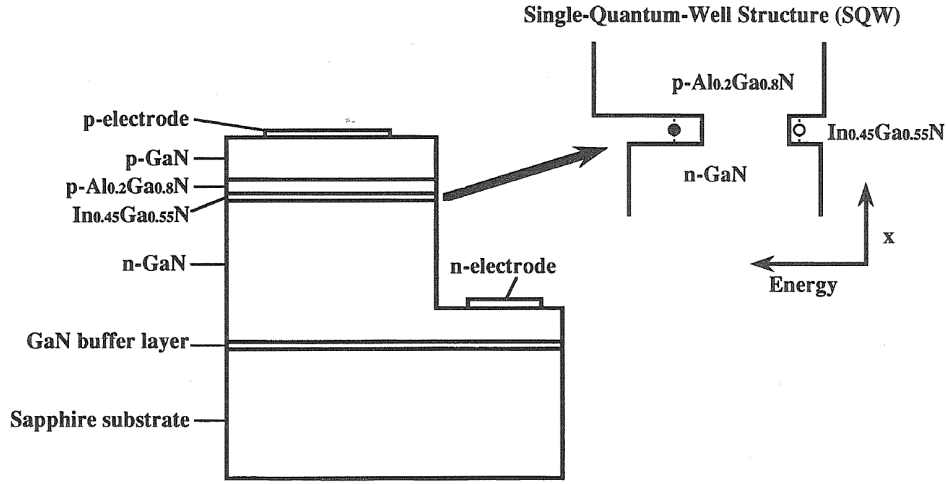


Figure 2.5: Vertical structure of a simple GaN-based LED. The arrow points to the band profile of the single quantum well and electron blocking layer at the p-side.^a From Ref. 3.

The wavelength of the light emitted by an LED depends on the available optical transitions. Quantum-mechanical confinement in the QW can separate the electron and hole energy states by more than the bandgap E_g , and the second key parameters for the LED color is therefore W_{DH} . Effects specific to the emission from In_xGa_{1-x}N QWs are discussed below in Sec. 2.2.2. The exact photon energy depends also on the type of recombination. For example, in a perfect crystal, an electron and a hole are tied together by Coulomb interaction and form an exciton. At low temperatures, excitonic recombination prevails, and the photon energy is E_g less the exciton binding energy. The emission spectrum is narrow, in the order of meV. The exciton can be bound to an impurity, such as a donor, which will further reduce the optical transition energy. The luminescence behaviour at low temperatures is irrelevant for LED operation, but can be used for sample characterization (see Secs. 3.4.3). At room temperature, where the characteristic thermal

^aNote that the indicated nominal In_xGa_{1-x}N composition represents the precursor ratio during crystal growth, and the In content in LED QWs is typically lower.

energy $k_B T$ is higher than the exciton binding energy for GaN, free electron-hole recombination dominates, and the thermally activated filling of the energy band broadens the emission spectrum to a theoretical linewidth of 46 meV.^[1]

White-light sources based on LEDs are made either by combining multiple active regions in one or several chips, or with wavelength converters. In the latter approach, for example, a simple blue-emitting LED device such as the one in Fig. 2.5 can be packaged in a transparent dome containing a Ce-doped YAG phosphor.^[3] The phosphor is then excited by the blue light and emits yellow fluorescence.

LEDs are superior to other light sources in the sense that the conversion efficiency of electrical energy to light of a specific wavelength can in principle be unity at room temperature. The efficacy of an LED is limited by several factors, among which are (i) power dissipation during the electrical injection of carriers into the active region, (ii) non-radiative recombination (via deep levels of crystal defects or Auger processes), and (iii) absorption of photons within the device. A detailed discussion of the efficacy of GaN-based LEDs, and some advanced device structures, can be found in Ch. 1 of Ref. 18.

To summarize this section, an LED is based on a direct bandgap semiconductor. The active region is a QW structure, embedded in a p-n junction. Color definition is obtained by bandgap engineering of the QW, which must take into account the carrier confinement. From a physics perspective, a high density of electron-hole pairs must be achieved in the QW with a spatial overlap of electron and hole wavefunctions. Also, non-radiative recombination pathways must be reduced. It will be seen in the next section, that although $\text{In}_x\text{Ga}_{1-x}\text{N}$ is a suitable material for bandgap engineering, the latter two criteria impose design limits on present-day GaN-based LEDs.

2.2 Properties of III-nitrides

Materials with a suitable electronic band structure for LEDs can be found among the III-V compound semiconductor crystals. Figure 2.6 shows their bandgap E_g (left-hand y-axis) and crystal lattice parameter (x-axis). The wavelength of photon emission corresponding to a band-to-band transition is shown on the right-hand y-axis. There, the visible spectrum is also represented by the perceived colors. In the red to yellow-green spectral range, LEDs can be made from $\text{In}_{0.5}(\text{Ga}_{1-x}\text{Al}_x)_{0.5}\text{P}$. This alloy is lattice-matched to GaAs substrates, and the heterostructure can therefore be realized without introducing crystal defects. With high Al content ($x > 70\%$), however, the bandgap becomes indirect, and true green LEDs can not be achieved with this material system. LEDs in the green and blue spectral range are made from $\text{In}_x\text{Ga}_{1-x}\text{N}$, an alloy of InN and GaN. Figure 2.6 reveals that the bandgap of this material can cover the entire visible range. It is also seen, however, that changing the alloy composition brings about drastic changes in lattice parameter, which can impair the crystal growth at the heterointerface and the optical properties. Lattice-matched solutions with quaternary (Al,Ga,In)N heterostructures have been investigated,^[19] but have proven difficult to implement. With the advent of successful III-nitride synthesis, research on LEDs based on II-VI films (II-sulfides and II-selenides are lattice-matched to GaAs) was supplanted in around 1995.^[20]

The main drawback of III-nitrides is the lack of a lattice-matched substrate for epitaxial crystal growth. Native GaN substrates have remained too expensive for LED production until today. Table 2.1 lists the lattice parameters and the thermal properties of the III-nitrides and of the substrate materials sapphire (Al_2O_3), 6H-SiC and Si. These substrate materials are used for GaN production by heteroepitaxy. The lattice mismatch is given

2 The GaN-InN material system for solid-state lighting

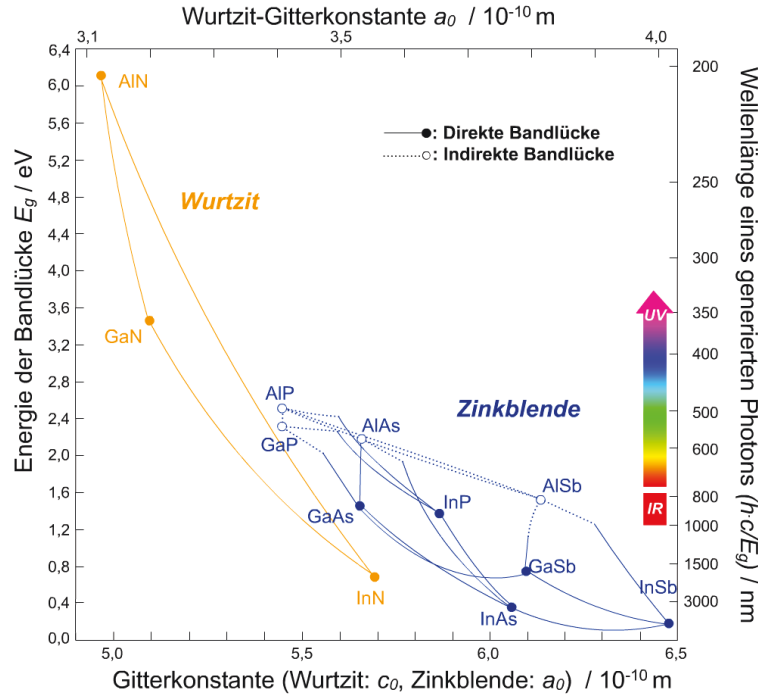


Figure 2.6: Bandgap and lattice parameter of III-V semiconductors. From Degreen, Wikimedia Commons.

for growth in the (0001)-plane, respectively the (111)-plane in cubic materials. The table shows that SiC is well suited for GaN growth, because it has a low misfit and a matching thermal expansion coefficient. SiC is expensive, however, and LED production has moved to sapphire, despite several disadvantages: the lattice mismatch is large, the mismatch in the thermal expansion causes wafer bowing, and the low thermal conductivity is detrimental to heat dissipation from simple devices such as in Fig. 2.5. GaN growth on Si will be discussed in Sec. 3.3. On these substrates AlN is sometimes used as an interlayer before GaN growth. Section 3.4 will address a novel approach to GaN growth on a Ti metal film, and the likely interface materials are included in Table 2.1 for completeness. The remainder of this section will focus on the properties of the III-nitride crystal that impact the light emission from an LED active region.

2.2.1 Crystal structure

GaN, when grown by MBE or MOVPE on common substrates [such as sapphire in the (0001)-plane], crystallizes in the hexagonal ‘wurtzite’ phase (α -GaN, h-GaN, space group $P6_3/mc$, no. 186) with a 2H stacking sequence. The less stable cubic polytype (‘sphalerite’ phase, β -GaN, c-GaN) with the 3C stacking can be synthesized on cubic substrates,^[21–23] generally with inferior crystal quality. The unit cells of the h-GaN polytype is drawn in Fig. 2.7(a), and that of c-GaN in Figs. 2.7(b) and (c), from two different perspectives. Low-index planes in the hexagonal unit cell are named in the literature as drawn in Fig. 2.8.^b

Comparing the figures 2.7(a) and (b) shows that the geometry of the chemical bonds in h-GaN and c-GaN is very similar. The gray oval areas highlight Ga-N pairs, which

^bIn keeping with the tradition at PDI, the crystallographic planes and directions are denoted with capitals in this work.

Table 2.1: Lattice parameters and thermal characteristics of III-nitrides and substrates for heteroepitaxy in the (0001)-plane. To clarify the mismatch value, the table lists for every material the length of the lattice translation vector which is compliant to the translation by the lattice parameter a in GaN. (The experimental determination of the in-plane orientation is discussed in Secs. 3.2.1 and 3.4.)

	space group	lattice parameters		thermal exp. $\Delta a/a$ (10^{-6}K^{-1})	thermal conductivity ($\text{W cm}^{-1} \text{K}^{-1}$)	compliance to GaN ($2d_{11\bar{2}0}^{\text{GaN}} = a^{\text{GaN}}$)	lattice mismatch (%)
<i>epilayers</i>							
AlN	P6 ₃ mc	3.10	4.97	4.2		$2d_{11\bar{2}0} = a$	−2.7
GaN	P6 ₃ mc	3.19	5.19	5.6			
InN	P6 ₃ mc	3.54	5.70			$2d_{11\bar{2}0} = a$	11.0
<i>substrates</i>							
sapphire	R $\bar{3}$ c	4.76	12.99	7.5	0.4	$2d_{3\bar{3}00} = a/\sqrt{3}$	−13.9
6H-SiC	P6 ₃ mc	3.08	15.11	4.2	4.9	$2d_{11\bar{2}0} = a$	−3.4
Si(111)	Fd $\bar{3}$ m	5.43		3.6	1.5	$d_{110} = a/\sqrt{2}$	20.4
<i>materials discussed in Sec. 3.4</i>							
TiN(111)	Fm $\bar{3}$ m	4.24				$d_{110} = a/\sqrt{2}$	−6.0
TiO(111)	Fm $\bar{3}$ m	4.18				$d_{110} = a/\sqrt{2}$	−7.3

alternate between two lateral positions in h-GaN, with an ABAB... stacking sequence (2H). When the stacking sequence extends to a third lateral position and is repeated as ABCABC... (3C), c-GaN is obtained. Figure 2.7(c) projects the c-GaN unit cell along the coordinate axes, making the cubic structure visible. During GaN crystal growth in C-direction, especially at low temperatures, stacking faults can occur. The stacking sequence, which is normally 2H, can change to 3C for one or several monolayers, creating thin layers of c-GaN in the h-GaN matrix. This will be discussed further in Sec. 5.3.2.

The wurtzite crystal structure has no inversion plane perpendicular to the C-axis, and h-GaN exhibits a spontaneous polarization $P_{\text{SP}} = -0.022 \text{ C/m}^2$ along this axis.^[26] III-nitrides have a high ionicity of the chemical bond, and the spontaneous polarization can be understood if the negative and positive charges of the Ga and N atoms are thought of as concentrated in ‘centers of gravity’. The lack of an inversion center means that these effective positive and negative charge centers are separated, and thus create an electric field. In the [0001]-direction, the crystal is said to be Ga-polar, because truncation of the Ga-N single bond [indicated by the gray area in Fig. 2.7(a)] leaves a Ga-terminated surface. In the opposite [000 $\bar{1}$]-direction, the crystal is N-polar. The wurtzite structure is non-polar on the M - and A -axes, and the effective polarization can in principle be chosen to suit the device application by selecting an oblique orientation.^[27,28] Present-day conventional GaN-based LEDs, however, are grown in the C-plane.

The polarization in nitride semiconductor heterostructures is critically dependent on strain: the forced deformation of the crystal structure induces a piezoelectric polarization P_{PZ} . As seen above, the relaxed lattice of InN is 11 % wider than that of GaN. A coherently grown $\text{In}_x\text{Ga}_{1-x}\text{N}$ QW on a planar GaN film experiences compressive in-plane strain. As seen in Fig. 2.6, blue LEDs are made with $x \approx 10\%$, equivalent to about -1% in-plane strain ($\Delta a/a$) in the QW. If no plastic relaxation occurs via the introduction of misfit dis-

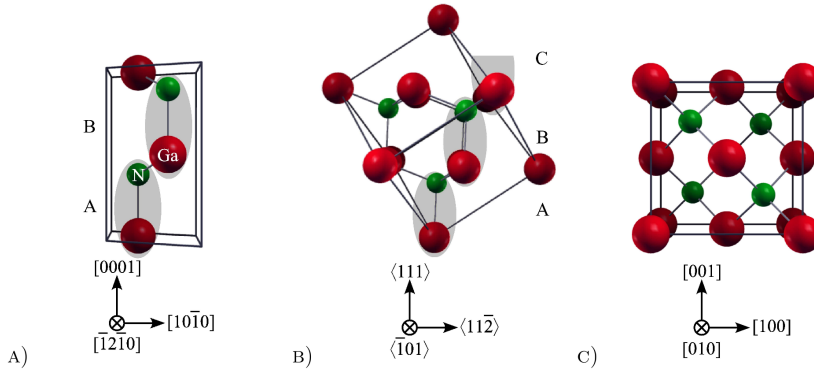


Figure 2.7: GaN unit cells of two polytypes differing in stacking sequence. (a) Hexagonal, or wurtzite, α -GaN with 2H stacking. (b) and (c) Cubic, or sphalerite, β -GaN with 3C stacking, in two projections. From Ref. 24

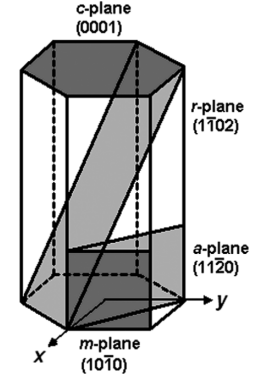


Figure 2.8: Planes in the hexagonal unit cell. From Ref. 25.

locations at the heterointerface, and the GaN film retains its bulk lattice constant, the QW is said to be fully elastically strained. In this situation, the Poisson effect induces a tensile out-of-plane strain ($\Delta c/c$) in C-direction of about 0.5 %. This strain creates a piezoelectric polarization $P_{PZ} = 0.008 \text{ C/m}^2$.^[29] Due to the lattice mismatch in this example, the strain changes abruptly at the heterointerface, and the polarization changes by P_{PZ} (if P_{SP} is equal in the neighboring materials). Under high tensile out-of-plane strain, the QW can be thought of as a plate capacitor, with positive charges at the Ga-face, and negative charges at the N-face. In GaN-based LEDs, the QW thickness is in the order of 3 nm, and the polarization field can be up to 2 MV/cm for typical $\text{In}_x\text{Ga}_{1-x}\text{N}$ compositions.^[28,30] The consequences for light emission will be introduced in the following. Elastic strain relaxation and the measurement of strain in $\text{In}_x\text{Ga}_{1-x}\text{N}/\text{GaN}$ heterostructures by x-ray diffraction and Raman spectroscopy will be the subject of Ch. 4.

2.2.2 Light emission from $\text{In}_x\text{Ga}_{1-x}\text{N}$ quantum wells

The bandgap of the $\text{In}_x\text{Ga}_{1-x}\text{N}$ alloy depends on the composition, the temperature, and the strain. References to the numerical determination of the bandgap is given in this paragraph for later use. In the presence of shear strain, the bandgap can be calculated with the Bir-Pikus 6×6 Hamiltonian. For this work, the parameters and an algorithm were provided by O. Brandt.^[31–33] If $\text{In}_x\text{Ga}_{1-x}\text{N}$ is under biaxial strain, as is the case in planar LED devices, an approximation for the bandgap can be given:

$$E_g(x, \varepsilon) = xE_g^{\text{InN}} + (1-x)E_g^{\text{GaN}} - bx(1-x) - c\varepsilon_{xx}. \quad (2.1)$$

In this expression, the bandgaps E_g^{InN} and E_g^{GaN} are 0.63 eV^[34] and 3.447 eV,^[35] respectively. The bowing parameter b was obtained by O. Brandt as 1.595 eV from a fit of the data in Ref. 35. He also derived the strain correction $c = 0.8 \text{ eV}$ from the elastic constants^[36] and the deformation potentials for fully biaxially strained $\text{In}_x\text{Ga}_{1-x}\text{N}$ on GaN.

In an $\text{In}_x\text{Ga}_{1-x}\text{N}$ quantum well the transition energy of radiative recombination deviates from the bandgap because of several effects:

- Due to localization of the wavefunction in the QW, the electron ground state is above E_C , and the first hole state below E_V . By itself, this effect results in a blueshift

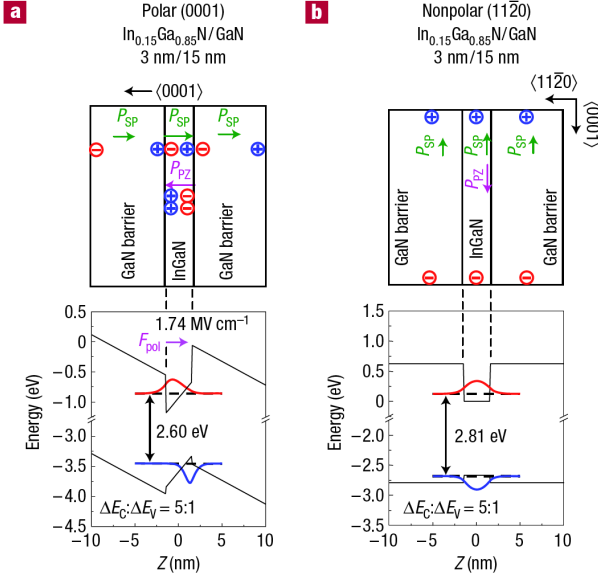


Figure 2.9: Illustration of the quantum-confined Stark effect (QCSE). $\text{In}_{0.15}\text{Ga}_{0.85}\text{N}/\text{GaN}$ QWs in the polar C-plane (a), and in the non-polar A-plane (b). The top images show the layer structure and polarization fields, the bottom images show the band profile. From Ref. 39.

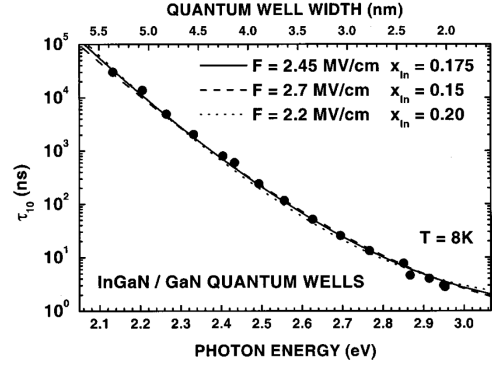


Figure 2.10: Time-resolved PL data from $\text{In}_x\text{Ga}_{1-x}\text{N}/\text{GaN}$ QWs of constant composition but varying thickness. With increasing thickness, the QCSE induces a redshift of the emission and a reduced probability of radiative recombination, reflected in the higher PL decay time τ_{10} . The piezoelectric field F is obtained as a fit parameter. From Ref. 40.

of the emission.

- The piezoelectric field draws the electron to the Ga-face of the QW, and the hole to the N-face. With increasing distance, the transition energy decreases, i. e. the emission is redshifted. This is the quantum confined Stark effect (QCSE).^[29,37]
- Local alloy fluctuations result in In-rich clusters with a bandgap lower than the average of the QW. Localization of carriers and recombination in such clusters induces a redshift.

The electron and hole states can be obtained for a QW with known structural parameters by solving Schrödinger-Poisson equations in a self-consistent way. For a planar film, a one-dimensional calculation along the plane normal is sufficient.^[38] The agreement of such calculations with experiments on planar films depends on the degree of alloy fluctuations, which induce a redshift. Figure 2.9, taken from a work by Chichibu *et al.*,^[39] illustrates the QCSE by comparing the results of the Schrödinger-Poisson calculation for $\text{In}_{0.15}\text{Ga}_{0.85}\text{N}/\text{GaN}$ QWs in the polar C-plane (a), and in the non-polar A-plane (b). The QW thickness is 3 nm. At the top, the layer structure and polarization fields are sketched, and the spontaneous and piezoelectric polarizations are shown together with the respective interface charges. At the bottom, the band profiles, ground states and wavefunction amplitudes are shown. The redshift of the transition caused by the QCSE in the polar QW is evident from the lower transition energy of 2.6 eV, compared to the transition in the non-polar QW of 2.8 eV.

A second consequence of the QCSE is a reduced probability of radiative recombination, because the electron and hole wavefunctions are spatially separated. This can be seen at low temperature, where the lifetime of the charge carrier pairs in time-resolved

PL (TRPL) is an indication for the transition probability. Figure 2.10, which is reproduced from Lefebvre *et al.*, Ref. 40, shows the time τ_{10} of PL intensity decay to a tenth of the maximum after pulsed excitation of $\text{In}_x\text{Ga}_{1-x}\text{N}/\text{GaN}$ QWs. The QWs have identical composition, and the variation in photon energy (bottom axis) is due to the QCSE and a variation in QW thickness. The corresponding QW thickness is shown at the top axis. Increasing the QW thickness from 2 nm to 5.5 nm increases τ_{10} by four orders of magnitude. Since competing non-radiative recombination paths are always present in real QW structures, the QCSE lowers the luminescence intensity dramatically for thick QWs. The thickness of QWs in polar GaN-based LEDs has to be kept in the order of 5 nm or below. The recombination in typical $\text{In}_x\text{Ga}_{1-x}\text{N}$ layers is aided by alloy fluctuations. (Details on $\text{In}_x\text{Ga}_{1-x}\text{N}$ growth will be given in Ch. 5.) In-rich clusters act as carrier localization centers and inhibit the spatial separation of electrons and holes by the QCSE.^[39]

Currently, GaN-based LEDs are available in the blue and green spectral range, with In content in the QWs up to about 17%. In the longer wavelength range, the internal quantum efficiency is drastically reduced at high current densities. The origin of this so-called ‘droop’ effect is under debate,^[41,42] but crystal defects likely play a role. The green-yellow spectral range is presently not covered by high-efficiency LEDs, neither made from $\text{In}_x\text{Ga}_{1-x}\text{N}$ nor from $\text{In}_{0.5}(\text{Ga}_{1-x}\text{Al}_x)_{0.5}\text{P}$. This fact is referred to as the ‘green gap’.^[43] If more In could be incorporated in the QW without compromising crystal quality, the red spectral range might be within reach of GaN-based LEDs. This could simplify the device integration of polychromatic light sources, and also alleviate the use of phosphorus.

One path to improving the luminous efficacy of GaN-based LEDs is to reduce the piezoelectric field in the QWs. To this end, planar devices can be grown on nonpolar or semipolar crystal planes, and devices have been produced in that way.^[28] Another way is to relieve the strain in polar QW by elastic relaxation. This is possible in axial heterostructures in nanowires, as will be shown in the following.

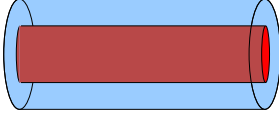
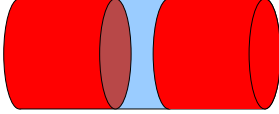
2.3 Nanowires as an alternative to planar LED device geometry

Lattice mismatch in heteroepitaxy poses two challenges for the design of an LED based on GaN films: First, a substrate such as SiC must be chosen that is almost lattice matched, or buffer layers must be introduced to manage strain and misfit dislocations, at the cost of thick epitaxial growth. Second, the luminescence intensity of $\text{In}_x\text{Ga}_{1-x}\text{N}$ QWs is compromised by strain and misfit dislocations. LED device concepts based on GaN nanowires (NW) can respond to both of these challenges. As will be discussed in detail in Sec. 3.3, GaN NWs can be grown bottom-up with high crystal quality on lattice-mismatched substrates. For the design of the active region in GaN NW LEDs, there are two principal possibilities that are summarized in Table 2.2.

GaN nanowires can be grown along the crystallographic C-axis. One possibility for the active region is then to grow $\text{In}_x\text{Ga}_{1-x}\text{N}$ QWs radially on the side facets. The side facets are non-polar, and although a radial QW would still be subject to strain induced by the lattice mismatch, the QCSE would be absent. Another aspect of this radial layout is the increased surface area of the active region, compared to a planar device. The second possibility is to arrange the same device structure as in Fig. 2.5 axially in the NW. When the in-plane dimension of a mismatched crystal heterostructure is small, interface strain can relax laterally. Axial NW heterostructures can be obtained by nanostructuring the active region after the growth of a C-plane film. With decreasing NW diameter, increased PL intensity,^[44] a blueshift of the emission,^[45,46] and a decreased radiative lifetime at low

2.3 Nanowires as an alternative to planar LED device geometry

Table 2.2: Strategies for LED devices based on GaN-nanowires grown along the C-axis.

In _x Ga _{1-x} N/GaN heterostructure geometry	quantum well alignment	characteristic differences to C-plane planar device
<p>radial</p> 	M-plane (nonpolar)	<ul style="list-style-type: none"> • no QCSE • increased area of the active region
<p>axial</p> 	C-plane (polar)	<ul style="list-style-type: none"> • reduced QCSE • elastic strain relaxation

temperature^[46] showed that the piezoelectric field in nitride QWs can thus be reduced. Post-growth structuring cannot, however, eliminate interface defects due to plastic relaxation. A further step is taken by using bottom-up grown NWs, which allow elastic strain relaxation during the growth. Defect-free heterointerfaces can be obtained in the bottom-up growth of axial nanowire heterostructures.^[11,47,48] A potential benefit common to both NW LED layouts is the enhanced outcoupling of light. This is based on the consideration that a light wave cannot be confined in a space smaller than the wavelength, and hence internal reflection is suppressed in comparison to planar films.^[49]

GaN nanowires are investigated in this thesis as a means to expand the possibilities of strain management in heterostructures. GaN NW-based LEDs with axial In_xGa_{1-x}N/GaN heterostructures are used as a practical example. Managing the strain in lattice-mismatched semiconductor heterostructures by introducing free surfaces in nanostructures is not only a perspective for LEDs, but can improve the performance of other devices as well. Azize *et al.* have shown, for example, that strain control enhances the carrier mobility in a transistor channel.^[50]

GaN NW-based LEDs with an axially arranged active region have been fabricated by several groups.^[8,51-57] Emission wavelengths were obtained that reach far into the infrared, indicating that this device structure may permit to bridge the ‘green gap’. Figure 2.11(a) shows the arrangement of substrate, base NW, and axial heterostructure that is common to the reported bottom-up grown GaN nanowire LEDs.

The strain relaxation in a QW placed axially in a NW can be calculated by the finite-element method, and the result is shown in Fig. 2.11(b). The relaxed lattice constant of the QW is larger than that of the base NW and cap. Therefore, the NW side facets bulge at the position of the QW. (As discussed above, the typical mismatch values in QWs of GaN-based LEDs are in the order of 1 %, and the displacement in the figure is exaggerated for clarity.) The component ε_{zz} of the strain tensor, indicating the lattice distortion in the direction of the NW axis, is represented by the color. The significant result is that large portions of the base NW, QW and cap, that are shown in green, are strain-free. Because of the lattice coherence, strain relaxation is gradual across the interfaces. The strain is non-uniform in the heterostructure, and the maximum and minimum values are observed at the surface (red in the QW and black in the base NW). An efficient way to estimate the strain in axial NW multi-quantum well structures will be presented in Ch. 4 The

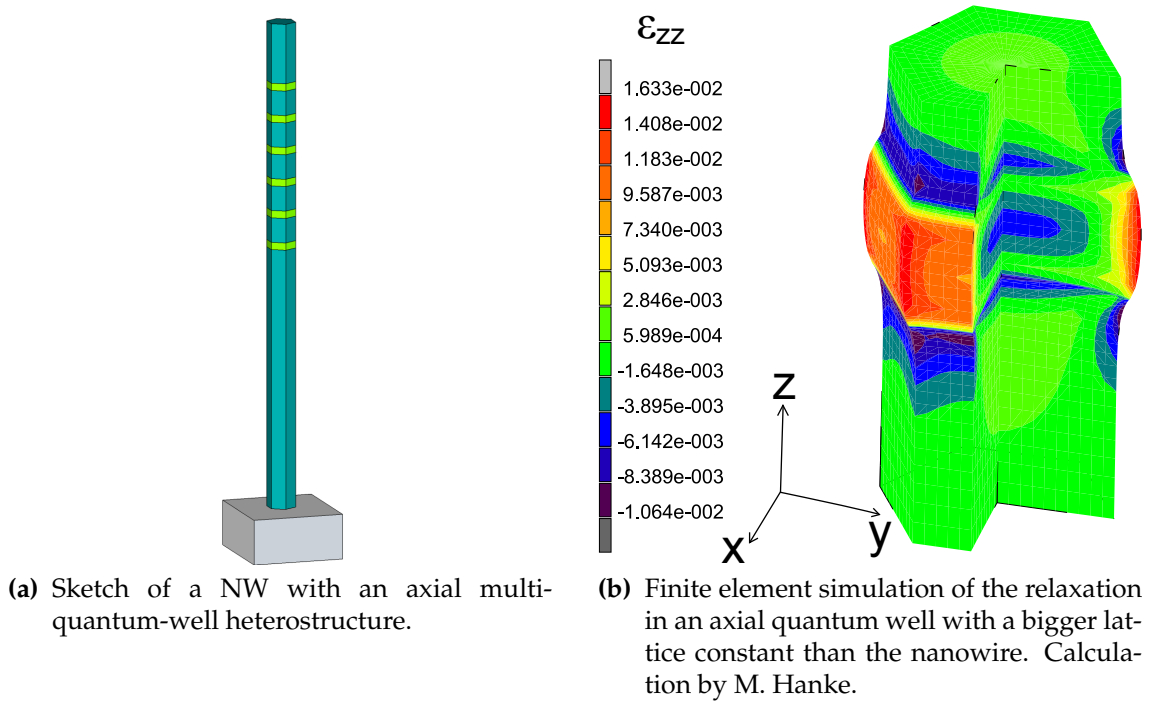


Figure 2.11: Arrangement and relaxation of axial $\text{In}_x\text{Ga}_{1-x}\text{N}/\text{GaN}$ MQWs in a nanowire.

possibilities of strain engineering in $\text{In}_x\text{Ga}_{1-x}\text{N}/\text{GaN}$ NWs will be discussed in Sec. 6.5.

To maximize elastic strain relaxation during crystal growth, and to use alternative substrates, the NWs must be produced in a bottom-up approach. Growth environments can be used that have been developed for planar films: MBE, MOVPE, and halide vapor epitaxy, for example. A long-established method for bottom-up NW synthesis is the vapor-liquid-solid growth.^[4] The crystal forms only within the footprint of the particle, leading to NW growth. GaN NWs can be synthesized with the help of a catalyst material, too. A more attractive way of producing such NWs is the self-induced growth by plasma-assisted molecular beam epitaxy (MBE),^[58] because this process does not require any foreign collector material and results in GaN of outstanding quality.^[59]

2.4 Integration of a nanowire LED device

The $\text{In}_x\text{Ga}_{1-x}\text{N}/\text{GaN}$ nanowire multi-quantum well structure, which was developed in this thesis, was tested in NW LED devices with Si substrates. The vertical structure of the test devices is essentially the same as the simple planar device shown in Fig. 2.5, but with four QWs. The self-induced NWs grow vertically on the substrate and can be contacted in parallel, as was already shown by Kishino and co-workers in 2004.^[8] They obtained a common p-contact by merging the NWs during lateral crystal growth in the Mg-doped p-GaN region. Highly doped n-Si(111) allows to use the substrate as a back contact.

In this work, the self-induced NWs were grown isolated from one another and planarized with spin-on-glass^c prior to depositing a transparent p-contact. This planariza-

^cHydrogen silsesquioxane (HSQ) electron beam spin-on resist, offered as 'Dow Corning XR-1541 E-Beam Resist.'

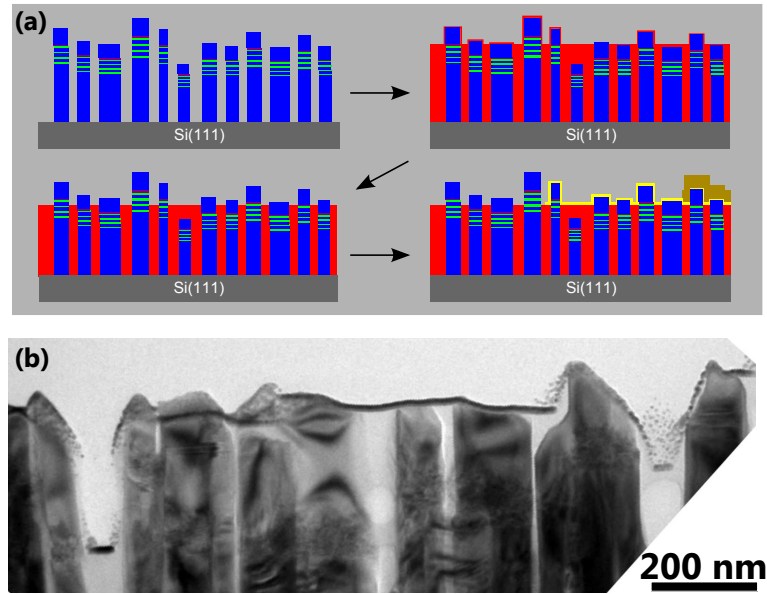


Figure 2.12: Nanowire LED device planarization and p-contact fabrication. (a) Process steps: self-induced GaN NWs with LED structure grow vertically on Si \rightarrow the space between the NWs is filled with spin-on-glass \rightarrow insulation of the p-GaN cap by spin-on-glass is removed by reactive ion etching \rightarrow deposition of Ni/Au transparent contact and Ti/Au electrode. (b) Cross-sectional transmission electron microscope bright-field image. The Ni/Au transparent contact is seen as a thin dark contrast connecting the NW tips.^[57]

tion has the benefit that the NWs form a stable layer. The ‘NW layer’ can, for example, be processed for emission from the n-side by removal of the substrate.^[60] The test devices discussed here, however, were made by the nanowire LED process developed at PDI by Friederich Limbach.^[12,57] His work included the definition of the n-doping of the GaN:Si NW base, the growth conditions for the GaN:Mg cap, and the planarization and contacting.

The sequence of process steps for planarization and fabrication of the p-contact is shown in Figure 2.12(a): (i) Self-induced n-GaN NWs with $\text{In}_x\text{Ga}_{1-x}\text{N}$ /GaN MQW, EBL and p-GaN cap grow vertically on Si(111), (ii) the space between the NWs is filled with spin-on-glass, (iii) the insulation of the p-GaN cap by spin-on-glass is removed by reactive ion etching, and (iv) a transparent Ni/Au contact (5 nm / 5 nm) and Ti/Au electrodes and bond pads (10 nm / 90 nm) are deposited. The cross-section transmission electron microscope image in Figure 2.12(a) shows a thin dark line connecting the NW tips, which represents the Ni/Au transparent contact and shows that all NWs within the image are contacted.

The n-contact is formed at the back side of the Si wafer by removing the oxide with an HF dip and depositing an Al/Au film (50 nm / 50 nm).

3 Growth and in-situ analysis of group-III-nitride nanowires

The aim of this thesis is the controlled synthesis of $\text{In}_x\text{Ga}_{1-x}\text{N}$ heterostructures in GaN nanowires. GaN nanowires do not only form the technical basis of heterostructures and prospective LED devices, but have also been studied in more depth. The concepts of GaN NW growth are presented in this chapter in preparation of the heterostructure synthesis. Studies on InN NW growth are available in literature.^[61,62] The specific problems of ternary alloy growth will be dealt with in Ch. 5.

For this thesis, GaN NWs were synthesized by molecular beam epitaxy. The distinguishing feature of this technique is the ultra-high vacuum. The mean free path is long enough for atoms to reach the substrate by a straight-line path.^[63] Precise control of the adatom fluxes by shutters is possible, and foreign material as well as particles formed by parasitic reactions in the growth chamber can largely be avoided. Another benefit of the long mean free path is the feasibility of *in-situ* surface analysis by electron diffraction and *in-situ* desorption study by line-of-sight QMS.

The growth of III-nitrides in MBE has been studied in the last twenty years in parallel with the industrialization of MOVPE-grown material.^[13,64] Aside from providing a technical solution for the synthesis of high-quality planar material, the focus has been on understanding the atomic processes during the crystal growth. More recently, III-nitride nanowire growth by MBE has also been studied in detail, and GaN nanowires are reproducibly obtained.^[58]

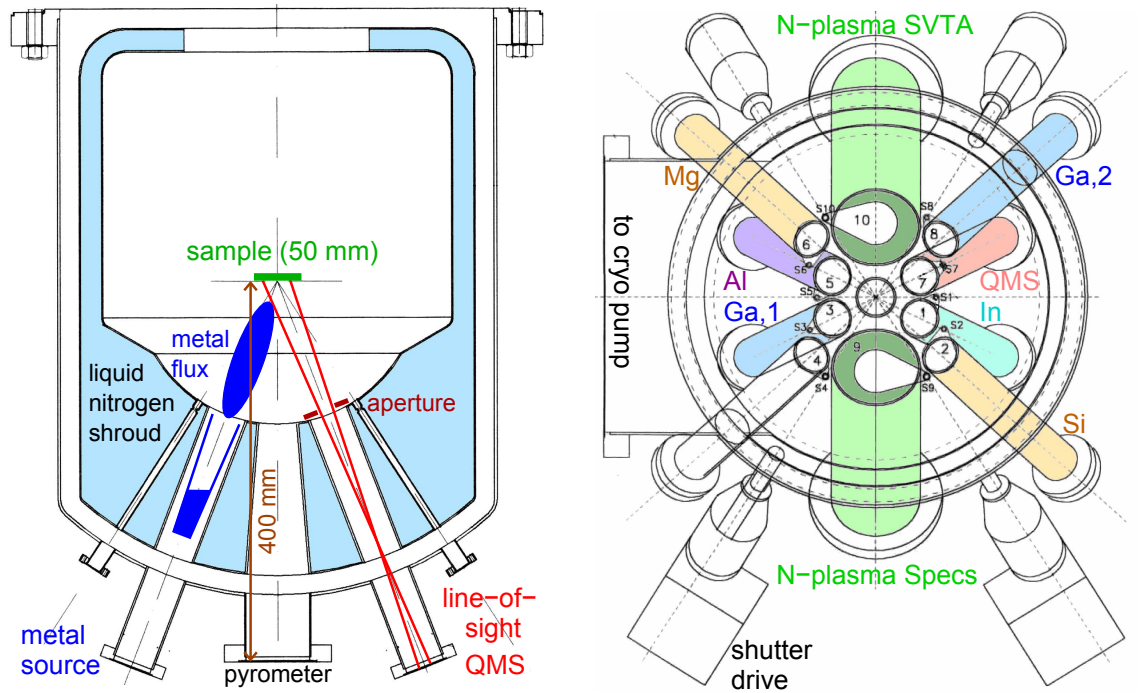
This chapter introduces the experimental methods used in MBE as well as the established models for the growth of III-nitrides in the form of planar films and nanowires. Finally, Sec. 3.4 will reveal how these principles can be applied to the development of a new GaN NW nucleation ‘recipe’ for the growth on a metal surface.

3.1 Molecular beam epitaxy

The experiments in this study were carried out in the MBE 8 system at the Paul-Drude-Institut, built in 1995 by *Createc Fischer GmbH*. A base pressure in the growth chamber below 10^{-10} torr was obtained^a in stand-by with a cryo pump and an ion getter pump. To achieve this base pressure, the growth chamber contains a cooling shroud filled with liquid nitrogen, where residual water vapor condenses. The cooling shroud is shown in the cross section in Fig. 3.1(a). During the growth experiments, the growth chamber pressure was typically 10^{-5} torr, with only the cryo pump working against an N_2 flow of 2 sccm. The sample is heated from above with a filament, controlled by a thermocouple (T/C). The sample temperature is monitored by a pyrometer mounted centrally at the bottom of the growth chamber.

The source ports are located at the bottom of the growth chamber at different angles from the sample surface normal. Figure 3.1(a) shows the alignment of the source ports

^aData log from growth chamber ion gauge (channel gc.ig1), March 2011.



(a) Scale drawing of the vertical cross section. The placement of a metal effusion cell is sketched with an idealized directional characteristic of the beam. The aperture limits the QMS collection area on the sample.

(b) Horizontal cross section in top view, indicating the source and QMS placement used from Feb. 2010 until Oct. 2011. The shutters are shown in closed position.

Figure 3.1: MBE 8 growth chamber setup, showing the arrangement of the sources and the QMS. Based on drawings from Createc Fischer GmbH.

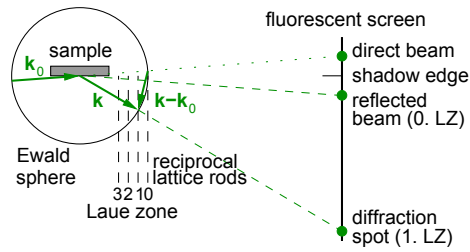
on the inner ring. Here is also visible that, in MBE 8, the large cooling shroud encloses the sources laterally, thereby eliminating the need for water cooling of the effusion cells (at the cost of nitrogen consumption). One source port is occupied by the line-of-sight quadrupole mass spectrometer (QMS). An aperture on the cooling shroud, also visible in Fig. 3.1(a), defines the collection area visible to the QMS to a circular area of 3 cm diameter in the middle of the sample. Active N can be provided by two radio-frequency plasma sources,^[65,66] herein named the *Specs* and *SVTA* sources, after their respective manufacturer. The fluxes of the metals In, Al, and Ga as well as of the dopants Si and Mg are obtained from effusion cells.^[63] Figure 3.1(b) depicts the placement of the cells for the growth experiments within this study. The calibration of the source fluxes is detailed in App. C.

3.2 In-situ analytical methods in molecular beam epitaxy

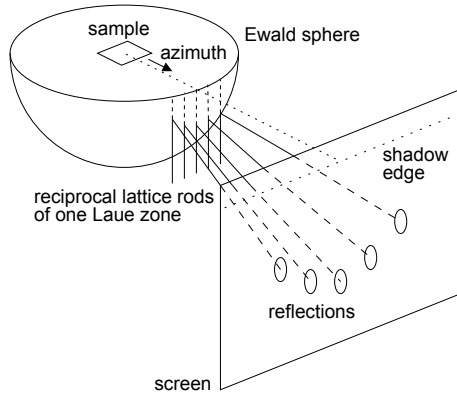
The ultra-high vacuum in MBE allows to perform extensive growth analyses *in situ*. Electron diffraction on the sample surface during growth will be discussed in this section, as well as the detection of the rate and mass of desorbing atoms. These two methods are complementary. As an example of their application, the consistency check of the pyrometer reading will be demonstrated in conclusion.

3.2.1 Reflection high-energy electron diffraction

Reflection high-energy electron diffraction (RHEED) is established as a powerful tool in MBE, and is routinely used to investigate growth mode, growth rate, flatness, crystal structure, adlayer formation, facet angles, and epitaxial relations of heterostructures.^[67–69] RHEED observation of well-known temperature-dependent processes, such as melting, evaporation^[70,71] and surface reconstruction^[72] can support the temperature calibration. The surface diffraction is illustrated in Fig. 3.2(a). Electrons hit the sample with the wave vector \mathbf{k}_0 . Constructive interference, and therefore high intensity of the scattered wave with the vector \mathbf{k} , is obtained when $(\mathbf{k}_0 - \mathbf{k})$ equals a translation in the reciprocal lattice. Elastic scattering requires that all possible \mathbf{k} are of equal length. They can thus be described by the ‘Ewald sphere’. Under grazing incidence on a perfectly flat crystal surface, the electron wave is scattered only from the topmost atomic layers. Information about the out-of-plane lattice is absent, and the reciprocal lattice points become vertical rods. Reflections on the screen can be constructed from the intersection of these rods with the Ewald sphere. The reflections appear on rings, as depicted in Fig. 3.2(b).



(a) Ewald construction.



(b) Projection onto the screen.

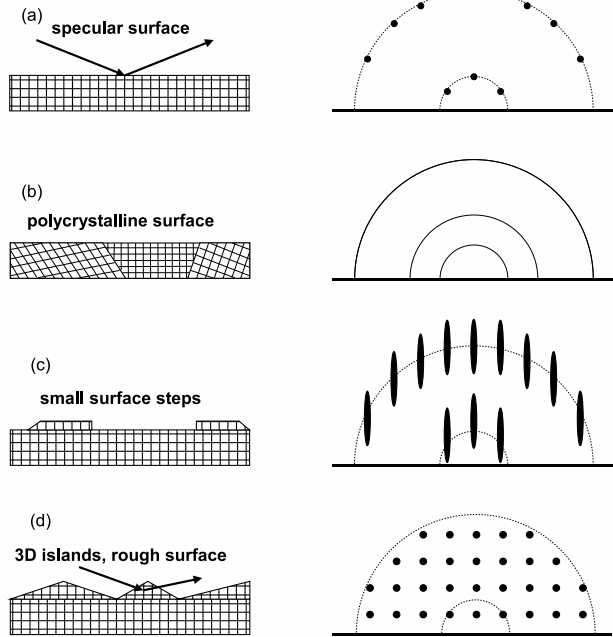


Figure 3.3: RHEED patterns. From Ref. 74.

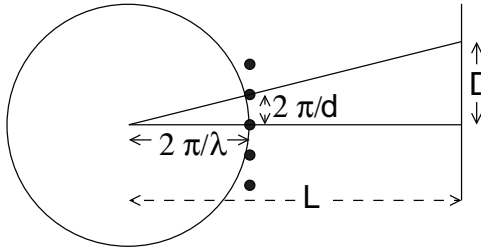
Figure 3.2: RHEED geometry.^[73]

The diffraction patterns are characteristic for the surface roughness. A detailed account is given by Ichimiya and Cohen in Ref. 68, Ch. 8. The principal features of RHEED patterns for the purpose of this thesis are shown in Fig. 3.3. Diffraction from a perfect crystal surface (a), with thin reciprocal lattice rods, leads to a pattern of laterally equidistant reflections located on circles centered on the incident beam. If the sample is polycrystalline (b), angular information with respect to rotation about the incident beam is lost, and a ring pattern appears. If the surface is not perfectly smooth, but composed of flat domains of finite size (c), the reciprocal lattice rods are broadened, and the intersections with the Ewald sphere form streaks. Finally, if the electron wave travels through three-

3 Growth and in-situ analysis of group-III-nitride nanowires

dimensional features on a rough surface (d), out-of-plane information is restored to the reciprocal lattice, which is 'projected' onto the screen.

The spacing of crystal planes d is inversely proportional to the distance D of the diffraction spots on the RHEED screen. Since the scattering angle is small, the Bragg condition can be simplified to Eq. (3.1). This equation is visualized by the intercept theorem.^[73] λ is the wavelength of the electron beam (accelerated at 20 kV in this work), and L is the distance between the sample and the screen (camera length). A practical procedure is to measure D for a pair of known reflections and calculate λL . Tentative assignment of other reflection spots on the screen to reciprocal lattice vectors can then be tested by comparing calculated and measured values for D .^[75,76]



$$\frac{2\pi/d}{D} = \frac{2\pi/\lambda}{L} \Rightarrow d = \frac{\lambda L}{D} \quad (3.1)$$

Typical RHEED images obtained during the growth of GaN NWs on Si(111) are shown in Fig. 3.4. The figure is organized in two columns, showing images of the screen in two angular positions of the sample that yield diffraction patterns of high symmetry. The orientation of the crystal dominating the diffraction is indicated by the coordinate system next to each image. Within each column, the sample orientation is unchanged, and the epitaxial relation of GaN NWs can be obtained. The spacing D of distinctive reflection spots and the corresponding crystal lattice spacing $\lambda L/D$ is also given for each image. Because of the characteristic horizontal spacing of the reflections, these two high-symmetry azimuths are sometimes called 'narrow-spaced' and 'wide-spaced'.

A clean Si(111) sample surface with the (7×7) reconstruction as shown in Fig. 3.4(a) is obtained after oxide removal with the Ga polishing procedure described in Sec. 5.2.^b

During the growth of GaN NWs at about 800 °C, clear transmission diffraction spots from h-GaN are observed. The GaN(0001) plane (C-plane) grows parallel to the Si(111) substrate surface. In-plane, GaN $[\bar{1}\bar{1}00] \parallel \text{Si}[11\bar{2}]$, and GaN $[11\bar{2}0] \parallel \text{Si}[\bar{1}\bar{1}0]$.^[77] In this orientation, GaN NWs match the Si lattice with a one atom to one atom correspondence and a strain of -17% .^{[78]c} Small imperfections of in-plane alignment (twist), that is a random fluctuation of rotation of the NWs about the growth axis, can not be seen in the stationary azimuths. If the in-plane orientation of the NWs is completely random, both the 'narrow' and 'wide' patterns will superimpose in any azimuth. Imperfections in out-of-plane alignment (tilt) will broaden the reflections to rings as sketched in Fig. 3.3(a). This effect is present to a small extent in the experimental images in Fig. 3.4(b). Forbidden reflections $hk.l$ in the narrow-spaced azimuth ($h = -k$) are 00.1, 00.3, 00.5, etc. In RHEED, they do appear due to diffraction from multiple NWs. In the wide-spaced azimuth ($h = k$) all reflections with *odd* l are forbidden. That is why the smallest vertical spacing in the latter azimuth is twice that of the former.^d

^bThe contrast of the reconstruction spots is not ideal, but typical for work on MBE 8 in July 2010. All the images shown in Fig. 3.4 are acquired under identical beam conditions.

^cA second possible orientation was reported in literature that would show the narrow-spaced GaN $[11\bar{2}0]$ azimuth aligned with the wide-spaced Si $[11\bar{2}]$ azimuth.^[78] No evidence for this orientation was found in the present work by RHEED, XRD or SEM (see App. B).

^dThe weak contrast at $\frac{1}{2}\frac{1}{2}.l$ with l odd is of unknown origin. This phenomenon is not specific to GaN NWs

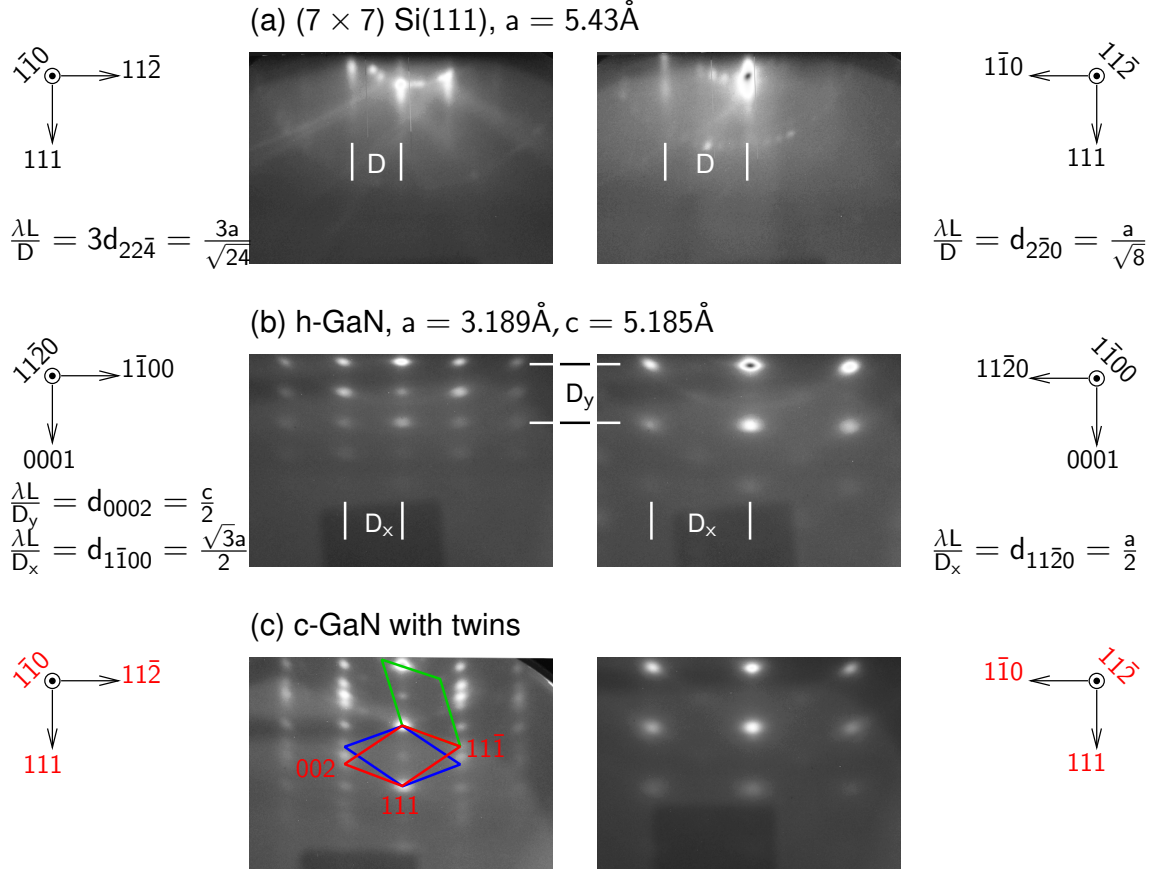


Figure 3.4: RHEED patterns of GaN grown on Si(111). Each column shows a fixed azimuth. The coordinate system of the dominant crystal and the spacing of the diffracting planes are shown on the margin. (a) (7×7) Si(111) reconstruction indicating a clean surface. These two images were acquired by T. Gotschke. (b) Diffraction pattern during GaN NW growth at about 800°C . (c) Additional diffraction spots in the narrow-spaced azimuth indicating the formation of GaN in the cubic polytype.

During GaN growth by MBE at lower temperatures, insertions of the cubic polytype, c-GaN, can form in nanoscale islands^[24,80] and in NWs.^[81] This can readily be observed by RHEED. The images in Fig. 3.4(c) are obtained during the same growth experiment as Fig. 3.4(b), but after lowering the growth temperature from about 800°C to about 600°C , the temperature typically used for the growth of $\text{In}_x\text{Ga}_{1-x}\text{N}$. In both azimuths the previously observed h-GaN reflections are still present, but in the narrow-spaced azimuth, diffraction from c-GaN is seen in addition. The translation vectors 002 , 111 and $11\bar{1}$ are shown in red, in the sketched coordinate system. These vectors construct some of the additional spots. Under these growth conditions, GaN forms a multitude of stacking faults and twins in the main (111) growth plane, but also on equivalent $\{111\}$ planes pointing away from the NW axis. Two of the possible twin orientations are indicated by the blue vectors which mirror the crystal about the ‘red 111 -axis’ in the growth plane, and the

and has also been observed in $\text{In}_x\text{Ga}_{1-x}\text{N}$ by TEM. The explanation attempt in Ref. 79 by $\text{In}_x\text{Ga}_{1-x}\text{N}$ ordering is unconvincing and contradicted by this observation on GaN NWs. [F. Glas, private communication]

3 Growth and in-situ analysis of group-III-nitride nanowires

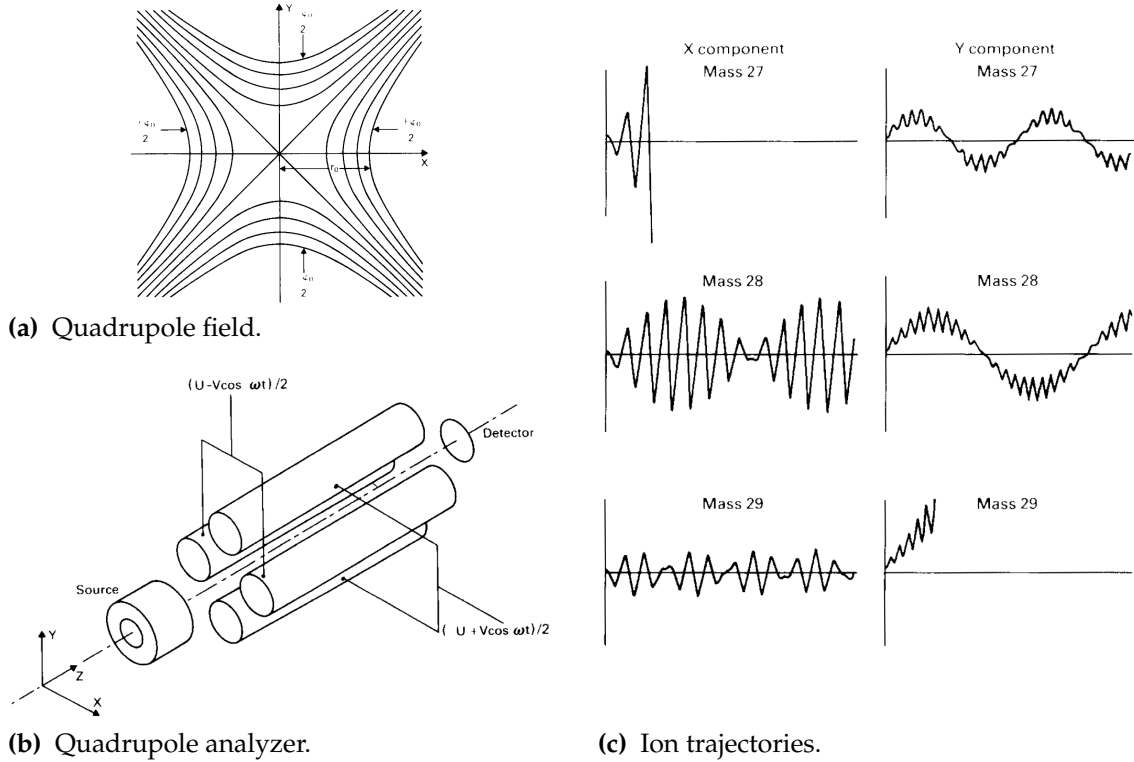


Figure 3.5: Quadrupole mass spectrometer: principle of operation. From Ref. 86.

green vectors which mirror about the 'red $11\bar{1}$ -axis'. c-GaN formation is not visible in the wide-spaced azimuth.

3.2.2 Line-of-sight quadrupole mass spectrometry

Mass spectroscopy is routinely used for the residual gas analysis in vacuum chambers. In the variant used here, the spectrometer is arranged in line-of-sight from the substrate and can identify the rate and species of desorbing atoms. The data from QMS is particularly useful for the quantitative study of growth kinetics, i. e. nucleation, decomposition, and desorption. Ga desorption from GaN^[82] and from Si^[70] were studied using QMS, as well as GaN decomposition.^[83] During MBE growth experiments, a drop in the desorption can indicate nucleation and the beginning of crystal growth. In this way, QMS has been used to study the nucleation of planar GaN films^[84] and GaN NWs.^[85]

The operational principle of a quadrupole mass spectrometer is well explained in an article by J. H. Batey.^[86] In brief, residual gas atoms are ionized at the entry to the mass spectrometer. The charged particles then travel in z -direction through an electric field with equipotential lines in the x, y -plane as shown in Fig. 3.5(a). This field is created between four electrodes, arranged as in Fig. 3.5(b), by a combination of direct and alternating voltages. A particle is deflected from its original path according to equations of motion which are generally divergent, but stable for a certain mass, defined by the quadrupole geometry and the applied potential. Batey illustrates this with the figure reproduced here in Fig. 3.5(c). Ions with a of mass 27 u have an unstable trajectory in the x -direction. Ions of 28 u have a stable trajectory and pass the filter, whereas heavier ions have an unstable trajectory in y -direction. The resulting ion current is a measure for the

partial pressure of an atomic species in the growth chamber.

In the present experiments, an SRS RGA200 QMS is mounted on a source port, in line of sight from the substrate, as shown in 3.1(a). The desorption of In and Ga atoms from the sample can thus be determined from the partial pressures of the ^{69}Ga and ^{115}In isotopes. This QMS possesses a continuous dynode electron multiplier to detect the ion current, which allows to measure partial pressures down to 10^{-12} torr.

3.2.3 In-situ metrology example: substrate temperature consistency check

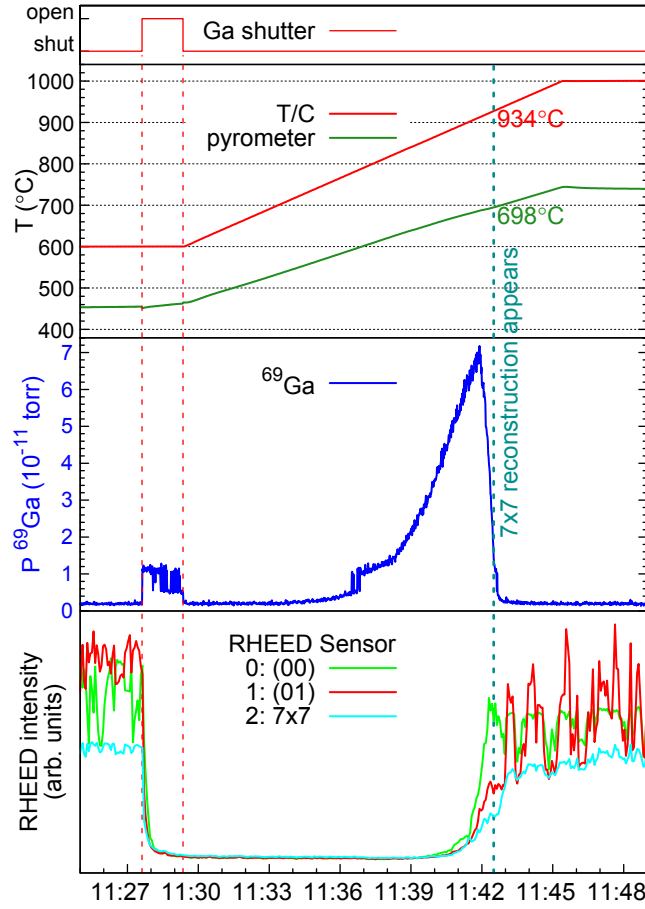
The information delivered by QMS and RHEED is complementary in the sense that QMS detects the desorption of adatoms while RHEED detects the appearance of a surface. This section will give an example of how these informations can be used in the MBE laboratory. QMS and RHEED are used for a consistency check of the pyrometer reading. At the same time, the temperature measurement in MBE is explained.

The sample holder temperature is regulated in MBE 8 by a PID controller in closed loop with a thermocouple (T/C). At the same time, the substrate temperature T is monitored with a Luxtron PhotriX pyrometer operating at 900 nm.^e GaN is transparent for infrared radiation and the pyrometer reading is therefore representative of the silicon surface. When an metal source shutter is opened, the reflection of the glowing effusion cell from the substrate can increase the pyrometer reading. The most representative value for T was obtained immediately before opening the metal source shutters. The biggest source of error in the pyrometer temperature is an obstruction of the viewport with debris, Ga droplets or parasitic growth. A quick check of the pyrometer reading was routinely carried out at the start of every growth experiment. This routine procedure can be followed in Fig. 3.6. The Ga shutter state, T/C and pyrometer temperatures, Ga desorption signal, and RHEED intensities are all plotted against the time of the day in (a). The RHEED image sensor areas where the intensities were integrated are marked in (b). By opening the Ga shutter, 40 ML Ga_{liq} are deposited onto the clean Si(111) substrate and subsequently evaporated at a fixed rate of temperature increase $dT/dt = 25^\circ\text{C}/\text{min}$. The same temperature reading should be obtained in every experiment at the moment time when all Ga is evaporated.^[70] The complete evaporation is indicated in two ways. Line-of-sight QMS shows the drop of the ^{69}Ga partial pressure, and the 7×7 reconstruction appears in RHEED. In the experiment shown here, at this moment, the pyrometer reads 698°C and the T/C 934°C . While the T/C reading is not representative of the sample temperature, the pyrometer reading can be reproduced with a typical precision of 1°C . This low deviation indicates the reliability of the pyrometer reading.^f

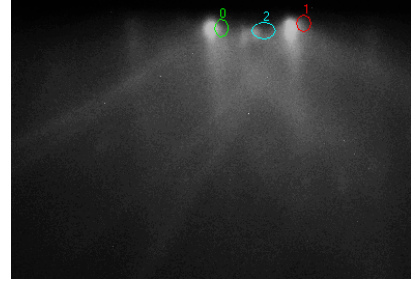
In the simple situation discussed here, QMS and RHEED deliver complementary information about the coverage of a surface with adatoms. In the study of NW growth, however, the diffraction pattern is always dominated by three-dimensional features, regardless of the presence of adatoms on the sample. This is most problematic during heterostructure growth, which ideally creates no changes in the diffraction pattern. GaN and

^eThe substrate is in the focal plane and a spot of 5 mm in the center of the 2" wafer is imaged. The difference between the thermocouple temperature reading and the substrate temperature given by the pyrometer could be more than $\pm 150^\circ\text{C}$, depending on the thermal gradient in the sample holder and parasitic thermovoltages at thermocouple interconnects in the vacuum chamber.

^fThis pyrometer check procedure is not as precise as the measurement of the time to full desorption at a constant temperature,^[71] but can be integrated efficiently with the temperature ramp-up immediately before GaN growth. In contrast to the typical standard deviation of 1°C , a stark difference of 40°C was observed in MBE 8 in Aug. 2010 as a result of viewport obstruction by a Ga droplet.



(a) (left) MBE protocol: Ga shutter times, thermocouple (T/C) and pyrometer temperature readings, ^{69}Ga partial pressure from QMS, and RHEED intensities.



(b) RHEED screen with indicated sensor areas for the intensity detection. 0: (00) specular beam. 1: (01) lattice rod. 2: 7×7 reconstruction. The pattern is not symmetric about the specular beam, because the sample orientation is slightly off the 'narrow' azimuth. The electron beam, and hence the position of the pattern relative to the sensor areas, swings with the heater filament current.

Figure 3.6: Illustration of the complementary *in-situ* techniques QMS and RHEED with the routine pyrometer test. A 40 ML adlayer of Ga_{liq} is first evaporated onto Si(111) by opening the Ga shutter for 104 s. The heater temperature is then raised at $25^\circ\text{C}/\text{min}$. The QMS detects an increasing ^{69}Ga desorption, until the adlayer is consumed. Complete desorption is indicated by the drop of the QMS signal and by the appearance of the 7×7 reconstruction.

$\text{In}_x\text{Ga}_{1-x}\text{N}$ in NW heterostructures can not be distinguished by RHEED for two reasons: First, the difference in diffraction pattern spacing is only in the order of 1 % ($x \approx 10\%$). Second, when the $\text{In}_x\text{Ga}_{1-x}\text{N}$ insertions are nm-sized, the electron beam is diffracted from both materials simultaneously. QMS, on the other hand, can be calibrated for any surface morphology, and can separate In and Ga directly. Within the *in-situ* methods, the weight is therefore shifted to QMS in this thesis.

3.3 Growth of GaN nanowires by molecular beam epitaxy

Crystal growth is a phase transition, and thermodynamics determines the driving force.^[87] A fully thermodynamic description is possible, however, only in special cases such as the crystal growth from a stoichiometric melt. This kind of growth close to equilibrium condition is considered as technologically difficult for GaN,^{[88]g} and impossible

^gThe melting temperature of the nitrides is very high, about 2800 K for GaN. Considering the reaction of synthesis of a metal nitride MeN , $\text{Me} + \frac{1}{2}\text{N}_2 \rightarrow \text{MeN}$, the strength of the triple bond of the N_2 molecule

3.3 Growth of GaN nanowires by molecular beam epitaxy

for $\text{In}_x\text{Ga}_{1-x}\text{N}$ within the miscibility gap.^[87]^h Contrarily, in MBE, growth occurs far from thermodynamic equilibrium, and the description must contain kinetic effects.^[91] Growth models take into account the competing processes of adsorption, desorption, surface diffusion, incorporation, and decomposition. A useful account of GaN growth by MBE is given in the Nitride Semiconductor Handbook by Hadis Morkoç, Vol. 1, Sec. 3.4.2.^[13]

The nucleation and growth of crystal films on a planar substrate is classically categorized into three mechanisms:^[92]

- atomic layer-by-layer growth of a bulk crystal, the Frank–van der Merwe (FM) growth,
- the formation of three-dimensional island, known as ‘Volmer–Weber’ (VW) growth,
- and layer growth up to a critical thickness, followed by roughening and three-dimensional island growth, the ‘Stranski–Krastanov’ (SK) mechanism.

These scenarios can be thermodynamically motivated, by considering the net energy difference of (i) crystallization from the vapor phase, (ii) the free surface energy of the adlayer and (iii) the interface energy of adlayer and substrate.^[93] If the growing film is of the same material as the substrate, or the interface energy is small compared to the surface energy of the adlayer, FM growth can occur. In contrast, high interface energy on a foreign substrate prevents wetting and leads to VW growth. In the event that a solid film on a foreign substrate initially wets the surface, strain may build up with increasing thickness, making further layer growth unfavorable, and thus leading to island growth by the SK mechanism.

GaN is grown in MBE at temperatures between 600°C and 900°C, and with V/III flux ratios close to unity. Up to now, device structures are grown almost exclusively in the C-plane. GaN substrates for homoepitaxy remain forbiddingly small and expensive. The typical choice of substrates is driven by cost, and has been evolving from silicon carbide via sapphire to silicon.^[94] GaN growth on foreign substrates by MBE either leads to a compact layer with a high defect density, or to a columnar structure with individual nanowires. The nanowires possess a hexagonal cross section bounded by *M*-plane side facets, and grow axially in the *C*-direction. Self-induced GaN NWs grown by plasma-assisted MBE on an AlN buffer layer and on silicon were reported since 1997.^[9,95] The V/III flux ratio and the growth temperature define the planar or columnar growth.^[96] These regimes are shown in Fig. 3.7 for growth under a fixed supply of N from the plasma source, $\Phi_{\text{N}} = 6 \text{ nm/min}$. At very high temperatures, all of the impinging Ga atoms desorb, and no growth occurs. The desorption of Ga is thermally activated, and therefore the required Φ_{Ga} to sustain any growth at all is an exponential function of the temperature. In the regime just below this temperature, the remaining Ga atoms are few compared to the N supply, and NWs are formed. This regime is characterized by a high V/III ratio. At yet lower temperatures, the critical amount of Ga remains on the surface for the growth of a compact layer. This regime is again defined by an exponential function governing the desorption of Ga.

shifts the balance to the constituent side of the reaction at high temperatures. In other words, the nitrides have a high decomposition N_2 pressure, requiring 20 kbar for growth of GaN from the solution at 2000 K. InN is even less stable.^[88]

^hThe $\text{In}_x\text{Ga}_{1-x}\text{N}$ alloy is thermodynamically unstable at high concentrations x and above a critical temperature T_c , and may decompose with no energy barrier into GaN and InN. The exact location of the miscibility gap has been discussed by Gerald B. Stringfellow.^[89] As he also acknowledges, however,

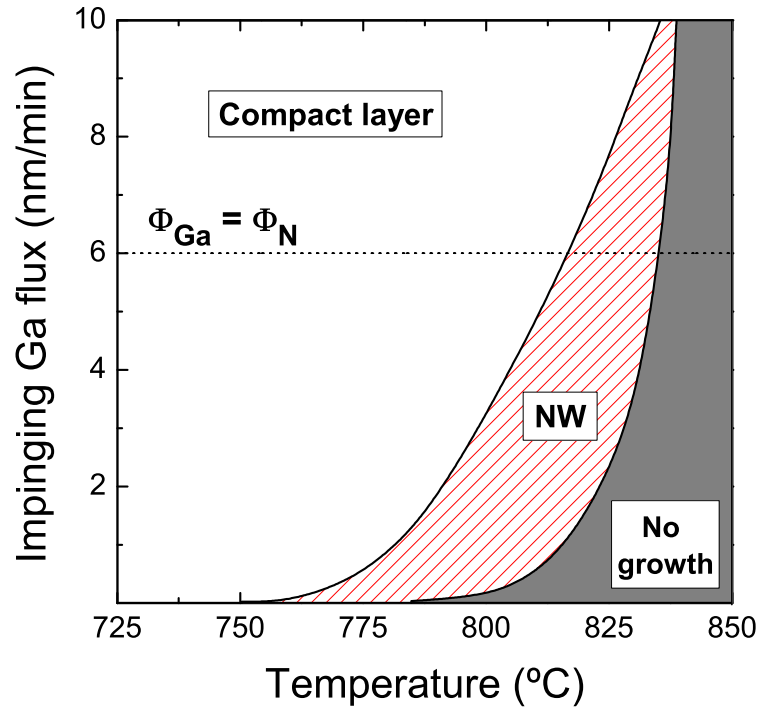


Figure 3.7: GaN growth diagram delimiting the compact and nanowire growth regimes as a function of Φ_{Ga} and T for a fixed nitrogen supply $\Phi_{\text{N}} = 6.0$ nm/min. From Ref. 96.

The growth of self-induced GaN NWs on silicon can be described by two successive regimes, that will be addressed in the following. The nucleation phase of GaN NWs can be described in terms of thermodynamics.^[97] During the later stage of NW growth, sidewall diffusion of adatoms contributes to the NW elongation.^[77,98] The classical thermodynamic growth models fall short of describing this behaviour, and instead, a kinetic description is then required.^[99]

3.3.1 GaN nucleation

Microscopic studies showed *ex situ* that the initial GaN nuclei are spherical cap-shaped both on AlN^[100] and on silicon^[10,97] substrates. An example of the latter is shown at the top of Fig. 3.8, reproduced from Ref. 97. In both cases, nucleation is followed by a shape transition and axial growth. The growth mode of GaN on AlN was classified as SK growth.^[101] This assignment is justified in the sense that GaN can arguably form a coherent interface on AlN, and the lateral dimension of a defect-free grain will be limited by the epitaxial misfit strain. The mechanism for GaN nucleation on silicon is less clear, because a Si_xN_y interlayer is formed in PAMBE.^[85,102–104] On the one hand, this interlayer transmits the crystal orientation of the substrate to the NW,^[103] indicating the same growth mechanism as on AlN.ⁱ (A comparison of the epitaxial alignment of GaN on both

infinitesimal compositional fluctuations will induce strain, which may stabilize the alloy against decomposition.^[90]

ⁱThe epitaxial orientation relationship between the GaN NWs and the Si substrate requires that the substrate is nitridated at high temperature,^[105] and is lost even then when the Si_xN_y becomes too thick.^[103]

3.3 Growth of GaN nanowires by molecular beam epitaxy

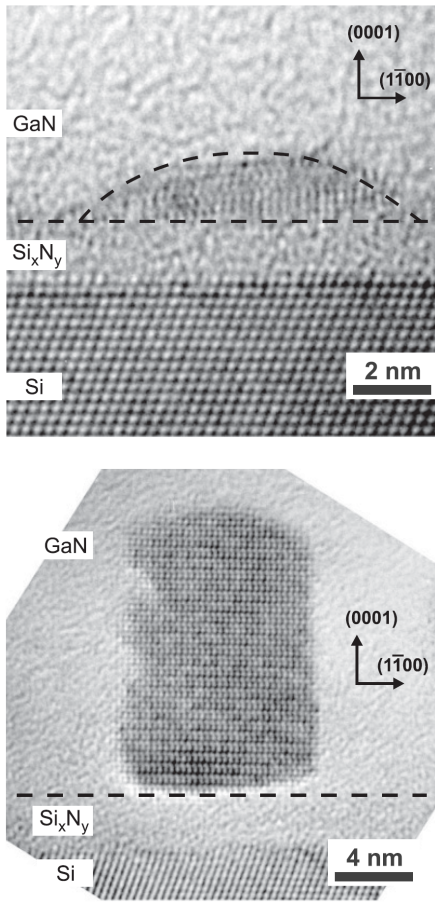


Figure 3.8: Shapes of GaN islands on Si_xN_y , seen by HRTEM in two samples grown for 7 min (top) and 16 min (bottom). From Ref. 97.

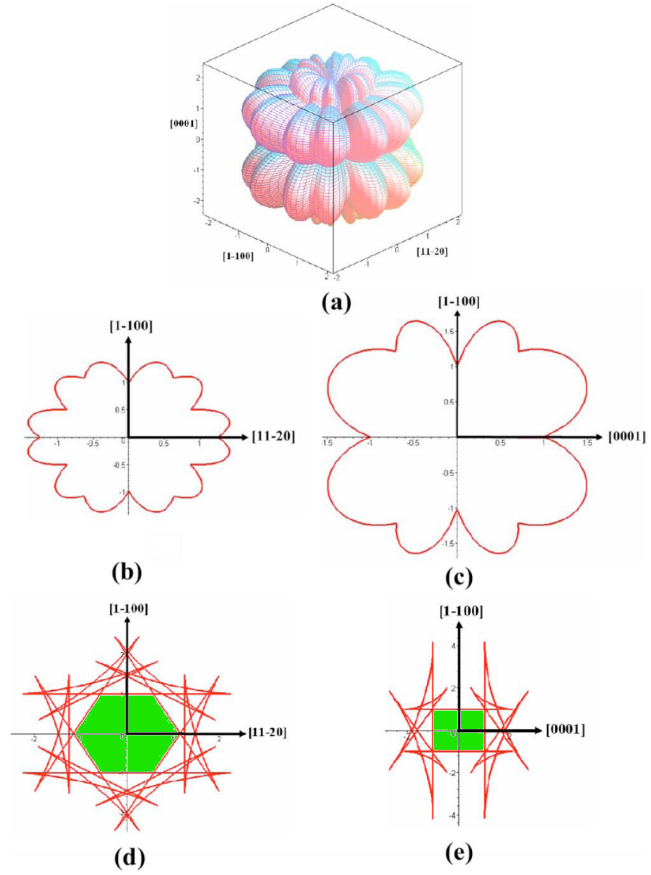


Figure 3.9: Surface energy plot in 3D (a), in (0001) cross section (b) and (11 $\bar{2}$ 0) cross section (c). (d) and (e) show Legendre transformations of (b) and (c), indicating the equilibrium crystal shapes (green areas). From Ref. 114.

AlN and Si_xN_y was experimentally obtained and is given in App. B.) On the other hand, the Si_xN_y interlayer is partially amorphous and poses a much weaker lattice constraint on the GaN.^[103] Hence, within the classical models, the nucleation of seed crystals for NW growth on Si is best described as VW growth.^[107,108]

GaN NWs were recently found to grow N-polar on Si, respectively Si_xN_y .^[109–111] On AlN, GaN growth follows the substrate polarity. Sergio Fernández-Garrido *et al.* recently reported on GaN NW growth experiments on N-polar AlN, yielding N-polar self-induced GaN NWs of similar morphology to those grown on Si.^[113] On Ga-polar AlN, however, a compact Ga-polar GaN layer was reported, and the few observed NWs were attributed to locally occurring inversion. In short, self-induced GaN NWs grow N-polar.

No systematic study for GaN NWs is available. For InN NWs, M. Seibt reported a critical amorphous layer thickness of 1.5 nm for the transmission of orientation information from the Si substrate to the NWs.^[106]

^jThese recent reports on N-polarity of GaN NWs on Si used several independent methods: CBED, EELS, resonant x-ray diffraction, and atomic resolution images from STEM. They are given precedence over earlier reports on Ga-polarity.^[59,112]

3.3.2 Thermodynamically driven faceting

For an early stage of growth, Consonni *et al.* hypothesize that GaN nuclei assume an equilibrium shape that minimizes the free surface energy.^[97] The authors report that this behaviour is even more predictable during the growth on Si_xN_y than on AlN, because epitaxial strain is negligible on the amorphous interlayer and because the interface area does not change during the shape transition. (In this way, the authors oppose the SK interpretation with strain as the driving force to shape change.) This interpretation is supported by the TEM image which is reproduced here in the bottom of Fig. 3.8. Another report on GaN NWs which grew in perpendicular out-of-plane alignment on amorphous SiO_2 ^[10] confirms that the shape transition to NW growth does not require a lattice constraint.

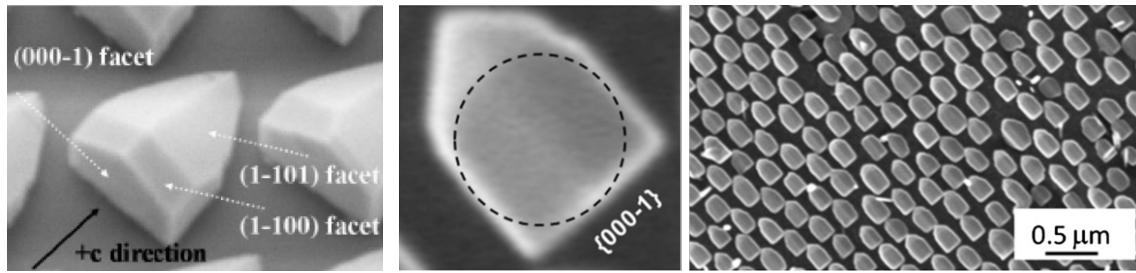
The equilibrium shape of a crystal can be derived from geometric operations on the surface energy plot, named after G. Wulff who first proposed it. Such a plot was created by Jindal and Shahedipour-Sandvik for GaN nanostructures using surface energies from a broken-bond model.^[114] [The absolute (00.1) and (00. $\bar{1}$) surface energies are difficult to verify.^[115]] Their Wulff-plot is reproduced here in Fig. 3.9(a), with cross sections in the C-plane in (b) and in the A-plane in (c). The transformation predicting the equilibrium shape is shown below. In Fig. 3.9(d), the green area corresponds the NW radial cross section. In this interpretation, Fig. 3.9(e) finally shows an axial cross section through a 'lying' NW, with the C-axis and the M-plane side facets drawn horizontally. The important conclusion is that, in equilibrium, both the (00.1) surface, the Ga-polar face, and the (00. $\bar{1}$) surface, the N-polar face, are flat. This is similar to the 'standing' NW shown in the TEM image at the bottom of Fig. 3.8.

A detailed model of GaN NW nucleation was recently developed by Dubrovskii *et al.*, who take into account a scaling growth anisotropy in addition to the anisotropy of the surface energy.^[108] Here, scaling growth means that the height h of an individual NW is linear with a power of its radius r , $h \propto r^{2.46}$, with the exponent experimentally obtained from SEM images. They achieve an analytic description of the critical nucleus size required for the transition from a spherical cap to a NW shape. Thereby, the view of GaN NW nucleation as a two-step process composed of VW island nucleation and subsequent NW facet development, as suggested by Fig. 3.8, is made physically plausible.

3.3.3 Nanowire elongation

Continued NW growth in MBE occurs under non-equilibrium conditions, and this has consequences for the shape and dimensions of the NWs. First, facets at the top of the NW are determined by the anisotropy in the growth rate. This is an important aspect for this thesis, because axial heterostructures are analyzed, and their interfaces preserve the NW top facet shape at the time of growth. Second, the NW axial growth rate is diffusion-limited.^[77,98] Both the observed effects of the faceting and of the axial growth rate on the heterostructure formation will be discussed in detail in Ch. 5.

The symmetry of the (00.1) and (00. $\bar{1}$) facets of a GaN crystal, which is predicted under equilibrium conditions in Fig. 3.9, is not generally observed in an experiment. Selective area growth (SAG) on A-plane GaN substrates should yield GaN islands which, when seen from above, correspond exactly to the cross section in Fig. 3.9(e). Fortunately, experimental results from two very different growth techniques have become available recently and are reproduced in Fig. 3.10. The images show that real GaN NWs can be expected to form flat (00. $\bar{1}$) top facets when growing N-polar, but terminate in semipolar-faceted



(a) MOVPE-grown GaN, SAG with SiO_2 mask. From Ref. 114. (b) MBE-grown GaN, SAG with Ti mask. The left image is a magnification of the overview in the right image. The circle marks the 150 nm mask opening. From Ref. 119.

Figure 3.10: SEM images of GaN crystals on A-plane GaN substrates. Literature data from two different growth techniques are shown, MOVPE and MBE. In both experiments, the GaN crystals were grown selectively in circular mask openings. Both experiments agree in a flat (00.1) N-polar facet, and show pyramids with semipolar facets on the opposite side of the crystal.

pyramids when growing Ga-polar. This is in agreement with the more usual reports on the morphology of out-of-plane grown C-axis GaN NWs with Ga-polarity on MOVPE-grown substrates,^[116–118] and N-polarity in self-induced NWs on Si.^{[109–111]^k}

The NWs studied in this thesis grow N-polar on silicon with a Si_xN_y interlayer, and hence flat top facets are expected.

The axial growth of GaN NWs occurs by direct impingement of adatoms on the top facet, and by impingement and diffusion on the sidewall.^[77,98] In kinetic descriptions of GaN growth, diffusion of N is not considered, because N adatoms are unstable against desorption as N_2 molecules. Impingement from the vapor on the sidewalls depends on the incidence angle and on the shadowing by other NWs.^[120,121] Since N does not diffuse, the positioning of the plasma cell has a particularly strong effect on the NW morphology.^[122] Different from the concept of surface energies, which was employed to model the nucleation phase, NW elongation results from differential sticking coefficients,^[77] respectively diffusion lengths, on the M- and C-planes. One consequence of adatom supply to the top facet of the NW via sidewall diffusion is that thick NWs grow slower than thin NWs: the sidewall capture area increases linearly with diameter, but the top facet area increases with the square of the diameter.^[98] For a quantitative analysis of the axial growth rate of self-induced GaN NWs, the reader is directed to Ref. 99. Radial growth of the GaN NWs is generally not completely suppressed, and can be fed by atoms impinging on the sidewalls, if their diffusion length does not permit incorporation on the top facet. A scaling growth anisotropy is derived for the relation of axial and radial growth by Dubrovskii *et al.* in Ref. 123.

The heights of individual GaN NWs in an ensemble fluctuate for two reasons: First, nucleation is a statistical process,^[124] and individual GaN islands can continue to nucleate while others have transformed into NWs and grow axially. Second, the growth rate of individual NWs may differ because of variations in their geometry or their surroundings. An overview of the statistical fluctuations encountered in the experimental work for this

^kWhile the top facet morphology of GaN NWs is a valuable indication for the crystal polarity, it must be noted that the oblique facets in Ga-polar GaN are observed only when the growth temperature is sufficiently high, and this morphological criterion must be used cautiously.^[113]

thesis will be given in Sec. 4.1. It has recently been found by Sabelfeld *et al.* that the high density of typical self-induced GaN NWs gives rise to cooperative phenomena.^[125] Their conclusion is of potential significance for future experimental work: the height distribution of self-induced NWs becomes progressively narrow over time.

3.4 Growth of GaN nanowires on amorphous substrates with metal interlayer

As presented above, the starting point of GaN NW growth can be coherent SK growth, or nucleation under a weak lattice constraint, or on an amorphous substrate. These cases were studied for GaN NW growth on AlN and Si, both requiring a crystal wafer, and on amorphous SiO₂. The question arises, if the absence of a lattice constraint, which makes NW fabrication unique compared to other semiconductor structures, can be exploited for the growth of GaN NWs on even more substrates. Growth on substrates other than single crystals could make GaN NWs more cost-effective and better scalable than planar GaN grown epitaxially. From a growth perspective, the choice of an alternative substrate is guided by three criteria. The material must

- withstand the GaN NW growth temperature of 800 °C for at least one hour. The substrate should not degrade or react chemically with GaN.
- be UHV-clean, i. e. not release contaminants into the vacuum chamber. Integration of foreign atoms from the substrate into the growing semiconductor could have undesired effects, such as a reduced carrier lifetime.
- possess a flat surface to allow device integration by planarization. The permissible roughness is defined by the length of the NW segment which makes the top contact. For the devices presented in this thesis, that would impose a limit to the roughness below 100 nm. The requirement to align the NWs in parallel poses an additional limit on the local curvature.

Other aspects of substrate selection, such as conductivity, transparency, reliability, system cost, toxicity, and so on, are out of the realm of crystal growth. For the simple GaN NW LED process used in this thesis (see Sec. 2.4), a conductive substrate is required, but post-growth removal of the substrate and subsequent contacting of the NWs is also feasible.^[60]

The temperature requirement limits the choices of substrate materials to ceramics, silica glass, stainless steels, Ni alloys, and high-melting-point metals, including Ti, Mo, and W.^[126] Stainless steels are not UHV-clean at GaN growth temperatures. An approach recently demonstrated by Samsung Electronics uses silica glass with a Ti interlayer as a substrate for GaN growth.^[127] This has several benefits for LED device integration: The polished glass surface is sufficiently flat for device processing, and the metal film serves both as a mirror and as a good ohmic back contact^[128] and electrode. The metal film is also helpful from a growth perspective: Sputtered Ti crystallizes as h.c.p. α -Ti (space group P6₃/mmc, no. 194). On silica glass, α -Ti can be grown preferentially in the close-packed (0001) plane,^[129] with a narrow distribution in the out-of-plane alignment of the grains (tilt). Explanations of this phenomenon have been sought in the low surface energy of the close-packed plane,^[130,131] similar to the cause for GaN NW formation hypothesized in Sec. 3.3.2. Choi *et al.* reported that the low-temperature GaN nucleation

3.4 Growth of GaN nanowires on amorphous substrates with metal interlayer

layer, which is typically grown in MOVPE,^[3] grows epitaxially on Ti and inherits the low tilt.^[127]

A Ti film on another carrier as a substrate for NWs would be suitable for the integration of a NW LED device, and this approach was followed also in this thesis. The possible benefits of NW LED devices over planar devices in terms of strain relaxation, defect reduction, In incorporation and outcoupling of light would remain regardless of the substrate. The purpose of this section is to show how self-induced GaN NWs grow on Ti in PAMBE.

3.4.1 Epitaxial growth of GaN on Ti interlayer

A series of self-induced GaN NW growth experiments was conducted on Ti metal films (series 30). Using a DC magnetron, 1 μm of Ti was sputtered onto three types of substrates. One sample was grown on C-plane Al_2O_3 , referred to herein as the ‘sapphire’ sample. To study the behaviour of Ti on amorphous substrates, experiments were also conducted on a Si(111) wafer with 100 nm of thermal oxide, the ‘oxide’ sample, and on silica glass, the ‘glass’ sample. A summary of the experimental steps for the three samples discussed here is given in Table 3.1. A comprehensive list of growth parameters is found in App. A.

Table 3.1: Preparation of samples with self-induced GaN NWs on Ti interlayer (series 30). 1 μm of Ti was sputtered onto each substrate using a DC magnetron.

sample alias	substrate for Ti film	nitridation and annealing	GaN growth	MQW growth
sapphire	C-plane Al_2O_3	T-ramp 850..760°C in 2 h under Ga and N flux	nucl. observed at 760°C, then 90 min growth	no
glass	silica glass	30 min annealing and 30 min nitridation at 760°C	90 min growth	no
oxide	100 nm thermal SiO_x on Si(111)	(no waiting time)	90 min growth at 760°C	yes

The GaN growth on Ti was monitored *in-situ* using RHEED. In the experiment with the sapphire sample, which is described first, the substrate was heated to about 850 °C within 20 min, and a streaky pattern was observed in RHEED, indicating a flat surface.¹ Ga and N fluxes $\Phi_{\text{N}} = 13 \text{ nm/min}$ and $\Phi_{\text{Ga}} = 2.4 \text{ nm/min}$ were then supplied to the substrate. From reference experiments conducted on Si(111) wafers, the source flux ratio $\text{V/III} = 5$ is known to result in GaN NWs. Immediately after opening the shutters, the spotty RHEED pattern shown to the left in Fig. 3.11(a) was observed. The correlation of this change with the N shutter opening, and the spacing D allow to associate this spotty pattern with f.c.c. $\delta\text{-TiN}$ in the (111) plane (metallic-yellow osbornite, space group $\text{Fm}\bar{3}\text{m}$, no. 225). Ti is known to be very reactive, forming TiN even under N_2 atmosphere at temperatures as low as 700 °C,^[133] and nitriding at low temperatures under N plasma.^[134,135] This cubic $\delta\text{-TiN}$ possesses a low tilt as indicated by the absence of concentric rings, and low twist as evinced by the absence of diffraction spots belonging to the

¹The pyrometer reading is calibrated for Si with an emissivity of 0.7. The emissivity of Ti has been reported around 0.6,^[132] and the pyrometer reading hence underestimates the surface temperature.

3 Growth and in-situ analysis of group-III-nitride nanowires

'wide-spaced' azimuth. [Prototypes of RHEED patterns from cubic and hexagonal crystals were shown in Fig. 3.4(c).] At about 850 °C no GaN nucleation was observed, and the substrate temperature was slowly reduced under continuous Ga and N flux. After two hours, at about 760 °C, additional GaN reflections indicated GaN nucleation. GaN NWs were grown for another 90 min, and the final RHEED pattern of GaN NWs is shown to the right in Fig. 3.11(a). This clear pattern [matching the prototype in Fig. 3.4(b)], and especially the absence of reflections in the 'wide-spaced' azimuth indicates an excellent epitaxial alignment of the NWs. The epitaxial relationship $\text{GaN}[1\bar{1}00] \parallel \delta\text{-TiN}[11\bar{2}]$, and $\text{GaN}[11\bar{2}0] \parallel \delta\text{-TiN}[1\bar{1}0]$, as indicated by the coordinate systems in Fig. 3.11, has already been reported for magnetron sputtered TiN films on GaN.^[128,136,137] In the present experiment, the crystallographic alignment between individual GaN NWs necessitates that the Ti film itself is grown epitaxially on Al_2O_3 in magnetron sputtering.^m To summarize, the epitaxial relationship of GaN and Ti was clearly seen in the sapphire sample.

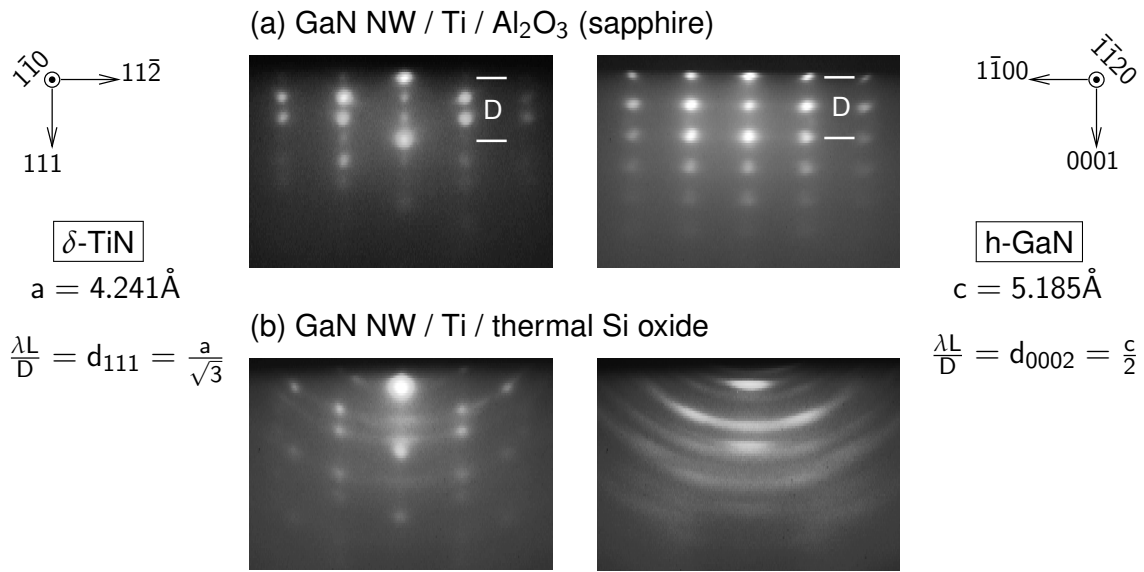


Figure 3.11: RHEED patterns in the 'narrow-spaced' azimuth, recorded immediately after shutter opening (left-hand column) and after 90 min GaN growth (right-hand column). (a) sapphire sample, first giving evidence of (111) $\delta\text{-TiN}$, and then of epitaxially aligned GaN NWs. (b) oxide sample, showing first a (111) cubic phase with high tilt and twist, and then reflections of GaN NWs, also with high misorientation. The main text explains that the cubic pattern in (b) can originate from $\delta\text{-TiN}$, or TiO , or a mixture of both.

Using the same Ga and N fluxes as for the sapphire sample, analogous experiments were carried out on the glass and oxide samples. The RHEED evolution during the growth of the latter will be discussed now. The Ga and N shutters were opened at a stable substrate temperature of about 760 °C. The first RHEED pattern in Fig. 3.11(b) was recorded 4 min after shutter opening, indicating the presence of islands of a cubic phase with significant tilt (The diffraction spots are elongated to circles, cf. Fig. 3.3(b)) and twist (superposition of 'narrow' and 'wide' patterns). In this experiment, the appearance of the

^mThe pattern in Fig. 3.11(a) was recorded with the flat on the sapphire wafer facing the RHEED screen, indicating a $\{11\bar{2}0\}$ -azimuth. The same crystallographic orientation is later taken on by the GaN NWs. This would not happen without the Ti interlayer, as GaN normally grows on C-plane sapphire rotated by 30°. [3]

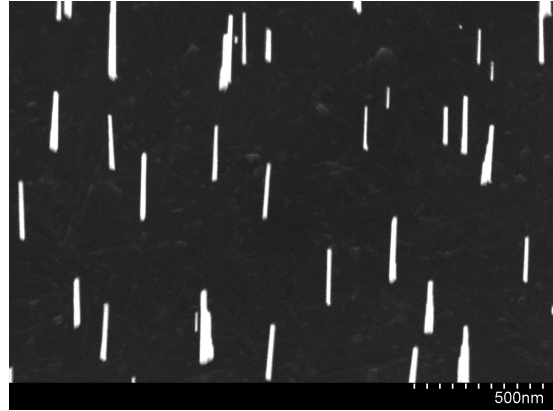
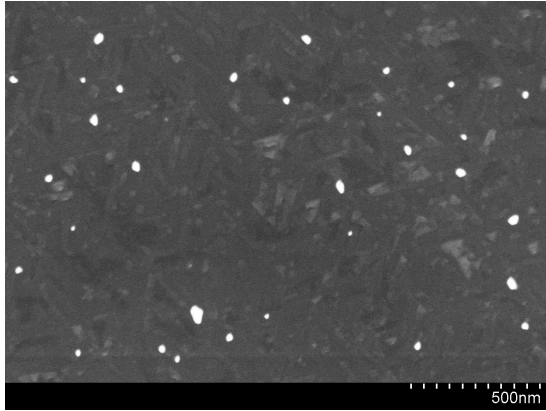
cubic phase did not coincide with the N shutter opening. As will be seen later by XRD, the cubic RHEED pattern likely stems from TiN or TiO, or a mixture of both. Again, GaN NWs were grown for 90 min, leading to the RHEED pattern on the right-hand side of Fig. 3.11(b). The partial distribution of reflection intensity on rings indicates that the tilt of the GaN NWs is almost random. Concurrent reflections of the ‘narrow’ and ‘wide’ azimuths indicate a high twist. This spread in orientation is either due to GaN growth on a rough surface, or to poorly oriented Ti on Si oxide. RHEED patterns observed from the glass sample were similar to the oxide sample, but due to cracks and bowing of individual flakes, the origin of the ring pattern can not be traced to growth-induced crystal tilt.

SEM images of the three samples are compared in Fig. 3.12. The GaN NWs appear white in the SEM images of the sapphire sample in Fig. 3.12(a). The density is only about 10^9 cm^{-2} , compared to typically 10^{10} cm^{-2} on Si.^[12] (It is higher around particle-like surface defects, data not shown). The NW diameter is below 50 nm, and no systematic tapering is visible. The NW growth axis is equal to the crystallographic C-axis, as is known from GaN NW growth on Si and indicated by the vertical alignment of (i) the NW axis in the SEM image, and (ii) the C-axis in the RHEED pattern. The low tilt of the NWs on the sapphire sample is confirmed. The glass and oxide samples are shown in Figs. 3.12(b) and (c), respectively. For both samples, the overview images on the left show that the NWs grow in domains of different density and average orientation. These domains are possibly defined by the initial α -Ti grain structure after sputtering. Within any one grain, the NW growth axis is subject to some random tilt, as can be seen in the detail images on the right. In some grains, an oblique NW orientation is preferred on average, which stands in contrast to growth on Si and on amorphous SiO_2 ,^[10] and indicates a strong epitaxial relationship to the substrate. The SEM observation of strong tilt between grains is in agreement with the circular RHEED pattern in Fig. 3.11(b). In the detail image of a domain with a high NW density on the oxide sample, the NW density is about $2 \times 10^9 \text{ cm}^{-2}$, higher than on the sapphire sample. It can be summarized that GaN NWs have grown on all three samples with Ti films, and that the size and shape of individual NWs is similar to those grown on Si. Between the samples, the NW orientation and density vary strongly. Since RHEED showed no evidence of GaN growth other than in C-direction, it can be concluded that the spread in GaN NW orientation reflects the spread in the C-axis of the grains in the Ti film. This means that the growth of Ti during sputtering on Si oxide is more disordered than on Al_2O_3 .

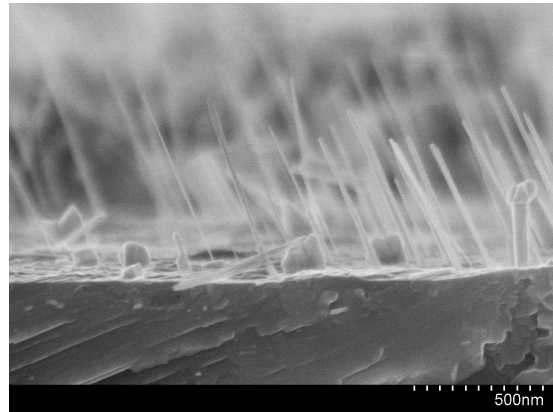
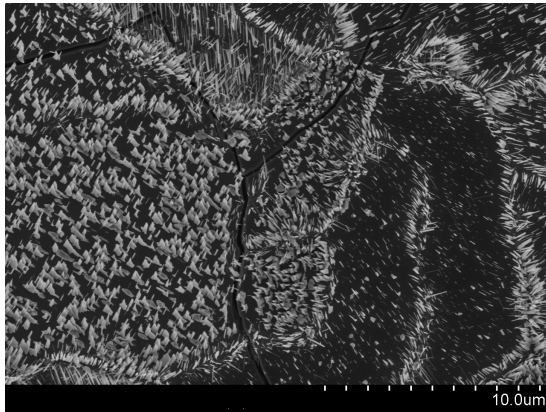
X-ray diffraction scans of an as-grown Ti film on silica glass and of the sapphire and oxide samples after NW growth are compared in Fig. 3.13. The diffraction peaks are indexed by the phase and plane using the *AtomWork Inorganic Material Database*.^[138] The assignment is tentative, but sufficiently precise for the study of GaN NW growth. X-ray diffraction of the as-grown α -Ti film as sputtered on glass confirms the preferential (0001) growth on an amorphous substrate. (The XRD peak is about 0.2° off the literature value, indicating a residual compressive out-of-plane strain of about 0.4%, the origin of which is unknown.) The absence of the α -Ti(0002) peak in the diffraction patterns of both the sapphire and the oxide samples indicates that the Ti film is consumed by nitridation and reaction with the substrate. Before the GaN growth on Ti is analyzed further, the reaction

ⁿAt the tips of the NWs in the oxide sample, steps are visible in the sidewalls. These steps are an effect of the $\text{In}_x\text{Ga}_{1-x}\text{N}$ MQW growth, to be discussed in detail in Sec. 5.3.3. The growth of the MQW region was performed at only about 620°C , giving rise to some parasitic $\text{In}_x\text{Ga}_{1-x}\text{N}$ and GaN growth in areas where no NWs had nucleated.

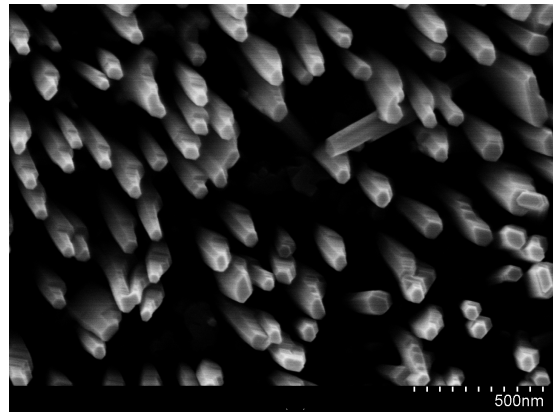
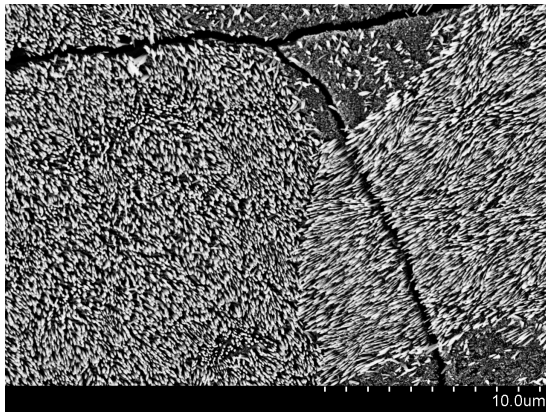
3 Growth and in-situ analysis of group-III-nitride nanowires



(a) Al_2O_3 substrate (sapphire sample). Low-density GaN NWs (white) grow perpendicular to the substrate. (right image: bird's-eye view)



(b) Silica glass substrate (glass sample). NWs grow in domains with different average orientation and density. The dark lines in the overview image are cracks in the Ti film. (right image: cross-section)



(c) SiO_x substrate (oxide sample).ⁿ The substrate grain structure and NW orientation are similar to (b). High NW density is observed in some grains on this sample.

Figure 3.12: SEM images of GaN grown on magnetron sputtered Ti layers on different substrates. The images are in plan view except where indicated. The data were acquired by A.-K. Bluhm.

3.4 Growth of GaN nanowires on amorphous substrates with metal interlayer

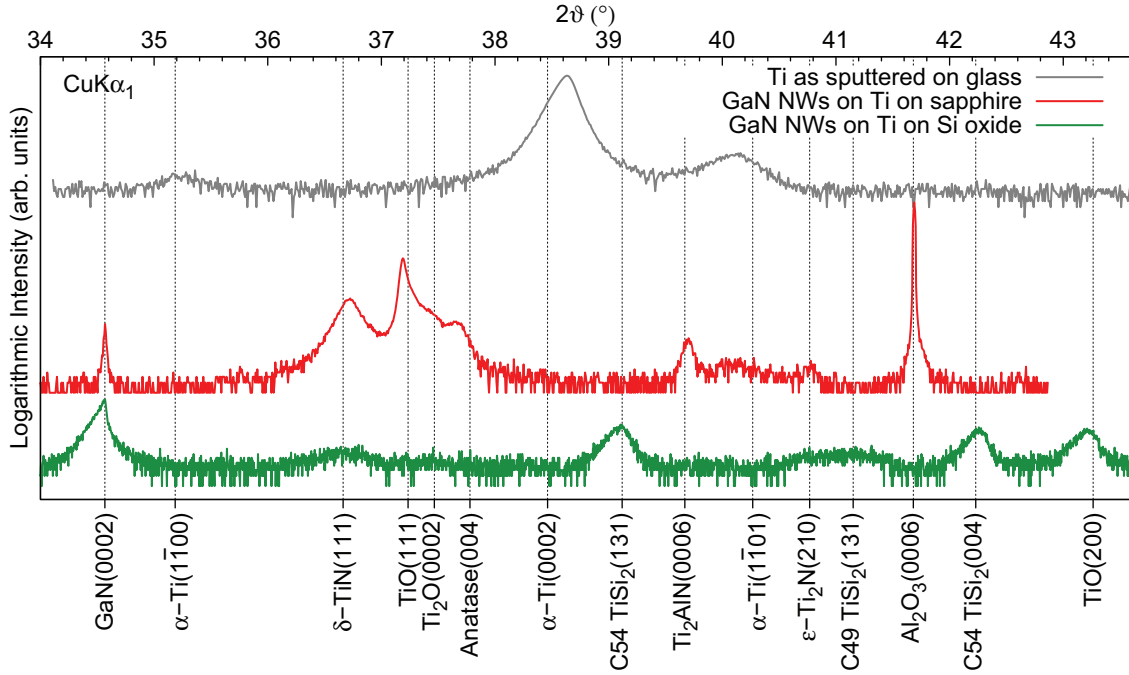


Figure 3.13: XRD profiles of Ti films as sputtered on glass, and after GaN NW growth and reaction with two different substrates: Al₂O₃ and thermal Si oxide on Si(111).

paths leading to Ti consumption will be summarized.

Based on the identified phases and literature reports, the following reactions have occurred:

Nitridation Ti and N form δ -TiN and ϵ -Ti₂N.^[139] The RHEED pattern prior to GaN growth on the sapphire sample was assigned to δ -TiN(111), and this crystal is also prominent in the XRD profiles. ϵ -Ti₂N may also be present.

Oxidation In all three studied samples, Ti reduces the substrate and oxidizes. Which oxides form, seems to depend on the amount of available oxygen and the temperature profile of the experiment. In the order of increasing O content, Ti₂O, TiO, and TiO₂ are formed, the latter in the polymorphs rutile and anatase. The Ti-rich (intermediate) oxides are known to form in the reaction with Al₂O₃.^[140] Initially, α -Ti can incorporate O in the octahedral voids, forming Ti₂O (hexagonal, space group P-3m1, no. 164).^[141] This may explain the Ti₂O(0002) peak in the sapphire sample, where the RHEED data led to the conclusion that the α -Ti film was highly oriented. The other Ti-rich oxide, f.c.c. TiO (Titanium(II) oxide, metallic-yellow, space group no. 225), is also present in the samples where Ti reacted with SiO₂.^[142] The sapphire sample XRD profile is dominated by the TiO(111) peak, close to δ -TiN(111). O was in fact detected *ex situ* on the sapphire sample surface by EDX (data not shown). Continued supply of O results in more stable TiO₂ (Titanium(IV) oxide, rutile and anatase modifications) in the glass sample (data not shown).

Reaction with metallic Al The reaction of Ti with Al₂O₃ releases metallic Al,^[140] which was detected by EDX on the sapphire sample surface (data not shown) and may have led to the formation of Ti₂AlN.

Silicidation Ti silicides [metastable C49 TiSi_2 (ZrSi_2 -type) and C54 TiSi_2] are formed where SiO_2 is decomposed by Ti.^[133] In the oxide sample, high-temperature silicidation occurred, and XRD shows the thermodynamically stable C54 TiSi_2 in two orientations.

Metallic α -Ti is hardly detected any more by XRD after the NW growth, and RHEED reflections of α -Ti (hexagonal pattern) were not observed prior to GaN growth. Thus, the Ti film reacts heavily, and the reactions start before GaN growth. It is not obvious, which of the reaction products of Ti forms the base for GaN NW nucleation. The cubic RHEED pattern from the sapphire sample in Fig. 3.11(a) is identified as δ -TiN(111) because of its appearance together with the N shutter opening. The epitaxial interface of TiN and GaN has been achieved even by sputtering TiN onto GaN at room temperature,^[136] and TiN is therefore a likely candidate as a substrate surface for GaN growth. The in-plane misfit is $d_{110}^{\text{GaN}}/3d_{224}^{\text{TiN}} = 6.3\%$. Based on the present data, however, this is not the only possibility. TiO(111) is also present in the samples, and has the same crystal structure and diffraction pattern, and very similar spacing as δ -TiN(111), as is depicted by the neighboring peaks in the XRD profile of the sapphire sample. Both are metallic-yellow in appearance and can not be distinguished by eye, either. In the oxide sample in particular, where the appearance of the cubic RHEED pattern [Fig. 3.11(b)] was not correlated with the N supply, it is possible that TiO(111) coexists with δ -TiN(111) at the surface,^[133] and that it takes part in GaN NW nucleation. The misfit is $d_{110}^{\text{GaN}}/3d_{224}^{\text{TiO}} = 7.9\%$.

Arguments exist both to support and to refute the possibility of the coexistence of δ -TiN(111) and TiO(111) on the sample surface when GaN nucleates. Speculatively, if GaN NWs grow epitaxially on TiO{111}, this would explain the misalignment of the GaN NWs in domains, that was seen in the SEM image of the oxide sample to the right of Fig. 3.12(c). In this sample, the out-of-plane XRD scan detected TiO(200) grains, whose {111} facets are, of course, 54° inclined from the surface normal. (The good epitaxial alignment of the NWs, shown by RHEED in the sapphire sample, would not contradict this assumption, because according to RHEED and XRD, TiO(111) must be very well aligned here, if present at the surface.) Contrary to the assumption of TiO on the surface is the simple second argument: N is continuously supplied from the top, and O from the bottom of the $1\text{ }\mu\text{m}$ Ti layer, but only until the 100 nm SiO_2 are consumed. It will take time for O to diffuse to the sample surface. In a nitridation study of Ti on Si oxide, Morgan *et al.* detected an “increasing replacement with depth of N by O atoms at substitutional sites in the TiN lattice.”^[133] If GaN growth commences early enough, it may occur entirely on δ -TiN(111).

TiSi_2 formation should not influence the GaN nucleation at the surface, because TiN rather than Si_3N_4 is the stable nitride. In the presence of N plasma, TiN should always form on top of TiSi_2 .^[133] Therefore, TiSi_2 is likely present at the substrate interface, but not at the surface.

In the case of the glass sample, the reaction of the Ti film with the substrate led to the formation of voids, cracks, bowing of individual flakes, and a partial delamination of the film and loss into the MBE chamber (images not shown). This did not occur in the oxide sample, probably due to the limited amount of O contained therein.

The findings of this section on the growth of GaN on Ti can be summarized as follows:

- GaN grows epitaxially on Ti. The orientation relationship is stricter than on Si(111), indicating a higher lattice constraint.

3.4 Growth of GaN nanowires on amorphous substrates with metal interlayer

- The nucleation density of GaN NWs likely varies for Ti grains of different crystallographic orientation.
- GaN growth on Ti is likely mediated by δ -TiN(111) or TiO(111), given that a cubic phase at the surface precedes NW nucleation. It can be noted that, in contrast to Si_xN_y , both are good conductors and would not limit NW LED device performance.^[137,143]
- In the sapphire sample, the surface likely contains more δ -TiN(111) than TiO(111). This is based on the evidence for Ti nitridation by RHEED and on the study by Morgan *et al.*
- For parallel NW device integration by planarization of NW ensembles, a highly (0001) oriented Ti film is required, respectively (111) oriented TiN or TiO.

A difficulty in interpreting the experiments presented in this section was the reaction of Ti with the sapphire and Si oxide substrates. An obvious remedy would be a less reactive metal, as a substrate for the NWs or as diffusion barrier between Ti and the substrate. One candidate is Mo, which is stable over SiO_2 up to 1000 °C.^[142] The challenge of achieving a highly oriented texture in the Ti film prior to GaN growth, in order to obtain perpendicularly aligned NWs, remains regardless of the substrate reactions.

3.4.2 GaN nucleation on Ti interlayer

The nucleation density of GaN NWs on Ti was about $1 \times 10^9 \text{ cm}^{-2}$ on the sapphire sample (Fig. 3.12(a), left image) and about $2 \times 10^9 \text{ cm}^{-2}$ on a densely populated grain of the oxide sample (Fig. 3.12(c), right image). Typical NW densities for self-induced growth on Si are higher by a factor of ten.^[12] Ti and Mo are used as mask materials in selective area growth (SAG),^[61,144] which means that they do not favor GaN nucleation. This raises the question, how a high NW nucleation density can be achieved.

With the present experimental data the low NW nucleation density on Ti films compared to that on Si wafers on the one hand, and the difference in density between the sapphire and the oxide samples on the other hand, cannot be explained. Nevertheless, two possible reasons shall be stated:

- The nucleation density may be dictated by the surface diffusion length of Ga adatoms, which is also an important factor in SAG.^[145] (More sophisticated descriptions of SAG involve the concept of incubation times on different surfaces,^[146] which also includes different desorption rates.)
- The different sample surfaces may favor N-polar and Ga-polar GaN growth to a different degree. As was discussed in Sec. 3.3.1, self-induced NWs grow N-polar, and compete with the growth of a compact Ga-polar layer if the substrate demands both.^[113]

The diffusion length of GaN on Ti and TiN can in principle be obtained from SAG experiments with a Ti mask on a GaN substrate. Such experiments have been reported, and NW spacings were in the order of 300 nm.^[144,147] In contrast, on Si, typical NW distances are below 100 nm, leading to coalescence.^[12] Explaining the observed low nucleation densities in the present examples solely in terms of high Ga diffusion lengths and random

nucleation on TiN, however, neglects the evidence from XRD for a possible co-existence of TiN and TiO on the sample surface.

The second possible reason for differences in NW density may be GaN growth in domains of different polarity. As was introduced in Sec. 3.3.3, self-induced GaN NWs grow N-polar. They are characterized by flat C-plane top facets, as is visible in Fig. 3.12(c). Sergio Fernández-Garrido has shown instructively in Ref. 113 that a high density of N-polar NWs is achieved if the substrate interface favors N-polar GaN growth. In agreement with an earlier publication by K. Bertness *et al.*^[77] he showed that, if the substrate favors Ga-polar GaN growth, a faceted GaN layer results from which N-polar NWs protrude only where inversion domains occur. The faceted Ga-polar GaN layer is less stable against thermal decomposition than the N-polar NWs, and its absolute thickness varies with growth temperature. The cross-section SEM image of the glass sample in Fig. 3.12(b) bears indeed some resemblance with the reports of K. Bertness *et al.*^[77] [their Fig. 2(d)] and S. Fernández-Garrido *et al.*^[113] [their Fig. 2(c)]. The interpretation is that most of the substrate surface promotes Ga-polar GaN growth, which does not lead to NWs of a high aspect ratio. In some small inversion domains, N-polar NWs nucleate and grow long and thin.

The interpretation of NW nucleation in limited domains of N-polar growth has another benefit, which was pointed out by Sergio Fernández-Garrido: it readily explains the low degree of coalescence which is displayed by the NWs grown on the Ti interlayer, compared to all-N-polar growth on Si. This is true even for the relatively high NW density shown in Fig. 3.12(c) compared to, for example, typical self-induced GaN NWs on Si in Fig. B.2(c) (p. 135).

Whereas the polar GaN crystal is always Ga-terminated on (0001) and N-terminated on (000 $\bar{1}$), the cubic δ -TiN and TiO (of the $m\bar{3}m$ class) possess a center of symmetry and are unpolar.^[148] This raises the question, if Ga- or N-polarity is preferred in GaN growth on these surfaces, and if a variation in NW nucleation density can be explained. For TiN(111), the epitaxial relation and atomically smooth interface with C-plane GaN are known from HRTEM studies,^[136] but the interface chemistry has not been proven so far.

In TiN and TiO, in the $\langle 111 \rangle$ directions, atomic layers are stacked which contain only Ti atoms or only nonmetal atoms. Any $\{111\}$ surface may therefore be Ti- or nonmetal-terminated. Under continuous supply of N adatoms, as in the present experiments, and considering that significant TiN formation occurs, as shown by XRD, it is presumed that the TiN surface is N-terminated. One could make a simple assumption by taking all bonds as cation-anion bonds, as has been done for AlN and TiN, which were supposed to form Al-N(TiN) bonds by Chen *et al.*^[149] In this picture of all-ionic bonds, the N in the $\{111\}$ surface of TiN has three Ti neighbors, making it plausible that only one Ga-N(TiN) bond is formed. In this case, GaN would grow N-polar on TiN. However, this picture is too simple. Whereas the bonding in GaN is highly ionic, TiN and TiO are both highly conductive and therefore show metallic bonding. Blaha *et al.* have calculated the valence electron densities around the nonmetal atoms in TiN and TiO.^[143] They found the electron density to be spherically symmetric around the nonmetal atom, and to show increasing localization from TiN to TiO. A theoretical treatment of the GaN interface to the cubic Ti compounds is missing so far. The simple picture of ionic bonds at the interface may be over-stressed. If it can be used at all, then GaN is more likely to grow N-polar on TiO than on TiN, because TiO has a more ionic bond character.

One of the initial questions in this section was the difference in NW density between the sapphire and oxide samples. This question can be restated as to what causes a higher

3.4 Growth of GaN nanowires on amorphous substrates with metal interlayer

density of inversion domains, where N-polar GaN growth is favored, in the oxide sample. The available experimental evidence was expended even before the above speculations about the GaN-TiN/TiO interface chemistry, and any further conclusion is necessarily a guess. Nevertheless, the possibility shall be pointed out: Let us remember the evidence for TiO formation, which was obtained from XRD in the last section. Even though it is plausible that the surface is dominated by TiN, TiO may coexist, and the distribution may be reflected in the polarity of GaN growth. In this interpretation, N-polar GaN NWs grow in TiO surface domains. This is in accord with the low density of NWs on the sapphire sample, and with the domains of inclined NWs and TiO(200) detection in XRD on the oxide sample.

3.4.3 Perspectives of Ti as an alternative substrate

To assess the optical quality of the GaN NWs grown a Ti film, PL data from the sapphire sample is shown in Fig. 3.14 in comparison to the luminescence from GaN NWs on Si. In the presence of crystal defects that are detrimental to the operation of an optoelectronic device, the PL spectra would reveal deviations of excitonic transitions. The room temperature PL shown in Fig. 3.14(a) shows only the free exciton transition at 3.4 eV. Defect luminescence, which is common in GaN at around 2.2 eV (yellow luminescence), is entirely absent from both samples. At 10 K, both spectra are dominated by the donor-bound exciton (D^0X), and the width of this line is as low as 1 meV. The free exciton (FX) transition is discernible in the shoulder. The luminescence from stacking faults (SF) is two orders of magnitude less intense than the excitonic emission. These results show that GaN NWs were grown on the Ti film with excellent crystal quality.

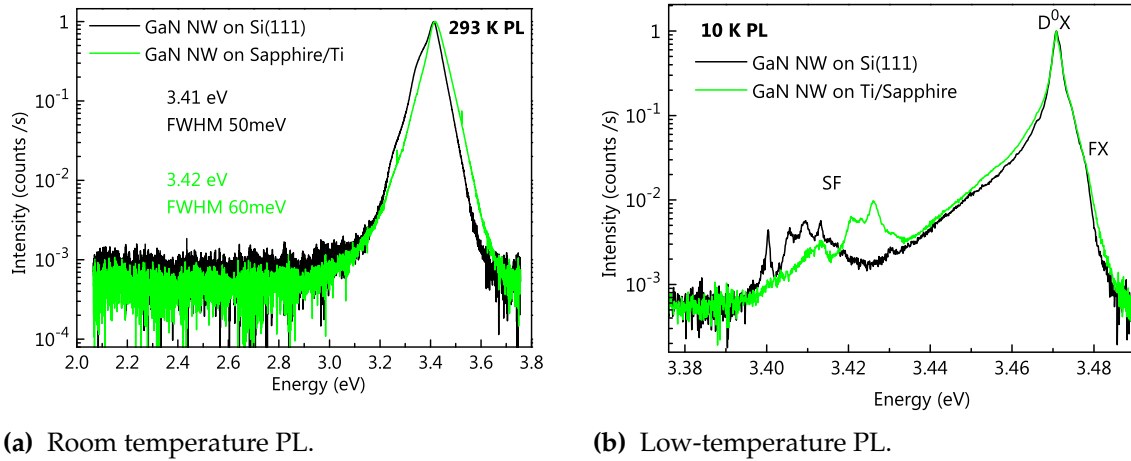


Figure 3.14: Comparison of PL data from GaN NWs grown on Ti (sapphire sample) and a reference sample of GaN NWs grown on Si. The data was acquired by C. Hauswald.

At this point, a first achievement of this thesis can be concluded. The growth of GaN nanowires on a metal film by MBE has been shown for the first time, with a crystal quality suitable for optoelectronic devices. The preliminary study revealed that GaN NWs grow epitaxially on Ti. In contrast to the growth on Si, the interface is expected to be highly conductive. The fabrication of a GaN nanowire LED device with the Ti film serving as an n-contact, with planarization and p-contacting according to Sec. 2.4 seems straightforward.

3 Growth and in-situ analysis of group-III-nitride nanowires

ward. One can imagine the possibility of nanowire synthesis on a metal surface to have a far-reaching impact on GaN-based LED device technology: single-crystal substrates could become obsolete, and the vacuum chamber for epitaxial growth could be designed around the application—not around the substrate wafer.

A lot of questions remain unanswered. From the physics of growth perspective, the nature of the interface between GaN and Ti is unclear. δ -TiN and, in particular, TiO were identified as likely candidates. This could be made more plausible by comparing *ab-initio* DFT calculations of the interface configurations. From the technological perspective, the epitaxial growth of GaN requests a highly C-plane oriented Ti film, even though it need not be single crystalline. Also, a carrier material for the Ti film that is suitable for MBE growth has yet to be found.

More materials, including other metal films as a growth surface, may be suitable for GaN growth. An unexpected result of this preliminary study is that TiN or TiO films, which can also be obtained by direct sputtering, are themselves candidates for an alternative substrate for GaN NWs.

4 Analytical tools for the structural investigation of nanowire ensembles

The development of controlled growth procedures for nanometer-sized semiconductor crystals requires reliable structural characterization techniques. The parameters of interest for one crystal are the defect density, the crystallite dimensions and the alloy composition. In technologically relevant epitaxial heterostructures, two different crystals are chemically bonded at their interface. This introduces two additional parameters: the crystallographic arrangement of the interface and the strain arising in coherently grown crystals with deviating stress-free lattice parameters.

In this work, a unique challenge is the fluctuation in dimensions, composition and strain, that is typical for $\text{In}_x\text{Ga}_{1-x}\text{N}/\text{GaN}$ heterostructures in self-induced GaN NWs. The diameter and axial growth rate of the NWs, and hence the $\text{In}_x\text{Ga}_{1-x}\text{N}$ dimensions and its average strain vary statistically from one NW to another. This rules out microscopy as a quantitative tool. Even though SEM and TEM are indispensable for our qualitative understanding of the NW morphology, the in-depth characterization of individual NWs and quantum wells can not quantitatively explain the behaviour of the NW ensemble as a whole. Volume probing techniques have to be employed. Then, the nanoscale dimensions of the $\text{In}_x\text{Ga}_{1-x}\text{N}$ insertions pose another challenge: the local strain at the heterointerface relaxes toward the surface, and this intrinsic variation in strain must be separated from the statistic fluctuation between NWs. Nanowires and NW heterostructures can not be analyzed by standard semiconductor characterization methods without redeveloping their interpretation. Research to this end within PDI was inspired by the experimental work for this thesis and carried out in parallel. The resulting techniques presented in this chapter are essential for the subsequent discussion of NW growth, morphology and properties.

Two primary methods are used in this work for the structural characterization of the $\text{In}_x\text{Ga}_{1-x}\text{N}/\text{GaN}$ NW ensembles. The first, x-ray diffraction (XRD), saw the one-hundredth anniversary of its application to the study of crystals last year.^[150] Nevertheless, the inhomogeneity of size, strain and composition, which is characteristic for $\text{In}_x\text{Ga}_{1-x}\text{N}/\text{GaN}$ NWs, required the development of specific strategies for the interpretation of x-ray diffraction on such structures. The results of that work will be summarized here. The second characterization technique for strain and composition of the NWs is Raman spectroscopy. Changes both in strain^[151] and in composition^[152,153] induce a spectral shift, and the understanding of strain in the NW heterostructures is equally important for the interpretation of Raman spectroscopy as it is for x-ray diffraction.

4.1 Statistical fluctuation of self-induced nanowire morphology

GaN NWs grown self-induced on Si(111) by MBE exhibit random fluctuations in size and orientation. This is illustrated by the STEM image in z-contrast in Fig. 4.1(a). The relevant dimensions are highlighted in Fig. 4.1(b): The length of an individual NW depends on

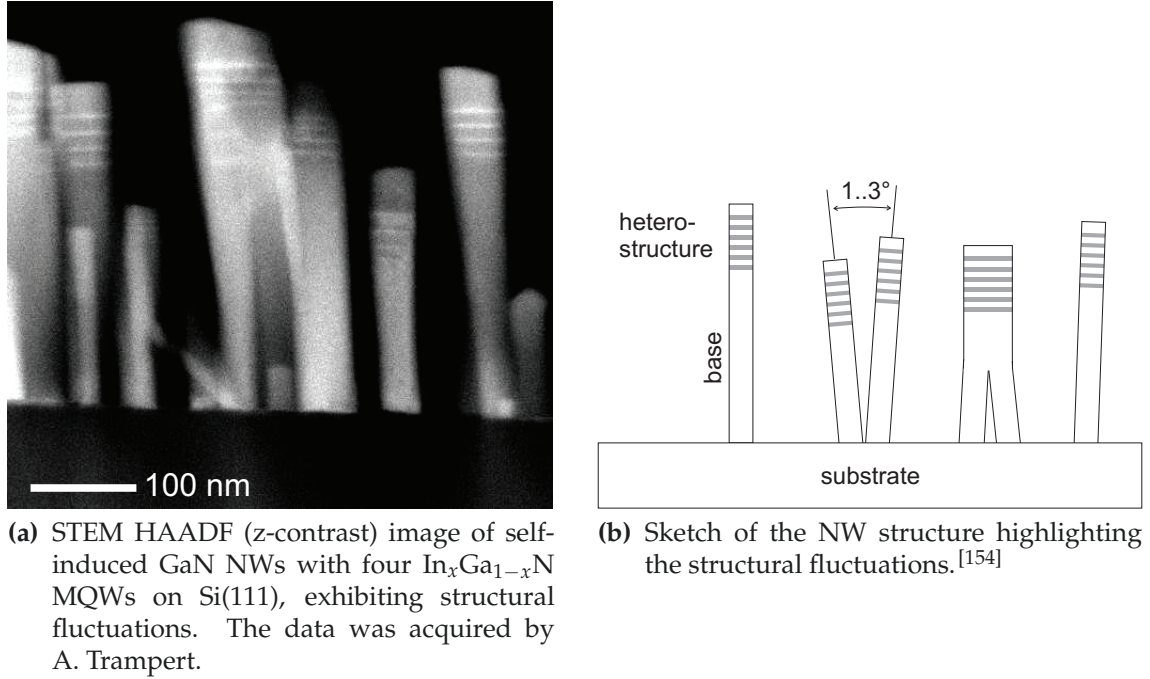


Figure 4.1: $\text{In}_x\text{Ga}_{1-x}\text{N}/\text{GaN}$ NWs grown self-induced by MBE: fluctuations in diameter, length, QW thickness and spacing, and tilt.

the growth time after its nucleation. If NWs continue to nucleate for some time until the substrate is completely shadowed, the NWs will display a dispersion in diameter and length. The epitaxial orientation to the substrate is not perfect, and the tilt of the NWs leads to additional deviations in NW diameter by coalescence.^[155] The axial growth rate of GaN NWs is related to their diameters: thinner NWs grow faster.^[98] This in turn leads to a variation σ_d in QW thickness and spacing from one NW to another. In addition, there may be other variations that cannot be seen in Fig. 4.1: The composition of the $\text{In}_x\text{Ga}_{1-x}\text{N}$ QWs can vary by σ_x on a local scale, within a NW, or from NW to NW. Finally, the NWs exhibit a significant in-plane twist,^[156] which is of little importance for this work.

The fluctuations in the $\text{In}_x\text{Ga}_{1-x}\text{N}$ MQWs in self-induced GaN NWs must be understood in order to relate their optical properties to their structure and eventually develop any device. The most immediate visualization of the impact that structural fluctuations have, are PL maps of NW ensembles, also referred to as ‘fluorescence microscopy’.^[158] Such an image is shown in Fig. 4.2. The diffraction-limited spots of different color and brightness indicate that the $\text{In}_x\text{Ga}_{1-x}\text{N}$ QWs vary strongly from one to another. Equally large variations in ensemble PL of such samples are known from literature.^[159,160]

To show the magnitude of the structural fluctuations at this point, the values are summarized in Table 4.1. Length and diameter fluctuations in NW ensembles can be obtained from SEM and TEM. Tilt and twist can be obtained directly from the width of x-ray rocking curves. Data for these fluctuations are given in App. B. These variations in the NW samples used in this study are typical for NWs obtained by self-induced growth and agree with literature reports. For the fluctuation in MQW spacing, no reference data is available. In this work σ_d was obtained from the simulation of XRD profiles, as will be treated in detail now in section 4.2. The assessment of compositional fluctuation σ_x in the $\text{In}_x\text{Ga}_{1-x}\text{N}$ QWs by Raman spectroscopy goes beyond the strain analysis and will

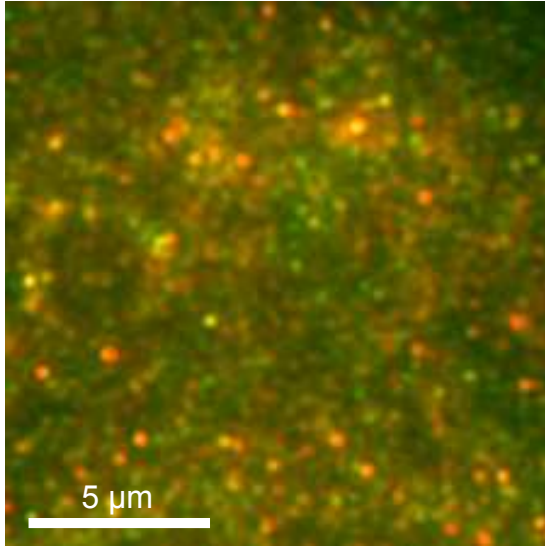


Figure 4.2: Room temperature photoluminescence micrograph of an $\text{In}_x\text{Ga}_{1-x}\text{N}/\text{GaN}$ NW ensemble as-grown on one wafer. The $\text{In}_x\text{Ga}_{1-x}\text{N}$ was selectively excited at 2.54 eV, and the emission was collected by a monochrome CCD camera through a green-yellow and an orange-red band pass filter. These data are superimposed to form the pseudocolor image.^[157] The data was acquired by S. De, Indian Institute of Technology Bombay, Mumbai.

be discussed in Sec. 5.5.3. No previous analysis of σ_x in NW MQWs is available. Nominally uniform $\text{In}_x\text{Ga}_{1-x}\text{N}$ NWs have recently been investigated by TEM^[161] and using x-ray fluorescence spectroscopy at the European Synchrotron Radiation Facility.^[162] The published results indicate a significant gradient along the NW axis, but these techniques cannot resolve the QW length scale.

4.2 Simulation of x-ray diffraction profiles for fluctuating layer thicknesses

The standard technique to characterize layer thicknesses and compositions in conventional planar superlattices is high-resolution x-ray diffraction and simulation.^a The lattice parameters of stress-free InN are 10 % larger than those of GaN. For practical purposes, the lattice parameters of the $\text{In}_x\text{Ga}_{1-x}\text{N}$ alloy change linearly with composition, an observation that is referred to as Vegard's law.^[163] X-ray diffraction measures the lattice parameter, and the composition can be directly inferred. Symmetric Bragg ω -2 θ scans yield information about the out-of-plane lattice spacing. In ideal fully strained planar films, the in-plane lattice is defined by the substrate, and therefore a sample is fully characterized by symmetric scans. In bottom-up grown NWs the strain state is more complex, the in-plane lattice spacing has to be determined, and much less work has been published than for planar films. Three previous reports used synchrotron radiation. A lateral relaxation in axial NW superlattices was shown for Si/Ge NW heterostructures by Hanke *et al.*^[164] Using grazing-incidence x-ray diffraction, the non-uniform radial strain distribution was analyzed for $\text{InAs}/\text{InP}_{1-x}\text{As}_x$ NW heterostructures by Eymery *et al.*^[165] In-situ-XRD during the growth of GaN/AlN NW superlattices was employed by Landré *et al.* to show the progressive relaxation with increasing MQW stack height.^[166] The composition of uniform unstrained semiconductor alloy NWs, such as $\text{In}_x\text{Ga}_{1-x}\text{N}$ NWs^[167] and $\text{InAs}_{1-x}\text{Sb}_x$ NWs^[168] has been determined from laboratory experiments. However, at the starting point of this thesis, no data had been shown from laboratory XRD experiments on NW superlattices. The primary difficulty arises from the structural fluctuations

^aA review of x-ray diffraction of III-nitrides is given in Ref. 25.

4 Analytical tools for the structural investigation of nanowire ensembles

Table 4.1: Structural fluctuations typical for the self-induced GaN NWs with $\text{In}_x\text{Ga}_{1-x}\text{N}$ MQWs grown and analyzed for this thesis.

NW dimension	range	deviation	method
diameter	30 nm to 85 nm		15 % and 85 % quantiles of distribution from cross-sectional SEM (Fig. B.1(a))
length	515 nm to 630 nm		as diameter
QW thickness and spacing		$\sigma_d = 2.5 \text{ nm}$	simulation of x-ray diffraction (Sec. 4.2)
QW composition		$\sigma_x = 0.2x$	simulation of Raman spectrum (Sec. 5.5.3)
tilt		3.2°	XRD ω -scan FWHM of symmetrical reflection (Fig. B.2(b))
twist		4.4°	XRD ϕ -scan FWHM of asymmetrical reflection (Fig. B.2(d)), corrected for in-plane angular distribution

in self-induced NWs, of which large ensembles have to be probed in order to achieve sufficient diffraction intensity. These fluctuations lead to a significant broadening of the peaks in the XRD profiles.

Figure 4.3 shows ω - 2θ scans across the GaN(0002) reflection from $\text{In}_x\text{Ga}_{1-x}\text{N}/\text{GaN}$ superlattices in a planar layer and in a nanowire sample. The data was acquired in the laboratory at PDI with $\text{CuK}\alpha_1$ radiation using a Panalytical X'Pert system with Ge(220) hybrid monochromator and Ge(220) analyzer crystal. Both XRD profiles are shown in the same scale. It is obvious that the planar superlattice exhibits a superior contrast of the diffraction peaks. While the out-of-plane lattice spacing in the NW MQW can be inferred from symmetric Bragg XRD scans, the low intensity of the satellites in conjunction with the statistical tilt and twist of the NWs prohibits the experimental assessment of the in-plane lattice spacing from asymmetric reflections. To determine the strain state, and thus relate the out-of-plane lattice spacing to an $\text{In}_x\text{Ga}_{1-x}\text{N}$ alloy composition, therefore requires *a priori* assumptions, which will be discussed next in Sec. 4.3.1.

Two parameters of the heterostructure composed of multiple $\text{In}_x\text{Ga}_{1-x}\text{N}$ and GaN layers can be obtained from the diffraction peaks simply by the Bragg condition:

- The zeroth order superlattice peak position ω_0 gives the average lattice constant in C-direction of the superlattice: $c_{\text{avg}} = 2d_{00.2} = \lambda / \sin \omega_0$, where λ is the wavelength of the x-rays.
- The positions ω_n of the satellites are related to the superlattice period d_{SL} via $d_{\text{SL}} = \lambda / [2(\sin \omega_n - \sin \omega_{n-1})]$.

When the diffraction maxima can be made out clearly, c_{avg} and d_{SL} are thus obtained with good precision. Two other parameters of great interest for the optical properties of the $\text{In}_x\text{Ga}_{1-x}\text{N}$ QW, the thickness d_{well} and the composition x , require an analysis of the diffraction intensity profile by simulation. The contrast of the superlattice satellite peaks of

the planar film is at least an order of magnitude, owing to the homogeneous layer thicknesses and comparatively abrupt interfaces in the film. The nanowire sample, however, exhibits very broad superlattice satellites of low intensity. Proof was given for the first time by the work for this thesis, that the shallow intensity maxima are indeed superlattice satellites,^[169] and not contributions from $\text{In}_x\text{Ga}_{1-x}\text{N}$ NW components of different composition, which can result at first glance in similar profiles.^[170] This will be discussed in detail in Sec. 5.4.

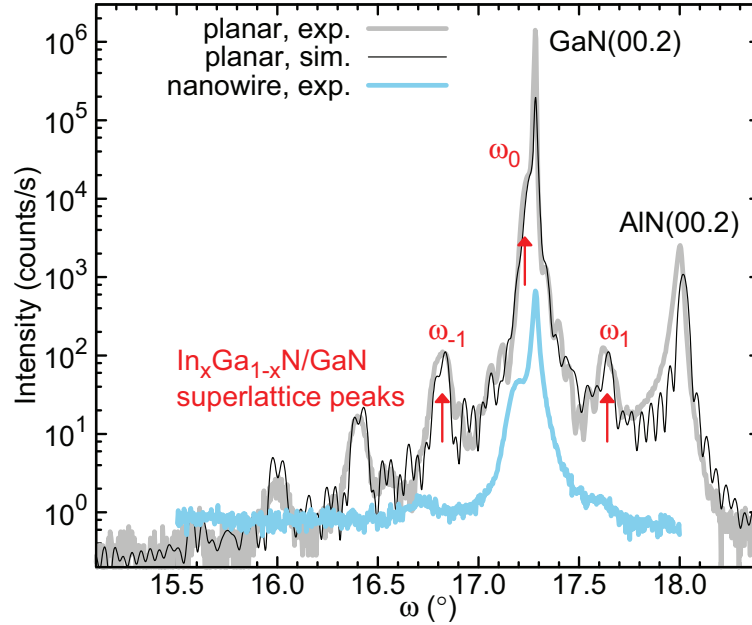


Figure 4.3: Symmetric Bragg XRD scans of planar and nanowire $\text{In}_x\text{Ga}_{1-x}\text{N}/\text{GaN}$ superlattices with six periods. The planar MQW sample was grown by MBE on commercially available virtual GaN templates which were produced by MOVPE on sapphire with an AlN interlayer. The XRD profile of the planar sample exhibits clear superlattice satellite peaks at ω_n ; the sample structure can be obtained from the parameters of the simulated profile. For comparison, experimental data from a sample of $\text{In}_x\text{Ga}_{1-x}\text{N}/\text{GaN}$ nanowires grown directly on Si(111) is given in the same scale, showing broad peaks of low intensity.

X-ray diffraction profiles can be analyzed in terms of kinematic theory, where independent scattering is assumed at different locations in the material, or dynamic theory, which accounts for multiple diffraction and absorption.^[171] Simulation tools for the dynamical calculation of XRD profiles from planar semiconductor heterostructures are available which allow to obtain the required structural information as fit parameters.^[172] In Fig. 4.3, the result of such a simulation is drawn onto the experimental curve from the planar MQW sample.^b The simulation parameters were $d_{\text{barrier}} = 8.6 \text{ nm}$, $d_{\text{well}} = 2.6 \text{ nm}$ and $x = 8 \%$. Because of the good agreement to the data, these parameters can be assumed to describe the planar sample structure well.

Previously available simulation tools could not accommodate the structural fluctuations inherent to superlattices in ensembles of self-induced NWs. Inspired by the work in this thesis, a new simulation technique for the XRD profiles was developed by Vladimir M. Kaganer.^[154] This method allows to relate the structural fluctuations and the peak

^bThe dynamical XRD simulation code *MadMax 0.99w* was provided by Oliver Brandt.

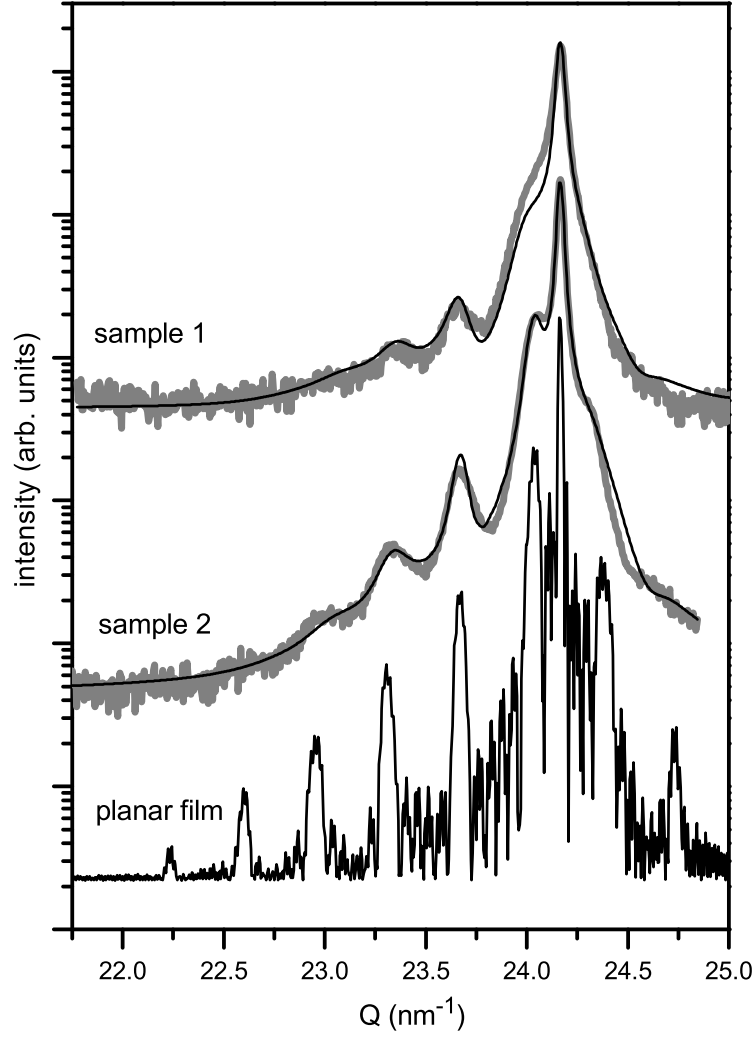


Figure 4.4: XRD profiles simulated in the kinematic approximation for an $\text{In}_x\text{Ga}_{1-x}\text{N}/\text{GaN}$ MQW in a planar film and in nanowire ensembles, with comparison to data from a NW sample (1) grown directly on Si(111) and another one (2) grown on an AlN buffer.^[154]

broadening quantitatively. As a consequence of the small coherence volume in the laboratory x-ray experiment and the random tilt of individual NWs out of the diffraction condition, the NWs in the ensemble are illuminated incoherently. A kinematic approximation can therefore be used to calculate diffraction profiles as a sum of intensities from individual NWs.^[154] The fluctuating segment thicknesses in the NW heterostructure are accounted for as independent Gaussian random variables.^c Input parameters for the calculation are the relative vertical misfit between the barrier and well layers, the barrier and the well thicknesses, and the standard deviations σ_d of the thickness distributions. Strain at the substrate interface and its successive relaxation in the base layer toward the active region is taken into account to accurately model the GaN(00.2) peak broadening.

^c Assuming a Gaussian fluctuation of the layer thicknesses is advantageous to the kinematic approximation, because the structure factor of an individual nanowire contains single exponential terms, which can then readily be averaged to account for the fluctuations. The details are given in Sec. VI of Ref. 154.

Since symmetric Bragg scans provide information about the out-of-plane lattice parameter only, an assumption about the strain state is made, that takes into account lateral relaxation of the nanowire heterostructures. The lateral relaxation approximation will be discussed in detail in Sec. 4.3.2.

Figure 4.4 shows the effect of the layer thickness fluctuation σ_d on the calculated diffraction profile. All measurement data and simulations are obtained for a six-period $\text{In}_x\text{Ga}_{1-x}\text{N}/\text{GaN}$ MQW. Sample 1 is an ensemble of NWs grown directly on Si(111), and the simulation was obtained with $d_{\text{SL}} = 19\text{ nm}$, $d_{\text{well}} = 3.8\text{ nm}$, $x \approx 20\%$ ^d and $\sigma_d = 2.4\text{ nm}$. The intensities and widths of the diffraction peaks are typical for the NW heterostructures studied in this thesis. The thickness fluctuations satisfactorily explain the broadening of the satellite peaks. Sample 2 possesses a similar heterostructure ($d_{\text{SL}} = 17.5\text{ nm}$), but the GaN nanowire base is grown on an AlN buffer layer. The thickness fluctuations are slightly smaller, $\sigma_d = 2.0\text{ nm}$, leading to more pronounced satellite peaks. Finally, if the calculation does not take into account any thickness fluctuation at all, with all other parameters as for sample 2, the ideal profile for a planar film is obtained.

With the kinematic simulation the important quantum well parameters d_{well} and x can in principle be derived from the diffraction peak intensities. This is an important advantage over the simple Bragg interpretation of the peak positions, even though the determination of these parameters is still imprecise. XRD profiles of many samples from series with fixed QW growth time and fluxes, and therefore nominally identical d_{well} , were analyzed for this thesis (series 18, 19, 23 and 27). It was found that the d_{well} obtained from fitting the kinematic simulation varied randomly by a up to a factor of two, even for samples with good contrast in the satellite peaks (series 27, experimental data in Fig. 5.10(b), simulations not shown). The determination of the quantum well parameters d_{well} and x in this thesis could therefore not rely entirely on this simulation.

The most significant benefit of this kinematic simulation of the XRD profiles is that it explains the characteristics of the experimental profiles in terms of thickness fluctuations. Therefore, this simulation is an instrument for the quantification of such fluctuations σ_d in self-induced NW heterostructures. It must be noted here that more recent progress in the analysis of these experimental structures has indicated local fluctuations in the composition of $\text{In}_x\text{Ga}_{1-x}\text{N}$ quantum wells in NWs.^[173] This will be discussed in Sec. 5.5.3. Such compositional fluctuations could partially account for the broadening of the satellites. An XRD simulation model taking into account both fluctuations in quantum well thickness and composition is not available to date, and in view of the low contrast of the satellite peaks in the experimental XRD data from NW heterostructures, it is doubtful if such an approach is feasible. The thickness fluctuations obtained from the present simulations will be regarded in this thesis as an upper estimate of the true thickness variations.

4.3 Elastic strain relaxation in axial nanowire heterostructures

Experimentally accessible characteristics such as the lattice parameter and phonon frequencies are a direct indication of the $\text{In}_x\text{Ga}_{1-x}\text{N}$ composition, under the condition that the alloyed crystal is stress-free. This is generally not the case in semiconductor film heterostructures, and NWs provide an additional degree of freedom, because stress is

^dThe exact composition given in Ref. 154 is invalid, because the lateral relaxation of the MQW stack, which introduces strain also into the GaN barrier as discussed below, was not properly taken into account. This is irrelevant, however, for the discussion of the thickness fluctuation σ_d in this section.

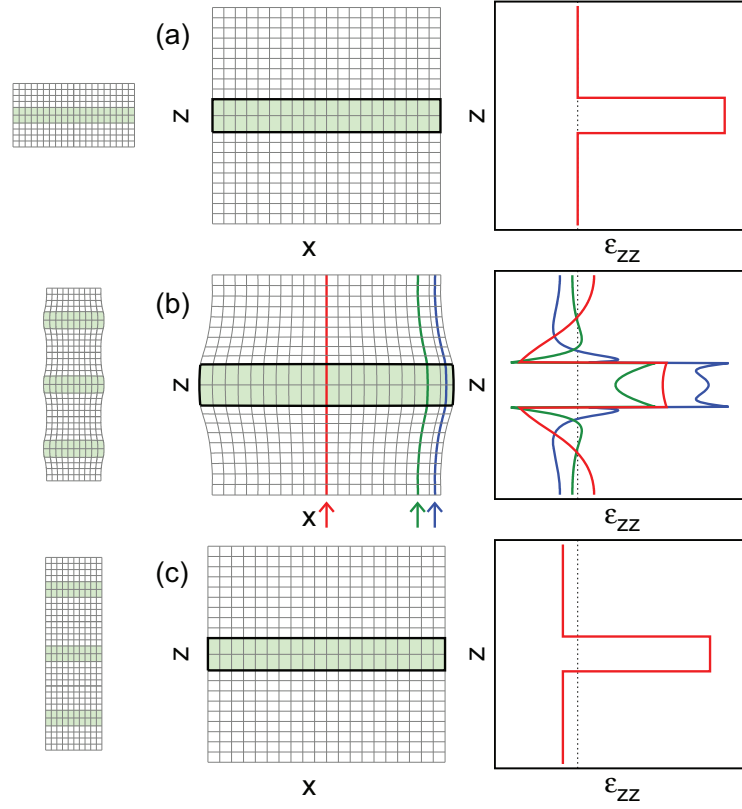


Figure 4.5: Strain states of lattice-mismatched crystal heterostructures with atomic displacement (left) and out-of-plane strain ϵ_{zz} (right). (a) Pseudomorphic epitaxial QW growth, the planar substrate remains strain-free. (b) Axial NW superlattice, non-uniform strain profile calculated with cylindrical model.^[174] The red, green and blue curves represent the displacement and strain at the radial positions indicated by the arrows (NW center, 80 % and 95 % of NW radius). (c) Axial NW superlattice, lateral relaxation estimate, QW and barrier assume a common average in-plane lattice parameter.

introduced at the heterointerface, but relaxes on a small length scale toward the NW surface. Yet, if the heterostructure geometry and hence the strain state is well defined, useful approximations can still be made that allow to derive the alloy composition from XRD and Raman data, as will be explained in the following. For the purpose of this thesis, the discussion can be limited to elastic relaxation and neglect the introduction of dislocations beyond a critical strain energy.

4.3.1 Strain states in mismatched heterostructures

For the description of the strain in $\text{In}_x\text{Ga}_{1-x}\text{N}/\text{GaN}$ heterostructures with interfaces in the C-plane, the growth axis is represented now by the Cartesian z -axis. The crystal is rotationally symmetric in the xy -plane (C-plane). Three distinct strain states will be considered in the following. When a thin film with the lattice constant a_2 grows epitaxially on a planar substrate with the lattice constant a_1 , the substrate remains unstrained and

the film experiences the in-plane strain $\varepsilon_{xx} = \varepsilon_{yy} = (a_1 - a_2)/a_2$.^e This situation, known as pseudomorphic growth, is typical for the growth of $\text{In}_x\text{Ga}_{1-x}\text{N}$ films below the critical thickness on C-plane GaN. Pseudomorphic growth is shown in Fig. 4.5(a) for $a_2 > a_1$. ε_{xx} is negative in the $\text{In}_x\text{Ga}_{1-x}\text{N}$ QW, shaded green on the left. The Poisson effect induces an out-of-plane strain ε_{zz} of opposite sign, plotted on the right, which depends on the elastic constants C_{13} and C_{33} , or in an equivalent expression, on the Poisson ratio ν :

$$\varepsilon_{zz} = -\frac{2C_{13}}{C_{33}}\varepsilon_{xx} = -\frac{2\nu}{1-\nu}\varepsilon_{xx}. \quad (4.1)$$

Throughout this work, the elastic constants for GaN from Ref. 36 are used: $C_{13} = 106$ GPa, $C_{33} = 398$ GPa, or $\nu = 0.21$.

If, on the other hand, the width of the heterointerface is on the nm-scale and it is surrounded by free surfaces, lateral elastic relaxation occurs in both materials. Figure 4.5(b) shows the displacement (left) and the out-of-plane strain (right) which were obtained analytically for an axial superlattice of thin quantum wells (a_2) and barrier material (a_1) in a cylinder, as described in Ref. 174. The strain is non-uniformly distributed. In the center, shown by the red line, the barrier crystal is laterally expanded, and since Eq. (4.1) holds, ε_{zz} becomes negative at the barrier side of the interface. The quantum well is still under lateral compression, and its ε_{zz} is positive, but smaller than in the pseudomorphic case of Fig. 4.5(a). Going outwards, the strain distribution remains qualitatively similar to the one in the center up to about 80 % of the cylinder radius, shown by the green line. Towards the surface the strain profile becomes complex as shown by the blue line at 95 % of the radius. This non-uniformity in strain is inherent to the axial NW heterostructure and is therefore present even if all structural fluctuations between the NWs of an ensemble are ruled out.

4.3.2 Lateral relaxation approximation

When an integral over local strain states is of interest, such as in the volume-probing x-ray diffraction, a simplified approximation can be made,^[174] as shown in Fig. 4.5(c). It is assumed that the in-plane lattice spacing takes on a constant value everywhere in the superlattice, because of the coherent growth. The in-plane strain ε_{xx} then takes on an average value, weighted by the thicknesses d_{barrier} of the barrier and d_{SL} of the superlattice period.^[176] The strain state of the quantum well is therefore described by

$$\varepsilon_{xx} = \frac{d_{\text{barrier}}}{d_{\text{SL}}} \frac{a_1 - a_2}{a_2} \quad (4.2)$$

in addition to Eq. (4.1). In the situation depicted in Fig. 4.5(c), this relaxation reduces the strain in the quantum well by the factor $d_{\text{barrier}}/d_{\text{SL}}$ compared to Fig. 4.5(a). Reciprocally, the thin quantum wells lead to a small lateral expansion and vertical compression of the barrier. The theoretical discussion below and the experimental validation in Sec. 6.5.2 will establish a criterion for the agreement of this *lateral relaxation approximation* with real NW heterostructures: The height of the superlattice stack of N periods, Nd_{SL} , must be at least as large as the NW diameter.

The statement in Eq. (4.2), that the strain state of an axial quantum well in a nanowire

^e ε_{xx} is sometimes given the index \parallel to indicate in-plane orientation,^[174] and sometimes in the context of biaxial strain given the index \perp .^[175] These forms are avoided here.

4 Analytical tools for the structural investigation of nanowire ensembles

is defined by the relative thicknesses of quantum well and barrier, is very important throughout this thesis for three reasons:

- A degree of freedom for strain design is introduced which is absent in crystalline films grown on a bulk substrate. During nanowire synthesis, the strain of a nanowire segment can be defined by choosing the neighboring segment lengths.
- In the analysis of x-ray diffraction, the stress-free lattice parameter and hence the $\text{In}_x\text{Ga}_{1-x}\text{N}$ composition can be derived from the strain in the quantum well.
- In Raman spectroscopy, the strain-induced frequency-shift, which depends on the segment lengths, can be separated from the composition-induced frequency-shift, which is devoid of this dependence.

Even though Eq. (4.2) can be intuitively understood it is not trivial, and the derivation which was published in Ref. 176 is cited here verbatim: Let us consider a periodic superlattice stack made from two materials, 1 and 2. Material 1 is taken as a reference for all strain values and material 2 possesses an eigenstrain ε_0 with respect to it. Let the lateral and the vertical eigenstrain components be equal to each other. Thus, the lattice constants c_1^0 and c_2^0 in the fully relaxed state are related by $\varepsilon_0 = (c_2^0 - c_1^0)/c_1^0$. The in-plane lattice parameter is approximated to assume a constant value throughout the whole stack, so that the in-plane total strain $\varepsilon_{1xx} = \varepsilon_{2xx} = \varepsilon_{xx}$. The same condition holds for the yy components. For the lateral relaxation of the superlattice (SL), two cases can be distinguished:

I. planar SL:	$\varepsilon_{xx} = 0$
II. nanowire SL:	$\xi_1\sigma_{1xx} + \xi_2\sigma_{2xx} = 0$ (4.3)

For a planar superlattice on a bulk substrate, lateral relaxation is absent, $\varepsilon_{xx} = 0$. In contrast, for an axial NW superlattice, the lateral stress σ_{xx} , averaged over the superlattice period, vanishes as in Eq. (4.3). ξ_1 and ξ_2 are the thickness fractions of the two materials ($\xi_1 + \xi_2 = 1$).

In both cases considered above, the superlattice is free to expand vertically and experiences no vertical stress, $\sigma_{zz} = 0$. Then, Hooke's law relates the strain components and allows to calculate the vertical strain. For material 1, where $\varepsilon_0 = 0$, one obtains

$$\sigma_{1zz} = \sigma_0[(1 - \nu)\varepsilon_{1zz} + \nu\varepsilon_{1xx} + \nu\varepsilon_{1yy}] = 0, \quad (4.4)$$

where $\sigma_0 = E/[(1 + \nu)(1 - 2\nu)]$. The Young modulus E and the Poisson ratio ν are taken to be identical for both materials. Since $\varepsilon_{xx} = \varepsilon_{yy}$, it follows

$$\varepsilon_{1zz} = -\frac{2\nu}{1 - \nu}\varepsilon_{xx}. \quad (4.5)$$

In material 2, only the difference between the total strain ε and the eigenstrain ε_0 leads to stress, and instead of Eq. (4.5) one obtains

$$\varepsilon_{2zz} - \varepsilon_0 = -\frac{2\nu}{1 - \nu}(\varepsilon_{xx} - \varepsilon_0). \quad (4.6)$$

For the case of NWs, the lateral strain ε_{xx} can be found by calculating the in-plane

stress:

$$\begin{aligned}\sigma_{1xx} &= \sigma_0[(1 - \nu)\varepsilon_{xx} + \nu\varepsilon_{yy} + \nu\varepsilon_{1zz}], \\ \sigma_{2xx} &= \sigma_0[(1 - \nu)(\varepsilon_{xx} - \varepsilon_0) + \nu(\varepsilon_{xx} - \varepsilon_0) + \nu(\varepsilon_{2zz} - \varepsilon_0)].\end{aligned}\quad (4.7)$$

Substituting these expressions into Eq. (4.3) yields the simple result

$$\varepsilon_{xx} = \zeta_2 \varepsilon_0, \quad (4.8)$$

which means that the degree of relaxation of material 2 is proportional to its contribution to the superlattice period. This was the claim of Eq. (4.2).

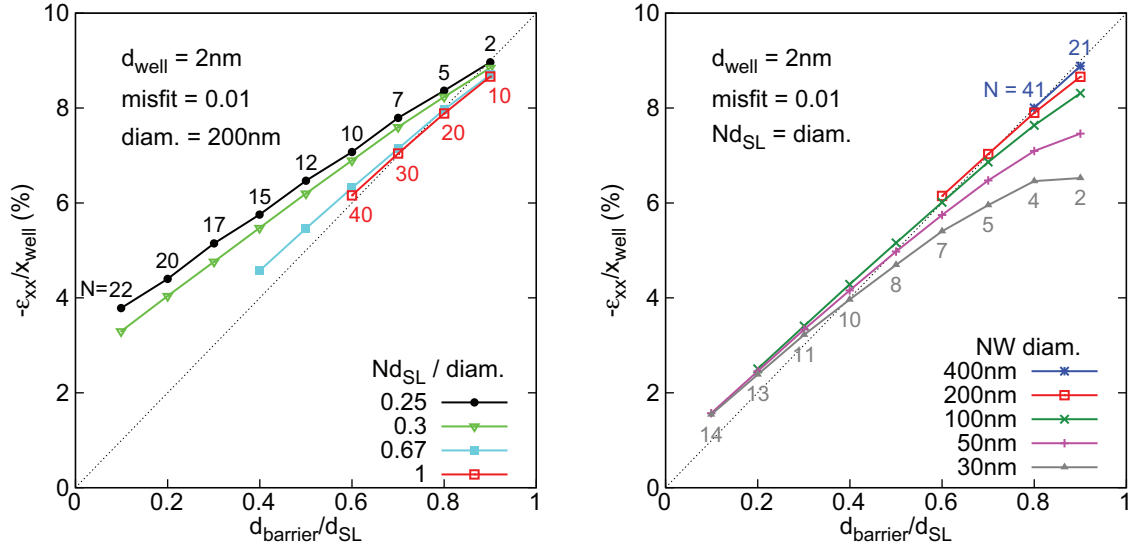
In a real NW heterostructure, the in-plane lattice parameter is of course not constant as was assumed here. In the following, the validity of the lateral relaxation approximation will be discussed. The detailed solution of the anisotropic elastic problem in a cylinder by Kaganer and Belov^[174] was already used to calculate the non-uniform displacement in Fig. 4.5(b). They came to the conclusion that the height of the whole heterostructure in comparison to the NW diameter is a good measure for the efficiency of the lateral relaxation. Figure 4.6 compares the average strain in axial NW QWs calculated by the formalism of Kaganer and Belov to the simple approximation in Eq. (4.2). The approximation is indicated by the thin dotted line in each graph. To obtain the average strain of the QWs in the exact calculation, the entire volume of all QWs from the NW heterostructure was randomly sampled in a Monte Carlo (MC) algorithm. Several calculations were made for a misfit of 1 %, corresponding to $\text{In}_x\text{Ga}_{1-x}\text{N}$ with $x = 10\%$. However, the criterion of the heterostructure height for the validity of the approximation is universal. Therefore, the plots show Eq. (4.2) in the form

$$\frac{\varepsilon_{xx}}{x_{\text{well}}} = \varepsilon_{\text{max}} \frac{d_{\text{barrier}}}{d_{\text{SL}}}, \quad (4.9)$$

where the constant ε_{max} is the maximum value for ε_{xx}/x in the fully strained case. For pure InN grown pseudomorphically on GaN, $\varepsilon_{\text{max}} = (a_{\text{GaN}} - a_{\text{InN}})/a_{\text{InN}} = -10\%$. The QW thickness $d_{\text{well}} = 2\text{ nm}$ is constant in all calculations. In a first set of simulations, NW heterostructures were simulated with different numbers N of periods of quantum wells and barriers, at a fixed NW diameter of 200 nm. In a second set of simulations, the NW diameter was varied, and the number of QWs was adjusted in keeping with the criterion for relaxation, that the stack height must at least equal the diameter. In order to keep the simulation in a parameter range that is accessible to the experimental methods in this thesis, the curves are shown for $N < 45$.^f

The simulation results in Fig. 4.6(a) show the effect of changing the MQW stack height Nd_{SL} for a fixed NW diameter. The red curve (empty squares) shows the situation where the criterion for the lateral relaxation approximation is met: Nd_{SL} equals the diameter. Here, the strain in the quantum well is predicted to a good precision by Eq. (4.2), represented by the dotted line. With $N = 40$ QW disks, the average strain in the QW ε_{xx} is reduced to $0.6\varepsilon_{\text{max}}$. Further reduction of the QW strain at this NW diameter would require a higher N , because the ratio $d_{\text{barrier}}/d_{\text{SL}}$ needs to be reduced, making the period smaller. When the stack height Nd_{SL} is allowed to become smaller than the NW diameter,

^fIt will be seen in Ch. 5 that the requirements for a pure axial growth of the $\text{In}_x\text{Ga}_{1-x}\text{N}/\text{GaN}$ active region, a high V/III ratio, is mutually exclusive with an efficient axial growth rate. In the current MBE 8 setup, the active region can be grown at about 1 nm/min.



(a) Impact of the MQW stack height Nd_{SL} on the average strain in the QWs. The NW diameter is the same in all points. The effective relaxation is less than predicted by the approximation for stack heights smaller than the diameter.

(b) Impact of the NW diameter on the average strain in the QWs. The condition that the superlattice stack height Nd_{SL} be equal to the NW diameter is met for all points. In thin NWs, the QWs are never fully strained, even for large $d_{barrier}/d_{SL}$.

Figure 4.6: Calculated strain relaxation in axial $\text{In}_x\text{Ga}_{1-x}\text{N}$ QWs in GaN NWs. The average strain from detailed calculations^[174] is compared to the approximation in Eq. (4.2), represented by the thin dotted line. The relative strain ϵ_{xx}/x_{well} , which for InN on GaN is at most -10% , is plotted as a function of $d_{barrier}/d_{SL}$. The number N of QW and barrier periods is written at each point of the top and bottom curves. The curves are drawn for $N < 45$.

as shown by the other three curves, the effective strain in the QW deviates progressively from Eq. (4.2). However, more relaxation of the QW than in the case of the red curve can still be obtained, without a higher N . The last point of the green curve (triangles) reduces the average strain to ca. $0.3 \epsilon_{max}$ with $N = 27$. Interestingly, the effective relaxation is still almost linear with $d_{barrier}/d_{SL}$ in this case, but the minimum attainable strain varies with the ratio of Nd_{SL} to NW diameter.

The second set of simulations reveals another systematic deviation from the approximation. The criterion that Nd_{SL} equals the NW diameter is always fulfilled in these simulations, and the NW diameter is varied. The red curve (empty squares) in Fig. 4.6(b) shows the same data as before. The same relaxation $\epsilon_{max} - \epsilon_{xx}$ in the QWs is achievable for all NW diameters, provided that N is high enough. Towards the strained side of the graph, it is apparent however, that the QWs in thinner NWs never come close to the maximum mismatch strain. Whereas for a diameter of 200 nm Eq. (4.2) is almost met, the QWs in a NW of only 30 nm relax to almost $0.6 \epsilon_{max}$, even if their thickness is very small compared to the barrier thickness.

These simulations of strain in axial $\text{In}_x\text{Ga}_{1-x}\text{N}/\text{GaN}$ NW heterostructures confirm that Eq. (4.2) is a good approximation under two conditions:

- To achieve very low strain in the QWs, the MQW stack height must be sufficiently high. A minimum height equal to the diameter was stated before as the criterion

for the lateral relaxation approximation.

- To achieve very high strain in the QWs, the NWs must be sufficiently thick.

The lateral relaxation approximation must be used with caution: A situation can be thought of, where the average strain in the QWs becomes almost independent of $d_{\text{barrier}}/d_{\text{SL}}$. To give an example, one can interpolate from the graphs in Fig. 4.6 that for 30 nm diameter and $N = 3$, the average strain could be designed only to vary between $0.4 \varepsilon_{\text{max}}$ ($d_{\text{barrier}}/d_{\text{SL}} = 0.1$, $Nd_{\text{SL}}/\text{diam.} \approx 0.2$) and $0.6 \varepsilon_{\text{max}}$. It is worth stressing that significant strain relaxation in NW superlattices, compared to the growth on bulk substrates, occurs even if Nd_{SL} is much smaller than the NW diameter. As indicated by Fig. 4.6(a), the relaxation $\varepsilon_{\text{max}} - \varepsilon_{xx}$ remains a linear function of $d_{\text{barrier}}/d_{\text{SL}}$ over a wide range of parameters.

4.3.3 Average out-of-plane lattice constant in mismatched heterostructures

The average out-of-plane lattice constant c_{avg} in mismatched MQW structures is an important parameter, because it is immediately determined from symmetric Bragg x-ray diffraction experiments. Following the above considerations, one can write

$$c_{\text{avg}} = \xi_1 c_1 + \xi_2 c_2 = \xi_1 c_1^0 (1 + \varepsilon_{1zz}) + \xi_2 c_1^0 (1 + \varepsilon_{2zz}). \quad (4.10)$$

For the case of planar layers on bulk substrate, where $\varepsilon_{xx} = 0$, out-of-plane strain from Eq. (4.5) and Eq. (4.6) can be substituted into Eq. (4.10), which becomes

$$c_{\text{avg}} = c_1^0 (1 + \xi_2 \varepsilon_{2zz}) = c_1^0 \left(1 + \frac{1 + \nu}{1 - \nu} \xi_2 \varepsilon_0 \right). \quad (4.11)$$

For GaN/In_xGa_{1-x}N superlattices, Vegard's law defines $\varepsilon_0 = x(c_{\text{InN}} - c_{\text{GaN}})/c_{\text{GaN}}$. With the average superlattice composition $x_{\text{avg}} = \xi_2 x$, this yields the familiar result:

$$\text{I. planar SL:} \quad \frac{c_{\text{avg}} - c_{\text{GaN}}}{c_{\text{InN}} - c_{\text{GaN}}} = \frac{1 + \nu}{1 - \nu} x_{\text{avg}}. \quad (4.12)$$

Contrarily, for NWs, Eq. (4.8) holds, and Eq. (4.10) becomes

$$c_{\text{avg}} = c_1^0 (1 + \xi_2 \varepsilon_0). \quad (4.13)$$

This means that c_{avg} is not subject to the Poisson effect:

$$\text{II. nanowire SL:} \quad \frac{c_{\text{avg}} - c_{\text{GaN}}}{c_{\text{InN}} - c_{\text{GaN}}} = x_{\text{avg}}. \quad (4.14)$$

After the detailed solution of the anisotropic elastic problem, Kaganer and Belov defined a relaxation factor f which allows to write Eq. (4.12) and Eq. (4.14) universally as $(c_{\text{avg}} - c_{\text{GaN}})/(c_{\text{InN}} - c_{\text{GaN}}) = f x_{\text{avg}}$.^[174] In the boundary case of planar superlattices (I.), $f = 1.53$ with the elastic constants for GaN. In the other extreme of lateral relaxation in nanowires (II.), $f = 1$. Kaganer and Belov calculated the x-ray diffraction profiles for the non-uniform displacement in cylindrical nanowire heterostructures with the quantum well thickness $d_{\text{well}} = 6$ nm and the superlattice period $d_{\text{SL}} = 20$ nm. They then obtained c_{avg} from the peak positions. Figure 4.7 shows f as a function of the NW diameter for numbers of disks N of 5, 10, and 25. For N periods, the MQW stack height is Nd_{SL} . The limiting case (I.) is obtained for $N = 5$ at nanowire diameters of 10000 nm, i. e. roughly

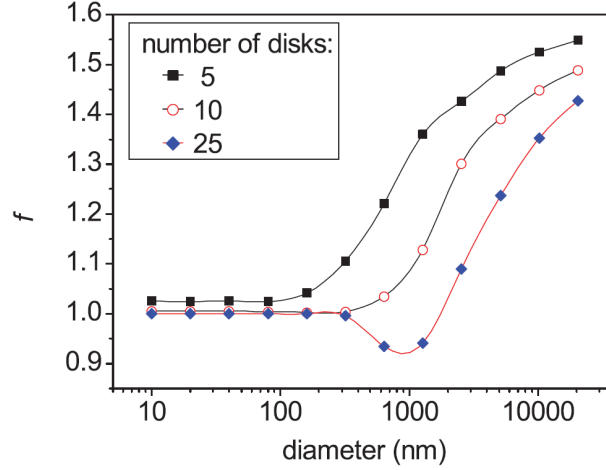


Figure 4.7: Relaxation factor f , describing the strain state of NW heterostructures with quantum well thickness $d_{\text{well}} = 6$ nm and superlattice period $d_{\text{SL}} = 20$ nm. In the limit for thin NWs, $f = 1$, lateral relaxation is complete and the Poisson effect vanishes on average. From Ref. 174.

one hundred times larger than the MQW stack height. Complete relaxation in the sense of case (II.), on the other hand, perfectly describes the x-ray diffraction profiles for ten MQW periods ($Nd_{\text{SL}} = 200$ nm) and nanowire diameters of 200 nm and below, i. e. not larger than the MQW stack height. If the latter condition is met, c_{avg} can be approximated as fully relaxed even with only five disks.

4.4 Resonant Raman spectroscopy

Raman spectroscopy measures the energy transfer during inelastic scattering of light. The difference in the energy of the incident and scattered photons corresponds to the difference of two energetic states of the material. Of particular interest here is the scattering by phonons, excited states of lattice vibrations. The phonon spectrum of nitride semiconductor crystals exhibits modes whose frequency depends on the chemical composition and on the strain state. The increased availability of laser light at suitable wavelengths and high-quality nitride semiconductor crystals has permitted the development of Raman spectroscopy as an analytical tool in the last twenty years, starting with the work of Hayashi *et al.* [153,177]

For the analysis of $\text{In}_x\text{Ga}_{1-x}\text{N}$ quantum wells, longitudinal optical (LO) phonons can be used, which scatter light by the so-called Fröhlich mechanism: In polar crystals such as III-nitrides, LO phonons are associated with longitudinal macroscopic electric fields which interact with electron-hole pairs excited by incident light. [178] In the analysis of thin semiconductor quantum wells, the Raman signal can be separated from that of the substrate by resonantly exciting material of a specific band gap.

The A_1 and $E_1(\text{LO})$ phonons are of particular interest for the study of thin $\text{In}_x\text{Ga}_{1-x}\text{N}$ quantum wells, because they can be detected with a particularly strong resonance enhancement. [179] Published measurements of the behaviour of the LO phonons often rely on C-plane $\text{In}_x\text{Ga}_{1-x}\text{N}$, for which the Raman selection rules allow the observation of the $A_1(\text{LO})$ mode. Contrary to planar layers, in as-grown ensembles of vertical nanowires light is coupled into and out of C-plane $\text{In}_x\text{Ga}_{1-x}\text{N}$ laterally through the side facets, i. e.

perpendicular to the C-direction. In this geometry, scattering by $E_1(\text{LO})$ phonons dominates over that by $A_1(\text{LO})$ phonons. Two independent ways to support this finding were described by Lazić *et al.*, who distinguished the two modes in InN NWs by their wavenumber,^[180,181] and by Carsten Pfüller, who showed that the LO mode is not observed in GaN NW ensembles as a function of the polarization configuration, and therefore does not correspond to the $A_1(\text{LO})$ mode.^[182,183] This is illustrated by the experimental spectra in Fig. 4.8, which is reproduced from his work. In the planar sample, the $A_1(\text{LO})$ mode is observed in the polarized $[z(y, y)\bar{z}]$ configuration (solid line), but not in the depolarized $[z(x, y)\bar{z}]$ configuration (dashed line). The observed mode in the NW sample does not show this dependence, indicating that it is $E_1(\text{LO})$, which is allowed only if the light enters and leaves the NWs through the sidewalls.

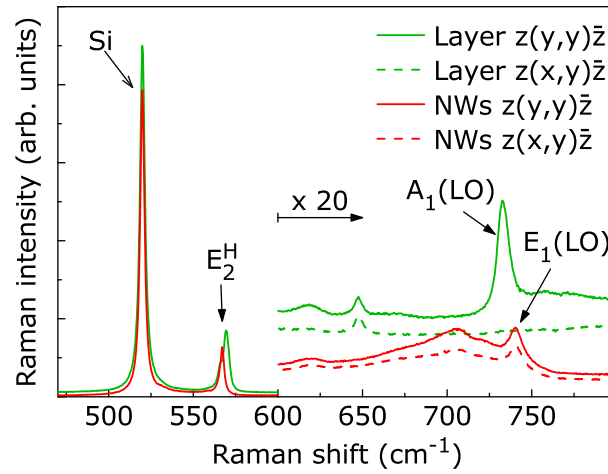


Figure 4.8: Raman spectra of a GaN layer (green) and a GaN NW ensemble (red), both grown on silicon. The Γ -point optical phonon of the Si substrate is visible at 520.5 cm^{-1} and the E_2^h phonon of GaN at 567 cm^{-1} . Above 600 cm^{-1} , the intensities are multiplied by 20. The LO modes are discussed in the text. From Ref. 182.

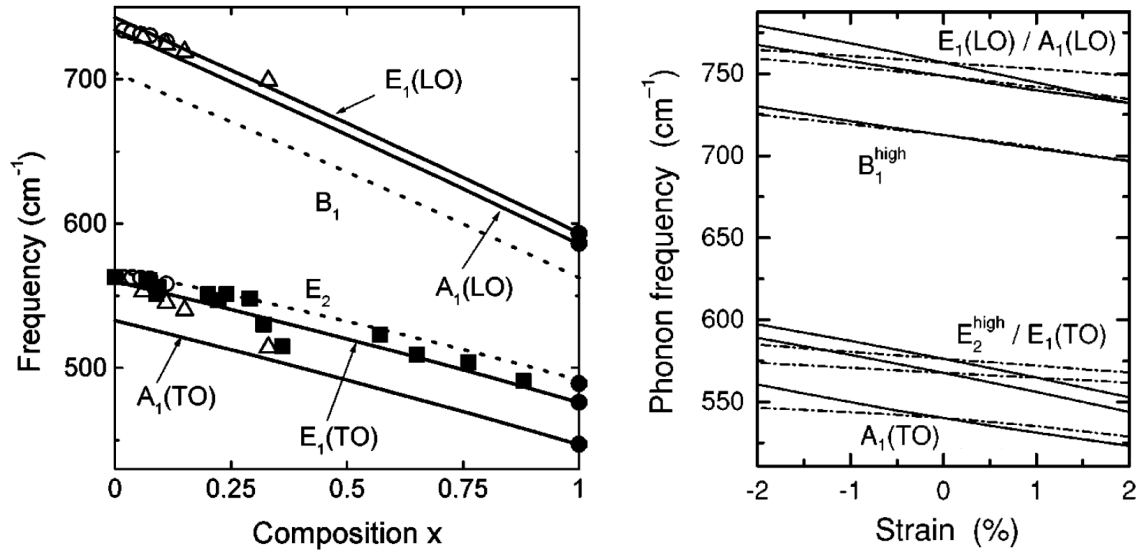
From the viewpoint of structural analysis, the main difference between x-ray diffraction and Raman spectroscopy is that the former probes the long-range correlation of atomic arrangement while the latter probes the local atomic neighborhood. The Fröhlich range of interaction under resonant conditions is in the order of $(50 \text{ Å})^3$.^[184] This is important for the analysis of the $\text{In}_x\text{Ga}_{1-x}\text{N}$ alloy, which is frequently observed to contain significant local fluctuations in composition. The interpretation of Raman data from $\text{In}_x\text{Ga}_{1-x}\text{N}$ is complicated by two factors. First, resonant Raman spectroscopy may probe only those fractions of the volume whose band gap is in resonance with the excitation.^[185] This is in contrast to x-ray diffraction, where neighboring volume elements contribute equally. The second source of ambiguity is the relation of composition and strain in pseudomorphically grown $\text{In}_x\text{Ga}_{1-x}\text{N}$. The difficulty in disentangling contributions of strain, composition and resonance has remained a drawback to the application of Raman spectroscopy to $\text{In}_x\text{Ga}_{1-x}\text{N}$ even in the latest work.^[186] The analysis of $\text{In}_x\text{Ga}_{1-x}\text{N}/\text{GaN}$ NWs presented in this thesis benefits from the well defined strain state in axial NW heterostructures described earlier in this chapter (4.3.1). The following considerations of the Raman shift in NW heterostructures are in preparation for Ref. 173.

4.4.1 Strain- and composition dependence of LO phonon frequency

The LO phonon frequencies ω_{LO} in the nitrides shift as a function of composition x and strain ε , which can be approximated by

$$\omega_{\text{LO}}^{\text{In}_x\text{Ga}_{1-x}\text{N}} = \omega_0^{\text{GaN}} + \Delta\omega_0(x) + \Delta\omega(\varepsilon). \quad (4.15)$$

In strain-free $\text{In}_x\text{Ga}_{1-x}\text{N}$, the A_1 and $E_1(\text{LO})$ phonon frequencies shift linearly with x , $\Delta\omega_0(x) = -149x \text{ cm}^{-1}$.^[187] This value has been obtained in calculation with a lattice-dynamical model by Grille *et al.*^[188] Figure 4.9(a) reproduces their graphical summary. The composition dependence of the $A_1(\text{LO})$ phonon frequency was experimentally confirmed in several works which are cited in Refs. 188 and 187.



(a) Phonon frequencies $\omega_0(x)$ in fully relaxed $\text{In}_x\text{Ga}_{1-x}\text{N}$. Lines: calculated. Symbols: experimental. From Ref. 188, experimental data sources are given there.

(b) GaN phonon frequencies $\omega(\varepsilon_{xx})$ in the case of biaxial strain (solid line) and uniaxial strain (dot-dashed line). Adapted from Ref. 175.

Figure 4.9: Phonon frequency shift in $\text{In}_x\text{Ga}_{1-x}\text{N}$ as a function of composition and strain.

For the shift of the $\text{In}_x\text{Ga}_{1-x}\text{N}$ phonon frequencies with strain $\Delta\omega(\varepsilon)$, no exhaustive report is available. The structural analysis presented in this thesis therefore makes use of literature values for the strain dependence of the phonon frequencies in GaN. To describe the strain dependence $\Delta\omega(\varepsilon)$ of the $A_1(\text{LO})$ phonon frequency, the phonon deformation potentials a and b can be used,

$$\Delta\omega(\varepsilon) = a(\varepsilon_{xx} + \varepsilon_{yy}) + b\varepsilon_{zz}, \quad (4.16)$$

as long as the crystal symmetry is preserved.^[151] Experimental values for the $A_1(\text{LO})$ phonon in GaN are $a = -782 \text{ cm}^{-1}$ and $b = -1181 \text{ cm}^{-1}$, per unit of strain. (Demangeot *et al.* in Ref. 189, Table IV.) In the case of pure biaxial strain where Eq. (4.1) holds, a and b can be combined in a biaxial coefficient

$$K_{\perp} = 2a - 2bC_{13}/C_{33} = \Delta\omega/\varepsilon_{xx}. \quad (4.17)$$

From the literature values one obtains $K_{\perp} = -935 \text{ cm}^{-1}$ per unit of strain for GaN.⁸ Experimental phonon deformation potentials for the $E_1(\text{LO})$ phonon are not available, but Wagner *et al.* have performed calculations in density-functional theory.^[175] Their comparison of strain dependencies of the phonon frequencies is reproduced in Fig. 4.9(b). For compressive biaxial strain, i. e. $\varepsilon_{xx} < 0$, as would be the case for $\text{In}_x\text{Ga}_{1-x}\text{N}$ grown on GaN, the strain dependence $\Delta\omega/\varepsilon_{xx}$ of the $E_1(\text{LO})$ phonon in GaN is equal to that of the $A_1(\text{LO})$ phonon. Figure 4.10 summarizes the values of K_{\perp} for the $A_1(\text{LO})$ phonon in GaN, InN, and $\text{In}_{0.18}\text{Ga}_{0.82}\text{N}$, which can be deduced from the literature today. There seems to be a tendency for a stronger strain-induced frequency shift with increasing In content, but there is a large uncertainty in this value. To conclude, in this thesis, $K_{\perp} = -1030 \text{ cm}^{-1}$ will be used for the $E_1(\text{LO})$ phonon in the $\text{In}_x\text{Ga}_{1-x}\text{N}$ QWs.

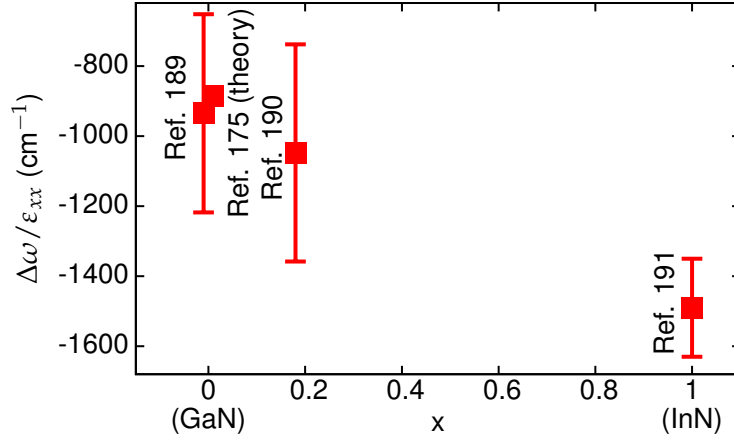


Figure 4.10: Literature values for the $A_1(\text{LO})$ phonon frequency shift under biaxial strain in GaN, InN, and the ternary alloy.

4.4.2 Simulation of Raman spectra for non-uniform strain in nanowire heterostructures

The previous section has provided the relation of the $E_1(\text{LO})$ phonon frequency to the strain and composition of $\text{In}_x\text{Ga}_{1-x}\text{N}$ layers in the biaxial strain state. For Raman spectroscopy to be useful in the analysis of NW heterostructures, it must be shown how this relation applies to the axial $\text{In}_x\text{Ga}_{1-x}\text{N}$ quantum wells under non-uniform strain as was shown in Fig. 4.5(b). To this end the Raman spectrum was simulated. To be able to compare simulated spectra with experimental data, local fluctuations of x and the effect of the resonant excitation must also be taken into account. The general form of the resonant Raman spectrum is

$$I(\omega) = \int_0^1 dx \underbrace{R(x)C(x)}_{\text{weighting factor}} L(x), \quad (4.18)$$

where the phonon lineshape $L(x)$ for a given In content x is weighted by the relative concentration of this particular In content $C(x)$, and by the relative Raman efficiency given by the resonance profile $R(x)$.^[186] The phonon lineshape is a Lorentzian around

⁸The nomenclature of Ref. 175 is followed here. In contrast, the biaxial pressure coefficient K^B explicitly given in Ref. 189 is in unit of stress and corresponds to \tilde{K}_{\perp} in Ref. 175.

4 Analytical tools for the structural investigation of nanowire ensembles

the $\omega_{\text{LO}}(x, \varepsilon)$ given by Eq. 4.15:

$$L(x) = \frac{1}{[\omega_{\text{LO}}(x, \varepsilon) - \omega]^2 + \Gamma_{\text{ph}}^2}. \quad (4.19)$$

The minimum width of a phonon peak, when the composition and strain are uniform, is $\Gamma_{\text{ph}} \approx 10 \text{ cm}^{-1}$. The resonance profile is also approximated by a Lorentzian, and the width Γ_g is 0.1 eV:^[186]

$$R(x) = \frac{1}{[E_{\text{exc}} - E_g(x, \varepsilon)]^2 + \Gamma_g^2}. \quad (4.20)$$

The experiments were carried out with $E_{\text{exc}} = 3.0 \text{ eV}$ (a Kr^+ laser line). For the purpose of simulating resonant Raman spectra, the bandgap E_g can be taken as the absorption energy, assuming that quantum confinement and the QCSE roughly compensate each other. For the detailed simulations, E_g was calculated as a function of the local composition and the local strain tensor with the Bir-Pikus 6×6 Hamiltonian (see Sec. 2.2.2). The distribution of the In content $C(x)$ is assumed to have a Gaussian form, characterized by the standard deviation σ_x .

Vladimir M. Kaganer extended the MC algorithm already used for the calculation of the average strain in NW heterostructures to account for random structural fluctuations. Resonant Raman spectra of NW ensembles can be simulated by adding the contributions of randomly generated NWs, each given by Eq. 4.18. The distribution $C(x)$ is inherent to the algorithm because the composition of every single NW is randomly generated. The non-uniformity of the strain is included by evaluating the strain tensor at randomly chosen positions in the quantum wells with the same formalism from Kaganer and Belov that was used for Figs. 4.5(b) and 4.6.^[174] If the simulation succeeds in modelling the experimental Raman spectra, the simulation parameters contain valuable information about the sample. First, the compositional uniformity, given by σ_x , will be obtained in this way in Sec. 5.5.3. Second, the strain ε in the QWs of several $\text{In}_x\text{Ga}_{1-x}\text{N}/\text{GaN}$ NW samples will be obtained in Sec. 6.5.2 to verify successful strain engineering.

In the remaining part of this chapter on analytical tools, the spectral broadening due to the impact of non-uniform strain on the Raman shift $\Delta\omega(\varepsilon)$ will be analyzed for different degrees of structural fluctuations in the NWs. As a starting point, simulations were done for six equidistant $\text{In}_x\text{Ga}_{1-x}\text{N}$ quantum wells in a GaN NW. For a NW diameter $\varnothing = 50 \text{ nm}$, $\text{In}_x\text{Ga}_{1-x}\text{N}$ quantum wells with $x = 20\%$, $d_{\text{well}} = 5 \text{ nm}$ and the period $d_{\text{SL}} = 19 \text{ nm}$, the green filled curve in Fig. 4.11 was obtained. The tail towards lower frequency shifts is due to more relaxed portions of the quantum wells close to the surface. The splitting of the peak is due to the different degrees of relaxation between the outer quantum wells, which are clamped on one side by the pure GaN NW, and the more relaxed inner quantum wells of the six-fold stack.

When self-induced $\text{In}_x\text{Ga}_{1-x}\text{N}/\text{GaN}$ NWs are synthesized by PAMBE, they exhibit a range of different diameters, as discussed in Sec. 4.1. The distribution which was experimentally obtained from cross-section scanning electron microscopy (see App. B) is repeated in the inset of Fig. 4.11. The MC algorithm was extended to take into account this variation of NW diameters. The red curve in Fig. 4.11 corresponds to the predicted Raman spectrum for the NW ensemble with this fluctuation in diameter. Compared to the single diameter case (green), the Raman peak is broadened and the distinction between inner and outer quantum wells is lost.

In real-world $\text{In}_x\text{Ga}_{1-x}\text{N}/\text{GaN}$ NW structures, additionally to the distribution in dia-

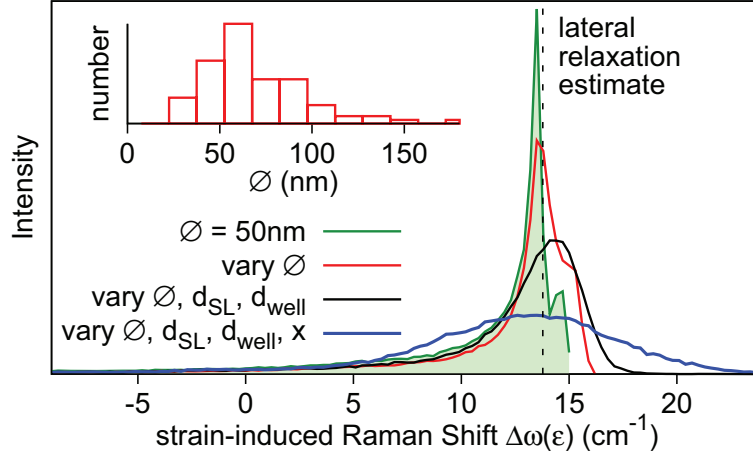


Figure 4.11: Calculated Raman shift for GaN NW with six $\text{In}_x\text{Ga}_{1-x}\text{N}$ quantum disks, $x = 20\%$, $d_{\text{well}} = 5\text{ nm}$, $d_{\text{SL}} = 20\text{ nm}$. Shaded green: fixed NW diameter. Red: distribution of NW diameters as shown in the inset for NWs grown by PAMBE. Black: variation of diameter and segment thicknesses, $\sigma_d = 2\text{ nm}$. Blue: additional variation of $\text{In}_x\text{Ga}_{1-x}\text{N}$ composition, $\sigma_x = 0.2x$.

meter, two more fluctuations in structure must be taken into account. For one, the thickness of the well and barrier segments fluctuates from NW to NW, as was shown in Sec. 4.2. The MC algorithm was now extended to cover this fluctuation with $\sigma_d = 2\text{ nm}$. The result is shown by the black curve in Fig. 4.11, and the peak is slightly broader yet compared to the red curve with diameter fluctuations alone. The second effect is the fluctuation in composition x . The result of adding a realistic fluctuation $\sigma_x = 0.2x$ is shown by the blue curve in Fig. 4.11. From a homogeneous alloy in the NW heterostructure to this strong fluctuation in composition, the Raman spectrum changes markedly from the black curve to the blue curve. The spectral broadening due to the alloy fluctuation σ_x significantly exceeds the previous broadening due to the layer thickness fluctuation σ_d and the distribution in diameter.

Using the approximation of lateral relaxation given in Sec. 4.3.2, the Raman frequency shift is derived by inserting the average strain in the $\text{In}_x\text{Ga}_{1-x}\text{N}$ QWs given by Eq. (4.2) into Eq. (4.17). The value obtained with the same x , d_{well} and d_{SL} as before is given by the dashed line in Fig. 4.11. As shown above, the lateral relaxation approximation can be used under these conditions, and the value for the frequency shift corresponds well to the peak position of the spectra obtained from integration over the non-uniformly stressed volume (green and red curves). Even when fluctuations of the segment thicknesses and composition are taken into account (black and blue curves), the agreement with the spectral peak position is acceptable. What the lateral relaxation approximation cannot show *a priori*, is the spectral broadening of the Raman peak. However, it was already observed by comparing the black and the blue curves in Fig. 4.11, that the alloy fluctuation has a bigger impact on the spectral broadening than the non-uniformity of the strain which is inherent to the heterostructure geometry. This allows an interesting conclusion: If the alloy fluctuation and the resonance can be accounted for, then a meaningful simulation of the Raman spectra is possible based on an *approximation of constant strain* in the QW, without the detailed numerical analysis of the strain distribution. This finding is more general than the estimate of the average strain by the lateral relaxation approximation. Even if the criteria for the latter are not met, a constant strain within the QWs can be

used to simulate Raman spectra. The experimental validation of this method requires thoroughly characterized samples and will be given in Sec. 5.5.3.

4.5 Conclusion

Ensembles of self-induced GaN NWs with $\text{In}_x\text{Ga}_{1-x}\text{N}$ heterostructures exhibit statistical structural fluctuations. A second effect are non-uniformities in strain which are intrinsic to their geometry. Both of these effects impact the measurement results in two important methods for the NW ensemble characterization: laboratory x-ray diffraction and Raman spectroscopy. A detailed description of the strain distribution within one NW is possible, and it is also necessary in order to deduce statistical distribution parameters from the measurement data. Within the discussion of the experimental data in the next chapter, σ_d will be derived from the simulation of XRD profiles. Once the segment heights and compositions are known from XRD, the alloy fluctuation σ_x will be derived from a MC simulation of the Raman spectra. For the design of growth experiments and devices, however, it is often desirable to obtain mean structural information efficiently. To correctly interpret the dominant LO phonon frequency in Raman spectra, the strain can be assumed as constant in the QWs. A simple approximation of the lateral relaxation in NW heterostructures can be used to obtain the mean strain and composition from XRD. This chapter has shown in detail, under which conditions the approximations of lateral relaxation and constant strain in the QWs are applicable, and how the experimental XRD profiles and Raman spectra can be interpreted.

5 Growth of $\text{In}_x\text{Ga}_{1-x}\text{N}/\text{GaN}$ nanowire heterostructures

In this chapter the impact of MBE growth conditions on the structural properties of $\text{In}_x\text{Ga}_{1-x}\text{N}/\text{GaN}$ nanowire heterostructures is described. During the preparation of this thesis, over 150 growth experiments were carried out, focusing on the nanowire heterostructures but including experiments with planar films for calibration and experiments with the base GaN NWs using a range of conditions and substrates. The calibration of the growth parameters is detailed in App. C. The effect of individual growth parameter changes on the nanowire heterostructure formation was analyzed by growing series of samples where only one parameter was changed. The reproducibility of the results was proven by repeated use of the same ‘recipe’, but also by comparing several series of samples with the same variable parameter but different setups of the epitaxy chamber.

The aim of this chapter is to provide rules for the design of $\text{In}_x\text{Ga}_{1-x}\text{N}/\text{GaN}$ NW growth experiments, where possible based on physical models of the growth processes. First, an account of the state of knowledge prior to this thesis is given. Then, in order to show the practical limitations for the design of the NW growth process, the experimental procedure is detailed step by step. The resulting microstructure and shape of typical $\text{In}_x\text{Ga}_{1-x}\text{N}$ insertions is then analyzed. The results on NW morphology are qualitative and based on individual microscopy observations. Even though no quantitative models are formulated, best practice rules for heterostructure design can be given. In the remaining sections, full use is made of XRD and Raman spectroscopy, the ensemble characterization techniques introduced in the last chapter, as well as the QMS in-situ tool for growth analysis. The key parameters for the active region, growth rate, quantum well thickness and composition are analyzed as a function of the experimental conditions, and the underlying physics is revealed.

5.1 Previous studies of $\text{In}_x\text{Ga}_{1-x}\text{N}/\text{GaN}$ nanowire heterostructure growth

The growth process of III-nitrides by plasma-assisted MBE^[65] was researched in the 1990s in parallel to the commercial introduction of GaN-based LEDs. In this context, the growth conditions for self-induced GaN NWs on Si(111) with high crystalline quality were identified.^[9] The application of $\text{In}_x\text{Ga}_{1-x}\text{N}/\text{GaN}$ nanowire heterostructures in an LED device on silicon was presented by Katsumi Kishino and co-workers in 2004.^[8] Subsequently, several groups published reports on the growth of GaN NWs^[192,193] and InN NWs^[194] on silicon.

Much less research had been carried out on the ternary $\text{In}_x\text{Ga}_{1-x}\text{N}$ alloy formation in NWs. The feasibility of $\text{In}_x\text{Ga}_{1-x}\text{N}$ NW synthesis over the entire compositional range had been shown in a halide chemical vapor deposition experiment.^[167] In MBE, the atomic processes governing the alloy formation are known for planar films (see Sec. 5.6.1):

The composition depends on the impinging fluxes and the thermally activated loss of In due to InN decomposition and desorption. This dependence was confirmed qualitatively in 2007 for $\text{In}_x\text{Ga}_{1-x}\text{N}$ NWs. Enrique Calleja and co-workers relied on the photoluminescence wavelength to determine the NW composition.^[103] $\text{In}_x\text{Ga}_{1-x}\text{N}$ NW samples of different composition, grown at different substrate temperatures, were also obtained by Georgakilas and co-workers.^[195] In the latter work, the difficulty in assessing the In content was highlighted by comparing values obtained from high resolution x-ray diffraction (XRD), energy dispersive x-ray analysis and photoluminescence.

The morphology of NW heterostructures has been studied in a few reports. Deviations from columnar growth with parallel *M*-plane side facets were reported, with In supply inducing the formation of branches^[196] or enlarging the NW diameter.^[193] One aspect of $\text{In}_x\text{Ga}_{1-x}\text{N}$ growth, known for planar layers and of potential importance in NW growth, is the segregation of In at the growth front. Such a segregation would lead to prolonged $\text{In}_x\text{Ga}_{1-x}\text{N}$ quantum well growth^[197], and a correct analysis of the thicknesses in MQW structures in NWs is therefore essential to understand NW growth.

Numerous experimental challenges are specific to the $\text{In}_x\text{Ga}_{1-x}\text{N}$ growth in the NW geometry. During the growth, the widely used RHEED method delivers less information than in planar growth experiments. In NWs, transmission diffraction of the electron beam prevails over surface diffraction, and reconstructions or adlayer accumulation can therefore not be detected. The characterization of samples also faces new challenges: because of the statistic distribution in NW height, popular depth-probing methods such as secondary ion mass spectroscopy (SIMS), Rutherford backscattering (RBS) and capacitance-voltage profiling^[198] can not separate the individual layers. Standard resistivity measurements such as radio frequency-free-carrier power absorption^[199] ('Leighton') or Hall measurements are prohibited by the NW geometry.

5.2 Experimental procedure

Self-induced GaN NWs were grown on 2'' Si(111) substrates by plasma-assisted molecular beam epitaxy. With the application in mind, a typical 'recipe' for an ensemble of NW LEDs is summarized in Table 5.1 and will be described now step by step. Such a typical LED 'run' takes 6 h 45 min. The focus of this work is the formation of the heterostructure, and therefore most samples contain only a subset of the LED structure: the base and the active region, but no doping. Parameters for all samples and their grouping in series are tabulated in App. A.

Prior to growth, the native Si oxide was removed *in situ* by depositing 100 monolayers (ML) of liquid Ga (Ga_{liq}) at a rate of 10 nm/min ($\approx 0.5 \text{ ML/s}$)^a and desorbing any Ga-O by raising the temperature. As discussed in Sec. 3.2.3, the appearance of the Si(111) 7×7 reconstruction in RHEED indicates that the desorption is complete and the substrate surface is clean and free of oxides. A second desorption of 40 ML Ga_{liq} , as shown in Fig. 3.6, serves to check the pyrometer reading and gave a standard deviation per growth

^aFor the Si(111) wafers used in this work, it was found that about 100 ML are required to obtain a surface free of oxides, indicated by the 7×7 reconstruction, in one deposition and desorption cycle. ML conversion: 1 ML Ga_{liq} is estimated to contain $1.4 \times 10^{15} \text{ atoms/cm}^2$. (The tabulated density at the melting point and a cubic arrangement is assumed. On a clean Si(111) surface, Ga atoms could attach one-to-one only with a density of $7.83 \times 10^{14} \text{ atoms/cm}^2$.^[200]) In a ML of GaN(00.1), one atom occupies an area of $\sqrt{3}a^2/2$, and the density is therefore $1.5 \times 10^{15} \text{ atoms/cm}^2$. The thickness of 1 ML GaN(00.1) is $c/2$. 1 ML Ga_{liq} therefore corresponds to the amount of Ga atoms in a 3.3 Å-thick GaN(00.1) layer.

Table 5.1: Step-by-step description of typical $\text{In}_x\text{Ga}_{1-x}\text{N}/\text{GaN}$ NW heterostructure and NW LED growth experiments.

step	t (min.)	T (°C)	active sources (InAlGa _N :SiMg)		comment
deposition of 100 ML Ga_{liq}	3	standby	Ga		
T -ramp and Ga-O flash-off					results in Si(111) 7×7
deposition of 40 ML Ga_{liq}	1	450	Ga		protocol in Fig. 3.6
T -ramp and pyrometer check					$dT/dt = 25^\circ\text{C}/\text{min}$
nitridation	5	780	N		
n-GaN base	90	780	Ga _N :Si		doping for LED only
In desorption test	2	780	In	N	protocol in Fig. 5.21
T -ramp			N		
$4 \times \left\{ \begin{array}{l} \text{barrier} \\ \text{quantum well} \\ \text{electron blocking} \\ \text{layer} \end{array} \right.$	8	600	Ga _N		
	1	600	In	GaN	
	16	600	AlGa _N	:Mg	LED only
p-GaN cap	180	600+	GaN	:Mg	LED only, slow T -rise during growth

series of 1.4°C (series 18 and 19) or 0.9°C (series 23).

Exposing the Si substrate to Ga and N flux at about 780°C invariably leads to the formation of silicon nitride, Si_xN_y .^[85,102,104] This interlayer affects the GaN nanowire orientation with respect to the Si crystal (see App. B). To allow a reproducible interlayer formation, the Si substrate was exposed to N plasma and thus nitridated for a fixed time of 5 min prior to GaN growth.

The defect density in GaN nanowires decreases rapidly with increasing distance from the substrate interface (Ref. 154, Sec. V). Therefore, base GaN nanowires were grown for 60 min to a length of 300 nm (series 12, 18, 19) or for 90 min to 500 nm (series 23, 27, 28). The GaN nanowire density, coalescence degree, diameter and axial growth rate depend on the substrate temperature and the V/III ratio.^[9] The nanowire base of a typical sample (series 23) was grown at $T = 780^\circ\text{C}$ with $\Phi_{\text{Ga}} = 2.5 \text{ nm}/\text{min}$ and $\Phi_{\text{N}} = 13 \text{ nm}/\text{min}$, yielding a V/III ratio of 5.1. The GaN nanowires were Si-doped in those samples that were processed as LEDs.^[12] The axial growth rate of the NW base can be determined by measuring the length in SEM images (see App. B). A typical axial growth rate of the base was $2.5 \text{ nm}/\text{min}$. To optimize the growth rate while keeping the V/III ratio in the NW growth regime, the maximum Φ_{N} which could be obtained from the plasma source was used throughout the growth ‘run.’

During the growth of the GaN nanowire base, the In source is brought to the operating temperature for the growth of the active region. As will be explained in Sec. 5.6.1, at

5 Growth of $\text{In}_x\text{Ga}_{1-x}\text{N}/\text{GaN}$ nanowire heterostructures

$\text{In}_x\text{Ga}_{1-x}\text{N}$ nanowire growth temperatures a flux $\Phi_{\text{In,des}}$ of In atoms is lost to desorption from the substrate. In those experiments where the $\text{In}_x\text{Ga}_{1-x}\text{N}$ growth is to be monitored in situ by line-of-sight QMS, the relation between $\Phi_{\text{In,des}}$ and the ^{115}In partial pressure P_{In} must be known. To achieve this calibration, the substrate temperature is kept high (at about 780 °C) after the growth of the base nanowires, the Ga shutter is closed, and the In shutter is opened.^b At this temperature, all the impinging In desorbs, $\Phi_{\text{In}} = \Phi_{\text{In,des}}$, and $P_{\text{In}}/\Phi_{\text{In,des}}$ can be calibrated. A typical value is $3 \times 10^{-11} \frac{\text{torr}}{\text{nm}/\text{min}}$. This value depends drastically on the surface morphology (it is two times higher for GaN nanowires than for clean silicon), and on the condition of the residual gas analyzer (P_{In} decreases to a tenth over the lifetime of the detector). This In desorption test must therefore be carried out after the growth of the GaN NW base in every individual experiment.

After the In desorption test, all metal flux is interrupted and within 5 min T is ramped down to about 600 °C for the growth of the active region. T is only monitored by the pyrometer, but regulated via a thermocouple which is remote from the substrate. The thermal capacity of the sample holder assembly delays the response to temperature changes. Therefore, the rate of change is progressively decreased towards the end of the ramp, and an additional 5 min for stabilization is allowed.^c The pyrometer reading 5 s prior to the growth of the active region is interpreted as the growth temperature T .

The heterostructure, which forms the active region in LED samples, is composed of alternating $\text{In}_x\text{Ga}_{1-x}\text{N}$ quantum wells with the thickness d_{well} , typically targeted around 2.5 nm, and GaN barriers with the thickness d_{barrier} , typically above 8 nm. These thicknesses are not changed within a sample, and the MQW stack forms a superlattice, inducing x-ray diffraction satellite peaks. As will be detailed in Sec. 5.4, the XRD profiles were used to determine the superlattice period, $d_{\text{SL}} = d_{\text{well}} + d_{\text{barrier}}$. The axial growth rate can be extracted from d_{SL} and was typically between 1 nm/min (series 23, 27, LEDs) and 2.5 nm/min (series 18 and 19). Generally, the metal flux during the growth of the active region is chosen lower than during the growth of the base, because at lower T , less metal atoms desorb, but still the effective V/III ratio at the surface has to be kept in the NW growth regime: N-rich. The active region was begun either with a barrier (series 18 and 19) or with a QW (series 23, 27, LEDs), and it was always terminated with a QW. The number of QWs varied: six quantum wells were found to deliver a good x-ray contrast of the superlattice, and were used in samples designed for growth analysis. LEDs (and the early series 11 and 12) were grown with four QWs.

Above the active region, the nanowires were p-doped with Mg for LED samples, in order to place the p-n junction in the active region. Only for LED samples, an electron blocking layer (EBL) with the nominal composition $\text{Al}_{0.16}\text{Ga}_{0.84}\text{N}$ followed the active region. The EBL is a design element of planar LED devices which decreases the loss of ‘hot electrons’ from the active region.^[201]

As a last step, a GaN cap was grown. Because the same Φ_{Ga} is used as in the active region, the growth rate can be extrapolated. In undoped MQW samples for structural analysis, the cap was typically grown to 30 nm.^d In LED samples, the GaN cap was p-

^bThe N shutter is left open during the QMS calibration to keep the conditions on the sample surface close to the actual $\text{In}_x\text{Ga}_{1-x}\text{N}$ growth, and to reduce GaN decomposition.

^cLonger stabilization times are required if the target T is undershot during the ramp. In MBE 8, between Nov. 2010 and Sep. 2011, temperature-sensitive junctions existed in the thermocouple leads, located at points with slowly changing temperature inside the growth chamber and thus superimposing a drift on the thermocouple temperature signal. This has led to contradicting judgements on the required stabilization time.

^dIt was thought initially that enough cap material must be provided for absorbing the incident beam in

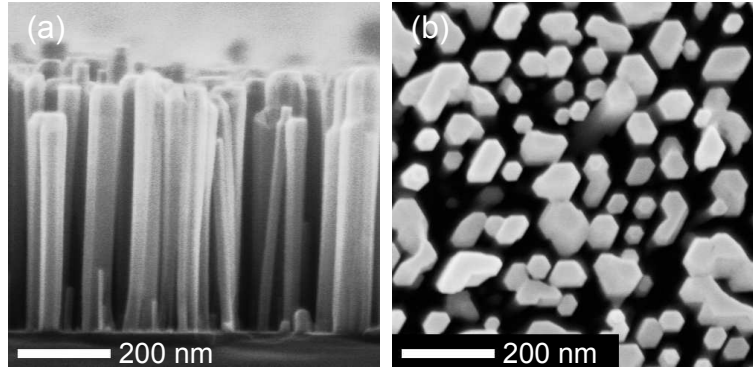


Figure 5.1: Scanning electron micrograph of GaN NWs on Si(111) with axial $\text{In}_x\text{Ga}_{1-x}\text{N}$ /GaN MQWs embedded at the tip, in cross-section (a), and plan view (b). The data was acquired by A.-K. Bluhm.^[202]

doped with Mg and a length of 180 nm was desired, to enable the electrical contacting of the nanowire ensemble by planarization, back-etching, and deposition of a contact. To reduce coalescence in LED samples, T was slowly ($dT/dt = 2^\circ\text{C}/\text{min}$) raised to 140°C above the active region growth temperature during the growth of the p-GaN segment.^[12]

Scanning electron micrographs of a typical sample with undoped base GaN NWs grown for 90 min and $\text{In}_x\text{Ga}_{1-x}\text{N}$ MQWs are shown in Fig. 5.1 in cross-section (a), and plan view (b).

5.3 Morphology of $\text{In}_x\text{Ga}_{1-x}\text{N}$ nanowire segments

The analysis of $\text{In}_x\text{Ga}_{1-x}\text{N}$ growth in axial NW segments has to begin with the confirmation that the intended structure could be experimentally obtained. Figure 5.2 compares the idealized structure (with six QWs) to scanning transmission electron microscopy (STEM) images of experimental structures (with four QWs). Figure 5.2(b) shows a bright-field contrast. Thick areas, crystalline areas and areas which contain heavy atoms appear dark, because the image is formed with the transmitted beam only and diffracted beams do not contribute. Figure 5.2(c) shows a high-angle annular dark field contrast (HAADF), also named z -contrast, because those electrons which are scattered incoherently contribute to the image, and the contrast is highly sensitive to the atomic number z of the scattering atoms. Both images show clearly the presence of a nanowire base, the $\text{In}_x\text{Ga}_{1-x}\text{N}$ /GaN MQW active region with four QWs, and a GaN cap. It is immediately apparent, however, that the length of the base as well as the spacing between the QWs varies strongly from NW to NW. As discussed in Sec. 4.1, this is a characteristic of self-induced GaN NWs. For the luminescence behaviour of $\text{In}_x\text{Ga}_{1-x}\text{N}$ QWs, the composition and thickness are essential parameters. To study quantitatively the ensembles of these structures and the devices made from them, the ensemble characterization techniques are essential which were introduced in Ch. 4 and which quantify the variations statistically. Nevertheless, microscope images of individual NWs are required to answer fundamental questions about the exact shape of the $\text{In}_x\text{Ga}_{1-x}\text{N}$ insertions, their polytype, the location of crystal defects and possible deviations from the NW morphology during

photoluminescence experiments. Raman spectroscopy then suggested that light is coupled to the NW through the sidewalls, as was shown in Sec. 4.4.

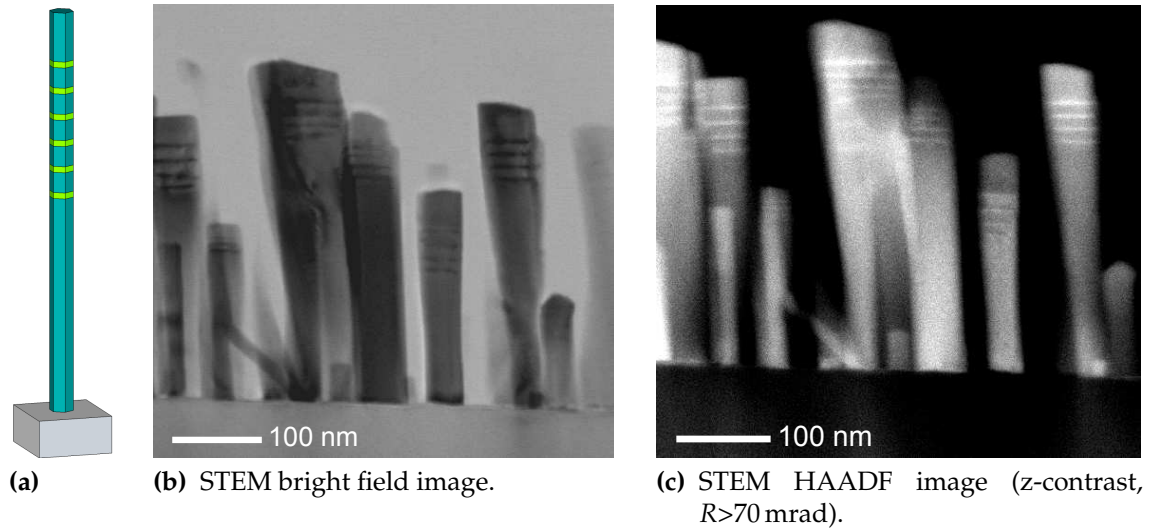


Figure 5.2: Scanning transmission electron microscopy images of a GaN NWs with four axial $\text{In}_x\text{Ga}_{1-x}\text{N}/\text{GaN}$ MQWs, on Si(111). The images were obtained in a JEOL 2100F microscope at 200 kV in a Si(110) zone axis. (a) sketches the intended structure (but with six QWs). The data was acquired by A. Trampert.

growth.

5.3.1 Microstructure of the $\text{In}_x\text{Ga}_{1-x}\text{N}$ insertion

The geometrical shape of the $\text{In}_x\text{Ga}_{1-x}\text{N}$ insertions can be more complex than the simple substitution of GaN NW growth by $\text{In}_x\text{Ga}_{1-x}\text{N}$ NW growth suggests. The difficulty in categorizing this shape becomes evident when recent literature reports are compared: Some reports on axial $\text{In}_x\text{Ga}_{1-x}\text{N}$ quantum wells in GaN nanowires show evidence from TEM that the $\text{In}_x\text{Ga}_{1-x}\text{N}$ insertions are surrounded by a GaN shell,^[170,203,204] while others do not,^[205–207] and some observe both cases as a function of growth condition.^[208,209] Without generalization, a neutral view of the available data and possible interpretations is given here.

TEM images of the active regions of two representative samples of this study were obtained. Figure 5.3(a) shows a sample with 4 QWs, the images were acquired during a brief session at the FEI Titan 80-300 Berlin Holography Special at 300 kV. Below the overview, two individual NWs are shown in high-resolution contrast close to an $\langle 11.0 \rangle$ zone axis. This contrast is not chemically sensitive, and it is difficult to determine the exact location of the QWs. The spacing of the dark stripes in the high-resolution images corresponds roughly to the average $d_{\text{SL}} = 11.5$ nm as determined for this sample from x-ray diffraction (data not shown), and they can therefore be associated with the MQWs, but the exact dimensions are unclear. It looks like a GaN shell is present, and the QWs do not extend to the side facets. In view of the inhomogeneous radial strain distribution, which was discussed in Sec. 4.3.1, and which also contributes to the contrast, the lateral extension of the QWs can not be determined from these high-resolution images. Figure 5.3(b) shows a sample with 6 QWs. The conventional and HRTEM characterization was carried out in a JEOL 3010 LaB6 electron microscope operated at 200 kV. These figures are bright-field images in two beam condition with $\mathbf{g} = 0002$. Those areas which fulfill

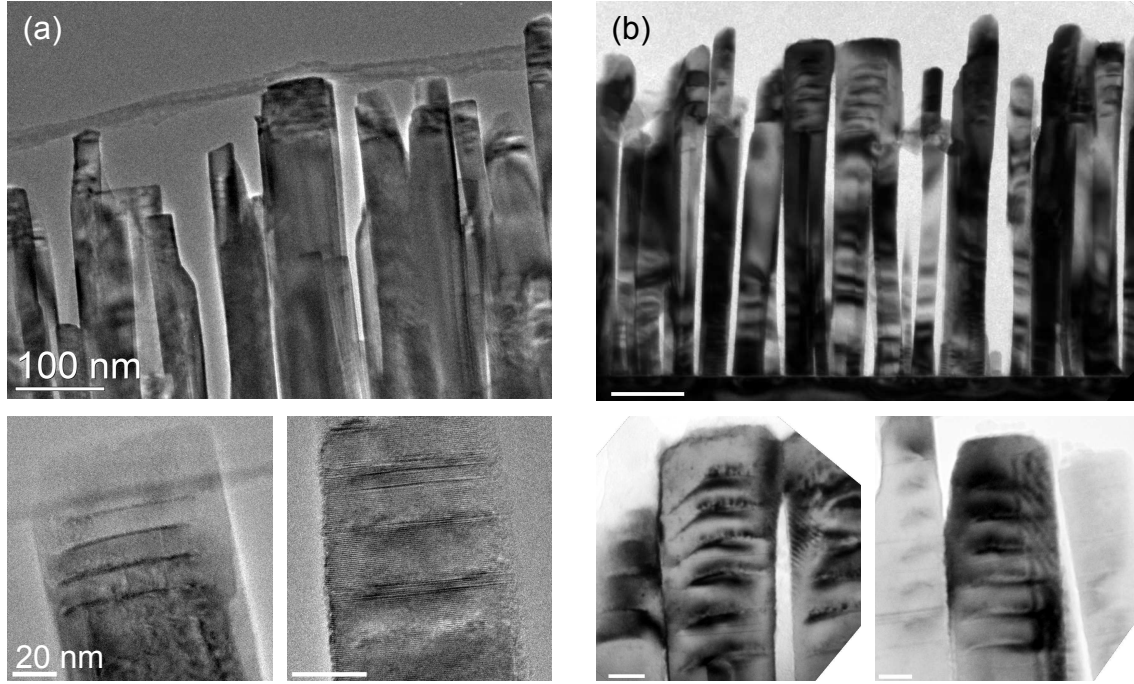


Figure 5.3: TEM images of $\text{In}_x\text{Ga}_{1-x}\text{N}/\text{GaN}$ NW samples. The images in the bottom row are details from the images above. All scale bars in the top row are 100 nm and in the bottom row 20 nm. (a) Active region with 4 QWs, the detail images are HRTEM images. The data was acquired by T. Niermann, TU Berlin. (b) Active region with 4 QWs, the detail images are bright field TEM images. The data was acquired by C. N. Huang.

the diffraction condition contribute preferably to the image. Therefore, a dark contrast can be expected due to inelastic scattering of electrons at atoms of high mass, where In is incorporated, but also at crystal defects where the diffraction condition is not met. A periodic arrangement of dark spots is visible in the detail images, with a spacing matching $d_{\text{SL}} = 19.3 \text{ nm}$ from x-ray diffraction (green curve in Fig. 5.15). Here again, the contrast is not strictly chemically sensitive, and the QW boundaries are obscured. This may have contributed to the divergent interpretations in the literature.

The different shapes of $\text{In}_x\text{Ga}_{1-x}\text{N}$ insertions in GaN NWs which were reported in the literature can be grouped into categories. Figure 5.4(a) symbolizes the cross section of an ideal axial heterostructure. This NW structure can be grown bottom-up^[11,205] or etched from a planar heterostructure,^[44,210,211] and an analytical strain analysis is possible and allows straightforward x-ray and Raman analysis as demonstrated in Ch. 4. The $\text{In}_x\text{Ga}_{1-x}\text{N}$ quantum disc embedded in a GaN shell, which is shown in Fig. 5.4(b) can occur in bottom-up growth if In is preferably incorporated in the center of the NW. This has been considered recently by Frank Glas by comparing the sum of the elastic energies and surface energies for the case of $\text{In}_x\text{Ga}_{1-x}\text{N}$ island growth to the case of $\text{In}_x\text{Ga}_{1-x}\text{N}$ covering the NW top facet.^[204,212] From this point of view, the formation of an $\text{In}_x\text{Ga}_{1-x}\text{N}$ cylinder in the center of the top facet is favorable. This structure has been claimed experimentally for bottom-up grown nanowire heterostructures based on a GPA analysis of HRTEM images.^[170,208] Another way to obtain the structure in Fig. 5.4(b) is to over-

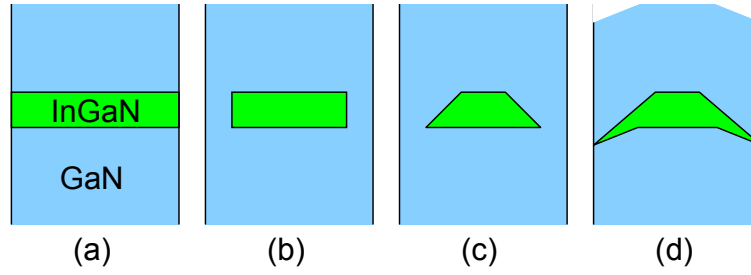


Figure 5.4: Shapes of $\text{In}_x\text{Ga}_{1-x}\text{N}$ insertions in GaN NWs. (a) Ideal axial heterostructure. (b) Cylindrical insertion surrounded by a shell. (c) Insertion in the shape of a truncated cone. (d) GaN nanowire grown with bevelled tip, with the InGa insertion assuming a lenticular shape.

grow a structure of the type in Fig. 5.4(a) radially with GaN.^e Several reports indicate the formation of $\text{In}_x\text{Ga}_{1-x}\text{N}$ insertions in the shape of a truncated cone, as shown in Fig. 5.4(c). Experimentally, this was claimed on the basis of HRTEM images.^[203,204] Interestingly, this shape was theoretically motivated by Niu, Stringfellow *et al.* on the basis of atomistic-strain-model Monte Carlo simulations, which also predict a non-uniform distribution of In within the insertion.^[215] Finally, it has been observed experimentally that the tip of MBE-grown GaN NWs can be composed of a C-plane top facet and bevelled edges, as sketched in Fig. 5.4(d). This bevelling is pronounced in Ga-polar GaN NWs obtained homoepitaxially on MOVPE-grown GaN templates.^[117,118] If $\text{In}_x\text{Ga}_{1-x}\text{N}$ grows on the NW tip, the insertion assumes a lenticular shape. As introduced in Sec. 3.3, GaN NWs grow N-polar on silicon or silicon nitride, and the top facet on such NWs is typically flat. The bright-field TEM images in Fig. 5.3(b), and also experimental data from other work,^[206,209] however, do resemble closely Fig. 5.4(d). Note that in these cases, the tip of the GaN NW cap is also clearly bevelled. The equilibrium shape of a crystal always shows microscopic facets as a function of strain and surface energies, and to which extent vicinal surfaces are observed in GaN NWs depends on the growth conditions.^[118]

Even after 20 years of extensive research on the $\text{In}_x\text{Ga}_{1-x}\text{N}$ alloy,^[3] the microstructure and particularly the local In content are a matter of debate, with the consensus that the material is highly disordered and In concentration variations on a nm-scale are typical.^[13,39,89] MBE growth under far-from-equilibrium conditions and the non-uniform strain in NW heterostructures render the modelling of the In distribution difficult.^[216] To investigate the local In content in the periphery of the quantum disc in experimental NW heterostructures, and thus decide which of the descriptions in Fig. 5.4 best represents the real structure, requires detailed microscopic analysis on series of samples covering a range of growth conditions. Such an analysis is not a part of this study.

The discussion of x-ray diffraction profiles and Raman spectroscopy in Ch. 4 has shown that despite the morphological fluctuations and the radially inhomogeneous strain in self-induced $\text{In}_x\text{Ga}_{1-x}\text{N}/\text{GaN}$ NWs, it is possible to obtain statistically relevant structural information. The approximation of lateral relaxation, which was introduced in Sec. 4.3.2, can be used for x-ray and Raman data. It was shown numerically that the deviations in the periphery of the quantum discs are negligible. On the same grounds it can be argued that the exact shape of the periphery and the classification according

^eShell growth around III-N nanowires can be obtained, for example, in MBE under metal-rich conditions^[213] or in MOVPE.^[214]

to Fig. 5.4 plays a minor role for those properties of NW heterostructures that are determined by their average strain state. The electronic properties of the quantum disc, however, which may depend on Fermi level pinning at the sidewall^[217,218] and on the local strain state, may well depend on the exact quantum disc shape and require a microscopic analysis. This topic will be addressed again in the discussion of the optical properties of the heterostructure in Sec. 6.3.4.

5.3.2 Polytype of the $\text{In}_x\text{Ga}_{1-x}\text{N}$ insertion

GaN NWs grow by MBE at high temperatures (around 780 °C) in the hexagonal wurtzite phase (h-GaN). When grown at low temperatures (around 600 °C), the GaN NWs exhibit stacking faults and layers of cubic GaN (c-GaN).^[81,219] Such low temperatures are used for the growth of $\text{In}_x\text{Ga}_{1-x}\text{N}$ segments, and formation of the cubic polytype has been found to coincide with In supply.^[196] It is, however, unknown so far how In supply affects c-GaN formation and if cubic $\text{In}_x\text{Ga}_{1-x}\text{N}$ is formed at all in the NWs.

The formation of cubic GaN can be detected *in situ* during NW growth by reflection high-energy electron diffraction (RHEED). Figure 5.5(a) shows the RHEED pattern during the growth of the GaN NW base, when only the reflections of hexagonal GaN were observed. In this experiment, the first layer of the active region was a GaN barrier grown at 585 °C. The appearance of additional reflections after lowering the growth temperature, as seen in Fig. 5.5(b), indicates the presence of cubic GaN before the In shutter is opened.

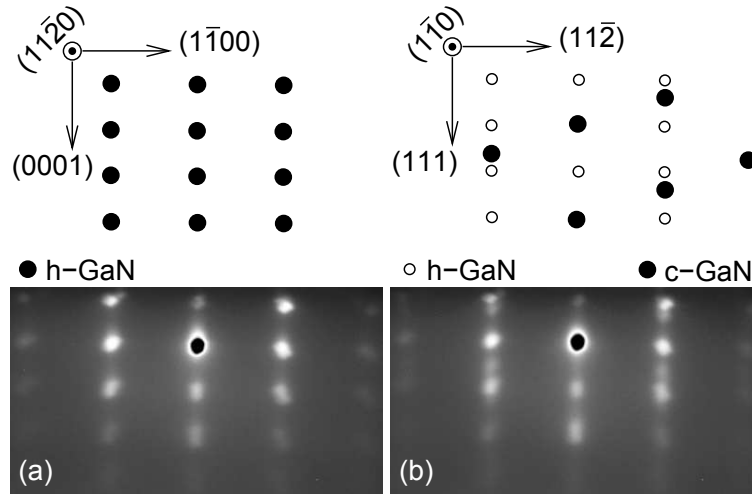
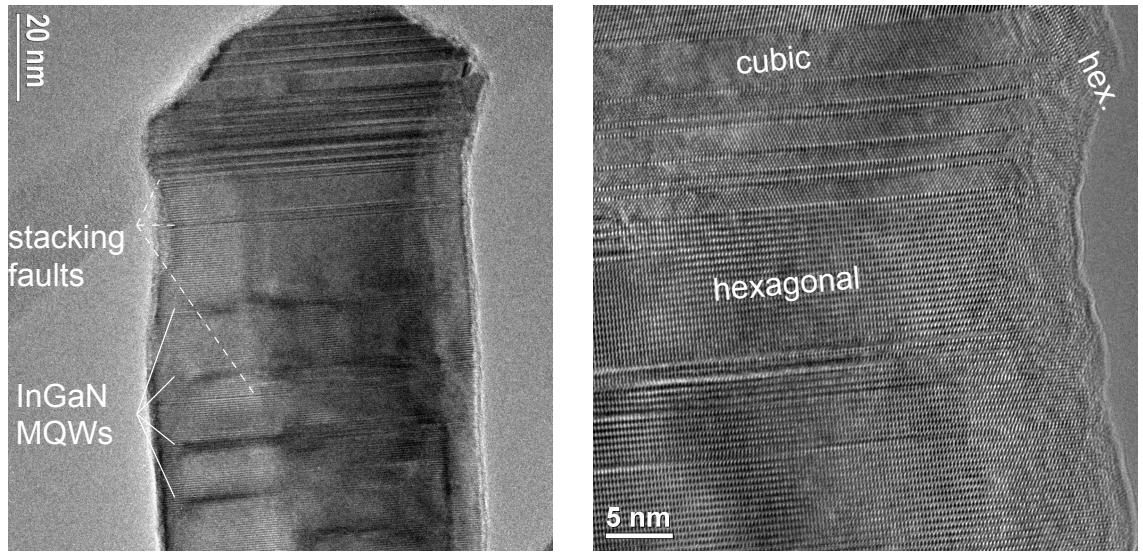


Figure 5.5: Evolution of the RHEED pattern during growth of (a) GaN NW base and (b) the active region, before opening the In shutter. The appearance of the cubic GaN diffraction pattern is depicted above for clarity (one of the twin patterns drawn).^[220]

The extent and the positioning of c-GaN in individual NWs is seen in HRTEM images. Figure 5.6(a) shows the active region of an $\text{In}_x\text{Ga}_{1-x}\text{N}/\text{GaN}$ NW and the GaN cap. The thin straight contours along the NW diameter are stacking faults. Their appearance is not correlated with the insertion of $\text{In}_x\text{Ga}_{1-x}\text{N}$ QWs. In the greater magnification in Fig. 5.6(b), cubic segments of different thickness can be identified. This image also reveals h-GaN growing on a c-GaN{111} side facet, thus introducing a change of crystal orientation with respect to the base NW. A trace of c-GaN growth on oblique {111} facets was



(a) Overview of the four axial $\text{In}_x\text{Ga}_{1-x}\text{N}/\text{GaN}$ MQWs in the active region and the GaN cap of a NW. Stacking faults in this individual NWs are mostly in the GaN cap. (b) HRTEM image showing hexagonal and cubic segments of varying thickness in an $\text{In}_x\text{Ga}_{1-x}\text{N}/\text{GaN}$ NW. Note the hexagonal segment growing on a cubic {111} side facet in the top right.

Figure 5.6: HRTEM images of two NWs, showing the location of stacking faults and cubic GaN segments in the active MQW region and the tip of the NW. The appearance of stacking faults is not correlated with the $\text{In}_x\text{Ga}_{1-x}\text{N}$ insertion. [The overview image is found in Fig. 5.3(a).] The data was acquired by T. Niermann, TU Berlin.

observed by RHEED in one extreme case, where the entire active region growth was substituted by a GaN segment grown at 585 °C. The RHEED pattern was shown in Fig. 3.4(c), p. 23 (the reflections corresponding to oblique growth are indicated by the green vectors).

Polytypism is a common phenomenon in catalyst-induced III-V nanowires, and is observed in GaN,^[59] GaAs, GaP^[221] and InSb.^[222] Explanations for polytypism in these cases involve, among others, the growth temperature and the composition of the catalyst droplet or the self-seeded particle. Apart from the influence of the growth temperature that was shown by Fig. 5.5, it is unknown how a polytype selection can be achieved in the self-induced $\text{In}_x\text{Ga}_{1-x}\text{N}/\text{GaN}$ NW heterostructures studied here. The formation of cubic GaN is clearly not induced by In incorporation. If, on the other hand, $\text{In}_x\text{Ga}_{1-x}\text{N}$ segments are always free of cubic segments, is unknown. HRTEM images such as Fig. 5.6(a) indicate that $\text{In}_x\text{Ga}_{1-x}\text{N}$ segments are mostly free from cubic inclusions. Another indication is that the quantum-confined stark effect (QCSE) has been observed in $\text{In}_x\text{Ga}_{1-x}\text{N}/\text{GaN}$ nanowires, indicating emission from a wurtzite crystal.^[223,224] Note that the latter point is controversial, as some authors have claimed the absence of the QCSE in such NW heterostructures.^[160,225,226] In sum, the indications of polytypism in the $\text{In}_x\text{Ga}_{1-x}\text{N}$ segments are not conclusive. For the synthesis and operation of GaN nanowire LED devices, cubic segments are not a fundamental obstacle at the current stage of technological development, even though it is conceivable that they could have a minor influence on the emission linewidth and the forward voltage drop. As will be treated in Sec. 6.4, the electroluminescence of nanowire LED demonstrator devices produced within this work showed no traces of optical emission from c-GaN insertions.

5.3.3 $\text{In}_x\text{Ga}_{1-x}\text{N}$ nanowire segment growth direction

For the design of nanowires with axial $\text{In}_x\text{Ga}_{1-x}\text{N}$ segments, the selectivity of the growth in C-direction as opposed to radial growth must be assured. It is known that $\text{In}_x\text{Ga}_{1-x}\text{N}$ heterostructures may deviate from the columnar growth of the GaN nanowire. The growth may proceed laterally and lead to a diameter increase^[8,192,193] or to branching morphology.^[196] Radial GaN and $\text{In}_x\text{Ga}_{1-x}\text{N}$ growth is preferred at higher metal fluxes, or at lower growth temperatures when the fluxes are kept constant.

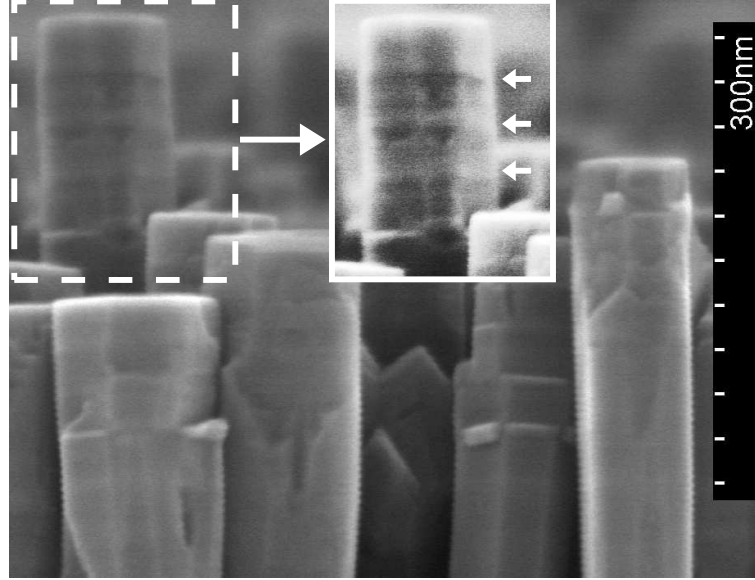


Figure 5.7: Scanning electron micrograph of GaN nanowire tips with an inserted $\text{In}_x\text{Ga}_{1-x}\text{N}/\text{GaN}$ heterostructure with a superlattice period of 33 nm. The inset shows the same NW with enhanced contrast. The data was acquired by A.-K. Bluhm.^[169]

The morphology of experimental $\text{In}_x\text{Ga}_{1-x}\text{N}$ NW structures can be obtained from field-emission scanning electron microscopy (SEM). The image in Fig. 5.7 was obtained with a *Hitachi S-4800*, detecting secondary electrons. The beam conditions were 10 kV, 9400 nA, and a working distance of 5900 μm . The arrows in the contrast-enhanced inset indicate the periodic contrast profile which evidences the axial MQWs. The contrast mechanism is not known. Nevertheless, the MQW region can be identified in this and other SEM images (including Fig. B.1(a), p. 134). The x-ray diffraction profile indicates $d_{\text{SL}} = 33 \text{ nm}$ for this sample. The spacing of the MQW is therefore similar to the marks in the scale bar, which is confirmed by the image.

Small branches originating at the QW position can also be seen in the SEM image in Fig. 5.7. This is an example of the deviation from axial NW growth which is reported for low V/III ratios.^[193] A more drastic occurrence of a local change in the V/III ratio was observed incidentally, when a NW LED sample was contaminated by In droplets during the In desorption test, i. e. after the growth of the NW base. An SEM image of this sample is shown in Fig. 5.8. It can be clearly seen that in the right half of the image, parasitic growth has occurred on the base NW sidewalls. This is likely due to prolonged In evaporation from the liquid In reservoir formed by the droplets. The contaminated areas were circular and had diameters of 40 μm and above (images not shown). The

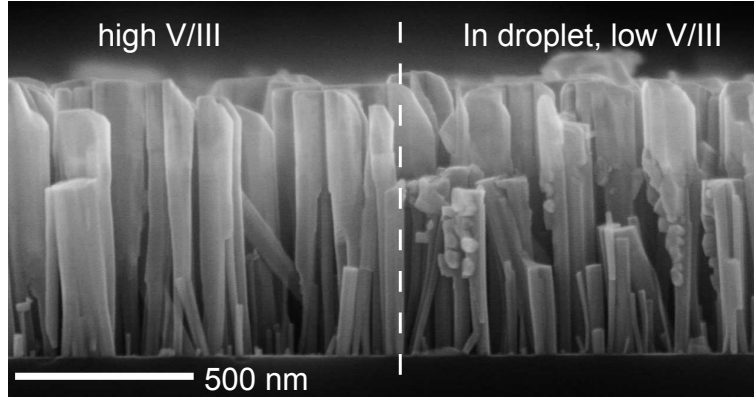


Figure 5.8: SEM cross section of an $\text{In}_x\text{Ga}_{1-x}\text{N}/\text{GaN}$ NW LED sample. This sample was contaminated by In droplets after the growth of the GaN base NWs. In the right half of the image, continuous In evaporation has decreased the V/III ratio and extensive parasitic growth on the base NW sidewalls has occurred. On the left half of the image, outside the In droplet area, no sidewall growth is visible on the base NWs. The data was acquired by A.-K. Bluhm.

image is taken at the boundary of the contamination, and NWs in the left half of the image show no growth on the sidewalls.

Table 5.2: Source fluxes for the growth of $\text{In}_x\text{Ga}_{1-x}\text{N}/\text{GaN}$ NWs with a tapered active region.

step	t (min.)	T (°C)	Φ_{In}	$\Phi_{\text{Ga},1}$	$\Phi_{\text{Ga},2}$	Φ_{N}	V/III	radial growth
GaN base	60	800		5.9		20	3.4	no
quantum well	0.5	598	5.7		3.0	20	2.3	yes
$3 \times \left\{ \begin{array}{l} \text{barrier} \\ \text{quantum well} \end{array} \right.$	3	598			3.0	20	6.7	no
	0.5	598	5.7		3.0	20	2.3	yes
GaN cap	5	598		5.9		20	3.4	no

Another deviation from the NW growth morphology, which is distinct from the formation of branches, is the increase of the NW diameter by radially homogeneous growth on the NW sidewall. This phenomenon has been observed in $\text{In}_x\text{Ga}_{1-x}\text{N}/\text{GaN}$ NW MQW structures which were grown with a low V/III ratio. The observation of $\text{In}_x\text{Ga}_{1-x}\text{N}$ diameter widening is in agreement with recent literature,^[209,227,228] but has not been quantified so far. An example is shown in Fig. 5.9 and will be discussed in some detail. Figure 5.9(a) shows the top portion of the NW ensemble. The diameter has increased during the active region growth and all NWs show a similar inverse tapering there. The reason can be found in the flux ratios, which are summarized in Table 5.2. The base NWs are grown with a V/III ratio of 3.4, leading to diameters of about 40 nm. For this series (series 12), a high In flux was used, with a surplus ratio $\Phi_{\text{In}}/\Phi_{\text{Ga}} \approx 2$. Due to an erroneous source calibration, the V/III ratio was only 2.3 during the growth of the $\text{In}_x\text{Ga}_{1-x}\text{N}$ QWs, and radial growth occurred.

In Fig. 5.9(b), the partial pressure P of ^{115}In detected by the line-of-sight QMS is shown

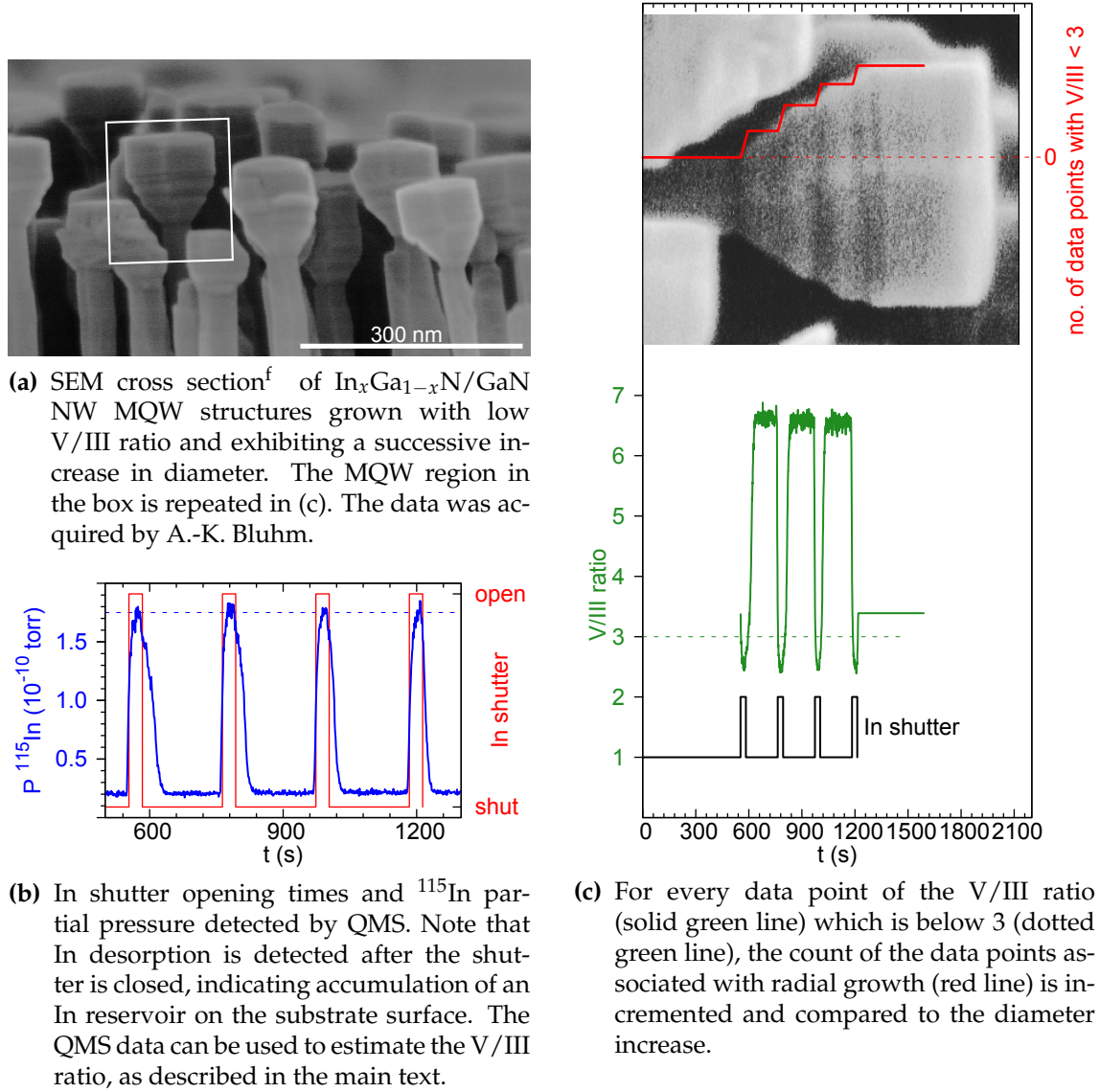


Figure 5.9: Increase of the NW diameter in the active region of a sample grown with low V/III ratio.

during the growth of the active region. When the In shutter is opened, P reaches $P_{\max} = 1.75 \times 10^{-10}$ torr (dashed blue line), indicating significant desorption $\Phi_{\text{In,des}}$. After closing the shutter, In desorption continues at a similar level, indicating that the impinging flux Φ_{In} was higher than the maximum $\Phi_{\text{In,des}}$ which can be desorbed at this temperature,^[229] and In accumulated on the sample surface. The local conditions at the surface became metal-rich, even though the nominal V/III ratio was 2.3. It can reasonably be expected that the V/III ratio remains low, and therefore the condition for radial growth is met, as long as P close to P_{\max} is observed.

The SEM image in Fig. 5.9(a) and particularly the enlarged and contrast-enhanced detail in 5.9(c) show that widening of the diameter is not continuous during the growth. It is easily seen that the side facets during the last GaN growth step are parallel. The plateaus that form during the growth of active region, therefore correspond to the barriers with V/III = 6.7. With the knowledge of the local material supply ratios at the

surface, the evolution of the NW morphology can be modelled. To quantify the local V/III ratio precisely, a calibration of $\Phi_{\text{In,des}}(P)$ or an assessment of x would be required, which are not available for this experiment. Also, assumptions about the diffusion of the atomic species would have to be made. However, a simple model can be based on the data presented so far. Even if $\text{In}_x\text{Ga}_{1-x}\text{N}$ with a significant composition x is formed, because of the large In surplus ratio, most of the impinging In desorbs. To estimate the effective Φ'_{In} from the measured $P^{115}\text{In}$, P_{max} can therefore be associated with the nominal impinging Φ_{In} . (This calibration is very rough, because we know that some of the impinging In accumulates and desorbs later.) For the active region one can then write $V/\text{III} = \Phi_{\text{N}} / (\frac{P}{P_{\text{max}}} \Phi_{\text{In}} + \Phi_{\text{Ga,2}})$. A background of $P_{\text{max}} = 2 \times 10^{-11}$ torr can be subtracted from the data for P . The resulting V/III during the growth of the active region is shown in Fig. 5.9(c) by the green line. For the growth of the GaN cap, V/III is nominally identical to the base NW growth, as listed in Table 5.2.

A stepwise increase in diameter is observed when the V/III ratio is low. In an attempt to correlate the V/III data with this observation, an arbitrary threshold is set at $V/\text{III} = 3$, and the data points are counted which fall below this threshold. Their number is shown by the red line in Fig. 5.9(c). Since the delay time of the In desorption after shutter closure, which was observed in Fig. 5.9(b), decreases from QW to QW, the steps in the red line become smaller. Interestingly, this seems to correspond to the observed stepwise diameter increase, which is also less pronounced in the last QW. Based on this, a simple model can be stated: *Below a V/III threshold value, inverse tapering of NWs occurs at a constant diameter widening rate, together with axial growth. Above the V/III threshold value, only axial growth occurs.* The precise axial growth rate is equally difficult to judge from the SEM image. A valid assumption, consistent with the periodicity proven by x-ray diffraction satellites (data not shown), is that the spacing of the QWs is constant, indicating that the axial growth rate is not limited by the material consumption of the additional radial growth. In view of the qualitative nature of the morphology assessment by SEM on one individual NW, this simple ‘growth model’, which employs a V/III threshold for radial growth, is sufficient to derive design rules. For high Φ_{In} , it is essential to include the information from QMS, because the duration of the radial growth periods exceeds the shutter opening time.

An idea put forth by Sergio Fernández-Garrido is that the local V/III ratio depends on the NW diameter and density as well as the nominal flux.^[230] According to this picture, N-rich growth conditions prevail as long as the metal atoms arriving in the neighborhood of the NW and diffusing to the C-plane top facet are outnumbered by directly impinging N atoms. Under metal-rich conditions, radial growth increases the area of the top facet. This increases the capture of N atoms and reduces the excess of metal atoms. The decreasing In excess according to Fig. 5.9(b) in correlation with the increasing NW diameter in Fig. 5.9(c) confirms this hypothesis experimentally. A consequence is that under such experimental conditions, further radial growth will re-establish N-rich conditions and then cease. The NWs will continue to grow axially, with a fixed diameter which is defined by the nominal V/III ratio and the NW density.

Both deviations from NW morphology with clean M -plane side facets, the formation of branches and inverse tapering, can be observed to occur in NW samples with an active region grown at low temperature and at low V/III ratios. In the design of experi-

^fThe view area of the SEM cross section is horizontally aligned with the Si(111) substrate. The systematic tilt of the NWs to the left (5° on average) is due to a substrate offcut and their epitaxial relation to the Si crystal.

ments for this thesis, branches and tapers were not desired and have not been studied intensely. From a symmetry consideration, however, the main difference seems to be the crystal structure: if M -plane growth of hexagonal $\text{In}_x\text{Ga}_{1-x}\text{N}$ occurs, a radially uniform diameter increase is expected. It can be argued that the exchange of adatoms between side facets is easy, because Ga is known to diffuse easily in the A -direction of the GaN M -plane,^[231] and no preference for a specific direction is expected. Branching, therefore, must be associated with a grain boundary between the branch and the NW. Such a change in crystallographic orientation can occur even in coherent epitaxial growth, by inclusion of a c-GaN segment and subsequent growth of h-GaN on an equivalent c-GaN {111} facet that is not parallel to the original NW growth front. This effect has been observed in an $\text{In}_x\text{Ga}_{1-x}\text{N}/\text{GaN}$ NW in Fig. 5.6(b) and is also known from literature.^[196,232]

5.3.4 Best practice: V/III, In/Ga, axial growth rate

This section has shown that $\text{In}_x\text{Ga}_{1-x}\text{N}/\text{GaN}$ nanowire heterostructures grown by PA-MBE exhibit variable morphology in terms of core-shell formation, polytype formation and disruption of the M -plane side facets by branches or diameter increase. While the growth mechanisms are not known for all of these phenotypes, the findings can be summarized in a small set of rules for the design of experiments targeted at the active region of $\text{In}_x\text{Ga}_{1-x}\text{N}/\text{GaN}$ nanowire LEDs with axial heterostructures.

Morphology The most efficient control of NW morphology is via *ex situ* SEM in plan view and cross section. *In situ*, a clear spotty RHEED image as in Fig. 5.5 is an indication for NWs with low tilt and few defects in the active region. Prolonged detection of In desorption by QMS after the In shutter is closed, as in Fig. 5.9(b), indicates In accumulation on the surface and thus metal-rich conditions which favour lateral growth.

Axial growth rate The growth rate of GaN base NWs can be obtained from SEM images and from the growth time, possibly subtracting the time for NW nucleation.^[99] The growth rate of the active region can be estimated by x-ray diffraction if a superlattice (of four or more) $\text{In}_x\text{Ga}_{1-x}\text{N}$ QWs and GaN barriers is prepared. The QWs, however, typically grow much faster than the barriers, as will be discussed in Sec. 5.4.3.

V/III ratio N-rich growth, i. e. a high V/III ratio, must be conserved to obtain NWs with M -plane side facets. The nominal V/III ratio for the GaN NW base is typically three or above (growth at about 800 °C), with the effective V/III ratio being always higher due to Ga desorption. At the lower growth temperature of the active region, less Ga desorbs, and a higher nominal V/III supply ratio must be used for the active region, typically eight or above (growth at 600 °C). To maximize the axial growth rate, the plasma source is set for maximum Φ_{N} and the metal fluxes are adjusted accordingly.

In/Ga Because of In desorption, the nominal In/Ga ratio should be higher than in the intended crystal composition. Excessive In surplus, however, lowers the V/III ratio. Also, the maximum desorbable amount of In depends on the substrate temperature, and excessive In surplus increases the risk of In surface accumulation and, therefore, metal-rich growth. A typical In/Ga ratio is one.

The experimental work in this thesis focused on the growth of $\text{In}_x\text{Ga}_{1-x}\text{N}$ segments in self-induced GaN NWs with the conservation of the NW geometry, i. e. a constant diameter from the base to the active region. Fluctuations in the length and diameter of self-induced NWs were observed (see Table 4.1). A common approach to avoid these fluctuations is to employ structured substrates for the selective area growth of NWs.^[61,146,147,233,234] However, two recent findings suggest that it may be possible to synthesize self-induced NWs systematically with narrow length and diameter distributions. These ideas are stated here **speculatively**:

Base NW length distribution Sabelfeld *et al.*^[125] recently found that the length distribution of self-induced GaN NWs evens out during the growth,^[235] a longer base NW growth time may thus be beneficial.

NW diameter distribution Sergio Fernández-Garrido has postulated a dependence of the NW diameter on the V/III ratio,^[230] and in Sec. 5.3.3 it was explained that effectively metal-rich growth may increase the NW diameter until the top facet collects enough adatoms to bring the effective V/III ratio up to N-rich NW growth conditions. Therefore, a speculative path to a uniform diameter distribution is a short, slightly metal-rich growth step, which may lead to a widening of the thinner NWs and equalize the diameters.

5.4 Active region growth rate

To tailor the segment length in a NW heterostructure by choosing the growth time, the axial growth rate must be known. For the NW base, on the length scale of hundreds of nm, this is easily obtained from SEM images. The growth conditions for the QWs are different, and their thickness and growth rate cannot be measured in this way. Instead, the method pursued here is to perform x-ray diffraction on superlattices of $\text{In}_x\text{Ga}_{1-x}\text{N}$ QWs and GaN barriers. As discussed in Sec. 4.2, due to the statistic fluctuations in self-induced NWs, the satellites are broad and of low intensity, and resemble the x-ray profile of NWs with separate $\text{In}_x\text{Ga}_{1-x}\text{N}$ insertions of different composition.^[170] Axial superlattices of high-In-content $\text{In}_x\text{Ga}_{1-x}\text{N}/\text{In}_y\text{Ga}_{1-y}\text{N}$ segments were reported by Kouno *et al.* to show x-ray diffraction satellite peaks, and the segment spacing was obtained, but no XRD data was shown.^[236] The purpose of this section is twofold: to establish laboratory x-ray diffraction as an analytical tool for axial NW heterostructures, and to obtain the growth rate of the active region. An unambiguous identification of superlattice satellites is possible by comparing a series of samples with a variation in the QW spacing d_{barrier} . The main results of this section were published in Ref. 169.

Two series of samples with superlattices consisting of six pairs of GaN barriers and $\text{In}_x\text{Ga}_{1-x}\text{N}$ quantum wells were analyzed. The growth parameters are given in Table 5.3. The fluxes of the metal effusion cells were calibrated by growing planar layers and measuring their thickness by SEM, as described in detail in App. C. It must be noted here only that $\Phi_{\text{Ga},2}$, in particular, is non-uniform across the substrate and therefore inaccurate. In series 18, separate Ga sources were used for the growth of the $\text{In}_x\text{Ga}_{1-x}\text{N}$ and GaN segments, with the benefit of keeping a constant V/III ratio during the growth of the active region, for an optimum GaN barrier growth rate. Series 27 was grown with only one Ga source being open during the the growth of the active region. The presence of In flux during the QW growth dictates a low Ga supply rate, and therefore a low growth rate of

the active region. In each series, the barrier thickness was varied by changing the barrier growth time from one sample to the next, while keeping all other parameters constant.

Table 5.3: Source fluxes for two series of $\text{In}_x\text{Ga}_{1-x}\text{N}/\text{GaN}$ NWs with a variation in barrier thickness.

series	step	t (min.)	T (°C)	Φ_{In}	$\Phi_{\text{Ga},1}$	$\Phi_{\text{Ga},2}$	Φ_{N}	V/III
18	GaN base	60	770		4.0		20	5
	$\text{In}_x\text{Ga}_{1-x}\text{N}$ QW	0.9	585	1.7		0.8	20	8
	GaN barrier	1.58, 3.36, 6.88	585		3.2	0.8	20	5
	GaN cap	8.0	585		3.2 ^g	0.8	20	5
27	GaN base	90	780		2.6		13	5
	$\text{In}_x\text{Ga}_{1-x}\text{N}$ QW	1.5	605	0.8	0.8		13	8
	GaN barrier	1.0, 2.0, 3.0, 9.5, 12.8, 22.7	605		0.8		13	16
	GaN cap	26	605		0.8		13	16

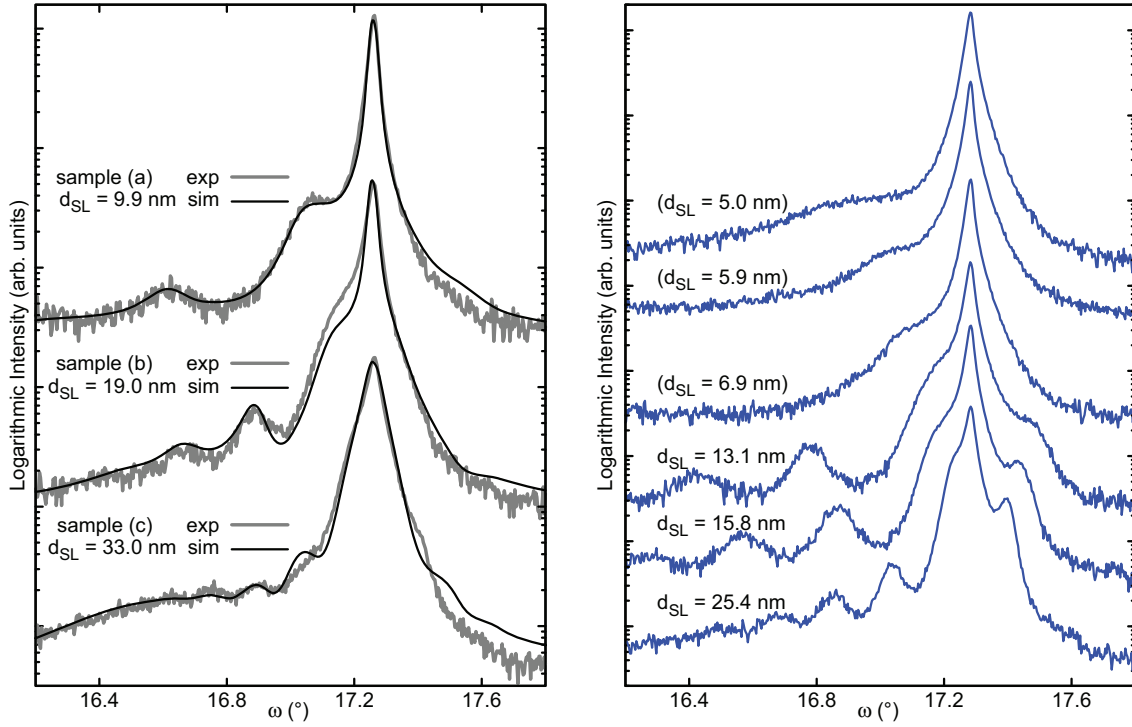
Symmetric Bragg ω - 2θ scans across the GaN(0002) reflection are shown in Fig. 5.10 for both series. Satellite peaks are clearly visible, but their intensity is only slightly higher than the background. In contrast, planar $\text{In}_x\text{Ga}_{1-x}\text{N}/\text{GaN}$ superlattices typically used for LED structures exhibit a signal-to-noise ratio of two orders of magnitude or more (cf. Fig. 4.3). The interpretation of these scans is not as straightforward as for planar layers, because the broad satellite peaks with low intensity could either correspond to thickness fringes from the $\text{In}_x\text{Ga}_{1-x}\text{N}/\text{GaN}$ superlattice or to individual $\text{In}_x\text{Ga}_{1-x}\text{N}$ layers with varying composition. However, the consideration of the entire series of samples shows that longer barrier growth time leads to more closely spaced peaks. The samples were designed such that the quantum wells can be assumed to be identical for all the samples. Therefore, the broad peaks are diffraction satellites due to the periodic superlattice. Only with these first experiments shown in Fig. 5.10(a) could laboratory XRD be established as an analytical tool for NW MQWs.

5.4.1 Graphical estimation of quantum well thickness and composition

Structural information can be extracted graphically from the XRD peak positions and Bragg's law (Sec. 4.2). The resulting values for d_{SL} are given in Table 5.4. d_{SL} is the sum of the barrier and quantum well thicknesses d_{barrier} and d_{well} . Whereas these cannot be directly inferred from the Bragg interpretation, information can be extracted by comparing the three samples under investigation. They were grown in the same way, and the only difference is the growth time for the GaN barriers between the wells. Assuming an abrupt change between well and barrier growth, the superlattice period as a function of barrier growth time t_{barrier} is

$$d_{\text{SL}} = d_{\text{barrier}} + d_{\text{well}} = R_{\text{barrier}}t_{\text{barrier}} + d_{\text{well}}, \quad (5.1)$$

^gIn the first sample of series 18 the GaN cap was grown without $\Phi_{\text{Ga},1}$.



(a) Samples from series 18. The simulations (black lines) take into account the superlattice peak broadening due to fluctuations of the layer thicknesses. The simulated superlattice period d_{SL} is given in the graphs.^[169]

(b) All samples from series 27. d_{SL} is derived from peak positions for the three samples with the longest t_{barrier} (bottom). For the three samples with short t_{barrier} , $d_{\text{SL}} = R_{\text{barrier}}t_{\text{barrier}} + d_{\text{well}}$ is given in parentheses (top).

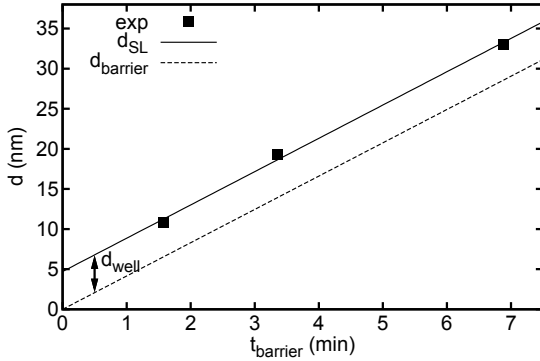
Figure 5.10: XRD ω - 2θ scans across the GaN(0002) reflection of $\text{In}_x\text{Ga}_{1-x}\text{N}/\text{GaN}$ NW superlattices.

where R_{barrier} is the GaN NW barrier growth rate. In Fig. 5.11(a), the superlattice periods obtained from the x-ray data from series 18 are plotted as a function of t_{barrier} . The linear relationship of Eq. (5.1) is confirmed and the barrier growth rate is determined to be $R_{\text{barrier}} = 4.1 \pm 0.2$ nm/min. The GaN NW growth rate in the active region is therefore comparable to the calibrated Ga flux $\Phi_{\text{Ga,barrier}} = 4.0$ nm/min for the growth of the samples in series 18. For series 27, the same analysis can be done for the three samples with the longest t_{barrier} , which exhibit distinct x-ray satellite peaks. The corresponding graph is shown in Fig. 5.11(b). Note the changed timescale due to the slow barrier growth with only one Ga source. Again, a barrier growth rate comparable to the calibrated flux is found: $R_{\text{barrier}} = 0.93 \pm 0.03$ nm/min and $\Phi_{\text{Ga,barrier}} = 0.8$ nm/min. The growth rate of self-induced GaN NWs has exceeded the calibrated planar growth rate more significantly in other studies.^[101] Caroline Chèze *et al.*^[237] and Sergio Fernández-Garrido (Ref. 71, Table 7.2) reported a factor of around two. In those studies, however, the growth temperature was higher (730 °C and 790 °C, respectively) than in the growth of the active region discussed here, and it can be assumed that the Ga diffusion length on the sidewalls was higher.

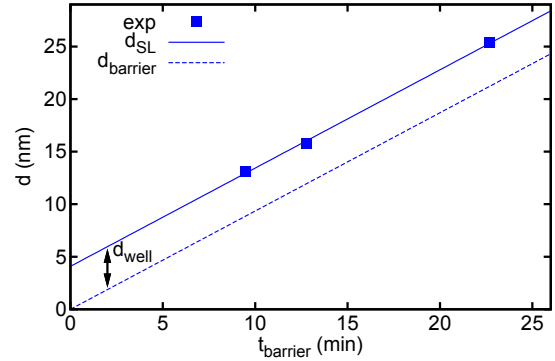
A plot of the type in Fig. 5.11 contains even more information. By extrapolating the straight line through the data points to $t_{\text{barrier}} = 0$, the contribution of the barrier is

Table 5.4: GaN NW samples with superlattices containing six $\text{In}_x\text{Ga}_{1-x}\text{N}$ QWs, grown with a variation in GaN barrier growth times, with all other parameters constant in each series. Based on $d_{\text{well}} = 4.7 \text{ nm}$ for series 18, and $d_{\text{well}} = 4.1 \text{ nm}$ for series 27 (derived in the main text), dependent values are included for x_{well} after Eq. (5.2), and for $d_{\text{barrier}}/d_{\text{SL}}$. For series 27, the italicized values for samples (a) to (c) are extrapolated from the results of samples (d) to (f).

		parameters from x-ray diffraction profiles									
		peak positions					simulations				
series, sample		t_{barrier} (min)	d_{SL} (nm)	x_{avg} (%)	x_{well} (%)	$\frac{d_{\text{barrier}}}{d_{\text{SL}}}$	d_{SL} (nm)	x_{avg} (%)	d_{well} (nm)	x_{well} (%)	σ_d (nm)
18	(a)	1.58	10.8	12.3	28.3	0.57	9.9	10.4	2.7	38	1.6
	(b)	3.36	19.3	7.3	30.0	0.76	19.0	6.1	3.8	30	2.4
	(c)	6.88	33.0	4.4	31.2	0.86	33.0	3.4	3.2	35	3.4
27	(a)	1.0	5.0	21.2	26.1	0.19					
	(b)	2.0	5.9	17.8	26.1	0.31					
	(c)	3.0	6.9	15.4	26.1	0.41					
	(d)	9.5	13.1	8.5	27.3	0.69					
	(e)	12.8	15.8	7.1	27.5	0.74					
	(f)	22.7	25.4	3.8	23.4	0.84					



(a) Samples from series 18. Growth of the GaN barrier with two Ga sources.^[169]



(b) Samples from series 27. Note the longer growth time with respect to (a), because only one Ga source was used. Only the three samples of the series with the longest t_{barrier} can be used for the analysis.

Figure 5.11: Superlattice periods d_{SL} experimentally obtained from the distances between XRD satellite peaks in two series of experiments. d_{SL} is the sum of the barrier and well thicknesses d_{barrier} and d_{well} and depends linearly on the barrier growth time t_{barrier} .

subtracted from d_{SL} and the absolute quantum well thickness is obtained from the axis intercept: $d_{\text{well}} = 4.7 \pm 1.0 \text{ nm}$ in Fig. 5.11(a) and $d_{\text{well}} = 4.1 \pm 0.5 \text{ nm}$ in Fig. 5.11(b).

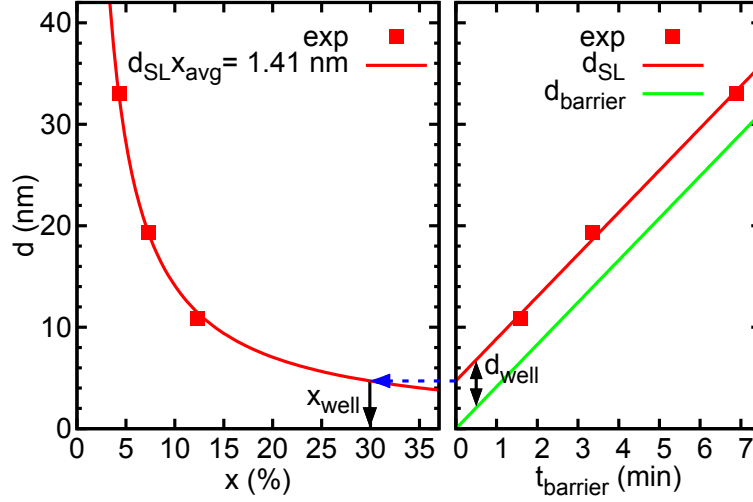


Figure 5.12: Graphical determination of x_{well} from growth data for t_{barrier} and x-ray data for d_{SL} . The experimental values are from $\text{In}_x\text{Ga}_{1-x}\text{N}/\text{GaN}$ NW superlattice samples in series 18.

This value needs to be taken with some caution, since an abrupt change from $\text{In}_x\text{Ga}_{1-x}\text{N}$ to GaN growth is presumed when the In shutter is closed. The activation energy for InN dissociation is lower than for In evaporation from droplets,^[229] and In segregation during quantum well growth is known for planar layers.^[197] Without taking other data into account, the same might be the case for NWs, and d_{well} from Eq. (5.1) can therefore be considered as a lower boundary for the well thickness.

The superlattice composition can be obtained via Bragg's law as was introduced in Sections 4.2 and 4.3.3. Assuming that the $\text{In}_x\text{Ga}_{1-x}\text{N}$ lattice parameter in C-direction follows Vegard's law and is increased due to elastic strain, the average composition is given by Eq. (4.12). The values of x_{avg} are given in Table 5.4.

To obtain the quantum well composition x_{well} , one can consider the product $d_{\text{SL}}x_{\text{avg}}$ which is the total amount of In incorporated into each superlattice period. This must be conserved regardless of the achieved quantum well thickness, and therefore

$$d_{\text{well}}x_{\text{well}} = d_{\text{SL}}x_{\text{avg}}. \quad (5.2)$$

Taking the data for series 18 from Table 5.4, the average over all samples is 1.41 ± 0.07 nm of equivalent InN layer thickness. The small standard deviation indicates that the quantum wells in the three samples are indeed very similar. The reproducibility of $d_{\text{SL}}x_{\text{avg}}$ in series 27 is also as good, with 1.06 ± 0.09 nm. Figure 5.12 illustrates, with the data of series 18, how x_{well} is derived. On the right, the extrapolation of d_{SL} to $t_{\text{barrier}} = 0$ is shown, yielding d_{well} . On the left, the constant product $d_{\text{SL}}x_{\text{avg}}$ is indicated by the hyperbola. Its value is averaged over the three samples. The actual d_{well} is projected onto this line by the dashed blue arrow and marks the average x_{well} of the three samples. Alternatively, the hyperbola could be drawn through an individual data point, giving the exact values of Table 5.4. The fact, that the data points $d_{\text{SL}}x_{\text{avg}}$ in Fig. 5.12 are all close to the curve, is due to their small standard deviation.

To summarize, the x-ray diffraction peaks could be traced to axial NW superlattices by the comparison of samples with a variation only in the barrier growth time. A graphical interpretation of the peak positions is possible. d_{SL} and x_{avg} follow immediately from

Bragg's law, and if the thickness of the QWs is identical within a series, then also d_{well} and x_{well} can be obtained.

5.4.2 Structural parameters from x-ray diffraction profile simulation

The x-ray profiles obtained from the NW heterostructures can be simulated when the statistic structural fluctuations are taken into account. The calculation, which was provided by Vladimir M. Kaganer, has been outlined in Sec. 4.2. The simulated curves in Fig. 5.10(a) were obtained with the parameters given in Table 5.4. The figure and the simulation parameters for the layer thicknesses and strain are reproduced here from our article, Ref. 169, even though two new findings suggest that the simulations could be improved. First, the lateral strain relaxation according to Eq. (4.14) requires a correction of x , as we clarified in Ref. 176. The values for x_{well} in Table 5.4 have been corrected. Second, it is known now that x fluctuates significantly within one sample, as will be shown in Sec. 5.5.3. An XRD profile simulation taking the fluctuation in x into account is not available so far.

The published simulation of the diffraction profiles yields the well thickness d_{well} and the In content x_{well} for each sample separately. Averaging over all samples, d_{well} is approximately 3.2 nm and the In content in the well is about 34 %. Fluctuations of the thicknesses of the individual layers are found to be rather large, $\sigma_d \approx 2.5$ nm. This is the most important result of the simulations, which remains valid regardless of the correction in the lateral strain relaxation. The value σ_d will be used for further discussions in this work. The average well thickness obtained from the simulation of the diffraction peaks is somewhat smaller than the one obtained from the axis intercept in Fig. 5.11(a), but agrees with it within the experimental error. Since the peak positions are well-defined, the smaller values for d_{well} from the simulation entail larger values for x_{well} .

The results in this section show that the structural parameters of NW superlattices can be determined from XRD data in two independent ways. The agreement between the two methods also strongly suggests an abrupt change from $\text{In}_x\text{Ga}_{1-x}\text{N}$ to GaN growth. As discussed above, d_{well} as obtained graphically in Fig. 5.11 is a lower boundary, because In segregation might prolong the QW growth. The simulation parameters however, are an estimate of the true d_{well} , and their agreement with the graphically obtained lower boundary makes In incorporation after closing the In shutter improbable.

5.4.3 Surface diffusion during quantum well growth

Now the structural information which was extracted from the XRD data can shed light on growth mechanisms. First, the data for series 18 is discussed. The axial growth rate of the $\text{In}_x\text{Ga}_{1-x}\text{N}$ QW, $R_{\text{well}} = d_{\text{well}}/t_{\text{well}}$ was determined from the analysis of the Bragg peak positions independently of the simulation. For series 18, $t_{\text{well}} = 0.9$ min and $R_{\text{well}} = 5.2 \pm 1.1$ nm/min, with the uncertainty accounting for the error in d_{well} . This value is compared now with the quantum well growth rate that follows from the fluxes calibrated for the growth of planar layers. This latter quantity is a product of the calibrated Ga flux $\Phi_{\text{Ga,well}} = 0.8$ nm/min and the additional contribution from the In source, which gives a factor $(1 + x_{\text{well}})$. Hence, the quantum well growth rate expected from the calibrated Ga flux can be estimated as $\Phi_{\text{Ga,2}} (1 + x_{\text{well}}) = 1.1$ nm/min. Obviously, the actual $\text{In}_x\text{Ga}_{1-x}\text{N}$ NW quantum well growth rate is much higher than the amount of supplied material implies. This counterintuitive finding hinges on the precision with which both sides of

the inequality are determined:

$$R_{\text{well}} = d_{\text{well}}/t_{\text{well}} > \Phi_{\text{Ga},2}(1 + x_{\text{well}}) \quad (5.3)$$

As mentioned above, $\Phi_{\text{Ga},2}$ is subject to a calibration error due to a non-uniform impingement on the sample surface. If however, the same Ga flux is supplied during the growth of the barrier and the quantum well, this source of error is eliminated. The GaN barrier grows at the rate of R_{barrier} , known from the XRD peak positions, and the $\text{In}_x\text{Ga}_{1-x}\text{N}$ QW, under the same Ga flux, could be expected to grow at the rate $R_{\text{well}} = R_{\text{barrier}}(1 + x_{\text{well}})$. The inequality (5.3) then becomes

$$R_{\text{well}} = d_{\text{well}}/t_{\text{well}} > R_{\text{barrier}}(1 + x_{\text{well}}). \quad (5.4)$$

The second set of samples with variation in barrier thickness, series 27, was grown with only one Ga source. $R_{\text{well}} = 2.7 \pm 0.34 \text{ nm/min}$ and $R_{\text{barrier}}(1 + x_{\text{well}}) = 1.2 \text{ nm/min}$. The error in x_{well} is small compared to $1 + x_{\text{well}}$ and can be neglected. This clearly confirms the finding that the axial growth rate of $\text{In}_x\text{Ga}_{1-x}\text{N}$ in NWs is significantly enhanced, by a factor of two, with respect to GaN.

In order to resolve this discrepancy one must take into account that the growth of self-induced GaN NWs is fed both from the impinging fluxes and the diffusion of Ga along the NW sidewalls to the tip.^[96,98,237] Hence, the increase in NW growth rate for the quantum wells necessitates higher diffusion flux of Ga in the presence of In. In other words, when the pure GaN barriers grow, not all of the impinging Ga reaches the NW. The reduced Ga diffusion must be due to the lower growth temperature of the active region compared to the NW base. This finding also explains why the barrier growth rate is only in the order of the calibrated growth rate, as stated above in Sec. 5.4.1, and not higher by a factor of about two, as reported in literature for GaN NW growth. It is already known that during NW nucleation In enhances the diffusivity of Ga atoms on the substrate, leading to the suppression of rough 2D layer growth.^[238] In the experiments presented here, In was supplied only after at least 400 nm long GaN NWs were grown (series 18), and thus the substrate surface was shadowed to a high degree. The conclusion can be drawn that In is an effective surfactant which enhances the diffusion of Ga atoms along the *M*-plane sidewalls of the NWs.

During the growth of the GaN barriers, when In is absent, the lower diffusion length prevents some of the impinging Ga adatoms from reaching the top facet. If they are instead incorporated on the sidewalls, prolonged growth of the active region should lead to an increase in NW diameter. To verify this, Fig. 5.13 compares SEM plan view images from the samples (a), (b), and (c) of series 18, with the effective growth times of the active region amounting to 16 min, 34 min, and 55 min, respectively.^h It can be seen that the NWs grow indeed progressively thick. This has consequences for the strain relaxation in the QWs, as was introduced in Sec. 4.3.2. The observation of increasing diameter within the samples of series 18 will be helpful for the interpretation of the Raman spectra in Sec. 6.5.2.

As discussed in Sec. 5.3.3, lateral growth of the NWs is expected for a low effective V/III ratio. [The lateral growth in the form of branches in sample (c) of series 18 was shown in Fig. 5.7.] The second series with a variation in barrier thickness, series 27,

^hIn series 18, the growth time of the active region is $6(t_{\text{barrier}} + t_{\text{well}}) + t_{\text{cap}}$. The effective growth duration of the GaN cap was 8 min for samples (b) and (c), but only 1.6 min for sample (a) due to an incidentally reduced Ga flux in the last growth step.

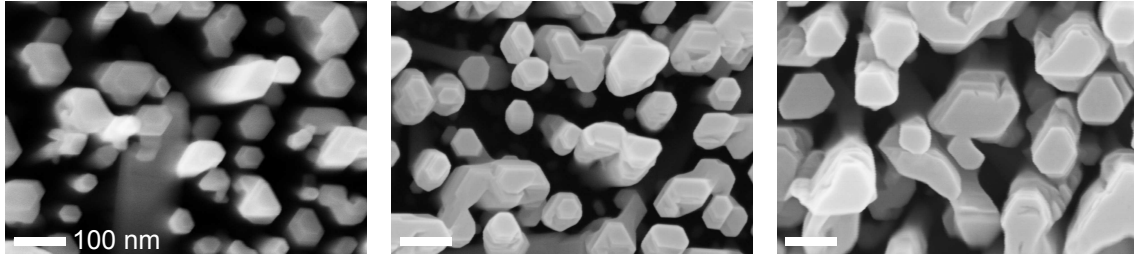


Figure 5.13: SEM plan view images of $\text{In}_x\text{Ga}_{1-x}\text{N}/\text{GaN}$ NW samples (a), (b), and (c) (left to right) from series 18. Growth times of the active region: 16 min, 34 min, and 55 min. The scale is identical in the three images. The data were acquired by A.-K. Bluhm.

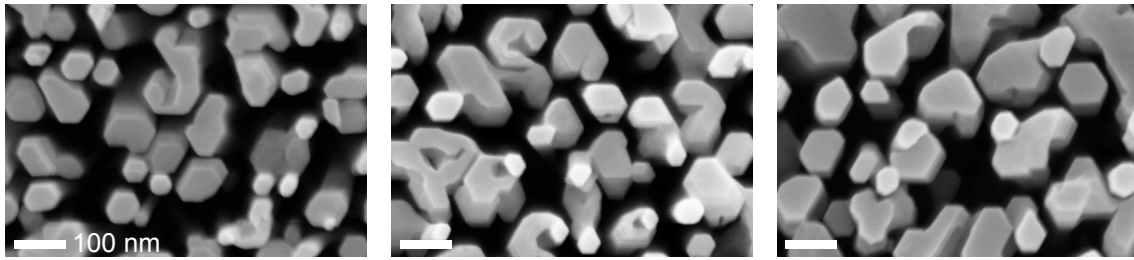


Figure 5.14: SEM plan view images of $\text{In}_x\text{Ga}_{1-x}\text{N}/\text{GaN}$ NW samples (c), (e), and (f) (left to right) from series 27. Growth times of the active region: 40 min, 99 min, and 149 min. The scale is identical in the three images. The data were acquired by A.-K. Bluhm.

was designed to minimize this effect. Table 5.3 summarized the growth parameters: for the second series, the V/III ratio during barrier growth was increased from 5 to 16, and the active region growth temperature was increased from 585 °C to 605 °C. [The lateral growth of branches is reduced, as seen in sample (e) of series 27 in Fig. B.1(a).] Since the maximum N supply is given by the plasma source, the Ga flux had to be reduced, and the axial growth rate in series 27 is only $R_{\text{barrier}} = 0.93 \text{ nm/min}$ compared to $R_{\text{barrier}} = 4.1 \text{ nm/min}$ in series 18, as stated above. For comparison the samples (c), (e), and (f) of the second series are chosen, whose active region growth times are 40 min, 99 min, and 149 min, and thus three times as long as in the previous series.ⁱ Plan view SEM images of the second series are shown in Fig. 5.14. The effect of increasing diameter with increasing growth time of the active region persists. In agreement with the conclusion from XRD data, Ga diffusion on the sidewalls is reduced during the growth of the GaN barriers.

The difference in the axial growth rate of the QWs by a factor as large as two compared to the barriers has two important consequences for the controlled growth of $\text{In}_x\text{Ga}_{1-x}\text{N}/\text{GaN}$ NW heterostructures. First, the increased Ga incorporation during $\text{In}_x\text{Ga}_{1-x}\text{N}$ growth at the tip of the NWs has to be taken into account for the QW thickness. This result is of vital importance for the rational growth of GaN nano LEDs and the development of a comprehensive growth model for $\text{In}_x\text{Ga}_{1-x}\text{N}$ quantum wells in self-induced NWs. Second, Ga diffusion is inhibited during the growth of the GaN barriers in the active region, leading to radial growth of the NWs. It was shown to be a surfactant, increasing Ga diffusion on the sidewalls. In future work, it may thus be possible to reduce lateral growth

ⁱIn series 27, the growth time of the active region is $5t_{\text{barrier}} + 6t_{\text{well}} + t_{\text{cap}}$, with $t_{\text{cap}} = 26 \text{ min}$.

of the GaN barriers by supplying a flux of In, small enough to preserve the effect of the potential barrier in the device, but large enough to enhance Ga diffusion.

5.5 Quantum well composition analysis

The composition analysis is perhaps the most challenging aspect of $\text{In}_x\text{Ga}_{1-x}\text{N}$ characterization in general, and more so in short NW segments. Prior to the work on this thesis, no convincing data had been published. Also in recent reports, $\text{In}_x\text{Ga}_{1-x}\text{N}$ composition values obtained from nominal beam composition, XRD, microscopy or luminescence are very rarely compared critically. In the previous section, the quantum well composition was obtained for series of samples with a variation in barrier thickness. The analysis in these cases was straightforward, but cannot be practically applied to samples of unequal composition. The interest of this section is directed at the analysis of series of samples with a systematic change in composition. A series of GaN NW samples with six $\text{In}_x\text{Ga}_{1-x}\text{N}/\text{GaN}$ MQWs was produced with the growth temperature of the active region, T_a , changed between samples from 583 °C to 637 °C while all fluxes and shutter opening sequences were identical. This series is numbered 19, and all growth parameters are listed in App. A. At these temperatures, the desorption of In cannot be neglected. Therefore, the resulting composition x depends on T_a .^[239] The statistical fluctuations in the NW ensembles require an $\text{In}_x\text{Ga}_{1-x}\text{N}$ composition analysis by volume-probing methods. Therefore, XRD and Raman spectroscopy are the primary tools. The results of this section were published in Ref. 220.

5.5.1 X-ray diffraction and transmission electron microscopy

The In concentration in the NW segments can be derived from laboratory x-ray scans of the GaN(0002) reflection as shown in Fig. 5.15. The zeroth and $\pm 1^{\text{st}}$ order satellite peaks are marked by arrows. Their positions can be used to determine the superlattice period d_{SL} and the average composition c_{avg} of the MQW stack via Bragg's law (see Sec. 4.2). For axial superlattices in NWs, lateral relaxation occurs. If the total height of the superlattice stack is larger than the NW diameter, the whole stack assumes a weighted average in-plane lattice constant. In this case the Poisson effect vanishes for c_{avg} (see Sec. 4.3.3). The average superlattice composition is hence given by Vegard's law: $x_{\text{avg}} = (c_{\text{avg}} - c_{\text{GaN}})/(c_{\text{InN}} - c_{\text{GaN}})$.

In the experiments shown in Fig. 5.15, the contrast of the XRD satellite peaks is not sufficient to determine the QW thickness d_{well} reliably by simulation. The QW growth conditions in this series are similar to the series 18 with barrier thickness variation (see Table A.1), and $d_{\text{well}} = 5 \text{ nm}$ is expected based on the discussion of the axial growth rate in Sec. 5.4.1. To cross-check the structure of the NW samples, TEM was performed on the sample grown at $T_a = 608 \text{ °C}$. Figure 5.16(a) shows a bright-field image of the sample cross section in two-beam condition with $\mathbf{g} = 0002$ at 200 kV. The Si substrate is located at the bottom. Visibly, the NWs fluctuate in diameter, length and tilt. In the center of Fig. 5.16(b) the complete heterostructure of one individual NW is presented. The six-fold periodic structure of the axial $\text{In}_x\text{Ga}_{1-x}\text{N}/\text{GaN}$ MQW is visible. The single period highlighted by the white box is imaged by high-resolution TEM as depicted in Fig. 5.16(c). Geometric phase analysis (GPA) reveals the In-induced strain in the C-direction as shown in Fig. 5.16(d).^[170] The strain $\Delta c/c$ is indicated with respect to the GaN barrier. It can be seen that it is reasonable to assume in the following the nominal value of $d_{\text{well}} = 5 \text{ nm}$.

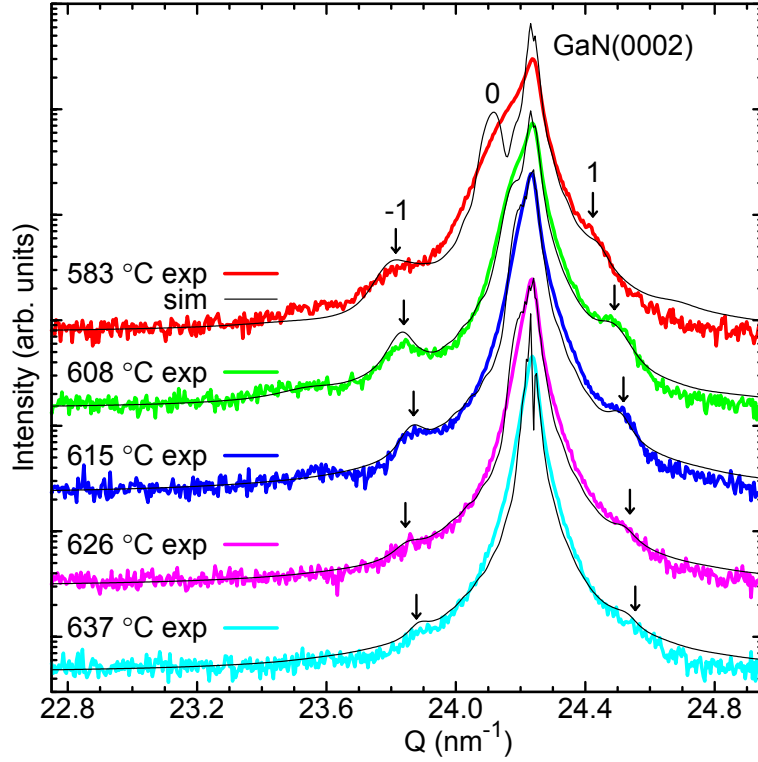


Figure 5.15: Experimental and simulated ω - 2θ scans across the GaN(0002) reflection of $\text{In}_x\text{Ga}_{1-x}\text{N}/\text{GaN}$ NW samples grown at different temperatures T_a (series 19). The periodic $\text{In}_x\text{Ga}_{1-x}\text{N}$ QWs give rise to the first order superlattice peaks as indicated by the arrows.^[220]

A line profile of $\Delta c/c$ along the NW axis was obtained from the area in the GPA map highlighted by the black box, and is given in Fig. 5.16(e). It must be emphasized that due to the large ensemble fluctuations it is virtually impossible to obtain statistically relevant information about the average In content of the NW ensemble from such images.

The composition of the QWs x is given by $d_{\text{well}}x = d_{\text{SL}}x_{\text{avg}}$, and will be derived now from the XRD peak positions. To quantify x , the statistical distribution in the layer thicknesses has to be taken into account. Only to determine this uncertainty quantitatively, the XRD profiles were simulated using the method described in Sec. 4.2, and the resulting curves are included in Fig. 5.15. A standard deviation of the segment heights $\sigma_d = 2.5\text{ nm}$ can account for the broadening of the satellite peaks. The square symbols in Fig. 5.17 (a) show x for $d_{\text{well}} = 5.0\text{ nm}$. x can be seen to decrease with increasing T_a . The estimates for x resulting from the thickness estimates $d_{\text{well}} \pm \sigma_d$, i. e. between 2.5 nm and 7.5 nm , are shown as error bars. For the sample grown at $T_a = 608^\circ\text{C}$ the strain $\Delta c/c$, as obtained from the XRD data, is marked for comparison in the strain profile from GPA in Fig. 5.16(e). The solid blue line corresponds to $d_{\text{well}} = 5.0\text{ nm}$, $\Delta c/c = 1.75\%$ and $x = 11.5\%$. The dashed lines give the estimates from XRD for the limiting QW thickness estimates as discussed above. Within the large experimental error, the data agree between this individual NW in HRTEM and the NW ensemble in XRD.

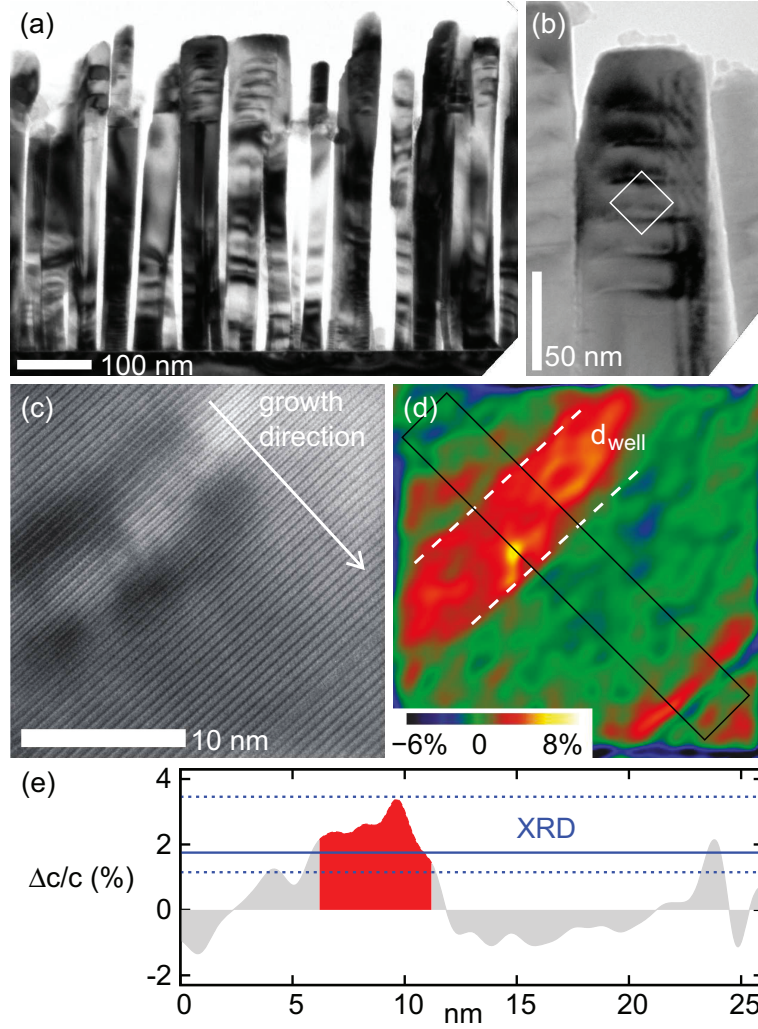


Figure 5.16: TEM analysis of axial $\text{In}_x\text{Ga}_{1-x}\text{N}$ QWs in GaN NWs. $T_a = 608^\circ\text{C}$. (a) NW ensemble in bright field contrast. (b) NW tip with embedded MQW. (c) HRTEM image of one QW, from the area marked by the box in (b). (d) $\Delta c/c$ map obtained from GPA, with the estimated QW thickness marked by dashed lines. (e) $\Delta c/c$ strain profile along the NW axis, obtained within the black box in (d). The approximate location of the QW is marked red, and the QW strain estimate from XRD is given by the blue lines (solid for $d_{\text{well}} = 5\text{ nm}$, dashed for $d_{\text{well}} = 5\text{ nm} \pm \sigma_d$). The data was acquired by C. N. Huang.^[220]

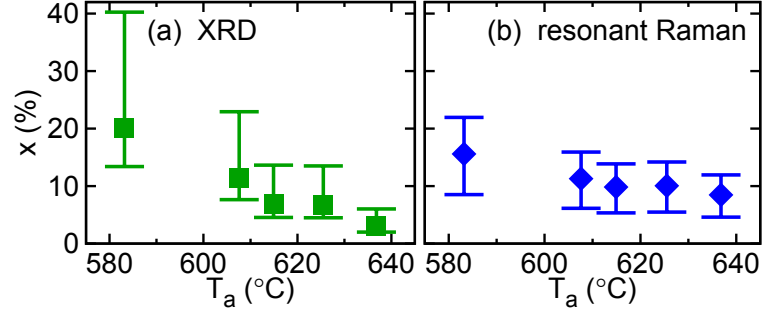


Figure 5.17: In content x in $\text{In}_x\text{Ga}_{1-x}\text{N}/\text{GaN}$ NW axial superlattices grown at different temperatures T_a (series 19). (a) x from XRD satellite peak positions (Fig. 5.15). (b) x derived from the $E_1(\text{LO})$ phonon frequency in the Raman spectra (Fig. 5.18). The uncertainty ranges are described in the main text.^[220]

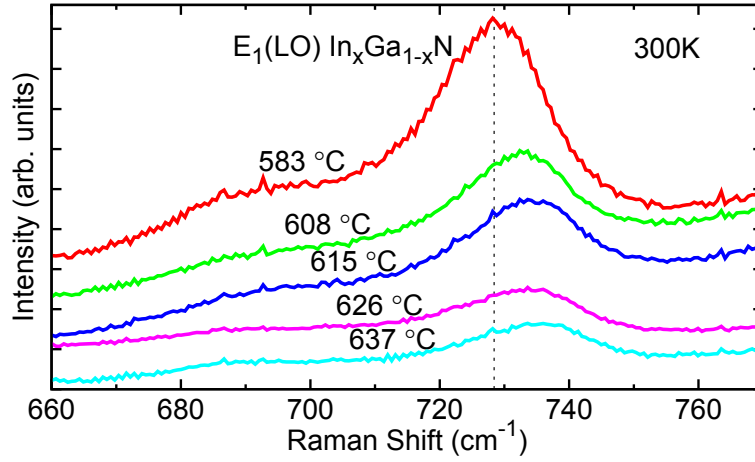


Figure 5.18: Raman spectra of $\text{In}_x\text{Ga}_{1-x}\text{N}/\text{GaN}$ nanowire axial superlattices grown at different temperatures T_a . The samples were resonantly excited at 3.0 eV. The dashed line marks the $E_1(\text{LO})$ phonon frequency peak position of the sample with the highest In content. The data was acquired by M. Ramsteiner.^[220]

5.5.2 Raman spectroscopy

A complementary estimation of x can be achieved by resonant Raman spectroscopy, as was introduced in Sec. 4.4.^[232] The frequency of LO phonons in $\text{In}_x\text{Ga}_{1-x}\text{N}$ depends on both the In content and the strain, as detailed in Sec. 4.4. In order to selectively enhance the Raman signal from the $\text{In}_x\text{Ga}_{1-x}\text{N}$ QWs, the samples were excited with a photon energy of 3.0 eV, i.e. close to the resonance with the fundamental band gap for $x \approx 10\%$. The efficiency of scattering by LO phonons via the Fröhlich mechanism can be considerably enhanced by choosing this kind of resonant Raman spectroscopy.^[179] In fact, the resonantly enhanced LO-phonon signal from the $\text{In}_x\text{Ga}_{1-x}\text{N}$ QWs is much stronger than that from the GaN base material. Using non-resonant conditions, Raman spectra from $\text{In}_x\text{Ga}_{1-x}\text{N}$ would not be detectable because of the small scattering volume provided by the thin QWs and the small separation between $\text{In}_x\text{Ga}_{1-x}\text{N}$ and GaN phonon frequencies at low In contents. The corresponding spectra of the samples are depicted in Fig. 5.18. They are dominated by the $E_1(\text{LO})$ phonon peak. The shoulder at 685 cm^{-1} might be attributed to the S band which is associated in literature with disorder or defects.^[187,240]

This feature does not bear on the analysis. With decreasing T_a , the $E_1(\text{LO})$ peak shifts toward lower frequencies.

In this section, a simple estimate of x is performed, based on the spectral peak position of the $E_1(\text{LO})$ phonon frequency and the following relation, which was already stated as Eq. 4.15: $\omega_{\text{In}_x\text{Ga}_{1-x}\text{N}} = \omega_0 \text{GaN} - 149x \text{ cm}^{-1} + \Delta\omega(\varepsilon)$. The strain state of the QWs can be taken into account by considering the two limiting cases. First, if the $\text{In}_x\text{Ga}_{1-x}\text{N}$ is full relaxed, $\Delta\omega(\varepsilon) = 0$. Second, if the QW is under biaxial strain, as can be found in publications on planar films, a higher LO phonon frequency is expected. A shift of $\Delta\omega(\varepsilon) = -58x \text{ cm}^{-1}$ for $\text{In}_x\text{Ga}_{1-x}\text{N}$ grown pseudomorphically on GaN can be assumed, based on the data given in Ref. 189 for GaN. The values for the composition x , which can be derived from the Raman peak position for these two limiting cases are indicated by the end points of the error bars in Fig. 5.17(b). The diamond data points x plotted in this diagram were derived under the assumption that the active region relaxes laterally and the relative strain is equal to $d_{\text{barrier}}/d_{\text{SL}}$, the claim made by Eq. 4.2. In agreement with the XRD results, x decreases with increasing T_a .

The range of In content deduced from the Raman measurements is smaller than the range derived from XRD. This difference could arise from the resonant excitation which favors regions with $x \approx 10\%$ if the composition fluctuates within a given sample. The weaker Raman signal for samples with higher T_a as seen in Fig. 5.18 is then explained by the detuning of the resonance condition for lower In content. In principle, another factor might be the superimposed contribution of $A_1(\text{LO})$ phonons, which would lead to an overestimation of x . While for the discussion in this section the absolute values of x as derived from XRD are used, the resonant Raman results can be viewed as an independent proof of the systematic In content variation with growth temperature.

5.5.3 Compositional fluctuations

Several types of compositional fluctuations are conceivable in the $\text{In}_x\text{Ga}_{1-x}\text{N}$ quantum well:

- The composition may fluctuate within one QW. As stated before, In concentration variations on a nm-scale are typical for this material.^[13,39,89]
- The average composition might differ from one QW to another within one NW. Very recent microscopy studies on similar structures have indicated that the In content may increase progressively as the active region grows,^[161,162,206] due to a widening of the crystal lattice.^[241] The general applicability of these findings is unclear so far.
- The In composition might differ from one NW to the next if, for example, the diffusion lengths of In and Ga on the sidewalls are unequal, and different NW diameters give rise to different ratios of the diffusion fluxes to the incorporation area on the top facet.^[98]

The experimental methods employed in this section, x-ray diffraction and Raman spectroscopy, are both volume-probing, and therefore in principle do not distinguish between these three fluctuations. It will be seen in the next chapter, however, that In incorporation is largely temperature-controlled. If it is assumed that strain and diffusion play a lesser role for the average In incorporation into each QW, then one can focus on the first type of

compositional fluctuations, on a nm-scale. In principle, such fluctuations are accessible to Raman spectroscopy, because they lead to spectral broadening of phonon lines.

Resonant Raman spectroscopy as an analytical tool for the analysis of $\text{In}_x\text{Ga}_{1-x}\text{N}/\text{GaN}$ NW heterostructures was introduced in Sec. 4.4. It was shown that the systematic and random fluctuations in strain can be simulated, and the strain dependence of the $E_1(\text{LO})$ phonon frequency was given. This information will be used now to simulate an experimentally obtained Raman spectrum, and to extract structural information from the simulation parameters. The analytic expression for the resonant Raman spectrum is repeated here from Eq. (4.18):

$$I(\omega) = \int_0^1 dx \underbrace{R(x)C(x)}_{\text{weighting factor}} L(x)$$

The factor $R(x)$ for the resonance requires the bandgap E_g of the $\text{In}_x\text{Ga}_{1-x}\text{N}$ QWs, which is itself composition- and strain-dependent. Two alternative simulation approaches are presented:

- The detailed solution for the anisotropic strain in the quantum disks is provided by Kaganer and Belov.^[174] Based on the strain tensor, the E_g can be calculated precisely with the Bir-Pikus 6×6 Hamiltonian (see Sec. 2.2.2). In a MC algorithm, volume elements of $\text{In}_x\text{Ga}_{1-x}\text{N}$ with all possible fluctuations can be sampled, and their contributions to the Raman spectrum can be summed up. As was introduced in Sec. 4.4.2, the statistical distribution of the composition $C(x)$ is included in the MC algorithm.
- The strain in a QW can be approximated as constant, because the spectral broadening of the phonon line by the non-uniformity of the strain is much less than the broadening by the compositional fluctuation. (The two cases were compared in Fig. 4.11.) In this approximation, the shear components of the strain vanish, and E_g can be obtained from Eq. (2.1). The Gaussian distribution of the alloy composition around the mean x_{avg} can be taken as $C(x) = \exp[-(x - x_{\text{avg}})^2 / (2\sigma_x^2)]$.

In both cases, the Gaussian alloy fluctuation is described by σ_x in units of x . The simulation depends on the width Γ_g of the resonance $R(x)$, and the minimal width Γ_{ph} of a phonon line, which includes the resolution of the experimental setup. As a starting point, the rough estimates $\Gamma_g = 0.1 \text{ eV}$ and $\Gamma_{\text{ph}} = 10 \text{ cm}^{-1}$ can be used.^[186]

The purpose of this section is to quantify the alloy fluctuation σ_x in the $\text{In}_x\text{Ga}_{1-x}\text{N}$ quantum wells. In order to obtain this parameter from the simulation of an experimental Raman spectrum, it is helpful to fix as many of the other parameters as possible. For this reason, the Raman spectrum of the well studied sample (a) from series 18 will be used. For this sample, x , d_{well} , and d_{barrier} are known from Sec. 5.4.1, σ_d from Sec. 5.4.2, and the NW diameter distribution from App. B can be used. The criterion for the lateral relaxation approximation is fulfilled. The remaining free structural parameter is σ_x .

Figure 5.19 displays the experimental Raman spectrum. The Γ -point optical phonon of the Si substrate is visible at 520.5 cm^{-1} , the E_2^h phonon of GaN at 567 cm^{-1} and the $E_1(\text{LO})$ peak from the $\text{In}_x\text{Ga}_{1-x}\text{N}$ QWs centered at 720.3 cm^{-1} . The $E_1(\text{LO})$ frequency for relaxed GaN is marked for reference at 741 cm^{-1} . $\omega_{\text{LO}}(x, \varepsilon)$ for $\text{In}_x\text{Ga}_{1-x}\text{N}$ was given in Eq. (4.15). In this sample, the redshift with increasing In content dominates over the blueshift with increasing strain.

The inset in Fig. 5.19 shows the $E_1(\text{LO})$ phonon line at a larger scale. The dashed red line shows the MC simulation, with the exact solution for the non-uniform strain dis-

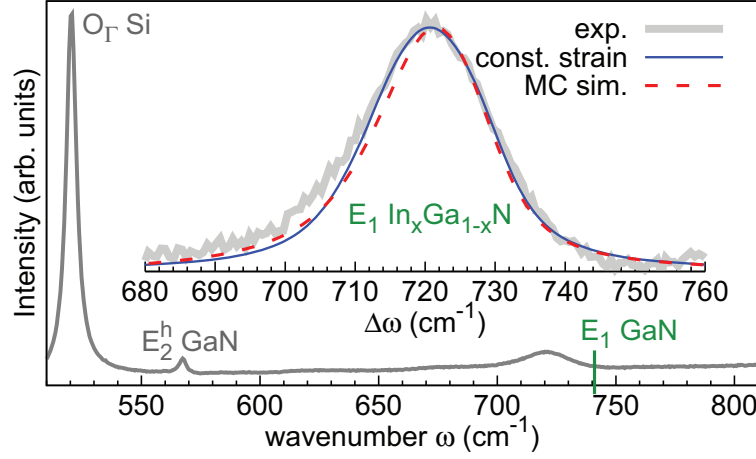


Figure 5.19: Comparison of simulated and experimental resonant Raman spectra for $\text{In}_x\text{Ga}_{1-x}\text{N}/\text{GaN}$ NWs on Si (sample (a) from series 18). The $E_1(\text{LO})$ feature of the experimental spectrum is repeated in the inset for comparison with the simulation. Dashed red curve: MC simulation averaging over $\text{In}_x\text{Ga}_{1-x}\text{N}$ volume elements with anisotropic strain. Blue curve: constant strain approximation. The simulations were performed by M. Ramsteiner.

tribution. A variation of the parameter σ_x has shown that, counterintuitively, the peak frequency is affected more than the width. The experimental phonon frequency is obtained with $\sigma_x = 0.2x$. The width of the experimental phonon line could be matched with the simulation parameter $\Gamma_{\text{ph}} = 10 \text{ cm}^{-1}$ for the minimum phonon linewidth. The second simulation, shown by the blue curve, was obtained with the approximation of constant strain in the QW. The simulation parameters σ_x and Γ_{ph} were the same as in the MC simulation with the detailed strain distribution.

The agreement of the two independent simulations with the experimental data is an important result for the characterization of $\text{In}_x\text{Ga}_{1-x}\text{N}$ quantum wells in NWs. This finding has two consequences:

- The $\text{In}_x\text{Ga}_{1-x}\text{N}$ alloy fluctuation in the QW was quantified by a Gaussian $\sigma_x = 0.2x$. This value will be assumed for every sample discussed in this thesis, because it can be obtained from the simulation of Raman spectra only if the other structural parameters are very well characterized, which in this case required a series of superlattice samples with good XRD contrast.
- The approximation of constant strain in the QW is valid for the interpretation of Raman spectra. It was already shown in Sec. 4.3.2 that Eq. (4.2) can correctly predict the average of non-uniform strain in the QWs. The agreement with the experiment as in Fig. 5.19 is required, however, to prove that the average strain also determines the Raman spectrum. *A priori* this was not given, because the strain distribution is anisotropic, and the shear components of the phonon deformation potentials are unknown.

With σ_x fixed, resonant Raman spectroscopy can be employed to determine another unknown structural parameter. Together with the straightforward approximation of constant strain, Raman spectroscopy will be used in Sec. 6.5.2 to quantify the average strain in specifically engineered heterostructures.

5.6 In incorporation in $\text{In}_x\text{Ga}_{1-x}\text{N}$ nanowire segments

NW growth by MBE offers the advantage of an *in-situ* analysis of In desorption by line-of-sight quadrupole mass spectrometry (QMS).^[229] This section demonstrates a quantitative analysis of the In loss during $\text{In}_x\text{Ga}_{1-x}\text{N}$ NW growth as a function of the substrate temperature. The In desorption was measured *in situ* and the composition x was deduced. In a series of samples, the change of the composition with growth temperature was verified *ex situ* by x-ray diffraction. It is shown that the temperature dependence of the In loss can be described in the same terms as planar growth, and that the $\text{In}_x\text{Ga}_{1-x}\text{N}$ composition can be controlled *in situ* by line-of-sight QMS. The results of this section were published in Ref. 202.

5.6.1 Processes during ternary $\text{In}_x\text{Ga}_{1-x}\text{N}$ alloy formation

The physical modelling of $\text{In}_x\text{Ga}_{1-x}\text{N}$ NW growth by MBE is more complex than in the case of the binaries GaN and InN, because the different behaviour of the constituent atom species has to be taken into account. The growth of ternary $\text{In}_x\text{Ga}_{1-x}\text{N}$ NWs has been studied since 2007.^[103,167] The composition x of $\text{In}_x\text{Ga}_{1-x}\text{N}$ NWs depends on the impinging fluxes and the substrate temperature T ,^[195] a correlation that is also known from planar layers. Planar $\text{In}_x\text{Ga}_{1-x}\text{N}$ growth has been much more extensively studied, because the alloy is used in the active region of LED devices. As a basis for this thesis, it is instructive to review the microscopic processes that affect x in planar $\text{In}_x\text{Ga}_{1-x}\text{N}$.

Atoms from the vapor phase are not directly incorporated into the crystal but adsorb first on the substrate surface. When Ga and In adatoms compete for incorporation into the crystal, Ga is incorporated preferably because the Ga-N bond strength is higher than the one of In-N.^[242] The maximum amount of In incorporation at low growth temperatures is hence given by the difference in N and Ga supply. Consequently, excess In segregates on the surface.^[197,243] Two additional factors are the thermal decomposition of InN,^[244] resulting in new In adatoms, and the desorption of In adatoms from the substrate surface.^[245] Both processes compete with the incorporation of In adatoms originating from the vapor phase and the reincorporation of In adatoms originating from the crystal. All of these atomic processes are sketched in Fig. 5.20(a).

The decomposition of $\text{In}_x\text{Ga}_{1-x}\text{N}$ can be described as a thermally activated process,

$$\Phi_{\text{InN,dec}} = Cx \exp(-E_a^{\text{dec}}/k_B T). \quad (5.5)$$

E_a^{dec} is the activation energy for InN decomposition at substrate temperature T , and C is a constant. In order to describe the resulting composition x as a function of the impinging fluxes Φ_{N} , Φ_{Ga} , and Φ_{In} , two situations must be distinguished: metal-rich (N-limited) growth, and N-rich growth. In the case of metal-rich growth, where $\Phi_{\text{Ga}} + \Phi_{\text{In}} > \Phi_{\text{N}}$, the reduction of incorporated N due to InN decomposition yields an effective N flux $\Phi_{\text{N,eff}} = \Phi_{\text{N}} - \Phi_{\text{InN,dec}}$, and x is given by

$$x = \frac{\Phi_{\text{N,eff}} - \Phi_{\text{Ga}}}{\Phi_{\text{N,eff}}} = 1 - \frac{\Phi_{\text{Ga}}}{\Phi_{\text{N}} - \Phi_{\text{InN,dec}}}. \quad (\text{metal-rich}) \quad (5.6)$$

Therefore, x does not depend on the impinging In flux. Equations (5.5) and (5.6) were shown by Averbeck and Riechert^[239] to describe planar $\text{In}_x\text{Ga}_{1-x}\text{N}$ growth by MBE under metal-rich conditions on the Ga-polar C-plane surface and thus constitute a quan-

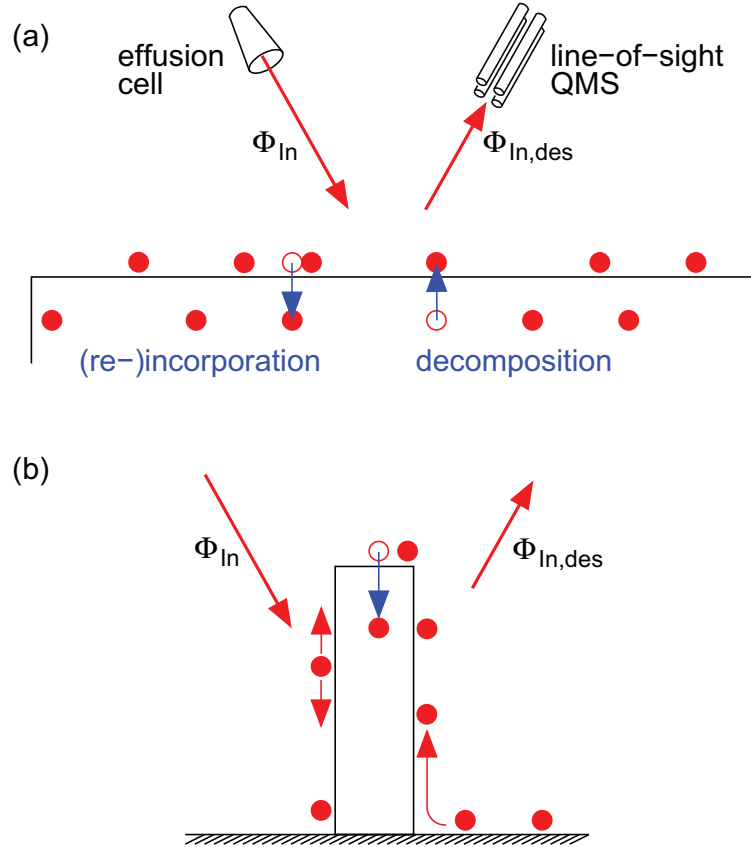


Figure 5.20: Atomic processes occurring during $\text{In}_x\text{Ga}_{1-x}\text{N}$ growth. (a) Impingement, incorporation, decomposition and desorption from a planar $\text{In}_x\text{Ga}_{1-x}\text{N}$ film via the formation of adatoms. Full spheres depict In atoms, open spheres the former position of In atoms. (b) Impingement, diffusion and desorption of adatoms on top facet and sidewall of a NW.^[202]

titative growth model. This approach was also confirmed for planar growth on the N-polar^[246] surface and on off-orientations.^[247] Nitride NWs grow in the N-polar C-direction in MBE.^[109,110] The literature value of E_a^{dec} for InN decomposition from the N-polar surface is 1.2 eV.^[248]

The growth of self-induced $\text{In}_x\text{Ga}_{1-x}\text{N}$ NWs by MBE requires N-rich conditions ($\Phi_{\text{N}} > \Phi_{\text{Ga}} + \Phi_{\text{In}}$). Then, In incorporation is not limited by the N supply, but by the decomposition of InN and the desorption of In adatoms $\Phi_{\text{In,des}}$. If all the In atoms which are not incorporated ultimately desorb, the composition is given by

$$x = \frac{\Phi_{\text{In}} - \Phi_{\text{In,des}}}{\Phi_{\text{Ga}} + \Phi_{\text{In}} - \Phi_{\text{In,des}}}. \quad (\text{N-rich}) \quad (5.7)$$

During $\text{In}_x\text{Ga}_{1-x}\text{N}$ growth decomposition, reincorporation and desorption occur simultaneously and determine the total In loss. The temperature dependence of these single processes is unknown and In loss under N-rich conditions has not been quantified.

In the growth of NWs, in addition mass transport and inhomogeneous strain have to be considered. As stated above, mass transport is more complex than for planar layers. Growth occurs predominantly at the tip of the NW, and adatoms arrive by di-

rect impingement as well as diffusion on the substrate and the sidewall, as depicted in Fig. 5.20(b).^[77,98,99,193] Impingement from the vapor is in turn subject to shadowing by other NWs.^[121] These factors may play a role in $\text{In}_x\text{Ga}_{1-x}\text{N}$ NW growth,^[249] because In adatoms enhance the diffusivity of Ga atoms on the substrate^[238] and on the NW sidewall,^[169] as was demonstrated in Sec. 5.4.3. It is unclear so far how these mass transport effects contribute to the final alloy composition. For example, In diffusion along the NW sidewalls increases with T , i. e. at higher T more In should be supplied to the top facet. At the same time, within the experimental range of temperatures, In desorption from the sidewalls might also decrease the diffusion length for increasing T and lead to a non-monotonic dependence of the In supply on T . Another fundamentally new aspect of NW growth is that strain in heterostructures relaxes elastically at the free NW sidewalls, and hence the strain state changes along the NW radius. This non-uniform interface strain may also affect the In incorporation, which is thought to be favored in the center of the NW top facet.^[170,204,215]

5.6.2 *In-situ* growth control by line-of-sight quadrupole mass spectrometry

In another series of GaN NW samples with $\text{In}_x\text{Ga}_{1-x}\text{N}/\text{GaN}$ MQWs, provisions were made to measure the In desorption *in situ*. The growth temperature of the active region was varied between 588 °C and 631 °C. All other parameters were kept identical, with $\Phi_{\text{N}} = 13 \text{ nm/min}$, $\Phi_{\text{In}} = 0.8 \text{ nm/min}$ and $\Phi_{\text{Ga}} = 0.8 \text{ nm/min}$, yielding a V/III flux ratio of 8.1 for the growth of the active region. The series used in this section is numbered 23, and the detailed listing of growth parameters can be found in App. A.

Equation (5.7) shows that for a quantitative description of In incorporation it is essential to measure In desorption. In MBE, the mean free path of atoms which have escaped the sample surface is long enough to assess desorbing fluxes by line-of-sight quadrupole mass spectrometry.^[84,85] As was shown in Fig. 3.1(a), the QMS is mounted in an effusion cell port at an angle of 21° to the surface normal. Atoms desorbing from the substrate can reach the QMS through an aperture which defines a circular collection area with a diameter of about 3 cm centered on the 2" wafer. The In partial pressure, detected by the QMS with a sensitivity of 10^{-12} torr, scales linearly with the desorbing In flux $\Phi_{\text{In,des}}$ from the substrate surface.

The partial pressure reading is significantly influenced by two factors. First, the high N background pressure of 10^{-5} torr during the growth changes the QMS response. Second, the directional characteristic of desorption from the substrate depends on the exact NW geometry. To quantify $\Phi_{\text{In,des}}$ with the observed partial pressure therefore requires a calibration for an identical NW geometry and background pressure. This procedure is shown in Fig. 5.21(a). After the growth of the self-induced GaN NW base the Ga flux is stopped at time $t = 0$ while the supply of active N continues and the substrate is held at about 800 °C. The In shutter is opened for 2 minutes. At this high temperature, all In arriving at the substrate desorbs and the In partial pressure detected by QMS immediately rises to the level corresponding to 100 % of the incident In flux. When the In shutter is closed, the In partial pressure instantaneously drops to the background level, i. e. 0 % of the incident In flux. Between $t \approx 300 \text{ s}$ and $t \approx 900 \text{ s}$, T is stabilized at 604 °C in preparation of the growth of a long $\text{In}_x\text{Ga}_{1-x}\text{N}$ segment. Figure 5.21(a) shows that upon opening the In shutter again for several minutes, the In desorption does not attain the level of the impinging flux, with the remaining In being incorporated into the NWs. In this particular case, 52 % of the incident In flux desorbs, and hence 48 % is incorporated.

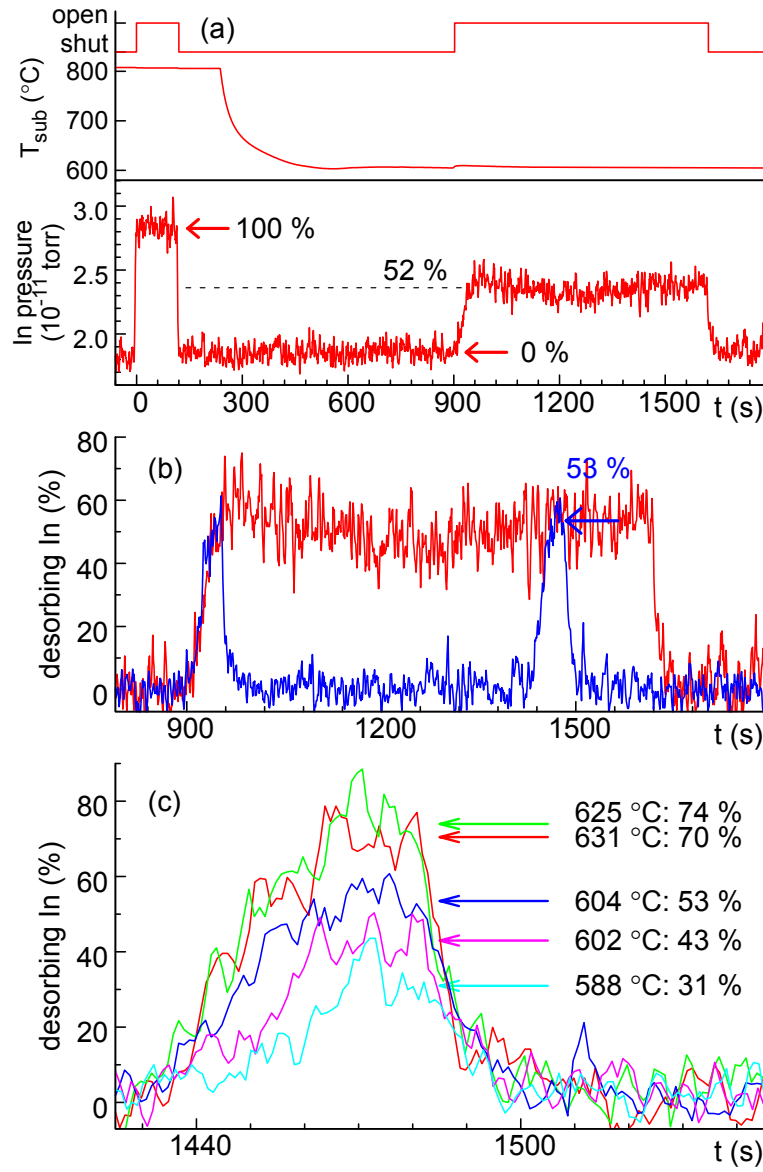


Figure 5.21: In desorption from the sample surface during the growth of $\text{In}_x\text{Ga}_{1-x}\text{N}/\text{GaN}$ NWs by MBE. (a) Calibration of full desorption and background pressure. In addition to the In partial pressure measured by line-of-sight QMS, the status of the In shutter and the substrate temperature are indicated. (b) Comparison of $\text{In}_x\text{Ga}_{1-x}\text{N}$ QW and extended NW segment growth at the same temperature. The amount of desorbing In is given relative to the full desorption as described in (a). (c) In desorption during $\text{In}_x\text{Ga}_{1-x}\text{N}$ QW growth for experiments at different substrate temperatures (series 23).^[202]

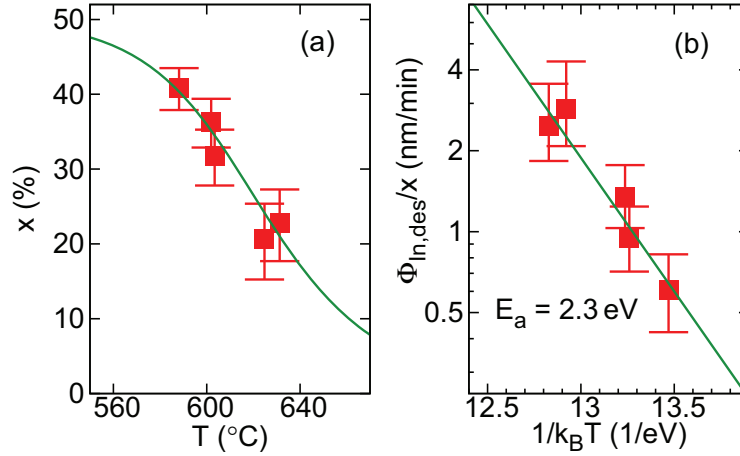


Figure 5.22: (a) $\text{In}_x\text{Ga}_{1-x}\text{N}$ QW composition x as predicted from desorbing In flux by Eq. (5.7), shown as boxes and error bars. The solid line represents the heuristic model for the In loss with the fit parameters as determined from (b). (b) Arrhenius-like plot of the experimental $\Phi_{\text{In,des}}$ from line-of-sight QMS. The solid line shows the fit with $E_a^{\text{des}} = 2.3 \pm 0.4 \text{ eV}$.^[202]

For the samples under investigation, $\text{In}_x\text{Ga}_{1-x}\text{N}$ QWs were introduced by opening the In shutter for 54 s. In Fig. 5.21(b), the In desorption during the growth of two consecutive QWs is shown by the blue line. The experiment was carried out at the same T as the growth of the longer $\text{In}_x\text{Ga}_{1-x}\text{N}$ segment in Fig. 5.21(a), of which the relative In desorption profile is repeated for comparison. Steady state with an In desorption of 53 % of the incident In flux is reached in the last 20 s of the QW growth. This is very close to the In desorption observed during the segment growth. During the growth of consecutive QWs, the same desorption signal is attained, indicating the formation of QWs with equal composition. Figure 5.21(c) compares the In desorption during the growth of the second QW in the whole series of experiments, with the arrows indicating the average reading over the last 20 s of the shutter opening time. As expected, more In desorbs at higher T . The fact that in Fig. 5.21(c) the indicated desorption at 625 °C is higher than at 631 °C can be attributed to an experimental error of $\pm 8 \%$ in the determination of $\Phi_{\text{In,des}}$.

5.6.3 Quantification of In loss

The data of Fig. 5.21(c) is analyzed now on the basis of the atomic processes described in section 5.6.1. To this end, the relative desorbing In flux values are converted into absolute fluxes, based on the calibration of the impinging In flux in equivalent growth rate units. The significant benefit of QMS is that with the data for the impinging and desorbing In fluxes, one can directly calculate the $\text{In}_x\text{Ga}_{1-x}\text{N}$ composition via Eq. (5.7). The predicted x is shown in Fig. 5.22(a) by the box symbols and error bars. A possible systematic error in the calibration of Φ_{In} and Φ_{Ga} is not taken into account. Within the QMS measurement uncertainty, the In content decreases with increasing substrate temperature, as was found *ex situ* in the series of samples analyzed in Sec. 5.5, and as is also the case for planar layers.^[239,244,246] The fairly large range of observed In concentrations demonstrates the crucial role of the substrate temperature. Very importantly, the QMS monitoring allows the *in-situ* control of the ternary alloy formation.

As the next step, the dependence of the In loss on T is analyzed. The growth of the NW

samples was N-rich. Therefore, InN decomposition, In reincorporation and In desorption determine the total In loss, which is accessible to the measurement as In desorbing from the substrate during the growth. The experimentally observed increase of In desorption with T follows

$$\Phi_{\text{In,des}} = C'x \exp(-E_a^{\text{des}}/k_B T), \quad (5.8)$$

as the Arrhenius-like plot in Fig. 5.22(b) indicates. The dependence of $\Phi_{\text{In,des}}$ on x is written in analogy to Eq. (5.5), because decomposition of InN is one of the processes involved in In loss, and the resulting desorbing flux certainly depends on x . The fit result $E_a^{\text{des}} = 2.3 \pm 0.4 \text{ eV}$ is an ‘apparent activation energy’ for the convolution of decomposition, reincorporation and desorption from all parts of the sample. E_a^{des} is higher than the published value of $E_a^{\text{dec}} = 1.2 \text{ eV}$ for InN decomposition from the N-polar surface.^[248] This contrast to the growth of planar layers under metal-rich conditions reveals the importance of In reincorporation and desorption during the growth of $\text{In}_x\text{Ga}_{1-x}\text{N}$ NWs under N-rich conditions. The value obtained here is similar to the activation energy of 2.5 eV that is given in Ref. 248 for In desorption from a liquid adlayer. However, this cannot be the sole origin of the apparent activation energy, because desorption from such an adlayer would not depend on x as is the case in Eq. (5.8).

Analogously to the growth model for $\text{In}_x\text{Ga}_{1-x}\text{N}$ under metal-rich conditions which was cited in section 5.6.1,^[239] one can formulate a quantitative model for the growth of $\text{In}_x\text{Ga}_{1-x}\text{N}$ NWs by MBE. Equation (5.8) can be substituted for $\Phi_{\text{In,des}}$ into Eq. (5.7). Solving the quadratic equation yields

$$x = \frac{\Phi_{\text{Ga}} + \Phi_{\text{In}} + A - \sqrt{(\Phi_{\text{Ga}} + \Phi_{\text{In}} + A)^2 - 4A\Phi_{\text{In}}}}{2A}, \quad (5.9)$$

where A stands for $C' \exp(-E_a^{\text{des}}/k_B T)$. Evaluating this expression with the fit result from the Arrhenius-like plot in Fig. 5.22(b) delivers the $\text{In}_x\text{Ga}_{1-x}\text{N}$ composition shown by the line in Fig. 5.22(a). The agreement with the predicted composition for the individual samples (boxes and error bars) is good because the fit parameters C' and E_a^{des} were obtained from the same set of experiments. These parameters are not universal constants and the model is therefore heuristic and has to be calibrated for each experimental setup.

5.6.4 Ex-situ verification of the growth model for $\text{In}_x\text{Ga}_{1-x}\text{N}$ nanowires

To verify the magnitude of the change in $\text{In}_x\text{Ga}_{1-x}\text{N}$ composition as a function of T with an established *ex-situ* tool, symmetric Bragg x-ray diffraction (XRD) experiments were performed. The profiles are shown in Fig. 5.23, and the arrows indicate the zeroth and $\pm 1^{\text{st}}$ order superlattice satellite peak positions. Still, the zeroth order superlattice peak position ω_0 can be determined with reasonable accuracy, and the average lattice constant of the superlattice is then given by Bragg’s law (Sec. 4.2). Vegard’s law provides the average composition x_{avg} in the axial NW superlattice as was shown in Sec. 4.3.3. In the inset in Fig. 5.23, x_{avg} is shown as a function of T . The average composition x_{avg} decreases by a factor of three between the samples grown at 588 °C and 631 °C.

The prediction for x from the QMS data in Fig. 5.22(a) decreases only by a factor of two between the same samples. Two factors may contribute to this deviation. First, XRD probes a single spot on the sample which is much smaller than the collection area of QMS. The substrate temperature is inhomogeneous and if the collection area contains slightly cooler regions, the In desorption at high growth temperatures is systematically

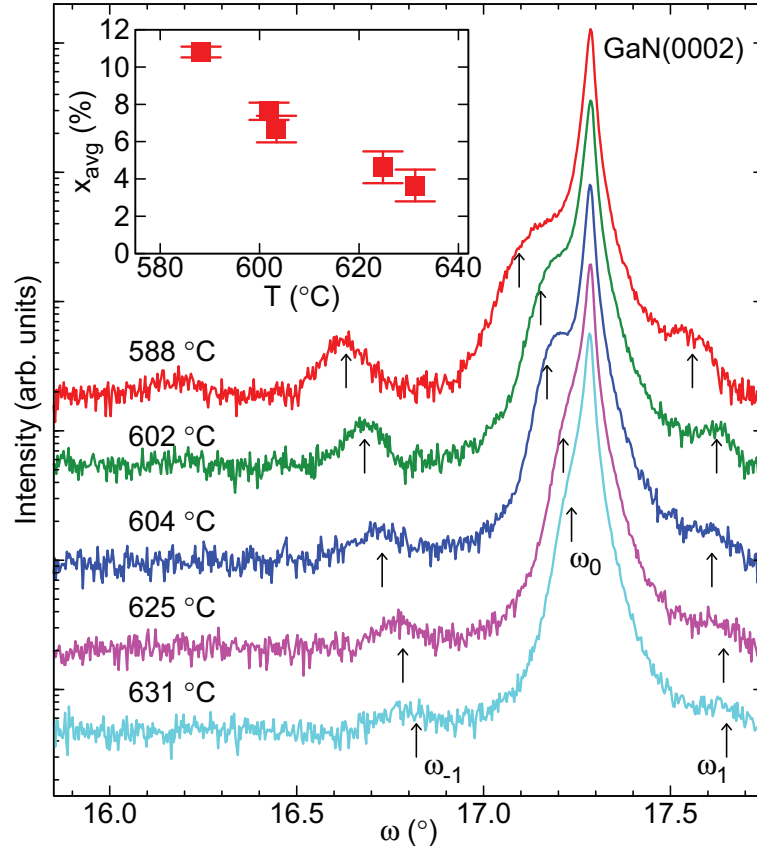


Figure 5.23: Symmetric Bragg XRD scans of $\text{In}_x\text{Ga}_{1-x}\text{N}/\text{GaN}$ NW superlattice samples (series 23). The inset shows the average superlattice composition x_{avg} derived from the zeroth order peak position ω_0 .^[202]

underestimated by averaging over the collection area. Then, x is overestimated from QMS data. Second, any parasitic incorporation of In on the NW sidewalls would reduce the desorbing In flux and again x would be overestimated.

A meaningful confirmation of the activation energy for the In loss as obtained from the QMS data in Fig. 5.21(c) requires the extraction of the In content x in the QWs from the XRD data. Here, the same reasoning as in the previous section is used: The composition x can be derived from $d_{\text{well}}x = d_{\text{SL}}x_{\text{avg}}$ if the contribution of the QW thickness d_{well} to the superlattice period d_{SL} is known, which is obtained from the XRD superlattice peak separation. For this series of samples (series 23), d_{SL} amounts to 10.4 nm with a standard deviation $\sigma_{d,\text{SL}} = 0.5$ nm between samples. However, only a rough estimate of d_{well} between 2.4 nm and 5.0 nm can be given, based on calibrated axial growth rates. (The comparison with a growth series allowing the extrapolation of barrier thicknesses that was helpful for the estimate of d_{well} in Sec. 5.5 is not available here.) The QW thickness in self-induced NW ensembles fluctuates randomly by as much as $\sigma_{d,\text{well}} = 2$ nm within one sample (Sec. 4.2), and the estimate of d_{well} for the ensemble of NWs can therefore not be verified within a microscopic analysis. As a result, the In loss can be judged from the XRD data only with a considerable error. This further highlights the importance of the QMS data.

Figure 5.24 shows estimates of the In content in the QWs as obtained from XRD. The

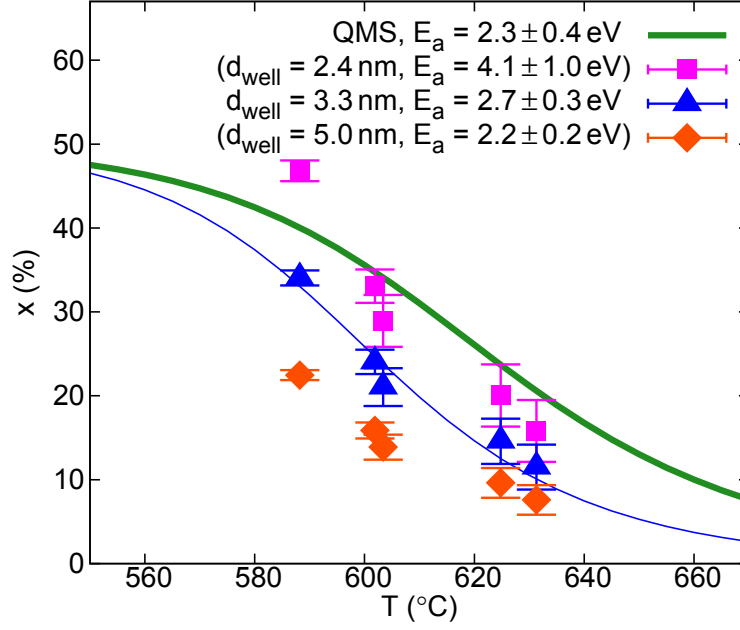


Figure 5.24: Estimates of x from XRD for the $\text{In}_x\text{Ga}_{1-x}\text{N}/\text{GaN}$ NW samples. The values were obtained for assumed QW thicknesses of 2.4 nm (squares), 3.3 nm (triangles) and 5.0 nm (diamonds). The lines represent the prediction for x based on XRD data (blue) and *in-situ* QMS data (green and thick).^[202]

values for x are given for different estimates of d_{well} as 2.4 nm, 3.3 nm, and 5.0 nm. Assuming $d_{\text{well}} = 2.4$ nm implies that x for the sample grown at 588 °C is almost 50 %, which in turn means that no desorption occurs. Desorption was clearly observed in QMS, however, and therefore sensible estimates of d_{well} should be higher. If, on the other hand, $d_{\text{well}} = 5.0$ nm is assumed, there is another contradiction to the QMS data. The resulting x from XRD is then much lower than the prediction from QMS, and one would be forced to conclude that QMS detects only a very small fraction of the In lost during QW growth. In view of the careful QMS calibration described above, this seems unlikely. A QW thickness $d_{\text{well}} = 3.3$ nm is a reasonable estimate, giving compositions in the middle between these boundary cases.

For the three estimates of d_{well} , $\Phi_{\text{In,des}}$ is obtained by Eq. (5.7) and the values for E_a^{des} when fitted to Eq. (5.8) range between 4.1 ± 1.0 eV and 2.2 ± 0.2 eV. (The error increases with the experimental error in x . As a result, the error in E_a^{des} , if obtained from XRD data, is large for small d_{well} and vice versa.) For $d_{\text{well}} = 3.3$ nm, $E_a^{\text{des}} = 2.7 \pm 0.3$ eV matches and confirms the value obtained from QMS. The dependence of x on T according to the model in Eq. (5.9) with the fit parameters as derived from XRD is given by the thin blue line in Fig. 5.24. The thick green line shows the higher prediction of x with the fit parameters from QMS. The deviation is due to the systematically different estimate of the composition between XRD and QMS as discussed above. The heuristic model expressed in Eq. (5.9) can be used in both cases, however, and the apparent activation energy as a fit parameter is equal in XRD and QMS within the errors.

This description of $\text{In}_x\text{Ga}_{1-x}\text{N}$ growth based on the net material flux to the growing alloy does not require the analysis of individual mass transport paths. This does not mean that mass transport phenomena never play a role. Sekiguchi *et al.* had conducted selective area growth experiments, and shown that more closely spaced NWs incorporate more

In.^[249] Within the picture of the net material supply to the growing $\text{In}_x\text{Ga}_{1-x}\text{N}$ at the NW tip, this indicates significant desorption from the NW sidewalls into the vacuum. In that case, however, the regular distance between the NWs was up to 300 nm. In contrast, free lengths of only tens of nm are found in the self-induced NWs (see Fig. 5.1) studied here, and the probability of escape of In atoms from the sidewalls is much lower.^[125]

5.7 Conclusion

$\text{In}_x\text{Ga}_{1-x}\text{N}/\text{GaN}$ MQWs in NWs can rationally be produced by bottom-up growth in MBE. The statistic nature of the self-induced growth process leads to large ensemble fluctuations and complicates the analysis in microscopy, but also in volume-probing methods. The new findings in this chapter are based on the *in-situ* desorption measurement by line-of-sight QMS and the *ex-situ* laboratory XRD measurements.

$\text{In}_x\text{Ga}_{1-x}\text{N}$ segments in NWs grow in MBE at temperatures around 600 °C under N-rich conditions. The microstructure of the $\text{In}_x\text{Ga}_{1-x}\text{N}$ insertion was detailed in Sec. 5.3. With regard to the polytype, RHEED and HRTEM observations confirm synchronous reports that sections of cubic GaN are formed in the MQW region. There is no indication, however, of significant formation of $\text{In}_x\text{Ga}_{1-x}\text{N}$ of the cubic polytype. Microscopy data has revealed the shape, and to some extent the dimension of the $\text{In}_x\text{Ga}_{1-x}\text{N}$ insertions. Like in other synchronous reports, it remains a challenge to distinguish clearly between disk-like $\text{In}_x\text{Ga}_{1-x}\text{N}$ segments covering the whole C-plane facet of the NW, and $\text{In}_x\text{Ga}_{1-x}\text{N}$ insertions surrounded by a GaN shell. Based on the individual TEM and HRTEM images shown in this work, a GaN shell seems to be present. This is made plausible by the finding in Sec. 5.4.3, that Ga diffusion on the sidewalls is reduced at the growth temperature of the active region. The evolution of the NW side facets during the growth of the MQW region is directly correlated to a change in the effective V/III ratio as evinced by the *in-situ* measurement of In desorption. If prolonged In desorption occurs after shutter closure, this indicates surplus In on the surface, and thus metal-rich growth, which favors lateral expansion of the NWs.

The lengths of short NW segments were studied in the laboratory by x-ray diffraction from the axial NW superlattices. As described in Sec. 5.4, series of growth experiments were designed that permit the interpretation of the x-ray measurements despite the ambiguity of the x-ray profiles due to ensemble fluctuations on the sample. An unforeseen effect was discovered, the relative acceleration of axial GaN NW growth in the presence of In adatoms. This effect needs to be taken into account when designing a growth experiment for a specific target thickness of the QWs.

The issue of composition analysis in short $\text{In}_x\text{Ga}_{1-x}\text{N}$ NW segments was addressed in Sec. 5.5. A quantitative *ex-situ* composition analysis was performed by x-ray diffraction and Raman spectroscopy, with support of the conclusion from one HRTEM image and GPA. It was seen that the error bars are very large, a phenomenon intrinsic to the self-induced NW growth. Nevertheless, methods are available for the first time that allow to correlate the $\text{In}_x\text{Ga}_{1-x}\text{N}$ composition in NW MQWs with the growth conditions and, as we shall see in the following chapter, with the optical properties.

Section 5.6 demonstrated that the formation of the ternary alloy $\text{In}_x\text{Ga}_{1-x}\text{N}$ in NWs can be treated in the same framework as planar layers: the thermally activated In loss determines the alloy composition. The resulting composition as a function of growth temperature can be modeled with an Arrhenius-like behavior of the loss from the substrate surface. For the quantitative description of the In loss it has not been necessary to invoke

effects of mass transport. Thus, one can speculate that in these experiments mass transport did not limit In incorporation. There are two limitations to the analysis presented in this thesis. First, any elastic effect on the $\text{In}_x\text{Ga}_{1-x}\text{N}$ composition during the growth would lead to a non-uniform distribution of In within the NW.^[170,204,215] The description here is limited to the average composition, because the characterization methods employed here, QMS and XRD, probe the entire $\text{In}_x\text{Ga}_{1-x}\text{N}$ NW ensemble. The second limitation is that the present data for N-rich growth do not permit to disentangle the activation energies for the processes of decomposition, desorption and reincorporation. The discussion of the atomic processes implies that growth experiments under metal-rich conditions could help to quantify the individual activation energies, but such conditions would prevent the growth of NWs. These observations have important consequences for the development of growth strategies. The alloy formation can be regulated via the substrate temperature and controlled *in situ* by QMS.

6 Properties of $\text{In}_x\text{Ga}_{1-x}\text{N}/\text{GaN}$ nanowire heterostructures

How does the structure of $\text{In}_x\text{Ga}_{1-x}\text{N}$ QWs in GaN NWs relate to the color and intensity of light emission? To which extent can the lattice mismatch strain be reduced in NW heterostructures compared to planar films? With the knowledge presented in the last chapters, $\text{In}_x\text{Ga}_{1-x}\text{N}/\text{GaN}$ NW heterostructures can systematically be grown by MBE to a range of specifications. In this chapter, their elastic and optical properties will be analyzed and compared to physical models. The intentions of this chapter are twofold: to understand the unique properties of the MBE-grown nanostructures, and to put into perspective their application in nanowire LEDs.

After a short review of the literature, the different degrees of freedom in the design of axial heterostructures are summarized. Dedicated series of growth experiments address these structural parameters, and the effects of systematic changes will be shown as an overview. Then, the luminescence of the $\text{In}_x\text{Ga}_{1-x}\text{N}/\text{GaN}$ NW heterostructures will be analyzed in detail and compared to physical models of the light emission. LED devices are presented, which contain the heterostructure developed in this thesis, and their performance is discussed. Finally, the distinguishing feature of these nanostructures, the strain relaxation inside the NW segments, is experimentally proven. The applicability of geometric estimates of the average strain is experimentally verified and compared to the theory from Ch. 4. In this way, the possibilities and limitations of strain engineering in NW heterostructures are clarified.

6.1 Previous studies of $\text{In}_x\text{Ga}_{1-x}\text{N}/\text{GaN}$ nanowire properties

In parallel with the reports on GaN and $\text{In}_x\text{Ga}_{1-x}\text{N}$ NW growth, a small body of literature about their properties had evolved at the time of starting this thesis. Driven by the potential application in solid state lighting, and certainly due to the relative simplicity of photoluminescence studies, most early reports focused on the optical properties.

Even before the properties of $\text{In}_x\text{Ga}_{1-x}\text{N}$ heterostructures in NWs were studied systematically in experiment and theory, they were manufactured as a part of nanocolumnar LED structures. Numerous production methods were demonstrated, which can be grouped into

- top-down etching from planar LED structures, mostly grown by MOVPE, and shown repeatedly since 2001,^[46,250,251]
- and bottom-up fabrication by nanocolumnar crystal growth in MO-HVPE^[49] and MBE,^[8,223] first shown in 2004.

These works were motivated by efficiency limitations in planar LEDs. Advantages during crystal growth, fewer heterointerface defects and higher In incorporation, were expected from the bottom-up techniques. Other benefits of the nanostructure, lateral strain relaxation and enhanced light-outcoupling, were expected from both approaches.

A study of top-down fabricated NW MQW structures by Chen *et al.* had shown an enhancement of the room temperature PL intensity in the NWs compared to the as-grown bulk sample.^[250] They concluded that the photoluminescence is robust to the etching and surface recombination did not pose a problem to nitride NWs. Shing-Chung Wang and co-workers showed a small blueshift and broadening in room temperature PL of etched NW MQWs compared to the as-grown planar sample.^[44] For the cause of the blueshift, they considered a reduction of the piezoelectric field due to strain relaxation, and hence a reduction of the QCSE. A later work from the same group added a numerical strain calculation to justify non-uniform relaxation, and hence broadening of the emission spectrum.^[45]

Etched NW structures also delivered the experimental data for a detailed modelling of the strain relaxation and electron and hole recombination inside $\text{In}_x\text{Ga}_{1-x}\text{N}$ QWs in NWs, published in 2009 by Wu *et al.*^[46] They analyzed $\text{In}_x\text{Ga}_{1-x}\text{N}/\text{GaN}$ NWs with diameters between 120 nm and 300 nm, containing a 100 nm-thick axial MQW stack. A reduction of the QCSE due to increased strain relaxation for thinner NWs was deduced from PL experiments in two ways: Both at room temperature and at 20 K, the emission was blueshifted for smaller diameters. Time-resolved PL experiments (TRPL) at low temperature showed the radiative decay time to be reduced for thinner NWs, indicating a better overlap of the electron and hole wavefunctions. The strain distribution was calculated, and the recombination energy was obtained at different radial positions in the NW from 1d-Schrödinger-Poisson calculations. Wu *et al.* concluded that the higher-energy part of the emission originates from the more strain-relaxed periphery of the quantum disks, because of higher emission rates. Their view was contested later because it does not provide for a lateral change in carrier density.^[252]

Only bottom-up grown NW MQWs can exploit advantages of the NW geometry during crystal growth, but they are in principle harder to study than etched NWs for several reasons: (i) no reference data from the planar device can be used, (ii) statistic thickness fluctuations and crystallographic misalignment play a role, and (iii) the exact shape of the $\text{In}_x\text{Ga}_{1-x}\text{N}$ QWs is often speculative (see Sec. 5.3.1). Few studies had been published on the luminescence of nominally uniform self-induced $\text{In}_x\text{Ga}_{1-x}\text{N}$ NWs, and the simple conclusion is that higher In content, obtained by lower growth temperature, leads to lower luminescence energy.^[103,195] The pioneering work on bottom-up grown GaN nanowire LEDs on Si with $\text{In}_x\text{Ga}_{1-x}\text{N}/\text{GaN}$ heterostructures by Katsumi Kishino and co-workers reported room temperature electroluminescence in the green to red spectral range.^[8] This group later studied the luminescence of GaN NWs on sapphire with one single axial $\text{In}_x\text{Ga}_{1-x}\text{N}$ QW. They measured single NWs, and explained the broad PL spectrum of an ensemble of NWs as the superposition of sharp individual lines at varying energies.^[159,160] They also found a biexponential PL decay, with decay times two orders of magnitude smaller than in comparable planar QWs, which they attribute to a suppression of the internal piezoelectric field in the NWs.

The magnitude of the QCSE in axial NW QWs had been an unresolved question. Whereas the early results of Kishino's group did not show the typical PL blueshift under higher excitation,^[159,160] it was observed by Armitage *et al.*^[223] Further, none of the earlier studies on $\text{In}_x\text{Ga}_{1-x}\text{N}$ NW luminescence quantify the QW or segment composition independently, and therefore cannot correlate luminescence and structure quantitatively.

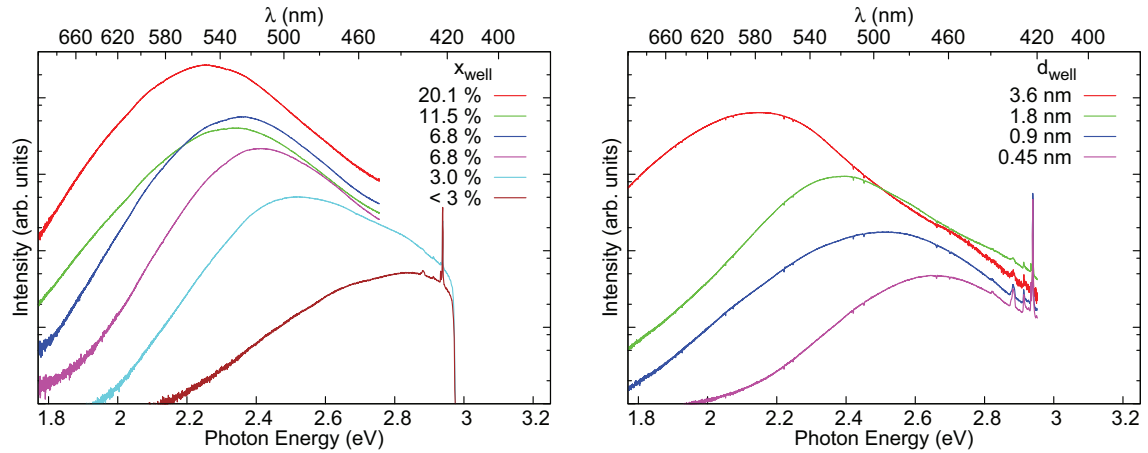
Strain relaxation in NW heterostructures had been treated theoretically and experimentally since 1998,^[164,210] and was clearly put in evidence for $\text{In}_x\text{Ga}_{1-x}\text{N}/\text{GaN}$ NWs by Stacia Keller *et al.* in 2006.^[211] They etched a patterned array of nanocolumns and

nanowalls out of an MOVPE-grown coherent planar MQW. The change of the in-plane lattice parameter in the MQW was shown by laboratory x-ray diffraction before and after etching. As was later shown theoretically,^[174] the NW and MQW dimensions in these experiments were in the limits for full lateral relaxation that were stated in Sec. 4.3. An effect of the strain relaxation on the optical properties was not shown.

6.2 Design options: $\text{In}_x\text{Ga}_{1-x}\text{N}$ segment composition, thickness and strain

The three principal degrees of freedom in the design of the axial NW MQWs are the $\text{In}_x\text{Ga}_{1-x}\text{N}$ composition x and segment thickness d_{well} , and the average strain, defined by the thickness ratio $d_{\text{barrier}}/d_{\text{SL}}$. As is established in this work, it is a unique property of axial MQWs in NWs that the strain in a given QW can be defined by the barrier thickness. In contrast, coherent growth of planar films on a bulk substrate defines the QW strain state irrespective of d_{barrier} . How these parameters affect the optical properties of the NW heterostructure is shown now in a compact overview.

The effect of a variation in x is shown in Fig. 6.1(a). The room temperature photoluminescence is given for a series of $\text{In}_x\text{Ga}_{1-x}\text{N}/\text{GaN}$ NW samples with all other parameters identical. With decreasing x , the emission peak shifts to higher energies. This is in line with the expected behaviour of a planar QW, even though the absolute emission energy and intensity cannot be explained with the simple model outlined in Sec. 2.2.2, as will



(a) Samples with a variation in QW composition x , created by changing the growth temperature of the active region (series 19). The composition is estimated for $d_{\text{well}} = 5$ nm (see Sec. 5.5). TEM images of the sample with $x = 11.5\%$ are shown in Fig. 5.3(b).

(b) Samples with a variation in QW thickness d_{well} , created by changing the QW growth time t_{well} (series 11). A rough estimate for the QW thickness is indicated: $d_{\text{well}} = 2t_{\text{well}}\Phi_{\text{Ga}}$. STEM images of the sample with $d_{\text{well}} = 3.6$ nm are shown in Fig. 5.2.

Figure 6.1: Room temperature photoluminescence of axial $\text{In}_x\text{Ga}_{1-x}\text{N}$ QWs in GaN NWs with an excitation at 3.0 eV (413 nm). Note the logarithmic intensity scale and the extremely large drop in intensity with blueshifting emission. Sharp lines around 2.9 eV are an artifact. Shortly before 3.0 eV, the signal is cut off by the filter. The data was acquired by C. Hauswald.

be shown later. The indicated values for x are estimates based on x-ray diffraction peak positions (from Sec. 5.5).

In Fig. 6.1(b) a series of samples with a variation in d_{well} is presented. In this series, x is constant. The emission energies are blue-shifted with decreasing d_{well} . Again, the systematic change in emission energy would fit the assumption of a QCSE as in planar QWs, but this model is contradicted by the increasing intensity towards lower emission energies. The indicated values for d_{well} are rough estimates, which are obtained from the QW growth time, the calibrated Ga flux and a factor of two, which accounts for the enhanced QW growth rate (from Sec. 5.4.3).

The ratio $d_{\text{barrier}}/d_{\text{SL}}$ defines the average strain in the QW, as was shown in Sec. 4.3.2. That this is really the case in experimental structures can be seen in the Raman spectra in Fig. 6.2(a). Data from a series of samples with a variation of $d_{\text{barrier}}/d_{\text{SL}}$ is shown. All other structural parameters are identical. The $\text{In}_x\text{Ga}_{1-x}\text{N}$ $E_1(\text{LO})$ phonon peaks, connected by the thick gray line as a guide to the eye, shift systematically to higher frequencies with increasing ratio $d_{\text{barrier}}/d_{\text{SL}}$, indicating an increasing average strain. The room temperature photoluminescence of the same series of samples is depicted in Fig. 6.2(b). It is evident that the luminescence differs strongly from sample to sample. The strain distribution within the QWs is non-uniform, as was shown in Sec. 4.3.1, and the QW luminescence can not be analyzed simply in terms of the average strain.

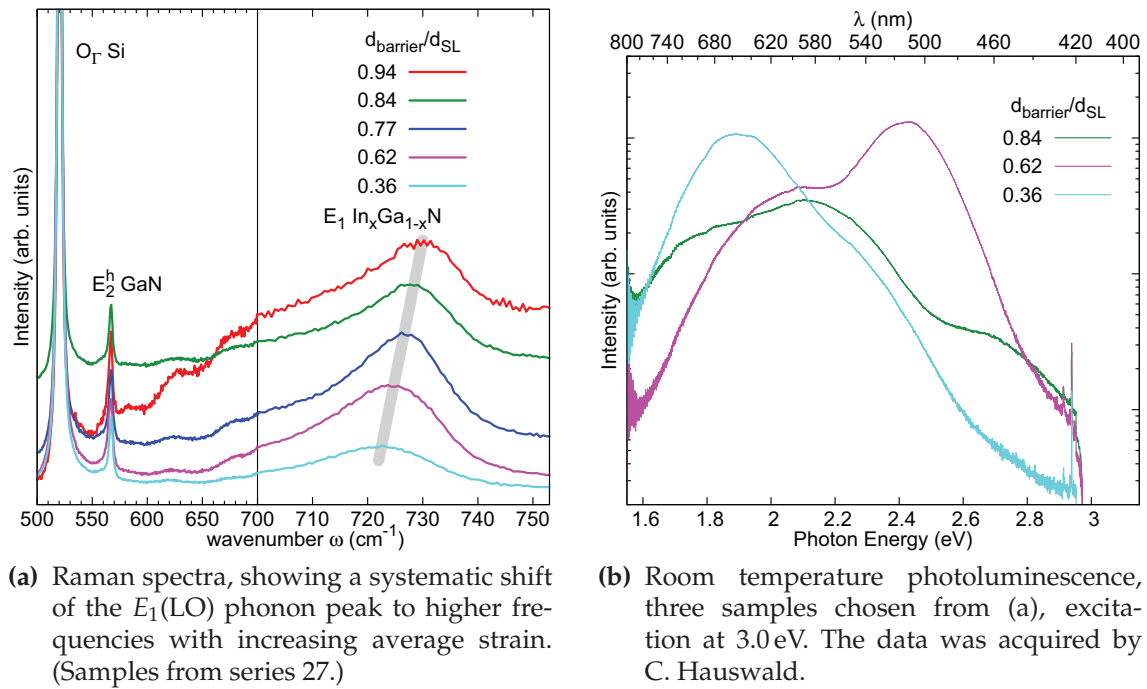


Figure 6.2: Optical properties of axial $\text{In}_x\text{Ga}_{1-x}\text{N}$ QWs in GaN NWs with a variation in strain, created by changing the barrier segment growth time. (The average strain in the QWs is shown in Sec. 6.5.2 to change linearly with $d_{\text{barrier}}/d_{\text{SL}}$.)

6.3 Luminescence

Light is emitted from the $\text{In}_x\text{Ga}_{1-x}\text{N}$ crystal by the relaxation of excited charge carriers. This is achieved in several ways:

Photoluminescence (PL) Charge carriers are excited by an incident laser beam. PL is a versatile, fast, non-destructive method which is routinely used in commercial production. In the laboratory, areas between $1\text{ }\mu\text{m}$ and tens of microns^[159] can be illuminated, allowing to address large NW ensembles or well-spaced individual NWs. PL can operate through a window on samples in a cryostat. $\text{In}_x\text{Ga}_{1-x}\text{N}$ can be selectively excited in heterostructures by choosing a laser line below the GaN bandgap.

Cathodoluminescence (CL) An electron beam in a scanning electron microscope excites charge carriers in the material, and within the carrier diffusion length, the light emission can be spatially correlated with SEM images.

Electroluminescence (EL) The goal of device development for solid state lighting is, of course, electrically driven light emission. Favorably, electrons and holes are injected into a p-n junction under electric current. EL measurements on $\text{In}_x\text{Ga}_{1-x}\text{N}/\text{GaN}$ NWs require the growth of a full LED structure and electrical contacting, and the results reflect the quality of the whole device and not only the active region.

Ensembles of NWs with statistic structural fluctuations possess distinct emission centers, which are visualized in this section by PL microscopy and CL. As a prerequisite to understanding the behavior of NW LEDs, these methods are used to analyze the local origin of the spectral components of the luminescence from as-grown $\text{In}_x\text{Ga}_{1-x}\text{N}/\text{GaN}$ NWs. The systematic investigation of ensemble luminescence then relies on PL with selective excitation of the $\text{In}_x\text{Ga}_{1-x}\text{N}$ QWs. The main results of this section were published in Ref. 220.

6.3.1 Distinction of single emission centers in nanowire ensembles

The description of the luminescence in this section is based on spectroscopy data from three independently grown NW samples. All samples possess six axial $\text{In}_x\text{Ga}_{1-x}\text{N}$ QWs. A photoluminescence spectrum from the first ensemble is shown in Fig. 6.3(a). The excitation is at 3.8 eV , that is above the band gap of GaN, and the sample is observed in plan view. The spectrum shows main emission bands at three peak positions:

2.2 eV, emission from the $\text{In}_x\text{Ga}_{1-x}\text{N}$ QWs.

3.0 eV, attributed to emission from insertions of cubic GaN (c-GaN).^[81] (Evidence for the formation of c-GaN was shown in Sec. 5.3.2.) The redshift with respect to the c-GaN room temperature band edge of 3.2 eV may be explained by the quantum-confined Stark effect (QCSE) in thin layers of c-GaN in a matrix of hexagonal GaN.^[219]

3.4 eV, the free exciton transition in the strain-free GaN NW base.

The identification of these luminescence bands will be backed in the following section by comparing the change in the ensemble luminescence for samples with different $\text{In}_x\text{Ga}_{1-x}\text{N}$ composition. Judging the origin of a luminescence from one ensemble spectrum alone

is difficult and has led to errors.^a Especially attributing the PL emission at 2.2 eV to $\text{In}_x\text{Ga}_{1-x}\text{N}$ requires proof, because GaN defect luminescence, known as the ‘yellow luminescence’, is also commonly observed in this energy range.^[254]

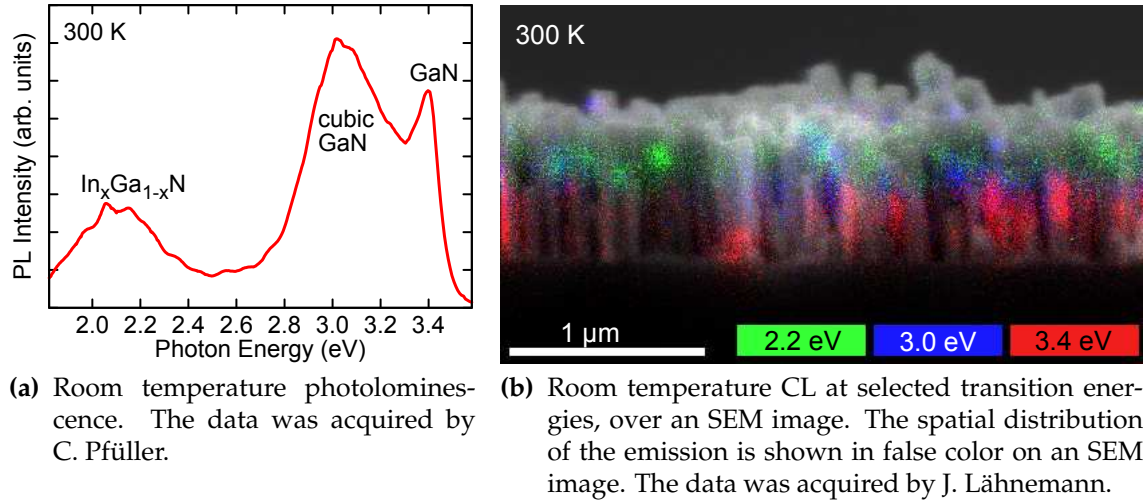
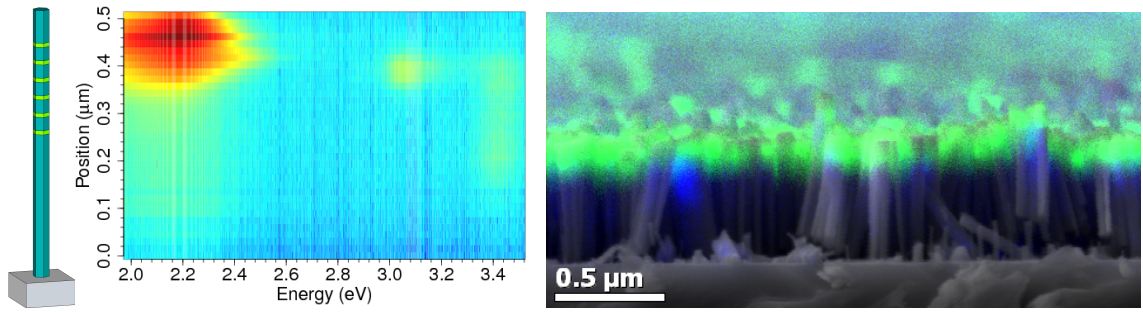


Figure 6.3: Comparison of the ensemble photoluminescence and cross-section cathodoluminescence of one GaN NW sample with $\text{In}_x\text{Ga}_{1-x}\text{N}/\text{GaN}$ MQWs. (An SEM close-up of the NW tips was shown in Fig. 5.7.)

Jonas Lähnemann localized the origin of the emission on the $\text{In}_x\text{Ga}_{1-x}\text{N}/\text{GaN}$ NW ensemble by investigating the cathodoluminescence in an SEM. A cross section image is shown in Fig. 6.3(b). The intensity of cathodoluminescence for three detection energies is laid over the image in false color. Emission at 2.2 eV (marked in green) is observed exclusively in the MQW region. CL at 3.0 eV (marked in blue) appears above the NW base, in keeping with the claim that it originates from c-GaN, which is formed at the lower growth temperature of the active region. Finally, CL at 3.4 eV (marked in red) originates mainly from the NW base. The spatial distribution of these three emissions was observed in all of the analyzed samples. Figure 6.4 shows room temperature CL data from another specimen. A spectral linescan is given in Fig. 6.4(a). Again, intense emission at 2.2 eV originates in the active region. c-GaN emission at 3.1 eV is detected just above the GaN base NW. The base shows a luminescence of 3.4 eV, but only above a height of 200 nm. J. Lähnemann attributed this fact to a higher density of defects which act as nonradiative recombination centers at the bottom of the NW. A weak luminescence from the base NW at 2.2 eV is attributed to defects (yellow luminescence). The CL and SEM overlay in Fig. 6.4(b), where the CL from $\text{In}_x\text{Ga}_{1-x}\text{N}$ and GaN is marked green and blue, respectively, indicates that the linescan is typical for this sample. Nevertheless, linescans of other NWs from the same sample (data not shown) exhibit variations in the spatial and spectral positions of the $\text{In}_x\text{Ga}_{1-x}\text{N}$ and c-GaN luminescence.

As seen in the CL overlay image in Fig. 6.3(b), the luminescence can fluctuate significantly from NW to NW. This fluctuation is addressed now by PL microscopy on a third sample. PL microscopy, or fluorescence microscopy, is an efficient way to measure lu-

^aLow-temperature luminescence from $\text{In}_x\text{Ga}_{1-x}\text{N}$ QWs in NWs was identified by one report at 3.26 eV,^[253] but may have been a donor-acceptor-pair transition in GaN.^[254] Another line observed at 3.34 eV^[255] may correspond to c-GaN segments.^[26,219] The same misinterpretation was likely applied to room temperature EL at 2.95 eV.^[51]



(a) Symbolized NW geometry (not to scale) and CL line scan of one individual NW at room temperature. The color palette represents the CL intensity on a log. scale. (b) CL and cross-section SEM of the NW ensemble. CL at 3.4 eV is marked in blue, CL at 2.2 eV in green.

Figure 6.4: Cathodoluminescence at different heights in another $\text{In}_x\text{Ga}_{1-x}\text{N}/\text{GaN}$ NW ensemble. The six $\text{In}_x\text{Ga}_{1-x}\text{N}$ QWs emitting at 2.2 eV can not be distinguished. c-GaN emission at 3.1 eV is observed at the beginning of the active region. GaN emission at 3.4 eV is observed in the base NW above a height of 200 nm. The data was acquired by J. Lähnemann.

minescence simultaneously across the as-grown NW ensemble.^[158] Figure 6.5 shows the fluctuation in color and intensity across this sample. The images are taken at different positions 1–4, all away from the wafer center, with the growth temperature being the highest at position 1 and decreasing systematically to position 4. With lower growth temperature, more In is incorporated, the $\text{In}_x\text{Ga}_{1-x}\text{N}$ band gap is smaller, and light of lower energy is emitted on average. For this reason, the ensemble color in the images changes from green to orange. The quantitative change of the emission energy with the $\text{In}_x\text{Ga}_{1-x}\text{N}$ composition will be the subject of the next section. The statistical fluctuation within one image is broad, and individual spots from green to red can be found in all four images, indicating significant variations from NW to NW.

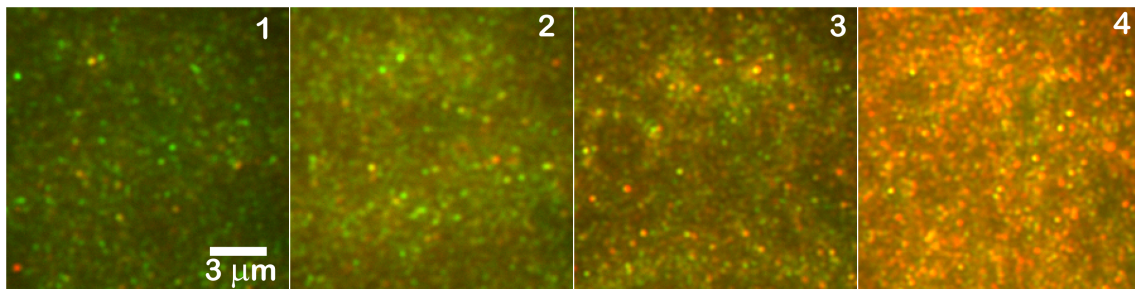


Figure 6.5: False color PL images of room temperature photoluminescence. The $\text{In}_x\text{Ga}_{1-x}\text{N}/\text{GaN}$ NW ensembles as-grown on one wafer were selectively excited at 2.54 eV.^[157] The images 1–4 were acquired at positions on the wafer with decreasing growth temperature. The emission was collected through band pass filters at 530–590 nm (green-yellow) and 590–690 nm (orange-red). The two channels are superimposed to form these color images. The spots in the images are diffraction-limited and do not correspond to individual NWs. The data was acquired by S. De, Indian Institute of Technology Bombay, Mumbai.

The fluctuation in luminescence across a sample raises the question if all of the NWs emit light in the $\text{In}_x\text{Ga}_{1-x}\text{N}$ band. The CL data from the second sample can be used for this purpose. Figure 6.6 shows an overlay of CL at 2.3 eV (marked in green) on a plan view SEM image. All the NWs contribute to this emission. It has been discussed recently by Friederich Limbach *et al.* that the density of luminescence spots in such samples is a function of coalescence. If the NWs are more connected than in the case of Fig. 6.6, carriers may diffuse toward energetically more favorable localization centers, and the number of luminescent spots will be reduced.^[57]

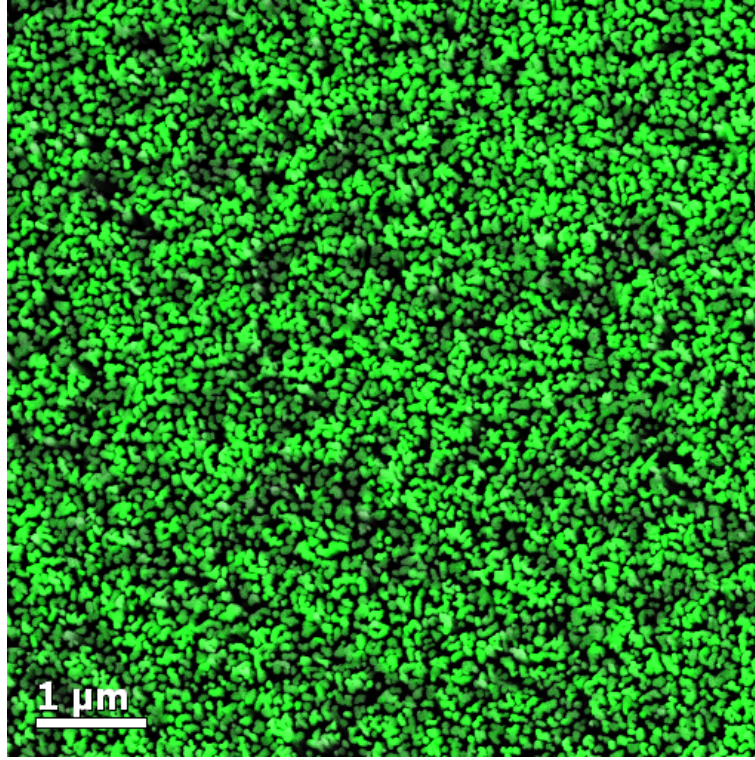


Figure 6.6: Cathodoluminescence at 2.3 eV in plan view, indicating that $\text{In}_x\text{Ga}_{1-x}\text{N}$ emission originates from all NWs on the sample. (5 kV, slit 5 mm, i. e. broad bandpass of 50 nm) The data was acquired by J. Lähnemann.

If one takes into account that the QW geometry defines its strain state, and that the $\text{In}_x\text{Ga}_{1-x}\text{N}$ luminescence depends critically on the composition, the strain and the QW thickness, then structural fluctuations are expected to result in a variation in luminescence. The structural fluctuations from NW to NW have been observed in microscopy, and were also used to explain the broadening of the XRD profiles. From the structural analysis presented in Ch. 5, it is not clear how similar the $\text{In}_x\text{Ga}_{1-x}\text{N}$ QWs within one NW are to one another. This raises the question whether the study of the luminescence properties can help to compare individual QWs. To detect luminescence from individual QWs, a high spatial resolution in the spectroscopic measurement is required. The best resolution is obtained in CL, where it is generally given by the scattering length (of about 30 nm in these studies)^[256] and the diffusion length. In the NWs studied here, the carrier diffusion may be limited by the next QW, where carriers are trapped.^[257] The CL overlay in Fig. 6.3(b) shows a sample with a particularly wide spacing of the QWs, $d_{\text{SL}} = 33$ nm. Yet, the QWs can not be separated in CL. No information about the uniformity of QWs

within one NW can therefore be obtained. Tourbot *et al.* recently reported on the CL of a similar structure, obtained in a scanning transmission electron microscope.^[204] They concluded that the CL emission from individual QWs has a tendency to shift to the red along the growth axis. It is unclear so far if this effect is systematic. It must be stressed that in any case, the effect is very small compared to the fluctuation in luminescence between NWs.^[204]

To summarize, all of the NWs in an ensemble emit light from the active region with significant fluctuations in wavelength and intensity. The emission from individual QWs cannot be resolved.

6.3.2 Photoluminescence of $\text{In}_x\text{Ga}_{1-x}\text{N}/\text{GaN}$ nanowire ensembles with different composition

The effect of the $\text{In}_x\text{Ga}_{1-x}\text{N}$ composition on the luminescence of NW heterostructures can be clarified now with the experimental data from the series of samples whose composition was carefully analyzed in Sec. 5.5 (series 19). In this series, different compositions were achieved as a function of the growth temperature T_a of the active region. Room temperature photoluminescence (PL) spectra are presented in Fig. 6.7(a) for excitation at 3.8 eV, i. e. above the band gap of GaN. As expected, they show three main emission bands. The spectra are normalized to the free exciton transition of 3.4 eV in the strain-free GaN NW base. The second peak at 3.0 eV is again attributed to emission from insertions of cubic GaN. The third PL emission peak in the energy range from 2.2 eV to 2.5 eV shifts systematically with T_a . In view of the variation in In content with T_a , we attribute this emission to the $\text{In}_x\text{Ga}_{1-x}\text{N}$ QWs. The shift in the peak position can be seen more clearly in the normalized spectra depicted in Fig. 6.7(b) which were obtained by direct excitation at 3.0 eV. This systematic shift proves that the emission at 2.2 eV cannot be identified with the defect emission known as the ‘yellow luminescence’.^[254] The intensity of the

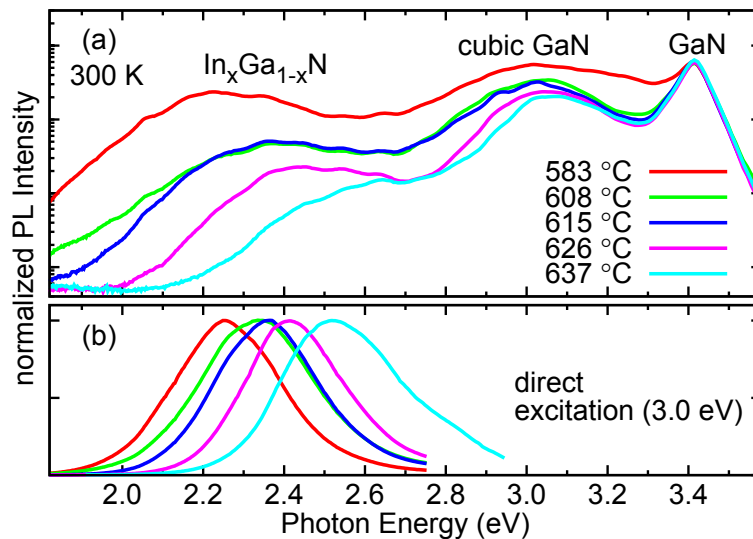


Figure 6.7: Room temperature PL spectra of $\text{In}_x\text{Ga}_{1-x}\text{N}/\text{GaN}$ NW axial superlattices grown at different temperatures T_a (series 19). (a) Excitation at 3.8 eV (logarithmic). (b) Direct excitation at 3.0 eV (linear). The data was acquired by C. Pfüller (a) and C. Hauswald (b).^[220]

$\text{In}_x\text{Ga}_{1-x}\text{N}$ emission decreases drastically with decreasing In content. This decrease in intensity with decreasing In content is unexpected and contradictory to experience with planar $\text{In}_x\text{Ga}_{1-x}\text{N}$ structures. The ordinary expectation would be that lower In content is accompanied by higher crystalline quality and a reduced QCSE, which would increase the emission intensity (as introduced in Sec. 2.2.2).

6.3.3 Calculation of transition energies

Figure 6.8 shows the observed peak positions for the emission from c-GaN and from the $\text{In}_x\text{Ga}_{1-x}\text{N}$ QWs as a function of T_a . To correlate the experimentally observed emission energies and structural parameters, Jonas Lähnemann calculated the expected transition energies by solving the one-dimensional Poisson and Schrödinger equations self-consistently with a program provided by Greg Snider.^[258] The inputs were the $\text{In}_x\text{Ga}_{1-x}\text{N}$ QW thicknesses d_{well} , the compositions x derived from XRD, and the published values for the bowed band-gaps,^[35] the band-offset,^[259] and the bowed polarization.^[260] The simulated transition energies are added to Fig. 6.8 for comparison with the experimentally observed PL peak positions. The green shaded range of values results from the estimates for x derived from XRD with different assumptions for d_{well} as was discussed above (in Sec. 5) and shown in Fig. 5.17(a). The PL at 3.0 eV is of almost constant energy, which supports the assignment of this emission to c-GaN insertions. In contrast, the luminescence around 2.2–2.5 eV, assigned to emission from $\text{In}_x\text{Ga}_{1-x}\text{N}$, systematically shifts to higher energies with decreasing In content. However, this shift is significantly smaller than the calculation predicts, regardless of the specific assumption for d_{well} . Thus, the situation in the NW based axial $\text{In}_x\text{Ga}_{1-x}\text{N}$ QWs differs considerably from that of planar QWs, for which one-dimensional calculations are in much better agreement with the experimental emission energies.^[261]

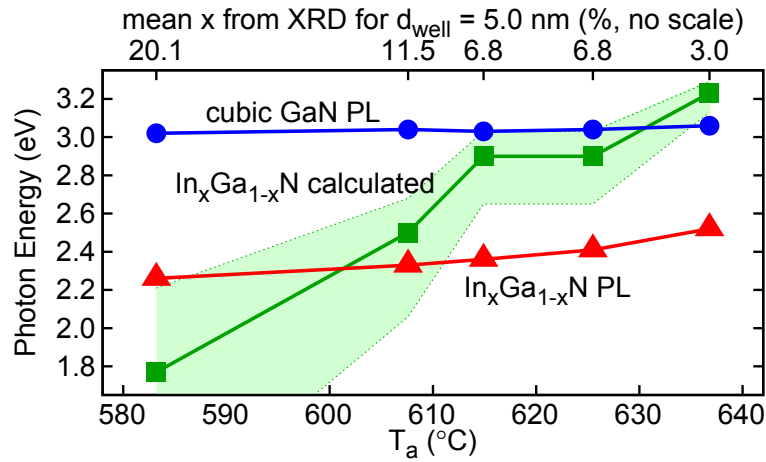


Figure 6.8: Experimental PL peak positions and calculated planar $\text{In}_x\text{Ga}_{1-x}\text{N}$ QW transition energies. The shaded area results from the maximum and minimum estimation of x and d_{well} from XRD.^[220]

6.3.4 Limitation of 1d-model and suggested carrier localization

Both the luminescence energy range observed here and the absence of bright emission above 2.7 eV normally expected for low In content are in accord with similar op-

tical measurements in other reports where the In content was not determined independently.^[51–54,203,226,262] This agreement is intriguing because it indicates a universal characteristic of axial $\text{In}_x\text{Ga}_{1-x}\text{N}/\text{GaN}$ NW heterostructures. Three types of carrier localization have been discussed to influence the emission energy and intensity of such heterostructures.

- First, exciton localization induced by compositional fluctuations was observed in similar samples.^[160,203,224] Sharp lines in low-temperature PL at excitation energy-independent positions are a signature of exciton localization. In addition to the literature reports, this effect was recently observed by C. Hauswald on individual NWs from the sample used in Fig. 6.4 (data not shown). Spatially direct exciton recombination alone, however, would explain neither the low absolute intensity nor the cross-over between the observed PL energy and calculated transition energy for the highest In content seen in Fig. 6.8.
- Second, Lähnemann *et al.* saw that individual electron and hole localization in separate potential minima with varying distance plays a role for $\text{In}_x\text{Ga}_{1-x}\text{N}$ QWs in GaN NWs.^[224] Very recently, R. Leonelli and co-workers reported on room-temperature TRPL measurements on samples with a similar structure to the ones studied here.^[263] They found that the radiative decay approaches a power-law, i. e. $I(t) \propto t^{-k}$.^[264] This observation stands in contrast to the exponential decay known from excitonic recombination, and indicates that electrons and holes are independently trapped at potential fluctuations in the $\text{In}_x\text{Ga}_{1-x}\text{N}$ QWs.^[265] A spatial separation of electrons and holes implies a reduced oscillator strength, thus accounting for the low PL intensity. If this separation occurs mainly in the lateral direction which is not affected by the QCSE, the redshift could be reduced compared with the one-dimensional calculations in axial direction.
- Third, a three-dimensional numerical analysis from B. Witzigmann and co-workers indicates that axial $\text{In}_x\text{Ga}_{1-x}\text{N}/\text{GaN}$ NW heterostructures exhibit laterally inhomogeneous strain resulting in band bending and a lateral separation of electrons and holes.^[252]

Carrier separation could explain the low PL intensity. Moreover, numerical studies for axial GaN/(Al,Ga)N QWs in NWs demonstrate that both geometry and chemical composition significantly affect the location of the potential minima in the conduction and valence band leading to carrier localization.^[266,267] It can further be taken into account that the TEM images in Sec. 5.3.1 as well as those found in the literature^[53,170,203] indicate that the $\text{In}_x\text{Ga}_{1-x}\text{N}$ QWs are laterally embedded in a GaN shell in contrast to the structure assumed in Ref. 252. Thus, although the detailed findings of Ref. 252 on where electrons and holes are localized cannot be generalized, the inhomogeneous strain could possibly account for the cross-over between the results of the one-dimensional model and the observed PL. In conclusion, the experimental data shows a clear trend of emission energy with In incorporation, even though it is weaker than expected. This finding suggests that the interplay of several mechanisms for carrier localization determines the luminescence from NW based $\text{In}_x\text{Ga}_{1-x}\text{N}/\text{GaN}$ heterostructures.

6.4 Impact of composition on $\text{In}_x\text{Ga}_{1-x}\text{N}$ nanowire LEDs

Nanowire LED demonstrator devices were made with the axial $\text{In}_x\text{Ga}_{1-x}\text{N}/\text{GaN}$ heterostructure developed in this thesis. To this end, samples were grown with the full LED ‘recipe’ from Table 5.1 (p. 65). The active region was embedded in a Si-doped NW base and a Mg-doped top segment. With the intention to show the change in emission color observed in the last section, the growth temperature was varied in this LED series (series 28): the active region was grown at 603 °C and 619 °C. The as-grown NW ensemble was then planarized and contacted by the process developed in the doctoral thesis of Friederich Limbach.^[12] This method of integrating NWs into an LED device was sketched in Sec. 2.4.

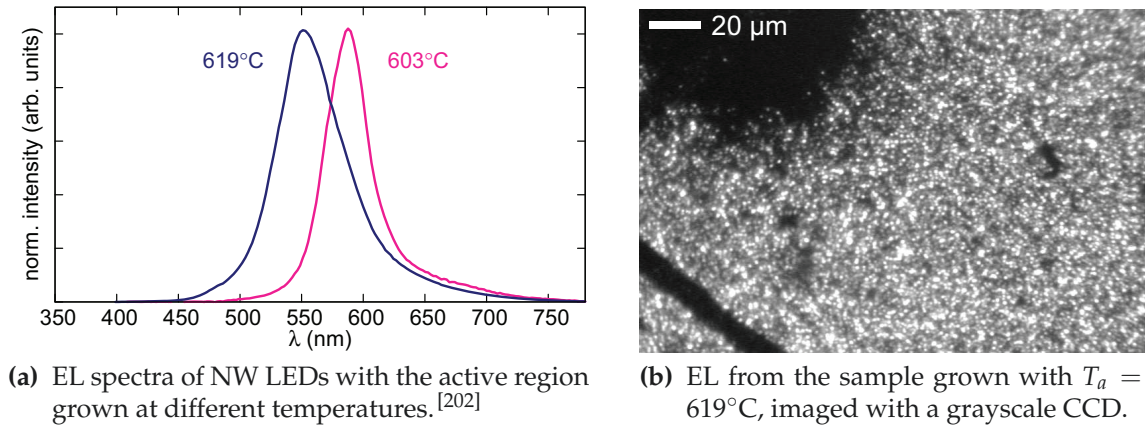


Figure 6.9: Electroluminescence acquired at 300 K from $\text{In}_x\text{Ga}_{1-x}\text{N}$ NW LEDs. The data was acquired by C. Hauswald.

The effect of the growth temperature T_a of the active region on the emission wavelength of the LEDs is shown in the electroluminescence spectra in Fig. 6.9(a). The sample with the active region grown at 619 °C shows an emission spectrum centered at 551 nm. The sample grown at 603 °C exhibits a longer dominant emission wavelength of 588 nm, which can be explained with the result of Sec. 5.6.3 by a higher In content of the QWs due to a lower loss of In during the growth.^[56] No emission from GaN or c-GaN is observed here, in contrast to the PL data in Figs. 6.3(a) and 6.7(a). Different from the electron-hole pair formation under excitation in a PL or CL experiment, electrons and holes are injected separately into the p-n junction. Recombination in the GaN base NW, as evinced by the CL line scan in Fig. 6.4(a), cannot occur in the EL experiments. Insertions of c-GaN, as detected by the same CL linescan close to the active region, are either not present at the p-n junction, or do not trap electrons or holes as efficiently as do the $\text{In}_x\text{Ga}_{1-x}\text{N}$ QWs. A difference in intensity of the emission from QWs with different In content, as in the PL spectra in Fig. 6.7 cannot be seen in the EL spectra, because the intensities are normalized here. Because of the fluctuating NW geometry and variations in the integration process, the transparency of the contact, the conductance of the samples and hence the carrier density in the MQWs, the EL intensity cannot be compared quantitatively. An image of the EL is shown in Fig. 6.9(b) for the sample grown at 619 °C. The intensity distribution is spotty, as was observed in PL microscopy in an undoped as-grown sample in Fig. 6.5. In the EL image, different intensities of the luminescing centers can be attributed to the differences in electrical conductivity of the contact and the NW, in addition to the already

significant fluctuation inherent to the MQW structure.^[57]

The wavelength of electroluminescence from the $\text{In}_x\text{Ga}_{1-x}\text{N}/\text{GaN}$ NW LEDs demonstrated here depends on the In content of the QWs, which is governed by the source fluxes and the growth temperature T_a of the active region. The present thesis has shown quantitatively both the composition-dependence on T_a (in Sec. 5.6.3), and the dependence of the optical transition energy on x (in Sec. 6.3.3). The central objective of the thesis, the control of the emission wavelength of GaN-based NW LEDs, is thus achieved.

6.5 Strain engineering in nanowire heterostructures

So far, the relaxation of lattice-mismatch strain in NW heterostructures has been relevant for the characterization of axial $\text{In}_x\text{Ga}_{1-x}\text{N}$ QWs intended as an LED active region. Strain influences many application-relevant properties of semiconductors, and it is interesting to exploit the analysis in Sec. 4.3 for deliberate strain control. In NW superlattices composed of two lattice-mismatched crystals, the axial thickness ratio of the two materials defines the strain distribution, with the thicker component being closer to relaxation and the thinner component being closer to the strain state of a pseudomorphic film. This effect has in principle been shown for NWs etched from planar heterostructures,^[210,211] but the strain was not quantified and systematically varied in these works. An advantage of bottom-up grown NWs over planar films is that misfit dislocations are less likely to occur. Thus, the heterointerface can be assumed coherent, and a detailed analysis of the strain distribution is possible. As was laid out before, the average in-plane strain of the segments of axial NW superlattices is given by Eq. (4.2) (repeated here):

$$\varepsilon_{xx} = \frac{d_{\text{barrier}}}{d_{\text{SL}}} \frac{a_1 - a_2}{a_2}$$

This approximation is valid under the two conditions that the total height of the superlattice stack is at least equal to the NW diameter, and that the NW is thick enough. It was shown in Fig. 4.6 that the relaxation deviates from the approximation if these conditions are not met, but remains linear with $d_{\text{barrier}}/d_{\text{SL}}$ for a wider range of parameters. The Poisson effect determines the out-of-plane strain, as given by Eq. (4.1) (repeated here):

$$\varepsilon_{zz} = -\frac{2C_{13}}{C_{33}}\varepsilon_{xx} = -\frac{2\nu}{1-\nu}\varepsilon_{xx}.$$

Figure 6.10 illustrates the principle of strain engineering. The out-of-plane strain ε_{zz} is calculated analytically with the formalism from Kaganer and Belov,^[174] taking into account the non-uniform and anisotropic strain distribution in the NW heterostructure. ε_{zz} is plotted vs. the position z along the NW axis. The superlattice is composed of two materials, the ‘barrier’ and the ‘well’ (QWs) material, with an arbitrary lattice mismatch of 40 % for the purpose of illustration. The QWs are under compressive (negative) in-plane strain and tensile (positive) out-of-plane strain. The NW diameter is ten times the QW thickness. The elastic constants are those of GaN, with the C -direction along the z -axis. Two situations are plotted, where $d_{\text{barrier}}/d_{\text{well}} = 3/4$ (blue) and $1/2$ (red), respectively. It can be seen that, on average over the QWs, ε_{zz} scales almost linearly with this ratio, as predicted by Eq. (4.2).

The purpose of this section is to demonstrate the applicability of the strain engineering principle to bottom-up grown GaN NWs with $\text{In}_x\text{Ga}_{1-x}\text{N}/\text{GaN}$ superlattices. Series of

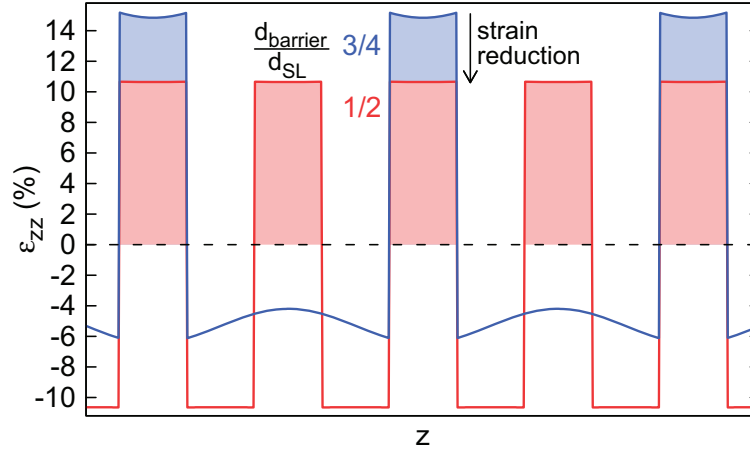


Figure 6.10: Principle of strain engineering in an axial NW superlattice. ε_{zz} is calculated in the center of the NW, $r = 0$, with the formalism of Ref. 174, and plotted vs. the position z along the NW axis. The NW diameter is ten times the QW thickness. The relaxed lattice constant of the QWs is 40% larger than that of the barrier material. The strain in the QWs (shaded area) is designed by the choice of the barrier thickness: two situations are plotted, where $d_{\text{barrier}}/d_{\text{well}} = 3/4$ (blue) and $1/2$ (red), respectively. It can be seen that ε_{zz} scales linearly with this ratio. The calculation was performed by V. M. Kaganer.

samples were grown, which contain identical $\text{In}_x\text{Ga}_{1-x}\text{N}$ QW segments. Their strain state was defined by choosing the GaN barrier thickness. The results of this section are being prepared for publication in Ref. 173. German and international patent applications were submitted for strain-engineered NW heterostructures in bottom-up grown NWs according to the principles shown here.^[268]

6.5.1 Evidence for strain relaxation in $\text{In}_x\text{Ga}_{1-x}\text{N}/\text{GaN}$ nanowires from resonant Raman spectroscopy

As introduced in Sec. 4.4, Raman spectroscopy is a non-invasive tool to measure strain in nitrides. It has already been proven useful in the analysis of strain relaxation in NW heterostructures.^[177,210,269,270] Resonant Raman spectroscopy allows selective probing of the $\text{In}_x\text{Ga}_{1-x}\text{N}$ QWs. The interpretation of Raman spectra in $\text{In}_x\text{Ga}_{1-x}\text{N}/\text{GaN}$ NWs has to take into account that the QWs are subject to non-uniform strain, and fluctuations in composition and in geometry. These fluctuations, which lead to broadening of the phonon line, were quantified in Sec. 5.5.3. It was shown that the resonant Raman spectra can satisfactorily be simulated with a MC algorithm, taking the exact strain distribution into account, or with an analytical evaluation of Eq. (4.18).

In the following, the effectiveness of strain engineering will be proven by extracting the strain from resonant Raman spectra. This information cannot be obtained from x-ray diffraction profiles. The characterization by XRD in Ch. 5 is based on the diffraction peak positions, and derives only the average out-of-plane strain in the entire MQW stack, and the period of the superlattice, relying *a priori* on full lateral relaxation of the heterostructure. As shown Sec. 4.2, the statistical fluctuations in the NW ensembles prohibit the extraction of the QW parameters with high precision from the simulation of XRD profiles. The strain inside the QWs is assumed here as constant, and is obtained from the

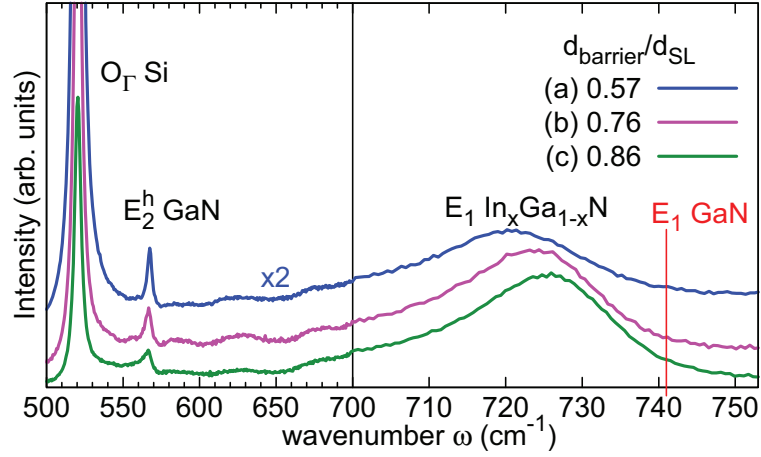


Figure 6.11: Resonant Raman spectra for three $\text{In}_x\text{Ga}_{1-x}\text{N}/\text{GaN}$ NW samples with different degrees of relaxation but constant x [samples (a) to (c) from series 18]. $d_{\text{barrier}}/d_{\text{SL}}$ quantifies the strain relative to the pseudomorphic (fully strained) case. The $E_1 \text{In}_x\text{Ga}_{1-x}\text{N}$ phonon mode shifts to higher frequencies with increasing strain. For comparison, the $E_1(\text{LO})$ frequency of fully relaxed GaN is indicated at 741 cm^{-1} . The ω -scale is enlarged above 700 cm^{-1} for clarity of the shift in E_1 .

simulation of the Raman spectra with the analytical integration of Eq. (4.18). The $E_1(\text{LO})$ phonon lineshape of the $\text{In}_x\text{Ga}_{1-x}\text{N}$ QWs depends on many parameters, and in order to obtain the strain reliably as a fit parameter in the simulation, very well characterized samples are required. The parameters which must be known are x , d_{well} , d_{barrier} , σ_d , σ_x , as well as the distribution of NW diameters. Of course, a series of samples is desirable with a systematic variation in strain of the QWs. These requirements are fulfilled by the samples of series 18 and 27. In both series, d_{barrier} is varied from sample to sample, and they are therefore expected to exhibit the strain dependence drawn in the illustration of the principle in Fig. 6.10. The QW composition and the segment spacings were determined by x-ray diffraction, and the parameters were summarized in Table 5.4. The alloy fluctuation $\sigma_x = 0.2x$ was obtained from the simulation of Raman data in Sec. 5.5.3.

Raman spectra of the $\text{In}_x\text{Ga}_{1-x}\text{N}/\text{GaN}$ NW samples from series 18 are shown in figure 6.11. The spectra were collected by resonant excitation with a photon energy of 3.0 eV in order to selectively excite the $\text{In}_x\text{Ga}_{1-x}\text{N}$ QWs. The Γ -point optical phonon of the Si substrate is visible at 520.5 cm^{-1} , the E_2^h phonon of GaN at 567 cm^{-1} and the $\text{In}_x\text{Ga}_{1-x}\text{N}$ $E_1(\text{LO})$ phonon of the QWs between 720 cm^{-1} and 725 cm^{-1} . The $E_1(\text{LO})$ phonon frequency for relaxed GaN is 741 cm^{-1} and is marked in Fig. 6.11. Due to the In content in the quantum wells, the experimental $E_1(\text{LO})$ phonon frequencies from all samples are shifted to lower wavenumbers. Since the three samples differ only in the strain of the QW, the difference in the E_1 peak positions reflects the strain dependence of the phonon frequency.^[269] In a simple picture, for d_{barrier} approaching the superlattice period d_{SL} , the QWs are subject to pseudomorphic strain as if grown on a GaN film. If, on the other hand, the QWs take up most of the superlattice period, i.e. $d_{\text{barrier}}/d_{\text{SL}} \ll 1$, the QWs relax completely. The amount of relaxation expected in realistic scenarios was shown in Fig. 4.6. The redshift of the $E_1(\text{LO})$ phonon in $\text{In}_x\text{Ga}_{1-x}\text{N}/\text{GaN}$ NW samples with equal x confirms the relaxation qualitatively. To be more precise, Table 5.4 showed that x increases slightly from 28 % in sample (a) to 31 % in sample (c), corresponding to a red-

shift of the phonon frequency $\Delta\omega_0(x) = -4.47 \text{ cm}^{-1}$ in fully relaxed material according to Eq. (4.15). Figure 6.11 shows clearly the opposite. The phonon peak frequencies increase from sample (a) to sample (c). This blueshift shift can only be caused by increasing strain. For samples of identical composition, the strain could simply be estimated from Eq. (4.17): $K_{\perp} = \Delta\omega/\varepsilon_{xx}$. Better precision is obtained in the following from simulations of the resonant Raman spectra.

6.5.2 Experimentally obtained relaxation in strain-engineered nanowire heterostructures

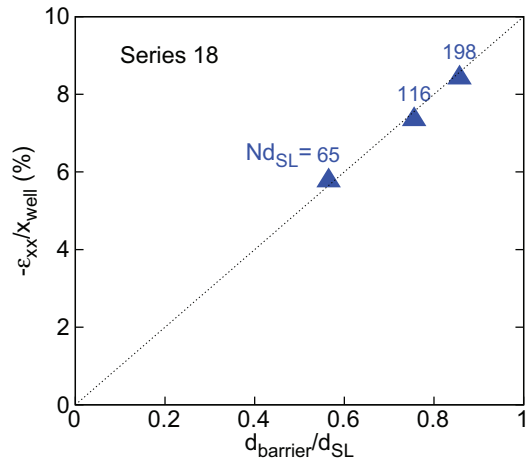
The experimental Raman spectra were simulated with the parameters from the previous characterization, and ε_{xx} was obtained as a fit parameter. The maximum strain, i. e. without relaxation, is of course given by the case of pseudomorphic growth of a planar film. The strain in NW segments can only be lower than the fully strained value, which is proportional to the composition x . In order to show the effectiveness of strain relaxation in the NW superlattices, the simulation results are plotted in Fig. 6.12 as $-\varepsilon_{xx}/x_{\text{well}}$, the strain relative to the composition. For the materials studied here, the maximum value ε_{max} on this scale is 10 %, corresponding to InN grown on a GaN bulk substrate. The lateral relaxation in NWs will reduce the ‘relative strain’, compared to the composition. Also shown in Fig. 6.12 are SEM plan view images of the first NW sample from each series [sample (a)], comparing the obtained NW diameter with the MQW stack height. A direct linear dependence of $-\varepsilon_{xx}/x_{\text{well}}$ on $d_{\text{barrier}}/d_{\text{SL}}$, as shown by the dashed line, is expected according to Eq. (4.2), if the MQW height is at least equal to the NW diameter. The respective diameters are symbolized in Figs. 6.12(b) and (d) as white circular areas.

Figure 6.12(a) shows the relative strain of the samples in series 18, with ε_{xx} obtained from the simulation of the Raman spectra. In the first sample [sample (a)], the GaN barrier constituted 57 % of the SL period, and the strain obtained from the Raman spectrum is about $0.6 \varepsilon_{\text{max}}$. The data from this series fits the constant strain approximation remarkably well, confirming for the first time the two fundamental concepts in this section:

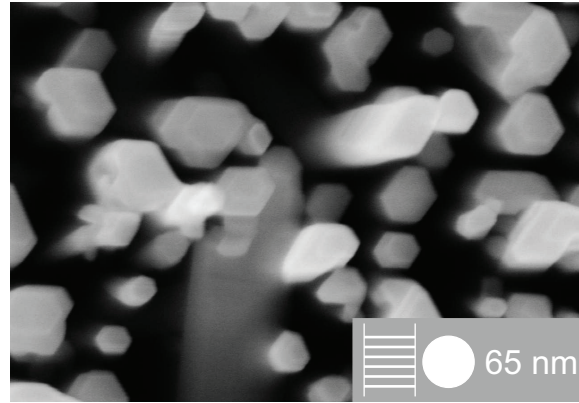
- The effectiveness of strain engineering in NW superlattice growth is confirmed.
- Raman spectroscopy is established as a tool to measure the strain in $\text{In}_x\text{Ga}_{1-x}\text{N}$ QWs.

Comparing the NWs in the plan view SEM image in Fig. 6.12(b) to the circular area indicating $Nd_{\text{SL}} = 65 \text{ nm}$, it is seen that the NWs vary in diameter, and this value is exceeded only by a few individual NWs, while most are thinner than 65 nm. The relative strain in Fig. 6.12(a), obtained from the Raman spectra, agrees with the approximation of full lateral relaxation, which does not take into account any specific diameter distribution. This agreement indicates that on average over the ensemble, the criterion for the lateral relaxation is met. Interestingly, Fig. 5.13 had shown that, due to radial growth in the active region at low temperature, the consecutive samples from series 18 exhibit increasing diameters. Recalling from Fig. 4.6(b) that thin NW heterostructures deviate from the linear approximation on the highly strained side, this widening of diameter contributes to the good agreement of the whole series of samples with the linear relaxation approximation.

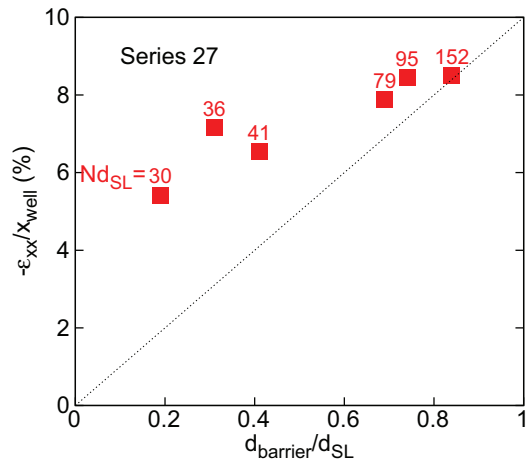
The same analysis of resonant Raman spectra was carried out for a second series of samples, equally well characterized by x-ray diffraction (series 27). In the second series, the barrier height was reduced to less than the QW height, further decreasing $d_{\text{barrier}}/d_{\text{SL}}$, and even more relaxation was expected than in the first series. Experimental Raman



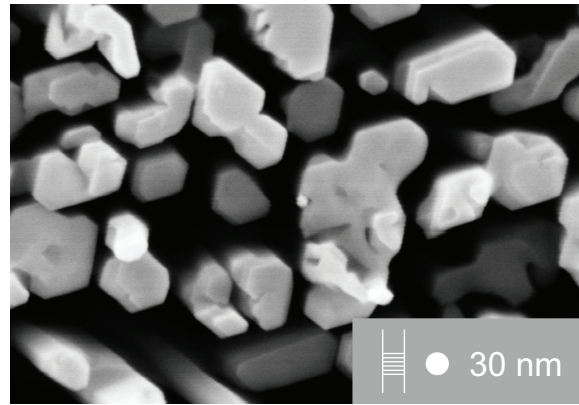
(a) Relative strain in series 18. The labels indicate the MQW stack height in nm.



(b) SEM plan view of the first sample from series 18. The MQW stack height is indicated with a circular area of corresponding diameter.



(c) Relative strain in series 27.



(d) SEM plan view of the first sample from series 27.

Figure 6.12: Relative strain of $\text{In}_x\text{Ga}_{1-x}\text{N}/\text{GaN}$ NW samples [Subfigs. (a) and (c)]. The sample structure was characterized by x-ray diffraction, and the strain was obtained as a fit parameter from simulations of the resonant Raman spectra. The simulations were carried out by M. Ramsteiner. Plan view SEM images in the same scale in (b) and (d) compare the NW diameters to the MQW stack height. The SEM data was acquired by A.-K. Bluhm.

spectra from this series of samples were depicted above in Fig. 6.2(a). The relative strain deduced from the resonant Raman spectra of this second series is shown in Fig. 6.12(c). Considering all six samples, the trend of increasing strain with increasing barrier height is observed, in agreement with the principle of strain engineering employed here. The data is seen, however, to deviate from the approximation of complete lateral relaxation of the superlattice. The likely reasons for such a deviation was discussed in Sec. 4.3.2. One of the requirements for the lateral relaxation approximation is that the total MQW stack height is at least equal to the NW diameter. Figure 4.6(a) revealed the effect of a violation of this requirement: If Nd_{SL} is too small, strain relaxation is obtained linearly

with $d_{\text{barrier}}/d_{\text{SL}}$, but the minimum strain predicted by the approximation is not achieved. In the second series studied here, Nd_{SL} is only about 30 nm in the first sample [sample (a)].^b The NW diameter distribution in this sample is seen in the plan view SEM image in Fig. 6.12(d) [in the same scale as Fig. 6.12(d)]. The white circular area has a diameter of 30 nm, indicating the NW size which would fulfill the condition for the approximation. Evidently, most of the NWs are much thicker, and therefore the lateral relaxation of the MQW segment is incomplete in this sample.

The comparison of the relaxation in the two series of samples discussed here is a direct proof of the validity of the design criterion for full lateral relaxation, which allows to use Eq. (4.2). The strain analysis in these self-induced NW heterostructures is complicated due to statistical fluctuations in structure, resonance effects in Raman spectroscopy, and uncertainties about elastic constants and phonon deformation potentials. The design criterion for strain engineering had so far been shown only numerically (in Sec. 4.3.2). In view of the multiple complications in analysis, the experimental proof of this concept is very valuable.

6.6 Conclusion

The guideline in the design of the experiments was the development of the active region of a GaN NW LED. The NW was axially structured to mimic the main features of a planar $\text{In}_x\text{Ga}_{1-x}\text{N}/\text{GaN}$ MQW. A systematic variation and analysis was undertaken of the parameters known to govern light emission from planar MQWs: (i) the $\text{In}_x\text{Ga}_{1-x}\text{N}$ QW composition, which defines the fundamental bandgap, (ii) the QW thickness, determining the quantum confinement, and (iii) the strain in QWs, which controls the piezoelectric field and hence the QCSE.

The effects of varying these parameters were summarized in Sec. 6.2. To an extent, the mechanisms known from planar $\text{In}_x\text{Ga}_{1-x}\text{N}$ QWs were found in the NW heterostructures. The luminescence experiments showed a clear trend of the emission energy with the In content of the QWs, in line with the expected change of the fundamental bandgap. Also, as was seen in Fig. 6.1(b), the emission energy is increased if the QW thickness is reduced under otherwise identical conditions. This is consistent with the expected effect of quantum confinement.

Despite these indications of a luminescence mechanism comparable to planar QWs, the $\text{In}_x\text{Ga}_{1-x}\text{N}$ QWs in the NWs studied here were found to behave fundamentally different. Most notably, the luminescence intensity was found to *decrease* with decreasing In content. No $\text{In}_x\text{Ga}_{1-x}\text{N}$ emission was detected in the blue spectral range, even though the QW composition and thickness realized in some samples would lead to blue emission in planar QWs. Also contrary to expectation is that the luminescence intensity *decreases* with reduced QW thickness, and hence reduced QCSE [see Fig. 6.1(b)]. Upon closer inspection, the correlation of the luminescence energy with a variation in the QW composition does not meet the expectations based on planar layers. Self-consistent Schrödinger-Poisson calculations performed with the experimental parameters predicted a much wider range of the emission energy as a function of the QW composition. Three types of carrier localizations were suggested in Sec. 6.3.4 to control the optical transitions in the $\text{In}_x\text{Ga}_{1-x}\text{N}$ QWs: (i) exciton localization induced by compositional fluctuations, (ii) individual electron and hole localization in separate potential minima, and (iii) lateral separation of

^bNote that XRD satellite peaks cannot be detected in sample (a) of series 27, and d_{SL} is interpolated from samples (d), (e), and (f). See Fig. 5.10(b).

electrons and holes by band bending as a result from inhomogeneous strain. An indication that the non-uniformity of the strain influences the luminescence in a way not understood so far is the seemingly uncorrelated shift of PL peak energy with strain in Fig. 6.2(b). Judging the consequences of the localization mechanisms requires detailed three-dimensional calculations of the electronic structure and the possible radiative transitions. Such calculations have only been initiated.

Working GaN nanowire LED devices with the active region developed here were processed by repeating the steps described in the doctoral thesis of F. Limbach,^[12] and this is taken as proof that such devices can be processed predictably and reproducibly. The homogeneity and the intensity of the light emission from these laboratory samples of NW LEDs are not comparable to developed LED products with planar active regions. Some limiting factors can be addressed technologically in a straightforward way. For example, the statistical fluctuations in self-induced growth may be controlled in selective area growth,^[271] and planarized NW ensembles may be contacted with the efficient processes developed for modern industrial LEDs.^[60] A more fundamental question is the suitability of axial NW MQW structures for the active region of LED devices. Although this topic has been discussed in recent years,^[252] no conclusion has emerged. The analysis in this chapter is the first published attempt at understanding quantitatively the axial NW MQW emission from series of samples with systematic variations in structure. The open question remains, which modifications of the NW MQW structure can enhance the luminescence intensity.

One of the features that sets apart $\text{In}_x\text{Ga}_{1-x}\text{N}/\text{GaN}$ NWs from planar films, next to defect-free growth on foreign substrates and large surface area, is the elastic relaxation of mismatch strain in the heterostructure. Practical examples were given in this chapter for the deliberate tuning of the strain in NW segments between the opposite cases of full relaxation and pseudomorphic films, without introducing plastic defects. For the first time, this strain-engineering technique could be rigorously shown here. The principle applies to heterostructures in other materials as well, for example CdSe/CdS .^[270]

In a more general sense, this chapter has demonstrated that the average strain and the luminescence wavelength of self-assembled $\text{In}_x\text{Ga}_{1-x}\text{N}$ nanostructures can be systematically tuned. A straightforward design rule was proven for engineering the average strain in mismatched axial NW heterostructures. The observed correlation of the luminescence wavelength with the NW structure indicates that the heterostructure growth is well controlled. Therefore, if gradual parameter changes should be theoretically predicted in the future to make axial $\text{In}_x\text{Ga}_{1-x}\text{N}/\text{GaN}$ NW heterostructures fit for any application, the self-assembled synthesis described here is readily applied.

7 Conclusions and Outlook

GaN nanowires (NWs) with axial $\text{In}_x\text{Ga}_{1-x}\text{N}$ /GaN superlattices were studied in this thesis as part of the development of a GaN-based NW LED at *Paul-Drude-Institut für Festkörperelektronik* (PDI). Among the expected technological benefits were the growth of GaN on a lattice-mismatched substrate, the defect-free bottom-up growth of the heterostructure and the reduction of the piezoelectric field compared to $\text{In}_x\text{Ga}_{1-x}\text{N}$ quantum wells in planar films. The work focused first on the fundamental mechanisms governing the NW crystal growth by molecular beam epitaxy, and then on the elastic and optical properties of the heterostructures as a function of the growth parameters. In one sentence, *a modeling of the physical growth processes was achieved that allows control of the emission wavelength of a GaN-based nanowire LED device.*

An LED in the layout chosen here has one of the simplest structures of any semiconductor device, and only the active region is studied here. Nevertheless, this thesis required research in four fields: (i) the nucleation and growth of GaN NWs, (ii) strain analysis, (iii) growth of $\text{In}_x\text{Ga}_{1-x}\text{N}$, and (iv) the elastic and optical properties of $\text{In}_x\text{Ga}_{1-x}\text{N}$ /GaN QWs. The separation of these topics is evident, for example, from the disjunct bodies of literature. Steps were made in all of these fields, and it seems appropriate to give them equal weight in the conclusion, to the benefit of a reader with a specific interest.

Ti as an alternative growth substrate for GaN nanowires

New results on GaN NW growth on a metal film by molecular beam epitaxy were reported in Ch. 3:

- Self-induced GaN NWs of high quality grow on α -Ti films with a strong epitaxial relation. As a consequence, for subsequent processing of a NW LED, the Ti film must exhibit a preferred (0001) orientation.
- The interface between the Ti metal film and the GaN crystal is likely mediated by δ -TiN(111) or TiO(111).

Suggested reasons for a low NW nucleation density on Ti, when compared to Si, include a higher diffusion length of Ga adatoms, or preferred Ga-polar growth, giving rise to N-polar NW growth only in small random domains. Possibly, N-polar NW growth occurs on surface areas containing TiO. Metal films can be deposited easily on a variety of carrier materials, and successful synthesis of GaN with high crystal quality on metal films can pave the way to new device designs. Especially GaN-based NW LEDs can be directly implemented, once a suitable carrier material for the Ti film is found.

Strain analysis in nanowire heterostructures

The development of quantitative growth models and the control of NW heterostructure device properties require reliable methods for the structural characterization. Large fluctuations are typical for ensembles of self-induced GaN NWs, and quantitative statistical

information is required that cannot be obtained from microscopy. Due to the NW geometry, however, several established semiconductor characterization tools fail. At the start of work on this thesis, important measurements were unavailable: that of the axial $\text{In}_x\text{Ga}_{1-x}\text{N}$ QW composition and compositional uniformity, QW thickness and strain, the thickness of the GaN barrier, as well as the fluctuations in these parameters. These characterization requirements inspired the statistical interpretation of laboratory x-ray diffraction (XRD) profiles and resonant Raman spectra. Vladimir M. Kaganer and Manfred Ramsteiner contributed substantially to this aspect of the work, shown in Ch. 4:

- The XRD profiles of axial $\text{In}_x\text{Ga}_{1-x}\text{N}/\text{GaN}$ superlattices in NWs are low in contrast, due to statistical fluctuations. Simulations in the kinematic approximation can take these fluctuations into account and provide structural parameters.
- The strain distribution in elastically relaxed NW superlattices is inherently non-uniform. An analytic expression for the strain at any point of a segmented cylinder was developed and published by V. M. Kaganer and A. Yu. Belov. From the detailed calculation, a criterion for full lateral relaxation can be deduced: the superlattice stack height must be larger than the NW diameter.
- The average strain in the $\text{In}_x\text{Ga}_{1-x}\text{N}$ QWs decreases linearly with the ratio of the GaN spacer thickness to the superlattice period. Even full relaxation is linearly approached if the criterion for full lateral relaxation is met.
- With regard to the average strain in the whole superlattice, the Poisson effect vanishes if the criterion for full relaxation is met. This is important for the interpretation of the zeroth order superlattice peak position in XRD profiles.
- The exact strain distribution can be used to simulate the broadening of the $E_1(\text{LO})$ phonon line in resonant Raman spectra of the $\text{In}_x\text{Ga}_{1-x}\text{N}$ QWs. Compared to realistic compositional fluctuations, the non-uniformity in strain contributes negligibly to the broadening, and resonant Raman spectra can be simulated by approximating the strain inside the QWs as constant.

For the experimental XRD profiles shown here, the precision of the structural characterization by the parameters of the kinematic simulation is low. Future work could extend the kinematic simulation of the XRD profiles to compositional fluctuations.

Growth of $\text{In}_x\text{Ga}_{1-x}\text{N}/\text{GaN}$ nanowire heterostructures

Growth models for planar $\text{In}_x\text{Ga}_{1-x}\text{N}$ films by MBE had been well developed, but the growth of NWs is more complex. In fact, no quantitative models for any ternary semiconductor NW growth existed at the time of beginning this work. In series of experiments, the growth parameters for $\text{In}_x\text{Ga}_{1-x}\text{N}/\text{GaN}$ NWs were varied one at a time, and the growth was monitored *in situ* by line-of-sight QMS. The new findings were laid out in Ch. 5:

- Increasing the metal flux induces a widening of the $\text{In}_x\text{Ga}_{1-x}\text{N}$ NW diameter by radial growth. At a typical $\text{In}_x\text{Ga}_{1-x}\text{N}$ growth temperature of 600°C the pivot value is about $V/\text{III} = 3$ during $\text{In}_x\text{Ga}_{1-x}\text{N}$ growth. Below this value, the growth is effectively metal-rich.

- A variation of the GaN barrier growth time between samples leads to different periodicities in the superlattices, which are then reflected by different satellite peak spacings in the XRD profiles. In view of the low contrast, only this experimental proof validated the interpretation of the XRD interpretation.
- Also from the variation of the GaN barrier growth time, the change in the superlattice period delivers the axial growth rate of GaN in the active region, and the average QW thickness. For the superlattices in self-induced NWs, this method delivers better precision than the simulation of the x-ray diffraction.
- In acts as a surfactant and enhances the diffusion of Ga atoms on the NW sidewalls. The axial growth rate of GaN in the active region is lower by a factor of two than that of $\text{In}_x\text{Ga}_{1-x}\text{N}$ for the same total metal flux. In the absence of In, Ga diffusion on the sidewalls is reduced at the growth temperature of the active region, and radial *M*-plane growth occurs.
- The incorporation of Ga atoms on the NW sidewalls during the growth of the active region supports and explains the indication from individual TEM images, that the $\text{In}_x\text{Ga}_{1-x}\text{N}$ insertions in the NWs are surrounded by a thin GaN shell. In particular, the growth of an $\text{In}_x\text{Ga}_{1-x}\text{N}$ island on the GaN NW top facets need not be postulated to explain this phenomenon.
- Resonant Raman spectroscopy was validated as a way to determine the average strain and composition in $\text{In}_x\text{Ga}_{1-x}\text{N}$ independently from XRD. Also, the compositional fluctuations were quantified.
- *In-situ* observation of In desorption during the growth allows to quantify the resulting In incorporation. The established model of planar $\text{In}_x\text{Ga}_{1-x}\text{N}$ growth, according to which the In incorporation is limited by thermally activated desorption, could be successfully applied to the growth of NWs. An effective activation energy was given to describe the net effect of the diffusion and desorption processes.

These findings allow the synthesis of axial $\text{In}_x\text{Ga}_{1-x}\text{N}/\text{GaN}$ NW heterostructures by MBE with controlled segment lengths and alloy compositions. The $\text{In}_x\text{Ga}_{1-x}\text{N}$ growth model developed here is based on statistical data. Elastic effects which may lead to a non-uniform distribution of In are not taken into account, because the characterization methods employed here probe the entire $\text{In}_x\text{Ga}_{1-x}\text{N}$ NW ensemble. Future work may improve the growth model by finding the individual activation energies for the processes of decomposition, desorption and reincorporation.

Optical and elastic properties of $\text{In}_x\text{Ga}_{1-x}\text{N}/\text{GaN}$ nanowire heterostructures

A significant drawback in earlier studies on $\text{In}_x\text{Ga}_{1-x}\text{N}/\text{GaN}$ NW heterostructures was the lack of reliable structural characterization and systematic control of individual parameters during the growth. With these methodological gaps being filled, several important findings were possible in Ch. 6. The first ones are specific to $\text{In}_x\text{Ga}_{1-x}\text{N}/\text{GaN}$ NW LED active regions:

- In some aspects, the luminescence energy depends on the QW composition and thickness as would be expected from a planar $\text{In}_x\text{Ga}_{1-x}\text{N}/\text{GaN}$ QW. *Ceteris paribus*, the emission energy increases both with increasing In content and with decreasing QW thickness. Contrary to the expected behavior, the luminous intensity was

7 Conclusions and Outlook

found to decrease with decreasing In content and with reduced QW thickness. No samples could be produced with dominant $\text{In}_x\text{Ga}_{1-x}\text{N}$ emission in the blue spectral range.

- Self-consistent Schrödinger-Poisson calculations performed with the experimental QW parameters, but in the approximation of a planar heterostructure, predicted a much wider range of the emission energy as a function of the QW composition.
- Three types of localizations were suggested as a cause of the deviation between the $\text{In}_x\text{Ga}_{1-x}\text{N}$ QW emission in axially structured NWs and in planar films: (i) exciton localization induced by compositional fluctuations, (ii) individual electron and hole localization in separate potential minima, and (iii) lateral separation of electrons and holes by band bending as a result from inhomogeneous strain.
- Nanowire LED demonstrator devices were fabricated. The electroluminescence spectra were dominated by the $\text{In}_x\text{Ga}_{1-x}\text{N}$ emission, and a variation of the emission wavelength was obtained by changing the growth temperature of the active region.

The findings on strain relaxation in axial NW heterostructures are applicable beyond the $\text{In}_x\text{Ga}_{1-x}\text{N}/\text{GaN}$ system in which they were shown here:

- The elastic relaxation of mismatch strain in NW heterostructures can be employed for strain engineering. A simple design rule was already derived from the numerical strain analysis to control the elastic relaxation by choosing the nanowire diameter and segment lengths.
- The average strain in $\text{In}_x\text{Ga}_{1-x}\text{N}$ QWs can be obtained as a fit parameter from simulations of the resonant Raman spectrum. NW heterostructure samples with a variation in the barrier thickness were used to prove the effectiveness of the strain engineering principle and to validate the boundary conditions for the design rules.

Working GaN nanowire LED devices can be processed predictably and reproducibly. Judging from the results of the present work, even the integration of a GaN nanowire LED device on a metal substrate seems practical. An unanswered fundamental question is the suitability of axial NW MQW structures for the active region of efficient LED devices. In this regard, the faint luminescence in the blue spectral range raises concern. Future research will have to model the optical transition mechanism in $\text{In}_x\text{Ga}_{1-x}\text{N}$ QWs in N-polar GaN NWs to answer this question. Examples of computational studies exist that have shown the spatial separation of carriers in axial NW heterostructures of III-nitride semiconductors. If it should be predicted that gradual modifications of the axial heterostructure geometry produce useful devices, the bottom-up synthesis can rely on the growth mechanisms given here.

The proposed strain engineering in bottom-up grown NW heterostructures is a method that can be used universally to tune crystal properties. In this work, the concept was proven with self-induced NWs possessing statistical fluctuations in diameter. One can imagine that strain definition will be all the more precise if the NW diameter is controlled, for example by selective areas growth. To name another example of extending this concept: it is equally applicable to nanowalls, introducing anisotropic in-plane strain, and creating a nanowire insertion that could carry current laterally.

A Sample list

The growth parameters for all samples used in this work are listed in Table A.1 on the following pages. Pyrometer readings are given for the growth temperature T_{base} of the GaN NW, and T_a of the active region.

Table A.1: List of $\text{In}_x\text{Ga}_{1-x}\text{N}/\text{GaN}$ NW samples used in this work. All samples were grown at PDI in MBE 8.
The samples are sorted after the variable parameter, or in the sequence in which they are used.

				base NW growth				active region growth						
				Φ_{N} ($\frac{\text{nm}}{\text{min}}$)	T_{base} ($^{\circ}\text{C}$)	t_{base} (min)	Φ_{Ga} ($\frac{\text{nm}}{\text{min}}$)	barrier			quantum well			main use in Figs.
sample	lab book date	structure	substrate					T_a ($^{\circ}\text{C}$)	t_{barrier} (min)	Φ_{Ga} ($\frac{\text{nm}}{\text{min}}$)	t_{well} (min)	Φ_{Ga} ($\frac{\text{nm}}{\text{min}}$)	Φ_{In} ($\frac{\text{nm}}{\text{min}}$)	
Series 11: variation of t_{well}														
M8923*	26.02.10	NW only	Si(111)	20	800	80	5.6							
M8934	12.03.10	NW + 4 QW	Si(111)	20	803	60	5.6	614	3.0	3.0	0.50	3.0	5.2	5.2,6.1(b)
M8937	22.03.10	NW + 4 QW	Si(111)	20	800	60	5.6	616	3.0	3.0	0.25	3.0	5.2	6.1(b)
M8938	23.03.10	NW + 4 QW	Si(111)	20	801	60	5.6	619	3.0	3.0	0.13	3.0	5.2	6.1(b)
M8944	26.03.10	NW + 4 QW	Si(111)	20	800	60	5.6	616	3.0	3.0	0.06	3.0	5.2	6.1(b)
Series 12: variation of T_a														
M8923 [†] *	26.02.10	NW only	Si(111)	20	800	80	5.6							
M8934 [†]	12.03.10	NW + 4 QW	Si(111)	20	803	60	5.6	614	3.0	3.0	0.5	3.0	5.2	
M8939	23.03.10	NW + 4 QW	Si(111)	20	800	60	5.6	636	3.0	3.0	0.5	3.0	5.2	5.3(a),5.6
M8942*	25.03.10	NW + 4 QW	Si(111)	20	798	60	5.6	655	3.0	3.0	0.5	3.0	5.2	
M8943*	26.03.10	NW + 4 QW	Si(111)	20	800	60	5.6	678	3.0	3.0	0.5	3.0	5.2	
Series 18: variation of t_{barrier}														
M8979	24.06.10	NW only	Si(111)	20	768	60	3.9							3.6
M8994	09.07.10	NW + 6 QW	Si(111)	20	770	60	3.9	583	1.58	4.0	0.9	0.8	1.7	5.11(a),5.13,5.19
M8995	12.07.10	NW + 6 QW	Si(111)	20	770	60	3.9	581	3.36	4.0	0.9	0.8	1.7	4.4,5.11(a),5.13

continued on next page

Table A.1 – continued from previous page

				base NW growth				active region growth						
				Φ_{N} ($\frac{\text{nm}}{\text{min}}$)	T_{base} ($^{\circ}\text{C}$)	t_{base} (min)	Φ_{Ga} ($\frac{\text{nm}}{\text{min}}$)	barrier			quantum well			main use in Figs.
sample	lab book date	structure	substrate					T_a ($^{\circ}\text{C}$)	t_{barrier} (min)	Φ_{Ga} ($\frac{\text{nm}}{\text{min}}$)	t_{well} (min)	Φ_{Ga} ($\frac{\text{nm}}{\text{min}}$)	Φ_{In} ($\frac{\text{nm}}{\text{min}}$)	
M8997	12.07.10	NW + 6 QW	Si(111)	20	771	60	3.9	582	6.88	4.0	0.9	0.8	1.7	5.7,5.11(a),5.13,6.3
Series 19: variation of T_a														
M81005	21.07.10	NW + 6 QW	Si(111)	13	770	60	3.9	583	3.36	2.8	0.9	0.7	1.6	5.15,5.18,6.1(a)
M81016	27.07.10	NW + 6 QW	AlN/Si(111)	13	829	60	3.4	585	3.36	2.8	0.9	0.7	1.6	4.4,5.5
M81011	26.07.10	NW + 6 QW	Si(111)	13	770	60	3.1	608	3.36	2.8	0.9	0.7	1.6	5.15,5.16,5.18,6.1(a)
M81017	27.07.10	NW + 6 QW	Si(111)	13	769	60	3.4	615	3.36	2.8	0.9	0.7	1.6	5.15,5.18,6.1(a)
M81013	26.07.10	NW + 6 QW	Si(111)	13	770	60	3.4	626	3.36	2.8	0.9	0.7	1.6	5.15,5.18,6.1(a)
M81014	27.07.10	NW + 6 QW	Si(111)	13	770	60	3.4	637	3.36	2.8	0.9	0.7	1.6	5.15,5.18,6.1(a)
M81015	27.07.10	NW + 6 QW	Si(111)	13	770	60	3.4	645	3.36	2.8	0.9	0.7	1.6	6.1(a)
M81023	30.07.10	NW + LT GaN	Si(111)	13	768	60	3.4	585		2.8				3.4(b),(c)
Series 23: variation of T_a , calibrated QMS														
M81096	17.01.11	NW + 6 QW	Si(111)	13	780	90	2.5	588	7.9	0.8	0.9	0.8	0.8	5.21,5.23
M81113	01.02.11	NW + 6 QW	Si(111)	13	779	90	2.5	602	7.9	0.8	0.9	0.8	0.8	4.2,5.21,5.23,6.5
M81089	10.01.11	NW + 6 QW	Si(111)	13	780	90	2.5	603	7.9	0.8	0.9	0.8	0.8	4.3,5.1,5.21,5.23
M81105	25.01.11	NW + 6 QW	Si(111)	13	782	90	2.5	625	7.9	0.8	0.9	0.8	0.8	5.21,5.23
M81095	14.01.11	NW + 6 QW	Si(111)	13	780	90	2.5	631	7.9	0.8	0.9	0.8	0.8	5.21,5.23

continued on next page

Table A.1 – continued from previous page

				base NW growth				active region growth						
lab book			substrate	Φ_{N} ($\frac{\text{nm}}{\text{min}}$)	T_{base} ($^{\circ}\text{C}$)	t_{base} (min)	Φ_{Ga} ($\frac{\text{nm}}{\text{min}}$)	T_a ($^{\circ}\text{C}$)	barrier		quantum well			main use in Figs.
sample	date	structure							t_{barrier} (min)	Φ_{Ga} ($\frac{\text{nm}}{\text{min}}$)	t_{well} (min)	Φ_{Ga} ($\frac{\text{nm}}{\text{min}}$)	Φ_{In} ($\frac{\text{nm}}{\text{min}}$)	
Series 27: variation of t_{barrier}														
M81257	12.07.11	NW + 6 QW	Si(111)	13	780	90	2.6	606	1.0	0.8	1.5	0.8	0.8	5.10(b),5.11(b)
M81263	21.07.11	NW + 6 QW	Si(111)	13	780	90	2.6	604	2.0	0.8	1.5	0.8	0.8	5.10(b),5.11(b),6.2
M81260	19.07.11	NW + 6 QW	Si(111)	13	780	90	2.6	608	3.0	0.8	1.5	0.8	0.8	5.10(b),5.11(b),6.2
M81262	21.07.11	NW + 6 QW	Si(111)	13	780	90	2.6	606	9.5	0.8	1.5	0.8	0.8	5.10(b),5.11(b),6.2
M81258	18.07.11	NW + 6 QW	Si(111)	13	778	90	2.6	606	12.8	0.8	1.5	0.8	0.8	5.10(b),5.11(b),6.2
M81261	20.07.11	NW + 6 QW	Si(111)	13	780	90	2.6	607	22.7	0.8	1.5	0.8	0.8	5.10(b),5.11(b),6.2
Series 28: variation of T_a in full LED structure														
M81275	23.08.11	full LED	Si(111)	13	781	90	2.6	603	7.9	0.8	0.9	0.8	0.8	6.9
M81274	22.08.11	full LED	Si(111)	13	781	90	2.6	619	7.9	0.8	0.9	0.8	0.8	6.9
Series 30: growth on Ti interlayer														
M81290*	16.12.11	NW	Si(111)	13	790	90	2.4							
M81295	22.12.11	NW	Ti/Al ₂ O ₃	13	760	90	2.4							3.11(a),3.12(a),3.14
M81321	27.01.12	NW + 6 QW	Ti/SiO _x /Si	13	760	90	2.4	620	8.0	0.5	2.0	0.5	0.8	3.11(b),3.12(b)
M81389	01.06.12	NW	Ti/silica glass	13	730	90	2.4							3.12(c)
individual samples														
M81002 ^S	19.07.10	RHEED 7 × 7	Si(111)											3.4(a)

continued on next page

Table A.1 – continued from previous page

				base NW growth				active region growth						
				Φ_{N} $(\frac{\text{nm}}{\text{min}})$	T_{base} $(^{\circ}\text{C})$	t_{base} (min)	Φ_{Ga} $(\frac{\text{nm}}{\text{min}})$	barrier			quantum well			main use in Figs.
sample	lab book date	structure	substrate					T_a $(^{\circ}\text{C})$	t_{barrier} (min)	Φ_{Ga} $(\frac{\text{nm}}{\text{min}})$	t_{well} (min)	Φ_{Ga} $(\frac{\text{nm}}{\text{min}})$	Φ_{In} $(\frac{\text{nm}}{\text{min}})$	
M81256	11.07.11	planar MQW	GaN/AlN/Al ₂ O ₃	6.6				590	3.6	2.2	0.8	2.2	1.8	4.3
M8957	16.04.10	NW + 4 QW	Si(111)	20	800	60	5.9	598	3.0	3.0	0.5	3.0	5.7	5.9
M81310	16.01.12	NW + 6 QW	Si(111)	13	780	90	1.5	605	8.0	0.5	2.0	0.5	0.8	6.4,6.6
M81325	10.02.12	full LED	Si(111)	13	780	90	1.5	605	8.0	0.5	2.0	0.5	0.8	5.8
M8872 ^{‡*}	19.05.09	NW + 2 QW	Si(111)	13	778	60	1.7	617	10.0	0.4	10.0	0.4	0.7	
MBE source calibration for series 11–19														
M8970	16.06.10	$\Phi_{\text{Ga},1}$	Si(111)											C.1
M8971 [§]	16.06.10	$\Phi_{\text{Ga},2}$	Si(111)											
M8980	24.06.10	Φ_{In}	SiC											
M8974 [¶]	18.06.10	Φ_{Al}	Si(111)											
M81066 [§]	24.11.10	$\Phi_{\text{N,Specs}}$	AlN/Si											
M8975	18.06.10	$\Phi_{\text{N,SVT}}$	Si(111)											

*For information only, data not shown in this work.

[†]Listed again for complete series overview.

[‡]Not a part of this thesis, listed only for comparison. Processed by M. Knelangen, luminescence reported in Refs. 170 and 224. T_a is estimated based on the temperature offset between thermocouple and pyrometer observed in this work [see Fig. 3.6(a)].

[§]Processed by T. Gotschke.

[¶]Processed by F. Limbach.

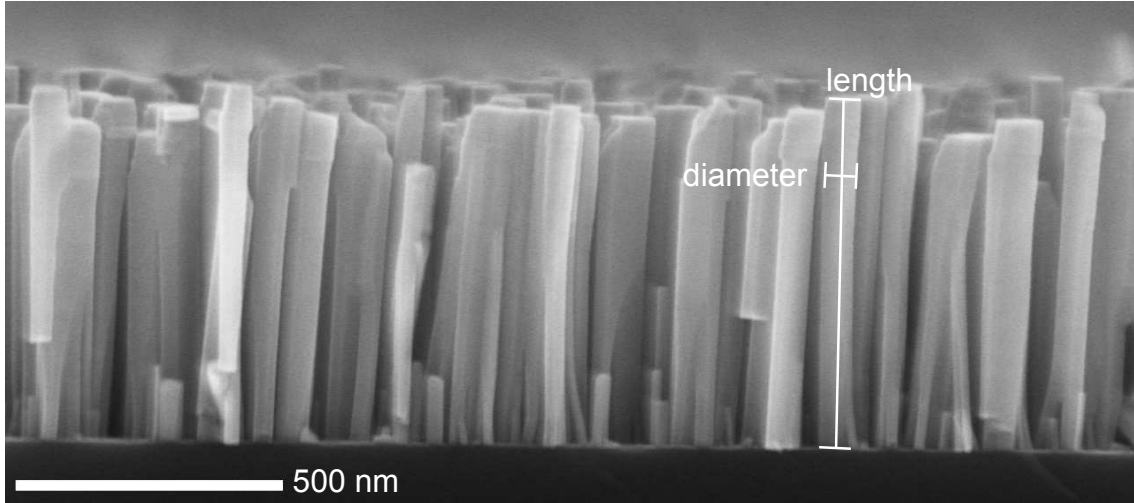
^{||}Processed by C. Chèze.

B Statistical fluctuation of self-induced GaN nanowire morphology

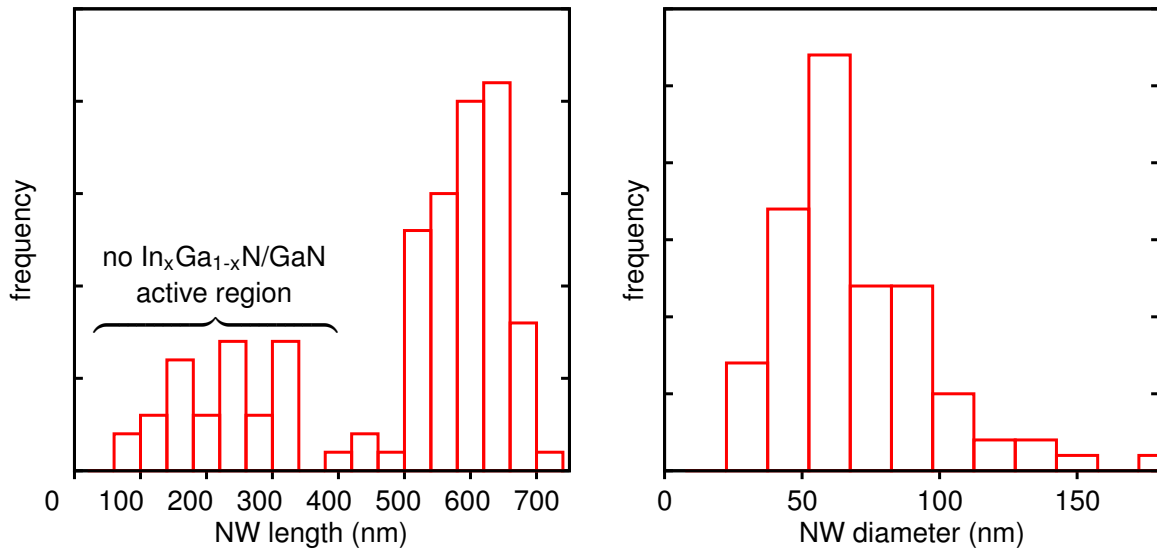
The length and diameter of self-induced GaN NWs fluctuates statistically. Length and diameter of individual NWs can both be measured in cross section scanning electron micrographs, as indicated in Fig. B.1(a). By comparison, assessment of the diameter in plan view SEM has proven difficult because of NW coalescence and terrace formation at the tip. The dimensions from 113 NWs were obtained by manual selection within the image processing software *ImageJ* 1.45s. The length distribution is shown in Fig. B.1(b). Sabelfeld *et al.* have recently proposed an explanation for the bimodal length distribution.^[125] NWs shorter than 365 nm are likely shadowed during $\text{In}_x\text{Ga}_{1-x}\text{N}$ growth and form no active region. This is confirmed by the CL cross-section in Fig. 6.4(b) which shows emission from the active region only from the top of the ensemble. The longer NWs are representative of the NW ensembles studied here. The diameter distribution is shown in Fig. B.1(c).

The crystal orientation of the silicon substrate is transmitted to the GaN NWs via a Si_xN_y interlayer. The interlayer is considered mostly amorphous even though it is preceded by the formation of $\beta\text{-Si}_3\text{N}_4$ and is able to transmit crystallographic information.^[85,102–104] The orientation of the GaN NWs is imperfect, with the GaN[0001] direction (C-direction) in the NW axis showing an out-of-plane tilt from the Si[111] substrate normal. This can be directly seen in Fig. B.2(a). The tilt can be assessed by x-ray diffraction.^[58] Rocking curves (ω -scans) of the symmetrical reflection GaN(00.2) are shown in Fig. B.2(b). An analyzer crystal was used, and it can be seen that the detector width is negligible, with a full width at half maximum (FWHM) of 0.2° . GaN NWs grown directly on Si(111) show a tilt of 3.2° FWHM. For comparison, a rocking curve is given from GaN NWs grown on AlN buffer layer, which improves the tilt to 0.8° FWHM.^[78,101] In-plane, GaN[10 $\bar{1}$ 0] (M-direction) is typically parallel to Si[11 $\bar{2}$], and GaN[11 $\bar{2}$ 0] (A-direction) is parallel to Si[110]. (This was shown in 3.2.1 and can most easily be seen in SEM: the M-plane side facets of the NWs never face the flat of the wafer which indicates a Si \langle 110 \rangle direction.) This in-plane orientation shows a twist, which is accessible to x-ray diffraction by rotating the sample around the Si[111] substrate normal (φ -scan) and measuring the intensity of an asymmetrical reflection such as GaN(10.5). The FWHM of the φ -scan is 11.8° for the self-induced GaN NWs grown directly on Si(111), which is again improved to 6.4° on an AlN buffer. The GaN(10.5) reflection points $\psi = 20.7^\circ$ away from the surface normal, and the true in-plane twist is about one third of the FWHM in this measurement geometry. For GaN NWs on Si(111) the true in-plane twist is 4.4° FWHM.^[156]

The statistical information about the fluctuations in NW morphology was summarized in Table 4.1.



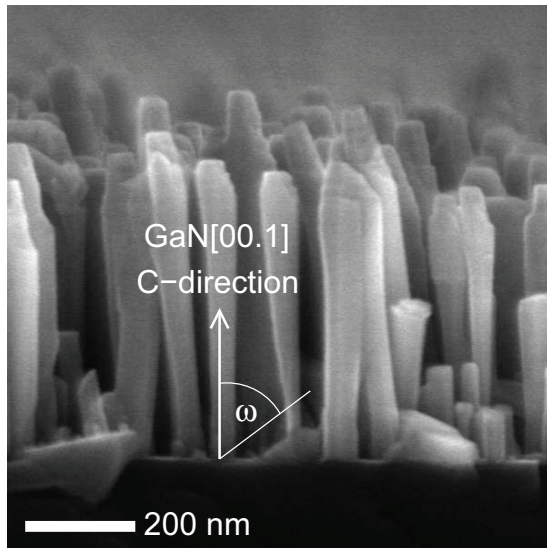
(a) SEM image of $\text{In}_x\text{Ga}_{1-x}\text{N}/\text{GaN}$ NWs in cross section. The data was acquired by A.-K. Bluhm.



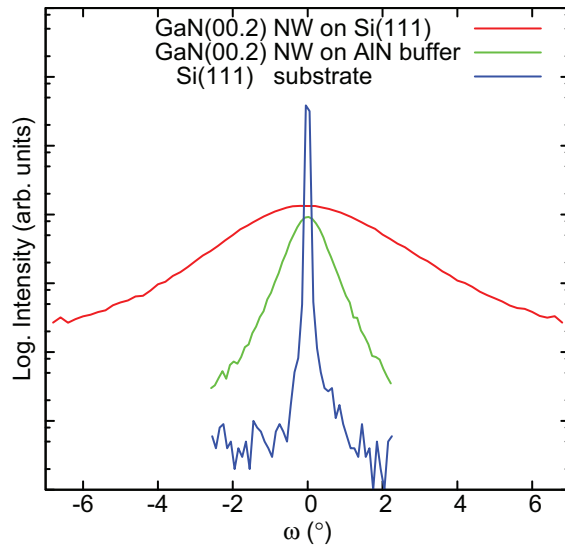
(b) Length distribution of the NWs.

(c) Diameter distribution of the NWs.

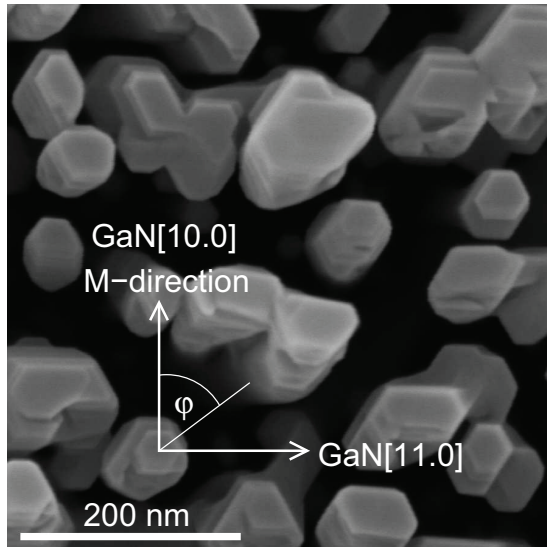
Figure B.1: Cross section SEM at cleave edge and histograms showing typical diameter and lengths of self-induced GaN NWs on Si(111). Only NWs from the foreground were evaluated, which are entirely visible without shadowing from other NWs.



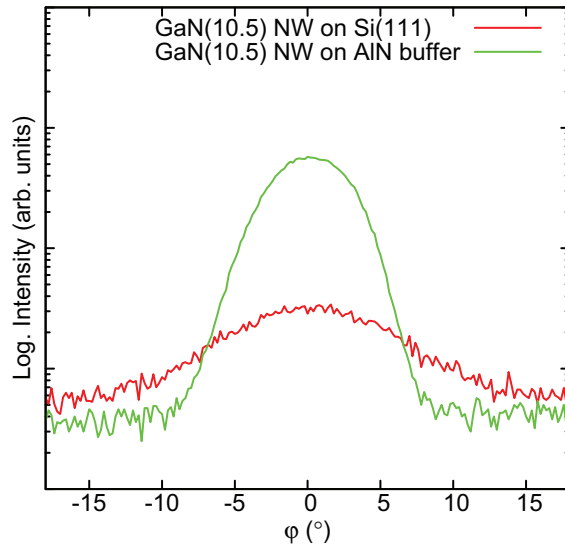
(a) SEM of $\text{In}_x\text{Ga}_{1-x}\text{N}/\text{GaN}$ NW in cross section. The data was acquired by A.-K. Bluhm. (Distortions in the SEM image are due to building vibrations.)



(b) XRD rocking curves (ω -scan) measured with an analyzer crystal and showing the tilt of GaN NWs grown directly on Si(111) and on an AlN buffer layer.



(c) SEM of $\text{In}_x\text{Ga}_{1-x}\text{N}/\text{GaN}$ NWs in plan view. The data was acquired by A.-K. Bluhm.



(d) XRD ϕ -scan of GaN(10.5) with open detector showing the twist of GaN NWs grown directly on Si(111) and on an AlN buffer layer.

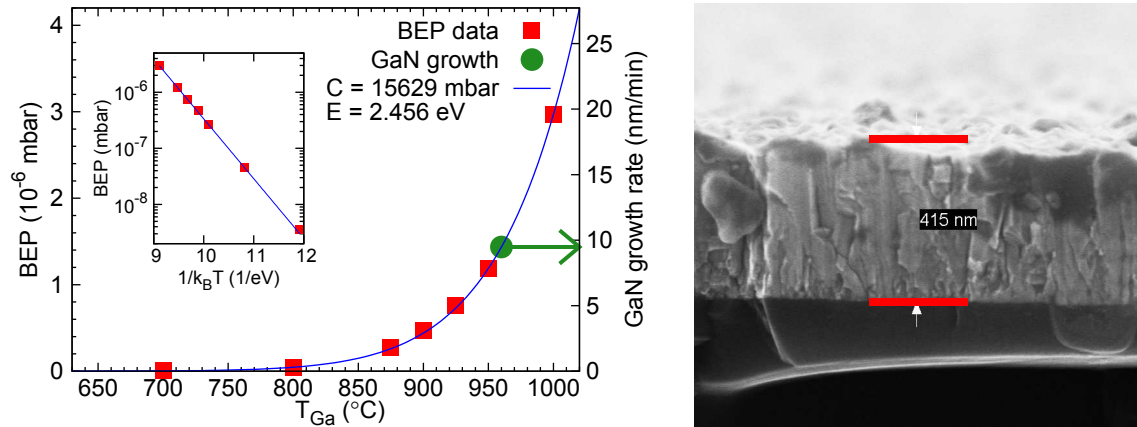
Figure B.2: Tilt and twist of self-induced NWs on Si(111) with and without an AlN buffer layer. The XRD rocking curves show that the AlN buffer layer improves the alignment of the GaN NWs with the crystallographic orientation of the substrate.

C Calibration of material supply rates in molecular beam epitaxy

The growth mode in molecular beam epitaxy is dictated by the source fluxes and the substrate temperature. The growth of layered structures such as LEDs involves time-critical changes of these parameters during the growth ‘run.’ The aim of the source calibration is, therefore, to make the adatom supply rates controllable.

To monitor the material supply rates from the In-, Al- and Ga-sources, an ionization vacuum gauge (ion gauge) can be brought into the position of the sample holder in the MBE 8 chamber. The beam equivalent pressure reading BEP is proportional to the flux density of the metal atoms. The BEP as a function of the effusion cell temperature can be approximated by an Arrhenius relation, $BEP(T) = C \exp(-E/k_B T)$. The activation energy E , and especially the proportionality factor C have to be obtained as fit parameters from BEP measurements, as is shown in Fig. C.1(a). In double-filament cells, the hot lip is kept at a constant temperature offset above T_{cell} . The effusion cells deplete successively, and regular measurements of the BEP are required to keep these parameters up to date.

Planar calibration layers of InN, AlN and GaN were grown under stoichiometric or slightly N-rich conditions with a known BEP . The thickness of the planar layers is measured by SEM, as shown in Fig. C.1(b) for a GaN layer. A rough surface is obtained due to the N-rich growth and the low substrate temperature of about 600 °C that was used to



(a) Measured BEP values. The inset shows the Arrhenius plot, delivering the fit parameters E and C . The data was acquired by C. Chèze and S. Fernández-Garrido.

(b) Thickness of a GaN calibration layer, grown N-rich on Si(111) at a substrate temperature of about 600 °C. $T_{\text{Ga}} = 960$ °C, $t = 45$ min.

Figure C.1: BEP measurement and growth rate calibration for Ga,1. To correlate the BEP with the metal flux, the growth rate is determined in an N-rich growth experiment. The arrow in (a) points to the growth rate of 9.2 nm/min, determined by SEM in the GaN layer shown in (b). This exemplary calibration was performed prior to the growth of the NW sample series 18.

C Calibration of material supply rates in molecular beam epitaxy

prevent Ga desorption. The material supply Φ to the substrate can be given in units of planar layer growth rate as a function of the *BEP*.^[229,272] The arrow in Fig. C.1(a) relates the calculated value $BEP(T_{\text{Ga},1})$ to the measured GaN growth rate of 9.2 nm/min, and this allows the scaling of the growth rate axis. In the MBE 8 system, the proportion of the growth rate to the *BEP* was typically in the order of $\Phi_{\text{Ga}}/BEP_{\text{Ga}} = 7 \frac{\text{nm}}{\text{min}}/10^{-6} \text{ mbar}$, depending on the response of the ion gauge. With the knowledge of $BEP(T_{\text{cell}})$ and $\Phi_{\text{cell}}/BEP_{\text{cell}}$, the metal supply rate can be controlled during the growth of complex layer structures by changing the cell temperature.

Active nitrogen was provided by radio-frequency (RF) plasma sources. The flux Φ_{N} was calibrated by growing planar GaN layers under Ga-rich conditions. Two N plasma sources were used. *SVTA RF-4.5*, operated with an N_2 flow of 2.2 sccm and an RF power of 500 W, delivered $\Phi_{\text{N}} = 20 \text{ nm/min}$. *Specs PCS-RF*, 2.0 sccm N_2 , 500W, $\Phi_{\text{N}} = 13 \text{ nm/min}$. For lower settings of RF power and N_2 flow, separate calibration layers were grown.

In the MBE 8 system, for the growth experiments reported in this thesis, the sources were placed at an incident angle of 21° (In, Al, Ga,1), 30° (N-plasma) and 40° (Ga,2, Si, Mg) from the surface normal, as shown in Fig. 3.1. The impinging flux can be inhomogeneous across the substrate. The substrate is heated by a filament, with a pyrolytic boron-nitride heat diffuser plate mounted between sample and heater. Heat transfer is also inhomogeneous across the substrate. The samples were not rotated during the growth for technical reasons. To keep calibration errors small, quantitative measurements of single spots (SEM, Pyrometry, XRD, PL) were always carried out within 10 mm of the center of the 2'' wafer.

Bibliography

- [1] E. F. Schubert, *Light-Emitting Diodes*. Cambridge University Press, 2. ed., 2006.
- [2] K. Takahashi, A. Yoshikawa, and A. Sandhu, eds., *Wide Bandgap Semiconductors*. Springer, 2007.
- [3] S. Nakamura, S. Pearton, and G. Fasol, *The Blue Laser Diode*. Springer, 2000.
- [4] R. S. Wagner and W. C. Ellis, "Vapor-liquid-solid mechanism of single crystal growth," *Appl. Phys. Lett.*, vol. 4, no. 5, pp. 89–90, 1964.
- [5] K. Haraguchi, T. Katsuyama, and K. Hiruma, "Polarization dependence of light emitted from gaas p-n-junctions in quantum-wire crystals," *J. Appl. Phys.*, vol. 75, pp. 4220–4225, Apr. 1994.
- [6] A. M. Ionescu and H. Riel, "Tunnel field-effect transistors as energy-efficient electronic switches," *Nature*, vol. 479, pp. 329–337, Nov. 2011.
- [7] F. Patolsky and C. M. Lieber, "Nanowire nanosensors," *Materials Today*, vol. 8, no. 4, pp. 20 – 28, 2005.
- [8] A. Kikuchi, M. Kawai, M. Tada, and K. Kishino, "Ingan/gan multiple quantum disk nanocolumn light-emitting diodes grown on (111) si substrate," *Jpn. J. Appl. Phys., Part 1*, vol. 43, no. 12A, pp. L1524–L1526, 2004.
- [9] M. A. Sánchez-García, E. Calleja, E. Monroy, F. J. Sanchez, F. Calle, E. Muñoz, and R. Beresford, "The effect of the iii/v ratio and substrate temperature on the morphology and properties of gan- and aln-layers grown by molecular beam epitaxy on si(1 1 1)," *J. Cryst. Growth*, vol. 183, no. 1-2, pp. 23 – 30, 1998.
- [10] T. Stoica, E. Sutter, R. J. Meijers, R. K. Debnath, R. Calarco, H. Luth, and D. Grutzmacher, "Interface and wetting layer effect on the catalyst-free nucleation and growth of gan nanowires," *Small*, vol. 4, pp. 751–754, June 2008.
- [11] M. T. Björk, B. J. Ohlsson, T. Sass, A. I. Persson, C. Thelander, M. H. Magnusson, K. Deppert, L. R. Wallenberg, and L. Samuelson, "One-dimensional heterostructures in semiconductor nanowhiskers," *Appl. Phys. Lett.*, vol. 80, no. 6, pp. 1058–1060, 2002.
- [12] F. Limbach, *Steps towards a GaN nanowire based light emitting diode*. PhD thesis, Humboldt-Universität zu Berlin, 2012.
- [13] H. Morkoç, *Handbook of Nitride Semiconductors and Devices*, vol. 1: Material Properties, Physics and Growth. WILEY-VCH Verlag, Weinheim, 2008.
- [14] F. Bloch, "Über die Quantenmechanik der Elektronen in Kristallgittern," *Z. Phys.*, vol. 52, pp. 555–600, 1929.

Bibliography

- [15] W. Shockley, *Electrons and Holes in Semiconductors*. Van Nostrand, 1950.
- [16] S. M. Sze, *Physics of Semiconductor Devices*. Wiley, 1969.
- [17] S. Nakamura, T. Mukai, and M. Senoh, "High-Brightness InGaN/AlGaN Double-Heterostructure Blue-Green-Light-Emitting Diodes," *J. Appl. Phys.*, vol. 76, pp. 8189–8191, Dec. 1994.
- [18] H. Morkoç, *Handbook of Nitride Semiconductors and Devices*, vol. 3: GaN-based Optical and Electronic Devices. WILEY-VCH Verlag, Weinheim, 2008.
- [19] P. Lefebvre, S. Anceau, P. Valvin, T. Taliercio, L. Konczewicz, T. Suski, S. P. Lepkowski, H. Teisseyre, H. Hirayama, and Y. Aoyagi, "Time-resolved spectroscopy of (al,gai)n based quantum wells: Localization effects and effective reduction of internal electric fields," *Phys. Rev. B*, vol. 66, p. 195330, Nov. 2002.
- [20] S. Nakamura, "A bright future for blue-green leds," *IEEE Circuit. Devic.*, vol. 11, pp. 19–23, May 1995.
- [21] G. Ramirez-Flores, H. Navarro-Contreras, A. Lastras-Martinez, R. C. Powell, and J. E. Greene, "Temperature-dependent optical band-gap of the metastable zincblende structure beta-gan," *Phys. Rev. B*, vol. 50, pp. 8433–8438, Sept. 1994.
- [22] O. Brandt, H. Yang, B. Jenichen, Y. Suzuki, L. Doweritz, and K. H. Ploog, "Surface reconstructions of zincblende gan/gaas(001) in plasma-assisted molecular-beam epitaxy," *Phys. Rev. B*, vol. 52, pp. R2253–R2256, July 1995.
- [23] H. Vilchis, V. Sanchez-R., and A. Escobosa, "Cubic gan layers grown by metalorganic chemical vapor deposition on gan templates obtained by nitridation of gaas," *Thin Solid Films*, vol. 520, pp. 5191–5194, 2012.
- [24] A. Pretorius, T. Yamaguchi, C. Kubel, R. Kroger, D. Hommel, and A. Rosenauer, "Structural investigation of growth and dissolution of inxga1-xn nano-islands grown by molecular beam epitaxy," *J. Cryst. Growth*, vol. 310, pp. 748–756, Feb. 2008.
- [25] M. A. Moram and M. E. Vickers, "X-ray diffraction of iii-nitrides," *Rep. Prog. Phys.*, vol. 72, p. 036502, Mar. 2009.
- [26] J. Lähnemann, O. Brandt, U. Jahn, C. Pfüller, C. Roder, P. Dogan, F. Grosse, A. Be-labbes, F. Bechstedt, A. Trampert, and L. Geelhaar, "Direct experimental determination of the spontaneous polarization of gan," *Phys. Rev. B*, vol. 86, p. 081302, Aug. 2012.
- [27] U. T. Schwarz and M. Kneissl, "Nitride emitters go nonpolar," *Phys. Status Solidi RRL*, vol. 1, pp. A44–A46, May 2007.
- [28] J. S. Speck and S. F. Chichibu, "Nonpolar and semipolar group iii nitride-based materials," *MRS Bull.*, vol. 34, pp. 304–312, May 2009.
- [29] T. Takeuchi, S. Sota, M. Katsuragawa, M. Komori, H. Takeuchi, H. Amano, and I. Akasaki, "Quantum-confined stark effect due to piezoelectric fields in gainn strained quantum wells," *Jpn. J. Appl. Phys., Part 2*, vol. 36, pp. L382–L385, Apr. 1997.

- [30] S. F. Chichibu, A. C. Abare, M. P. Mack, M. S. Minsky, T. Deguchi, D. Cohen, P. Kozodoy, S. B. Fleischer, S. Keller, J. S. Speck, J. E. Bowers, E. Hu, U. K. Mishra, L. A. Coldren, S. P. DenBaars, K. Wada, T. Sota, and S. Nakamura, "Optical properties of ingan quantum wells," *Mater. Sci. Eng., B*, vol. 59, pp. 298–306, May 1999.
- [31] S. Ghosh, P. Waltereit, O. Brandt, H. T. Grahn, and K. H. Ploog, "Electronic band structure of wurtzite gan under biaxial strain in the m plane investigated with photorefectance spectroscopy," *Phys. Rev. B*, vol. 65, p. 075202, Feb. 2002.
- [32] P. Misra, U. Behn, O. Brandt, H. T. Grahn, B. Imer, S. Nakamura, S. P. DenBaars, and J. S. Speck, "Polarization anisotropy in gan films for different nonpolar orientations studied by polarized photorefectance spectroscopy," *Appl. Phys. Lett.*, vol. 88, p. 161920, Apr. 2006.
- [33] P. Misra, O. Brandt, H. T. Grahn, H. Teisseyre, M. Siekacz, C. Skierbiszewski, and B. Lucznik, "Complete in-plane polarization anisotropy of the a exciton in unstrained a-plane gan films," *Appl. Phys. Lett.*, vol. 91, p. 141903, Oct. 2007.
- [34] J. Kamimura, K. Kishino, and A. Kikuchi, "Photoluminescence properties of selectively grown inn microcrystals," *Phys. Status Solidi RRL*, vol. 6, pp. 157–159, Apr. 2012.
- [35] P. Schley, R. Goldhahn, A. T. Winzer, G. Gobsch, V. Cimalla, O. Ambacher, H. Lu, W. J. Schaff, M. Kurouchi, Y. Nanishi, M. Rakel, C. Cobet, and N. Esser, "Dielectric function and van hove singularities for in-rich $\text{In}_x\text{Ga}_{1-x}\text{N}$ alloys: Comparison of n- and metal-face materials," *Phys. Rev. B*, vol. 75, p. 205204, May 2007.
- [36] A. Polian, M. Grimsditch, and I. Grzegory, "Elastic constants of gallium nitride," *J. Appl. Phys.*, vol. 79, pp. 3343–3344, Mar. 1996.
- [37] D. A. B. Miller, D. S. Chemla, T. C. Damen, A. C. Gossard, W. Wiegmann, T. H. Wood, and C. A. Burrus, "Electric-field dependence of optical-absorption near the band-gap of quantum-well structures," *Phys. Rev. B*, vol. 32, no. 2, pp. 1043–1060, 1985.
- [38] P. Waltereit, O. Brandt, J. Ringling, and K. H. Ploog, "Electrostatic fields and compositional fluctuations in (in,ga)n/gan multiple quantum wells grown by plasma-assisted molecular-beam epitaxy," *Phys. Rev. B*, vol. 64, pp. 245305–, Nov. 2001.
- [39] S. F. Chichibu, A. Uedono, T. Onuma, B. A. Haskell, A. Chakraborty, T. Koyama, P. T. Fini, S. Keller, S. P. Denbaars, J. S. Speck, U. K. Mishra, S. Nakamura, S. Yamaguchi, S. Kamiyama, H. Amano, I. Akasaki, J. Han, and T. Sota, "Origin of defect-insensitive emission probability in in-containing (al, in, ga) n alloy semiconductors," *Nat. Mater.*, vol. 5, pp. 810–816, Oct. 2006.
- [40] P. Lefebvre, A. Morel, M. Gallart, T. Taliercio, J. Allègre, B. Gil, H. Mathieu, B. Dami-lano, N. Grandjean, and J. Massies, "High internal electric field in a graded-width ingan/gan quantum well: Accurate determination by time-resolved photoluminescence spectroscopy," *Appl. Phys. Lett.*, vol. 78, pp. 1252–1254, Feb. 2001.
- [41] M. Peter, A. Laubsch, W. Bergbauer, T. Meyer, M. Sabathil, J. Baur, and B. Hahn, "New developments in green leds," *Phys. Status Solidi A*, vol. 206, no. 6, pp. 1125–1129, 2009.

Bibliography

- [42] Ü. Özgür, X. Ni, X. Li, J. Lee, S. Liu, S. Okur, V. Avrutin, A. Matulionis, and H. Morkoç, "Ballistic transport in ingan-based leds: impact on efficiency," *Semi-cond. Sci. Technol.*, vol. 26, no. 1, p. 014022, 2011.
- [43] K. P. O'Donnell, M. A. D. Maur, A. Di Carlo, and K. Lorenz, "It's not easy being green: Strategies for all-nitrides, all-colour solid state lighting," *Phys. Status Solidi RRL*, vol. 6, pp. 49–52, Feb. 2012.
- [44] T. H. Hsueh, H. W. Huang, C. C. Kao, Y. H. Chang, M. C. Ou-Yang, H. C. Kuo, and S. C. Wang, "Characterization of ingan/gan multiple quantum well nanorods fabricated by plasma etching with self-assembled nickel metal nanomasks," *Jpn. J. Appl. Phys., Part 1*, vol. 44, pp. 2661–2663, Apr. 2005.
- [45] P. C. Yu, C. H. Chiu, Y. R. Wu, H. H. Yen, J. R. Chen, C. C. Kao, H. W. Yang, H. C. Kuo, T. C. Lu, W. Y. Yeh, and S. C. Wang, "Strain relaxation induced microphotoluminescence characteristics of a single ingan-based nanopillar fabricated by focused ion beam milling," *Appl. Phys. Lett.*, vol. 93, p. 081110, Aug. 2008.
- [46] Y. R. Wu, C. H. Chiu, C. Y. Chang, P. C. Yu, and H. C. Kuo, "Size-dependent strain relaxation and optical characteristics of ingan/gan nanorod leds," *IEEE J. Sel. Top. Quantum Electron.*, vol. 15, pp. 1226–1233, July 2009.
- [47] E. Ertekin, P. A. Greaney, D. C. Chrzan, and T. D. Sands, "Equilibrium limits of coherency in strained nanowire heterostructures," *J. Appl. Phys.*, vol. 97, p. 114325, June 2005.
- [48] F. Glas, "Critical dimensions for the plastic relaxation of strained axial heterostructures in free-standing nanowires," *Phys. Rev. B*, vol. 74, p. 121302, Sept. 2006.
- [49] H. M. Kim, Y. H. Cho, H. Lee, S. I. Kim, S. R. Ryu, D. Y. Kim, T. W. Kang, and K. S. Chung, "High-brightness light emitting diodes using dislocation-free indium gallium nitride/gallium nitride multiquantum-well nanorod arrays," *Nano Lett.*, vol. 4, pp. 1059–1062, June 2004.
- [50] M. Azize and T. Palacios, "Top-down fabrication of algan/gan nanoribbons," *Appl. Phys. Lett.*, vol. 98, p. 042103, Jan. 2011.
- [51] A.-L. Bavecove, G. Tourbot, E. Pugeoise, J. Garcia, P. Gilet, F. Levy, B. André, G. Feuillet, B. Gayral, B. Daudin, and L. S. Dang, "Gan-based nanowires: From nanometric-scale characterization to light emitting diodes," *Phys. Status Solidi A*, vol. 207, no. 6, pp. 1425–1427, 2010.
- [52] W. Guo, M. Zhang, A. Banerjee, and P. Bhattacharya, "Catalyst-free ingan/gan nanowire light emitting diodes grown on (001) silicon by molecular beam epitaxy," *Nano Lett.*, vol. 10, p. 3355, Aug. 2010.
- [53] R. Armitage and K. Tsubaki, "Multicolour luminescence from ingan quantum wells grown over gan nanowire arrays by molecular-beam epitaxy," *Nanotechnology*, vol. 21, no. 19, p. 195202, 2010.
- [54] H. W. Lin, Y. J. Lu, H. Y. Chen, H. M. Lee, and S. Gwo, "Ingan/gan nanorod array white light-emitting diode," *Appl. Phys. Lett.*, vol. 97, p. 073101, Aug. 2010.

- [55] K. Kishino, J. Kamimura, and K. Kamiyama, "Near-infrared ingan nanocolumn light-emitting diodes operated at 1.46 μm ," *Appl. Phys. Express*, vol. 5, p. 031001, Mar. 2012.
- [56] H. P. T. Nguyen, K. Cui, S. Zhang, S. Fatholouloumi, and Z. Mi, "Full-color ingan/gan dot-in-a-wire light emitting diodes on silicon," *Nanotechnology*, vol. 22, no. 44, p. 445202, 2011.
- [57] F. Limbach, C. Hauswald, J. Lähnemann, M. Wölz, O. Brandt, U. Jahn, A. Trampert, R. Calarco, L. Geelhaar, and H. Riechert, "Current path in light-emitting diodes based on iii-n nanowire ensembles," *Nanotechnology*, vol. 23, p. 465301, 2012.
- [58] L. Geelhaar, C. Chèze, B. Jenichen, O. Brandt, C. Pfüller, S. Münch, R. Rothemund, S. Reitzenstein, A. Forchel, T. Kehagias, P. Komninou, G. P. Dimitrakopoulos, T. Karakostas, L. Lari, P. R. Chalker, M. H. Gass, and H. Riechert, "Properties of gan nanowires grown by molecular beam epitaxy," *IEEE J. Sel. Top. Quantum Electron.*, vol. 17, no. 4, p. 878, 2011.
- [59] C. Chèze, L. Geelhaar, O. Brandt, W. M. Weber, H. Riechert, S. Munch, R. Rothemund, S. Reitzenstein, A. Forchel, T. Kehagias, P. Komninou, G. P. Dimitrakopoulos, and T. Karakostas, "Direct comparison of catalyst-free and catalyst-induced gan nanowires," *Nano Res.*, vol. 3, pp. 528–536, July 2010.
- [60] M. Mandl, T. Schimpke, A. Pfeuffer, H. Specht, P. Rode, and M. Strassburg, "Thin-film nanorod leds grown by mbe at pdi." OSRAM Opto Semiconductors GmbH, internal presentation, 29. June 2012.
- [61] C. Denker, *InN and In-rich InGaN Nanocolumns*. PhD thesis, Georg-August-Universität Göttingen, 2011.
- [62] R. Calarco, "Inn nanowires: Growth and optoelectronic properties," *Materials*, vol. 5, no. 11, pp. 2137–2150, 2012.
- [63] M. A. Herman and H. Sitter, *Molecular Beam Epitaxy*. Springer, 1996.
- [64] S. Strite and H. Morkoç, "Gan, aln, and inn - a review," *J. Vac. Sci. Technol., B*, vol. 10, pp. 1237–1266, July 1992.
- [65] W. E. Hoke, P. J. Lomonias, and D. G. Weir, "Evaluation of a new plasma source for molecular-beam epitaxial-growth of inn and gan films," *J. Cryst. Growth*, vol. 111, pp. 1024–1028, May 1991.
- [66] SVTA, *RF PLASMA SOURCE MODEL 4.53 MANUAL*. SVT Associates, Inc., Eden Prairie, MN 55344, USA, 1998.
- [67] W. Braun, *Applied RHEED*. Springer, 1999.
- [68] A. Ichimiya and P. J. Cohen, *Reflection high-energy electron diffraction*. Cambridge University Press, 2004.
- [69] N. J. C. Ingle, A. Yuskas, R. Wicks, M. Paul, and S. Leung, "The structural analysis possibilities of reflection high energy electron diffraction," *J. Phys. D: Appl. Phys.*, vol. 43, no. 13, p. 133001, 2010.

Bibliography

- [70] S. King, R. Davis, and R. Nemanich, "Kinetics of Ga and In desorption from (7×7) Si(111) and (3×3) 6H-SiC(0001) surfaces," *Surf. Sci.*, vol. 602, no. 2, pp. 405 – 415, 2008.
- [71] S. Fernández-Garrido, *Crecimiento de nitruros del grupo III por epitaxia de haces moleculares para la fabricación de diodos electroluminiscentes en el rango visible-ultravioleta*. PhD thesis, Universidad Politécnica de Madrid, 2009.
- [72] C. W. Hu, H. Hibino, T. Ogino, and I. S. T. Tsong, "Hysteresis in the (1×1) – (7×7) first-order phase transition on the si(111) surface," *Surf. Sci.*, vol. 487, pp. 191–200, July 2001.
- [73] M. Wölz, "Molekularstrahlepitaxie nanoskaliger Goldinseln auf Si(100) Substraten," diplomarbeit, Georg-August-Universität Göttingen, 2002.
- [74] C. Chèze, *Investigation and comparison of GaN nanowire nucleation and growth by the catalyst-assisted and self-induced approaches*. PhD thesis, Humboldt-Universität zu Berlin, 2009.
- [75] J. W. Edington, *Practical Electron Microscopy in Materials Science*, vol. 4. Typical Electron Microscope Investigations. MacMillan, 1976.
- [76] D. B. Williams, *Transmission Electron Microscopy*, vol. II. Plenum Press, 1996.
- [77] K. Bertness, A. Roshko, L. Mansfield, T. Harvey, and N. Sanford, "Mechanism for spontaneous growth of gan nanowires with molecular beam epitaxy," *J. Cryst. Growth*, vol. 310, no. 13, pp. 3154 – 3158, 2008.
- [78] L. Largeau, D. L. Dheeraj, M. Tchernycheva, G. E. Cirlin, and J. C. Harmand, "Facet and in-plane crystallographic orientations of gan nanowires grown on si(111)," *Nanotechnology*, vol. 19, no. 15, p. 155704 (5pp), 2008.
- [79] M. Rao, N. Newman, and S. Mahajan, "The formation of ordered structures in in-gan layers," *Scr. Mater.*, vol. 56, no. 1, pp. 33 – 36, 2007.
- [80] A. Pretorius, *Transmission electron microscopy of GaN based, doped semiconductor heterostructures*. PhD thesis, Universität Bremen, 2006.
- [81] J. Renard, G. Tourbot, D. Sam-Giao, C. Bougerol, B. Daudin, and B. Gayral, "Optical spectroscopy of cubic gan in nanowires," *Appl. Phys. Lett.*, vol. 97, no. 8, p. 081910, 2010.
- [82] S. Guha, N. A. Bojarczuk, and D. W. Kisker, "Surface lifetimes of ga and growth behavior on gan(0001) surfaces during molecular beam epitaxy," *Appl. Phys. Lett.*, vol. 69, pp. 2879–2881, Nov. 1996.
- [83] S. Fernández-Garrido, G. Koblmüller, E. Calleja, and J. S. Speck, "In situ gan decomposition analysis by quadrupole mass spectrometry and reflection high-energy electron diffraction," *J. Appl. Phys.*, vol. 104, no. 3, p. 033541, 2008.
- [84] G. Koblmüller, P. Pongratz, R. Averbeck, and H. Riechert, "Delayed nucleation during molecular-beam epitaxial growth of gan observed by line-of-sight quadrupole mass spectrometry," *Appl. Phys. Lett.*, vol. 80, pp. 2281–2283, Apr. 2002.

- [85] C. Chèze, L. Geelhaar, A. Trampert, and H. Riechert, "In situ investigation of self-induced gan nanowire nucleation on si," *Appl. Phys. Lett.*, vol. 97, p. 043101, July 2010.
- [86] J. H. Batey, "Quadropole gas analysers," *Vacuum*, vol. 37, no. 8-9, pp. 659–668, 1987. Special Issue Modern Vacuum Practice.
- [87] G. B. Stringfellow, *Organometallic Vapor-Phase Epitaxy: Theory and Practice*. Academic Press, 2nd ed., 1999.
- [88] S. Porowski and I. Grzegory, "Thermodynamical properties of iii-v nitrides and crystal growth of gan at high n-2 pressure," *J. Cryst. Growth*, vol. 178, pp. 174–188, June 1997.
- [89] G. Stringfellow, "Microstructures produced during the epitaxial growth of ingan alloys," *J. Cryst. Growth*, vol. 312, no. 6, pp. 735 – 749, 2010.
- [90] W. S. Karpov, S Yun, "Suppression of phase separation in Ingan due to elastic strain," *MRS Internet J. Nitride Semicond. Res.*, vol. 3, pp. 16–1, 1998.
- [91] A. Madhukar, "Far from equilibrium vapor-phase growth of lattice matched iii-v compound semiconductor interfaces - some basic concepts and monte-carlo computer-simulations," *Surf. Sci.*, vol. 132, no. 1-3, pp. 344–374, 1983.
- [92] M. Wuttig and X. Liu, *Ultrathin Metal Films*, vol. 206 of *Springer Tracts in Modern Physics*. Springer, 2004.
- [93] E. Bauer, "Phänomenologische theorie der kristallabscheidung an oberflächen. i," *Z. Kristallogr.*, vol. 110, pp. 372–394, Jan. 1958.
- [94] Osram Opto Semiconductors GmbH, "Forschungserfolg: Erste Gallium-Nitrid-LED-Chips auf Silizium im Pilotstatus." Press release, 12. Jan. 2012.
- [95] M. Yoshizawa, A. Kikuchi, M. Mori, N. Fujita, and K. Kishino, "Growth of self-organized gan nanostructures on al₂o₃(0001) by rf-radical source molecular beam epitaxy," *Jpn. J. Appl. Phys., Part 2*, vol. 36, pp. L459–L462, Apr. 1997.
- [96] S. Fernández-Garrido, J. Grandal, E. Calleja, M. A. Sánchez-García, and D. Lopez-Romero, "A growth diagram for plasma-assisted molecular beam epitaxy of gan nanocolumns on si(111)," *J. Appl. Phys.*, vol. 106, no. 12, p. 126102, 2009.
- [97] V. Consonni, M. Hanke, M. Knelangen, L. Geelhaar, A. Trampert, and H. Riechert, "Nucleation mechanisms of self-induced gan nanowires grown on an amorphous interlayer," *Phys. Rev. B*, vol. 83, p. 035310, Jan. 2011.
- [98] R. K. Debnath, R. Meijers, T. Richter, T. Stoica, R. Calarco, and H. Lüth, "Mechanism of molecular beam epitaxy growth of gan nanowires on si(111)," *Appl. Phys. Lett.*, vol. 90, no. 12, p. 123117, 2007.
- [99] V. Consonni, V. G. Dubrovskii, A. Trampert, L. Geelhaar, and H. Riechert, "Quantitative description for the growth rate of self-induced gan nanowires," *Phys. Rev. B*, vol. 85, p. 155313, Apr. 2012.

Bibliography

- [100] V. Consonni, M. Knelangen, L. Geelhaar, A. Trampert, and H. Riechert, "Nucleation mechanisms of epitaxial gan nanowires: Origin of their self-induced formation and initial radius," *Phys. Rev. B*, vol. 81, p. 085310, Feb. 2010.
- [101] R. Songmuang, O. Landré, and B. Daudin, "From nucleation to growth of catalyst-free gan nanowires on thin aln buffer layer," *Appl. Phys. Lett.*, vol. 91, p. 251902, Dec. 2007.
- [102] C.-L. Wu, J.-C. Wang, M.-H. Chan, T. T. Chen, and S. Gwo, "Heteroepitaxy of gan on si(111) realized with a coincident-interface aln/beta-si[sub 3]n[sub 4](0001) double-buffer structure," *Appl. Phys. Lett.*, vol. 83, no. 22, pp. 4530–4532, 2003.
- [103] E. Calleja, J. Ristić, S. Fernández-Garrido, L. Cerutti, M. A. Sánchez-García, J. Grandal, A. Trampert, U. Jahn, G. Sánchez, A. Griol, and B. Sánchez, "Growth, morphology, and structural properties of group-iii-nitride nanocolumns and nanodisks," *Phys. Status Solidi B*, vol. 244, no. 8, pp. 2816–2837, 2007.
- [104] K. Hestroffer, C. Leclere, V. Cantelli, C. Bougerol, H. Renevier, and B. Daudin, "In situ study of self-assembled gan nanowires nucleation on si(111) by plasma-assisted molecular beam epitaxy," *Appl. Phys. Lett.*, vol. 100, no. 21, p. 212107, 2012.
- [105] A. Wierzbicka, Z. R. Zytkeiwicz, S. Kret, J. Borysiuk, P. Dluzewski, M. Sobanska, K. Klosek, A. Reszka, G. Tchutchulashvili, A. Cabaj, and E. Lusakowska, "Influence of substrate nitridation temperature on epitaxial alignment of gan nanowires to si(111) substrate," *Nanotechnology*, vol. 24, p. 035703, Jan. 2013.
- [106] M. Seibt, "Structure and chemistry of nitride nanowires studied by transmission electron microscope techniques," in *Sino-German-Symposium on "The Growth and Overgrowth of Group III-Nitride Nanowire Structures and their Device Applications"*, 5.–7. July 2010.
- [107] S. Fernández-Garrido, J. Grandal, E. Calleja, and M. A. Sánchez-García, "On the nucleation and growth of self-assembled gan nanocolumns by molecular beam epitaxy," *unpublished*, 2010.
- [108] V. G. Dubrovskii, V. Consonni, A. Trampert, L. Geelhaar, and H. Riechert, "Scaling thermodynamic model for the self-induced nucleation of gan nanowires," *Phys. Rev. B*, vol. 85, p. 165317, Apr. 2012.
- [109] X. Kong, J. Ristić, M. A. Sánchez-García, E. Calleja, and A. Trampert, "Polarity determination by electron energy-loss spectroscopy: application to ultra-small iii-nitride semiconductor nanocolumns," *Nanotechnology*, vol. 22, p. 415701, Oct. 2011.
- [110] K. Hestroffer, C. Leclere, C. Bougerol, H. Renevier, and B. Daudin, "Polarity of gan nanowires grown by plasma-assisted molecular beam epitaxy on si(111)," *Phys. Rev. B*, vol. 84, p. 245302, Dec. 2011.
- [111] M. I. den Hertog, F. González-Posada, R. Songmuang, J. L. Rouviere, T. Fournier, B. Fernandez, and E. Monroy, "Correlation of polarity and crystal structure with optoelectronic and transport properties of gan/aln/gan nanowire sensors," *Nano Lett.*, vol. 12, no. 11, pp. 5691–5696, 2012.

- [112] F. Furtmayr, M. Vielemeyer, M. Stutzmann, J. Arbiol, S. Estrade, F. Peiro, J. R. Morante, and M. Eickhoff, "Nucleation and growth of gan nanorods on si (111) surfaces by plasma-assisted molecular beam epitaxy - the influence of si- and mg-doping," *J. Appl. Phys.*, vol. 104, p. 034309, Aug. 2008.
- [113] S. Fernández-Garrido, X. Kong, T. Gotschke, R. Calarco, L. Geelhaar, A. Trampert, and O. Brandt, "Spontaneous nucleation and growth of gan nanowires: The fundamental role of crystal polarity," *Nano Lett.*, 2012.
- [114] V. Jindal and F. Shahedipour-Sandvik, "Theoretical prediction of gan nanostructure equilibrium and nonequilibrium shapes," *J. Appl. Phys.*, vol. 106, no. 8, p. 083115, 2009.
- [115] J. Elsner, M. Haugk, G. Jungnickel, and T. Frauenheim, "Theory of Ga, N and H terminated GaN (0001)/(000 $\bar{1}$) surfaces," *Solid State Commun.*, vol. 106, no. 11, pp. 739 – 743, 1998.
- [116] D. Cherns, L. Meshi, I. Griffiths, S. Khongphetsak, S. V. Novikov, N. R. S. Farley, R. P. Campion, and C. T. Foxon, "Defect-controlled growth of gan nanorods on (0001) sapphire by molecular beam epitaxy," *Appl. Phys. Lett.*, vol. 93, p. 111911, Sept. 2008.
- [117] H. Sekiguchi, K. Kishino, and A. Kikuchi, "Formation of ingan quantum dots in regularly arranged gan nanocolumns grown by rf-plasma-assisted molecular-beam epitaxy," *Phys. Status Solidi C*, pp. n/a–n/a, 2010.
- [118] S. Albert, A. Bengoechea-Encabo, P. Lefebvre, F. Barbagini, M. A. Sánchez-García, E. Calleja, U. Jahn, and A. Trampert, "Selective area growth and characterization of ingan nano-disks implemented in gan nanocolumns with different top morphologies," *Appl. Phys. Lett.*, vol. 100, no. 23, p. 231906, 2012.
- [119] A. Bengoechea-Encabo, S. Albert, M. A. Sánchez-García, L. L. Lopez, S. Estrade, J. M. Rebled, F. Peiro, G. Nataf, P. de Merry, J. Zuñiga-Pérez, and E. Calleja, "Selective area growth of a- and c-plane gan nanocolumns by molecular beam epitaxy using colloidal nanolithography," *J. Cryst. Growth*, vol. 353, pp. 1–4, Aug. 2012.
- [120] C. T. Foxon, S. V. Novikov, J. L. Hall, R. P. Campion, D. Cherns, I. Griffiths, and S. Khongphetsak, "A complementary geometric model for the growth of gan nanocolumns prepared by plasma-assisted molecular beam epitaxy," *J. Cryst. Growth*, vol. 311, pp. 3423–3427, June 2009.
- [121] T. Gotschke, T. Schumann, F. Limbach, T. Stoica, and R. Calarco, "Influence of the adatom diffusion on selective growth of gan nanowire regular arrays," *Appl. Phys. Lett.*, vol. 98, p. 103102, Mar. 2011.
- [122] E. Galopin, L. Largeau, G. Patriarche, L. Travers, F. Glas, and J. C. Harmand, "Morphology of self-catalyzed gan nanowires and chronology of their formation by molecular beam epitaxy," *Nanotechnology*, vol. 22, no. 24, p. 245606, 2011.
- [123] V. G. Dubrovskii, V. Consonni, L. Geelhaar, A. Trampert, and H. Riechert, "Scaling growth kinetics of self-induced gan nanowires," *Appl. Phys. Lett.*, vol. 100, p. 153101, Apr. 2012.

Bibliography

- [124] V. Consonni, A. Trampert, L. Geelhaar, and H. Riechert, "Physical origin of the incubation time of self-induced gan nanowires," *Appl. Phys. Lett.*, vol. 99, no. 3, p. 033102, 2011.
- [125] K. K. Sabelfeld, V. M. Kaganer, F. Limbach, P. Dogan, O. Brandt, L. Geelhaar, and H. Riechert, "Cooperative phenomena in the growth of dense nanowire ensembles," *manuscript in preparation*, 2013.
- [126] M. Ashby, "Ashby Diagram for Temperature and Strength." Technical Whitepaper, Zeus Industrial Products, Inc., 2005.
- [127] J. H. Choi, A. Zoukarnineev, S. Il Kim, C. W. Baik, M. H. Yang, S. S. Park, H. Suh, U. J. Kim, H. Bin Son, J. S. Lee, M. Kim, J. M. Kim, and K. Kim, "Nearly single-crystalline gan light-emitting diodes on amorphous glass substrates," *Nat. Photonics*, vol. 5, pp. 763–769, Dec. 2011.
- [128] S. Ruvimov, Z. Liliental-Weber, J. Washburn, K. J. Duxstad, E. E. Haller, Z. F. Fan, S. N. Mohammad, W. Kim, A. E. Botchkarev, and H. Morkoç, "Microstructure of ti/al and ti/al/ni/au ohmic contacts for n-gan," *Appl. Phys. Lett.*, vol. 69, pp. 1556–1558, Sept. 1996.
- [129] V. Chawla, R. Jayaganthan, A. K. Chawla, and R. Chandra, "Microstructural characterizations of magnetron sputtered ti films on glass substrate rid d-3471-2011," *J. Mater. Process. Technol.*, vol. 209, pp. 3444–3451, Apr. 2009.
- [130] Z. A. Matysina, "The relative surface energy of hexagonal close-packed crystals," *Mater. Chem. Phys.*, vol. 60, pp. 70–78, July 1999.
- [131] J. L. F. Da Silva, C. Stampfl, and M. Scheffler, "Converged properties of clean metal surfaces by all-electron first-principles calculations," *Surf. Sci.*, vol. 600, pp. 703–715, Feb. 2006.
- [132] G. Teodorescu, *RADIATIVE EMISSIVITY OF METALS AND OXIDIZED METALS AT HIGH TEMPERATURE*. PhD thesis, Auburn University, Alabama, 2007.
- [133] A. E. Morgan, E. K. Broadbent, K. N. Ritz, D. K. Sadana, and B. J. Burrow, "Interactions of thin ti films with si, sio₂, si₃n₄, and sioxny under rapid thermal annealing," *J. Appl. Phys.*, vol. 64, pp. 344–353, July 1988.
- [134] J. Moon, T. Ito, J. S. Ma, and A. Hiraki, "Formation of tin by nitridation of magnetron sputtered ti-films using microwave plasma cvd," *J. Cryst. Growth*, vol. 115, pp. 589–595, Dec. 1991.
- [135] J. Musil, J. Vlček, V. Ježek, M. Kubásek, R. Čerstvý, T. Tölg, M. Benda, M. Kolega, and J. Musil, Jr., "Plasma nitriding of sputtered ti films," *Mater. Sci. Eng., A*, vol. 163, pp. 181–186, May 1993.
- [136] P. Komninou, G. P. Dimitrakopoulos, G. Nouet, T. Kehagias, P. Ruterana, and T. Karakostas, "Interfacial dislocations in tin/gan thin films," *J. Phys.: Condens. Matter*, vol. 12, pp. 10295–10300, Dec. 2000.
- [137] J. W. Gerlach, T. Hoche, F. E. Frost, and B. Rauschenbach, "Ion beam assisted mbe of gan on epitaxial tin films," *Thin Solid Films*, vol. 459, pp. 13–16, July 2004.

- [138] Y. B. Xu, M. Yamazaki, and P. Villars, "Inorganic materials database for exploring the nature of material," *Jpn. J. Appl. Phys., Part 1*, vol. 50, p. 11RH02, Nov. 2011.
- [139] W. Pies and A. Weiss, *Landolt-Börnstein, Gruppe III, Vol. 7. Part c1: Schlüsselement N*, ch. VI.1.5.1 Binäre Nitride, pp. 36–40. Springer, 1978.
- [140] M. Koyama, S. Arai, S. Suenaga, and M. Nakahashi, "Interfacial reactions between titanium film and single-crystal α - Al_2O_3 ," *J. Mater. Sci.*, vol. 28, pp. 830–834, Feb. 1993.
- [141] I. I. Kornilov, V. V. Vavilova, L. E. Fykin, R. P. Ozerov, S. P. Soloviev, and V. P. Smirnov, "Neutron diffraction investigation of ordered structures in titanium-oxygen system," *Metall. Trans.*, vol. 1, no. 9, pp. 2569–2571, 1970.
- [142] R. Beyers, R. Sinclair, and M. E. Thomas, "Phase-equilibria in thin-film metallizations," *J. Vac. Sci. Technol., B*, vol. 2, no. 4, pp. 781–784, 1984.
- [143] P. Blaha and K. Schwarz, "Electron-densities and Chemical Bonding In TiC, TiN, and TiO Derived From Energy-band Calculations," *International Journal of Quantum Chemistry*, vol. 23, no. 4, pp. 1535–1552, 1983.
- [144] H. Sekiguchi, K. Kishino, and A. Kikuchi, "Ti-mask selective-area growth of gan by rf-plasma-assisted molecular-beam epitaxy for fabricating regularly arranged ingan/gan nanocolumns," *Appl. Phys. Express*, vol. 1, p. 124002, Dec. 2008.
- [145] S. Ishizawa, H. Sekiguchi, A. Kikuchi, and K. Kishino, "Selective growth of gan nanocolumns by al thin layer on substrate," *Phys. Status Solidi B*, vol. 244, pp. 1815–1819, June 2007.
- [146] T. Schumann, T. Gotschke, F. Limbach, T. Stoica, and R. Calarco, "Selective-area catalyst-free mbe growth of gan nanowires using a patterned oxide layer," *Nanotechnology*, vol. 22, no. 9, p. 095603, 2011.
- [147] A. Bengoechea-Encabo, F. Barbagini, S. Fernández-Garrido, J. Grandal, J. Ristić, M. A. Sánchez-García, E. Calleja, U. Jahn, E. Luna, and A. Trampert, "Understanding the selective area growth of gan nanocolumns by mbe using ti nanomasks," *J. Cryst. Growth*, vol. 325, pp. 89–92, June 2011.
- [148] W. Kleber, *Einführung in die Kristallographie*. VEB Verlag Technik Berlin, 1977.
- [149] D. Chen, X. L. Ma, and Y. M. Wang, "Thickness-dependent structural transformation in the aln film," *Acta Mater.*, vol. 53, pp. 5223–5227, Nov. 2005.
- [150] F. Walther, P. Knipping, and M. v. Laue, *Mathematisch-Physikalische Klasse, Sitzungsberichte*, ch. Interferenzerscheinungen bei Röntgenstrahlen. Eine quantitative Prüfung der Theorie für die Interferenz-Erscheinungen bei Röntgenstrahlen., pp. 303–322, 363–373. Bayerische Akademie der Wissenschaften, 1912.
- [151] R. J. Briggs and A. K. Ramdas, "Piezospectroscopic study of the raman spectrum of cadmium sulfide," *Phys. Rev. B*, vol. 13, pp. 5518–5529, Jun 1976.
- [152] R. Tsu, H. Kawamura, and L. Esaki, "Raman scattering of local and collective phonon modes in $\text{Ga}_{1-x}\text{Al}_x\text{As}$," in *Proc. of Int. Conf. Phys. of Semiconductors, Warsaw* (M. Miasek, ed.), vol. 2, p. 1135, Elsevier, Amsterdam, 1972.

Bibliography

- [153] K. Hayashi, K. Itoh, N. Sawaki, and I. Akasaki, "Raman-Scattering in $\text{Al}_x\text{Ga}_{1-x}\text{N}$ alloys," *Solid State Commun.*, vol. 77, pp. 115–118, Jan. 1991.
- [154] V. M. Kaganer, M. Wölz, O. Brandt, L. Geelhaar, and H. Riechert, "X-ray diffraction profiles from axial nanowire heterostructures," *Phys. Rev. B*, vol. 83, p. 245321, 2011.
- [155] V. Consonni, M. Knelangen, U. Jahn, A. Trampert, L. Geelhaar, and H. Riechert, "Effects of nanowire coalescence on their structural and optical properties on a local scale," *Appl. Phys. Lett.*, vol. 95, p. 241910, Dec. 2009.
- [156] B. Jenichen, O. Brandt, C. Pfüller, P. Dogan, M. Knelangen, and A. Trampert, "Macro- and micro-strain in gan nanowires on si(111)," *Nanotechnology*, vol. 22, p. 295714, July 2011.
- [157] S. M. De, D. K. Das, A. Layek, A. Raja, M. K. Singh, A. Bhattacharya, S. Dhar, and A. Chowdhury, "Optoelectronic behaviors and carrier dynamics of individual localized luminescent centers in ingan quantum-well light emitting diodes," *Appl. Phys. Lett.*, vol. 99, p. 251911, Dec. 2011.
- [158] S. De, A. Layek, A. Raja, A. Kadir, M. R. Gokhale, A. Bhattacharya, S. Dhar, and A. Chowdhury, "Two distinct origins of highly localized luminescent centers within ingan/gan quantum-well light-emitting diodes," *Adv. Funct. Mater.*, vol. 21, no. 20, pp. 3828–3835, 2011.
- [159] Y. Kawakami, S. Suzuki, A. Kaneta, M. Funato, A. Kikuchi, and K. Kishino, "Origin of high oscillator strength in green-emitting ingan/gan nanocolumns," *Appl. Phys. Lett.*, vol. 89, p. 163124, Oct. 2006.
- [160] R. Bardoux, A. Kaneta, M. Funato, Y. Kawakami, A. Kikuchi, and K. Kishino, "Positive binding energy of a biexciton confined in a localization center formed in a single $\text{In}_x\text{Ga}_{1-x}\text{N}/\text{gan}$ quantum disk," *Phys. Rev. B*, vol. 79, pp. 155307–, Apr. 2009.
- [161] T. Kehagias, "Nanoscale indium variation along ingan nanopillars grown on (111) si substrates," *Phys. E (Amsterdam)*, vol. 42, pp. 2197–2202, July 2010.
- [162] J. Segura-Ruiz, G. Martinez-Criado, J. A. Sans, R. Tucoulou, P. Cloetens, I. Snigireva, C. Denker, J. Malindretos, A. Rizzi, M. Gomez-Gomez, N. Garro, and A. Cantarero, "Direct observation of elemental segregation in ingan nanowires by x-ray nanoprobe," *Phys. Status Solidi RRL*, vol. 5, pp. 95–97, Mar. 2011.
- [163] L. Vegard, L. Vegard, "Die Konstitution der Mischkristalle und die Raumfüllung der Atome," *Z. Phys.*, vol. 5, no. 1, pp. 17–26, 1921.
- [164] M. Hanke, C. Eisenschmidt, P. Werner, N. D. Zakharov, F. Syrowatka, F. Heyroth, P. Schafer, and O. Konovalov, "Elastic strain relaxation in axial si/ge whisker heterostructures," *Phys. Rev. B*, vol. 75, p. 161303, Apr. 2007.
- [165] J. Eymery, F. Rieutord, V. Favre-Nicolin, O. Robach, Y. M. Niquet, L. Froberg, T. Martensson, and L. Samuelson, "Strain and shape of epitaxial inas/inp nanowire superlattice measured by grazing incidence x-ray techniques," *Nano Lett.*, vol. 7, pp. 2596–2601, Sept. 2007.

- [166] O. Landré, D. Camacho, C. Bougerol, Y. M. Niquet, V. Favre-Nicolin, G. Renaud, H. Renevier, and B. Daudin, "Elastic strain relaxation in gan/aln nanowire superlattice," *Phys. Rev. B*, vol. 81, p. 153306, Apr. 2010.
- [167] T. Kuykendall, P. Ulrich, S. Aloni, and P. Yang, "Complete composition tunability of ingan nanowires using a combinatorial approach," *Nat. Mater.*, vol. 6, pp. 951–956, Dec. 2007.
- [168] B. M. Borg, K. A. Dick, J. Eymery, and L. E. Wernersson, "Enhanced sb incorporation in inassb nanowires grown by metalorganic vapor phase epitaxy," *Appl. Phys. Lett.*, vol. 98, p. 113104, Mar. 2011.
- [169] M. Wölz, V. M. Kaganer, O. Brandt, L. Geelhaar, and H. Riechert, "Analyzing the growth of $\text{In}_{x}\text{Ga}_{1-x}\text{N}/\text{GaN}$ superlattices in self-induced gan nanowires by x-ray diffraction," *Appl. Phys. Lett.*, vol. 98, no. 26, p. 261907, 2011.
- [170] M. Knelangen, M. Hanke, E. Luna, L. Schrottke, O. Brandt, and A. Trampert, "Monodisperse (in, ga)n insertions in catalyst-free-grown $\text{GaN}(0001)$ nanowires," *Nanotechnology*, vol. 22, no. 36, p. 365703, 2011.
- [171] P. F. Fewster, "X-ray diffraction tools and methods for semiconductor analysis," *Microscopy Of Semiconducting Materials 1999, Proceedings*, vol. 164, pp. 197–206, 1999.
- [172] O. Brandt, P. Waltereit, and K. H. Ploog, "Determination of strain state and composition of highly mismatched group-iii nitride heterostructures by x-ray diffraction," *J. Phys. D: Appl. Phys.*, vol. 35, pp. 577–585, Apr. 2002.
- [173] M. Wölz, M. Ramsteiner, V. M. Kaganer, O. Brandt, L. Geelhaar, and H. Riechert, "Strain-engineering of nanowire multi-quantum wells demonstrated by phonon frequency shift," *manuscript in preparation*, 2013.
- [174] V. M. Kaganer and A. Y. Belov, "Strain and x-ray diffraction from axial nanowire heterostructures," *Phys. Rev. B*, vol. 85, p. 125402, 2012.
- [175] J. M. Wagner and F. Bechstedt, "Properties of strained wurtzite gan and aln: Ab initio studies," *Phys. Rev. B*, vol. 66, p. 115202, Sept. 2002.
- [176] M. Wölz, V. M. Kaganer, O. Brandt, L. Geelhaar, and H. Riechert, "Erratum: "analyzing the growth of $\text{In}_{x}\text{Ga}_{1-x}\text{N}/\text{GaN}$ superlattices in self-induced gan nanowires by x-ray diffraction"," *Appl. Phys. Lett.*, vol. 100, no. 17, p. 179902, 2012.
- [177] H. Harima, "Properties of gan and related compounds studied by means of raman scattering," *J. Phys.: Condens. Matter*, vol. 14, pp. R967–R993, Sept. 2002.
- [178] M. Cardona, ed., *Light Scattering in Solids I*. Springer, 1983. See chapter 2 by A. Pinczuk and E. Burstein.
- [179] S. Lazić, M. Moreno, J. M. Calleja, A. Trampert, K. H. Ploog, F. B. Naranjo, S. Fernandez, and E. Calleja, "Resonant raman scattering in strained and relaxed ingan/gan multi-quantum wells," *Appl. Phys. Lett.*, vol. 86, p. 061905, Feb. 2005.
- [180] S. Lazić, E. Gallardo, J. M. Calleja, F. Agullo-Rueda, J. Grandal, M. A. Sánchez-García, and E. Calleja, "Raman scattering by longitudinal optical phonons in inn nanocolumns grown on $\text{Si}(111)$ and $\text{Si}(001)$ substrates," *Phys. E (Amsterdam)*, vol. 40, pp. 2087–2090, Apr. 2008.

Bibliography

- [181] A. Cantarero, A. Cros, N. Garro, M. I. Gomez-Gomez, A. Garcia-Cristobal, M. M. de Lima, B. Daudin, A. Rizzi, C. Denker, and J. Malindretos, "Optical properties of nitride nanostructures," *Ann. Phys. (Berlin)*, vol. 523, pp. 51–61, Jan. 2011.
- [182] C. Pfüller, *Optical properties of single semiconductor nanowires and nanowire ensembles*. PhD thesis, Humboldt-Universität zu Berlin, 2011.
- [183] C. Pfüller, M. Ramsteiner, O. Brandt, F. Grosse, A. Rathsfeld, G. Schmidt, L. Geelhaar, and H. Riechert, "Raman spectroscopy as a probe for the coupling of light into ensembles of sub-wavelength-sized nanowires," *Appl. Phys. Lett.*, vol. 101, pp. 083104–4, Aug. 2012.
- [184] I. Sela, V. V. Gridin, R. Beserman, R. Sarfaty, D. Fekete, and H. Morkoç, "Distribution of atoms in mixed iii-v compounds," *J. Appl. Phys.*, vol. 63, pp. 966–968, Feb. 1988.
- [185] D. Behr, J. Wagner, A. Ramakrishnan, H. Obloh, and K. H. Bachem, "Evidence for compositional inhomogeneity in low in content (inga)n obtained by resonant raman scattering," *Appl. Phys. Lett.*, vol. 73, pp. 241–243, July 1998.
- [186] R. Oliva, J. Ibáñez, R. Cuscó, R. Kudrawiec, J. Serafinczuk, O. Martinez, J. Jimenez, M. Henini, C. Boney, A. Bensaoula, and L. Artus, "Raman scattering by the E_2 and $A_1(\text{LO})$ phonons of $\text{In}_x\text{Ga}_{1-x}\text{N}$ epilayers ($0.25 < x < 0.75$) grown by molecular beam epitaxy," *J. Appl. Phys.*, vol. 111, no. 6, p. 063502, 2012.
- [187] M. R. Correia, S. Pereira, E. Pereira, J. Frandon, and E. Alves, "Raman study of the $a(1)(\text{lo})$ phonon in relaxed and pseudomorphic ingan epilayers," *Appl. Phys. Lett.*, vol. 83, pp. 4761–4763, Dec. 2003.
- [188] H. Grille, C. Schnittler, and F. Bechstedt, "Phonons in ternary group-iii nitride alloys," *Phys. Rev. B*, vol. 61, pp. 6091–6105, Mar. 2000.
- [189] F. Demangeot, J. Frandon, P. Baules, F. Natali, F. Semon, and J. Massies, "Phonon deformation potentials in hexagonal gan," *Phys. Rev. B*, vol. 69, p. 155215, Apr. 2004.
- [190] M. R. Correia, S. Pereira, J. Frandon, M. A. Renucci, E. Alves, A. D. Sequeira, and N. Franco, "Analysis of strain depth variations in an $\text{in}_{0.19}\text{ga}_{0.81}\text{n}$ layer by raman spectroscopy," *Phys. Status Solidi C*, vol. 0, no. 1, pp. 563–567, 2002.
- [191] X. Q. Wang, S. B. Che, Y. Ishitani, and A. Yoshikawa, "Experimental determination of strain-free raman frequencies and deformation potentials for the e_2 high and $a(1)(\text{lo})$ modes in hexagonal inn," *Appl. Phys. Lett.*, vol. 89, p. 171907, Oct. 2006.
- [192] R. Meijers, T. Richter, R. Calarco, T. Stoica, H. P. Boehm, M. Marso, and H. Luth, "Gan-nanowhiskers: Mbe-growth conditions and optical properties," *J. Cryst. Growth*, vol. 289, pp. 381–386, Mar. 2006.
- [193] J. Ristić, E. Calleja, S. Fernández-Garrido, L. Cerutti, A. Trampert, U. Jahn, and K. H. Ploog, "On the mechanisms of spontaneous growth of iii-nitride nanocolumns by plasma-assisted molecular beam epitaxy," *J. Cryst. Growth*, vol. 310, no. 18, pp. 4035 – 4045, 2008.
- [194] T. Stoica, R. Meijers, R. Calarco, T. Richter, and H. Luth, "Mbe growth optimization of inn nanowires," *J. Cryst. Growth*, vol. 290, pp. 241–247, Apr. 2006.

- [195] A. P. Vajpeyi, A. O. Ajagunna, K. Tsagaraki, M. Androulidaki, and A. Georgakillas, "Ingan nanopillars grown on silicon substrate using plasma assisted molecular beam epitaxy," *Nanotechnology*, vol. 20, no. 32, p. 325605, 2009.
- [196] Y. H. Kim, J. Y. Lee, S.-H. Lee, J.-E. Oh, H. S. Lee, and Y. Huh, "Indium-related novel architecture of gan nanorod grown by molecular beam epitaxy," *Chem. Phys. Lett.*, vol. 412, no. 4-6, pp. 454 – 458, 2005.
- [197] P. Waltereit, O. Brandt, K. H. Ploog, M. A. Tagliente, and L. Tapfer, "In surface segregation during growth of (in,ga)n/gan multiple quantum wells by plasma-assisted molecular beam epitaxy," *Phys. Rev. B*, vol. 66, pp. 165322–, Oct. 2002.
- [198] P. Blood, "Capacitance-voltage profiling and the characterisation of iii-v semiconductors using electrolyte barriers," *Semicond. Sci. Technol.*, vol. 1, pp. 7–27, July 1986.
- [199] G. L. Miller, D. A. H. Robinson, and J. D. Wiley, "Contactless measurement of semiconductor conductivity by radio frequency-free-carrier power absorption," *Rev. Sci. Instrum.*, vol. 47, no. 7, pp. 799–805, 1976.
- [200] J. Zegenhagen, M. S. Hybertsen, P. E. Freeland, and J. R. Patel, "Monolayer growth and structure of ga on si(111)," *Phys. Rev. B*, vol. 38, pp. 7885–7888, Oct. 1988.
- [201] X. Ni, X. Li, J. Lee, S. Liu, V. Avrutin, Ü. Özgür, H. Morkoç, and A. Matulionis, "Hot electron effects on efficiency degradation in ingan light emitting diodes and designs to mitigate them," *J. Appl. Phys.*, vol. 108, p. 033112, Aug. 2010.
- [202] M. Wölz, S. Fernández-Garrido, C. Hauswald, O. Brandt, F. Limbach, L. Geelhaar, and H. Riechert, "Indium incorporation in $\text{In}_x\text{Ga}_{1-x}\text{N}/\text{GaN}$ nanowire heterostructures investigated by line-of-sight quadrupole mass spectrometry," *Cryst. Growth Des.*, vol. 12, pp. 5686–5692, 2012.
- [203] Y.-L. Chang, J. L. Wang, F. Li, and Z. Mi, "High efficiency green, yellow, and amber emission from ingan/gan dot-in-a-wire heterostructures on si(111)," *Appl. Phys. Lett.*, vol. 96, no. 1, p. 013106, 2010.
- [204] G. Tourbot, C. Bougerol, F. Glas, L. F. Zagonel, Z. Mahfoud, S. Meuret, P. Gilet, M. Kociak, B. Gayral, and B. Daudin, "Growth mechanism and properties of ingan insertions in gan nanowires," *Nanotechnology*, vol. 23, p. 135703, Apr. 2012.
- [205] W. Guo, A. Banerjee, P. Bhattacharya, and B. S. Ooi, "Ingan/gan disk-in-nanowire white light emitting diodes on (001) silicon rid d-4370-2011," *Appl. Phys. Lett.*, vol. 98, p. 193102, May 2011.
- [206] H. Kirmse, I. Häusler, W. Neumann, P. Kmoninou, T. Kehagias, M. Soumelidou, T. Koukoula, T. Karakostas, F. Furtmayr, and M. M. Eickhoff, "Electron energy loss spectroscopy study of (in,ga)n heterostructure nanowires (poster)," in *Microscopy of Semiconducting Materials XVII*, 4-7 April 2011, Cambridge, UK, 2011.
- [207] T. Kehagias, T. Koukoula, G. P. Dimitrakopoulos, E. Kaselaki, T. Koukoula, J. Kioseoglou, F. Furtmayr, H. Kirmse, W. Neumann, M. Eickhoff, T. Karakostas, and P. Komninou, "Nanostructure of ingan/gan superlattices in gan nanowires," in *MRS Fall Meeting*, 2011.

Bibliography

- [208] G. Tourbot, C. Bougerol, A. Grenier, M. D. Hertog, D. Sam-Giao, D. Cooper, P. Gilet, B. Gayral, and B. Daudin, "Structural and optical properties of ingan/gan nanowire heterostructures grown by pa-mbe," *Nanotechnology*, vol. 22, no. 7, p. 075601, 2011.
- [209] G. Tourbot, *Croissance par épitaxie par jets moléculaires de nanofils InGaN/GaN*. PhD thesis, Université de Grenoble, 2012.
- [210] A. A. Darhuber, T. Grill, J. Stangl, G. Bauer, D. J. Lockwood, J. P. Noel, P. D. Wang, and C. M. S. Torres, "Elastic relaxation of dry-etched si/sige quantum dots," *Phys. Rev. B*, vol. 58, pp. 4825–4831, Aug. 1998.
- [211] S. Keller, C. Schaake, N. A. Fichtenbaum, C. J. Neufeld, Y. Wu, K. McGroddy, A. David, S. P. DenBaars, C. Weisbuch, J. S. Speck, and U. K. Mishra, "Optical and structural properties of gan nanopillar and nanostripe arrays with embedded ingan/gan multi-quantum wells," *J. Appl. Phys.*, vol. 100, p. 054314, Sept. 2006.
- [212] F. Glas, "Energetics of quantum dot formation in heterostructured nanowires," in *GdR Nanofils Workshop, Porquerolles*, p. 21, 2011.
- [213] K. Cui, S. Fatholouloumi, M. G. Kibria, G. A. Botton, and Z. T. Mi, "Molecular beam epitaxial growth and characterization of catalyst-free inn/inxga1-xn core/shell nanowire heterostructures on si(111) substrates," *Nanotechnology*, vol. 23, p. 085205, Mar. 2012.
- [214] R. Koester, J.-S. Hwang, D. Salomon, X. Chen, C. Bougerol, J.-P. Barnes, D. L. S. Dang, L. Rigutti, A. de Luna Bugallo, G. Jacopin, M. Tchernycheva, C. Durand, and J. Eymery, "M-plane core-shell ingan/gan multiple-quantum-wells on gan wires for electroluminescent devices," *Nano Lett.*, Oct. 2011.
- [215] X. Niu, G. B. Stringfellow, and F. Liu, "Phase separation in strained epitaxial ingan islands," *Appl. Phys. Lett.*, vol. 99, pp. 213102–3, Nov. 2011.
- [216] M. Lopuszynski and J. A. Majewski, "Ordering in ternary nitride semiconducting alloys," *Phys. Rev. B*, vol. 85, p. 035211, Jan. 2012.
- [217] B. S. Simpkins, M. A. Mastro, C. R. Eddy, and P. E. Pehrsson, "Surface depletion effects in semiconducting nanowires," *J. Appl. Phys.*, vol. 103, p. 104313, May 2008.
- [218] F. Furtmayr, J. Teubert, P. Becker, S. Conesa-Boj, J. R. Morante, J. Arbiol, A. Chernikov, S. Schäfer, S. Chatterjee, and M. Eickhoff, "Carrier Confinement in GaN/Al_xGa_{1-x}N Nanowire Heterostructures for $0 < x \leq 1$," *ArXiv e-prints*, Sept. 2011.
- [219] G. Jacopin, L. Rigutti, L. Largeau, F. Fortuna, F. Furtmayr, F. H. Julien, M. Eickhoff, and M. Tchernycheva, "Optical properties of wurtzite/zinc-blende heterostructures in gan nanowires," *J. Appl. Phys.*, vol. 110, p. 064313, Sept. 2011.
- [220] M. Wölz, J. Lähnemann, O. Brandt, V. M. Kaganer, M. Ramsteiner, C. Pfüller, C. Hauswald, C. N. Huang, L. Geelhaar, and H. Riechert, "Correlation between In content and emission wavelength of In_xGa_{1-x}N/GaN nanowire heterostructures," *Nanotechnology*, vol. 23, p. 455203, 2012.

- [221] K. A. Dick, P. Caroff, J. Bolinsson, M. E. Messing, J. Johansson, K. Deppert, L. R. Wallenberg, and L. Samuelson, "Control of iii-v nanowire crystal structure by growth parameter tuning," *Semicond. Sci. Technol.*, vol. 25, p. 024009, Feb. 2010.
- [222] B. Mandl, K. A. Dick, D. Kriegner, M. Keplinger, G. Bauer, J. Stangl, and K. Deppert, "Crystal structure control in au-free self-seeded insb wire growth," *Nanotechnology*, vol. 22, p. 145603, Apr. 2011.
- [223] R. Armitage, "Luminescence characterization of ingan/gan vertical heterostructures grown on gan nanocolumns," in *MRS Proceedings Volume 1144* (Y. Cui, E. P. A. M. Bakkers, L. Lauhon, and A. Talin, eds.), vol. 1144, pp. LL16–04, 2008.
- [224] J. Lähnemann, O. Brandt, C. Pfüller, T. Flissikowski, U. Jahn, E. Luna, M. Hanke, M. Knelangen, A. Trampert, and H. T. Grahn, "Coexistence of quantum-confined stark effect and localized states in an (in,ga)n/gan nanowire heterostructure," *Phys. Rev. B*, vol. 84, p. 155303, Oct. 2011.
- [225] W. Guo, M. Zhang, P. Bhattacharya, and J. Heo, "Auger recombination in iii-nitride nanowires and its effect on nanowire light-emitting diode characteristics," *Nano Lett.*, Mar. 2011.
- [226] H. P. T. Nguyen, S. Zhang, K. Cui, X. Han, S. Fatholouloumi, M. Couillard, G. A. Botton, and Z. Mi, "p-type modulation doped ingan/gan dot-in-a-wire white-light-emitting diodes monolithically grown on si(111)," *Nano Lett.*, vol. 11, pp. 1919–1924, May 2011.
- [227] S. Albert, A. Bengoechea-Encabo, P. Lefebvre, M. A. Sánchez-García, E. Calleja, U. Jahn, and A. Trampert, "Emission control of ingan nanocolumns grown by molecular-beam epitaxy on si(111) substrates," *Appl. Phys. Lett.*, vol. 99, p. 131108, Sept. 2011.
- [228] T. Kouno and K. Kishino, "Well-arranged novel ingan hexagonal nanoplates at the tops of nitrogen-polarity gan nanocolumn arrays," *AIP Adv.*, vol. 2, p. 012140, Mar. 2012.
- [229] C. S. Gallinat, G. Koblmüller, J. S. Brown, and J. S. Speck, "A growth diagram for plasma-assisted molecular beam epitaxy of in-face inn," *J. Appl. Phys.*, vol. 102, no. 6, p. 064907, 2007.
- [230] S. Fernández-Garrido, T. Gotschke, E. Calleja, L. Geelhaar, and O. Brandt, "Control of the axial and lateral growth of self-induced gan nanowires by molecular beam epitaxy," in *IWN*, 2012.
- [231] L. Lymperakis and J. Neugebauer, "Large anisotropic adatom kinetics on nonpolar gan surfaces: Consequences for surface morphologies and nanowire growth," *Phys. Rev. B*, vol. 79, no. 24, p. 241308, 2009.
- [232] F. Limbach, T. Gotschke, T. Stoica, R. Calarco, E. Sutter, J. Ciston, R. Cuscó, L. Artus, S. Kremling, S. Hofling, L. Worschech, and D. Grutzmacher, "Structural and optical properties of ingan-gan nanowire heterostructures grown by molecular beam epitaxy," *J. Appl. Phys.*, vol. 109, p. 014309, Jan. 2011.

Bibliography

- [233] S. Ishizawa, K. Kishino, and A. Kikuchi, "Selective-area growth of gan nanocolumns on si(111) substrates using nitrided al nanopatterns by rf-plasma-assisted molecular-beam epitaxy," *Appl. Phys. Express*, vol. 1, p. 015006, Jan. 2008.
- [234] K. A. Bertness, A. W. Sanders, D. M. Rourke, T. E. Harvey, A. Roshko, J. B. Schlager, and N. A. Sanford, "Controlled nucleation of gan nanowires grown with molecular beam epitaxy," *Adv. Funct. Mater.*, vol. 20, pp. 2911–2915, Sept. 2010.
- [235] P. Dogan, O. Brandt, C. Pfüller, A. K. Bluhm, L. Geelhaar, and H. Riechert, "Gan nanowire templates for the pendeoepitaxial coalescence overgrowth on si(111) by molecular beam epitaxy," *J. Cryst. Growth*, vol. 323, pp. 418–421, May 2011.
- [236] T. Kouno, A. Kikuchi, and K. Kishino, "Growth of high-in-content ingan multiple quantum disk nanocolumns on si(111) by rf plasma-assisted molecular-beam epitaxy," *Phys. Status Solidi B*, vol. 243, no. 7, pp. 1481–1485, 2006.
- [237] C. Chèze, L. Geelhaar, B. Jenichen, and H. Riechert, "Different growth rates for catalyst-induced and self-induced gan nanowires," *Appl. Phys. Lett.*, vol. 97, p. 153105, Oct. 2010.
- [238] O. Landré, R. Songmuang, J. Renard, E. Bellet-Amalric, H. Renevier, and B. Daudin, "Plasma-assisted molecular beam epitaxy growth of gan nanowires using indium-enhanced diffusion," *Appl. Phys. Lett.*, vol. 93, p. 183109, Nov. 2008.
- [239] R. Averbeck and H. Riechert, "Quantitative model for the mbe-growth of ternary nitrides," *Phys. Status Solidi A*, vol. 176, no. 1, pp. 301–305, 1999.
- [240] A. G. Kontos, Y. S. Raptis, N. T. Pelekanos, A. Georgakilas, E. Bellet-Amalric, and D. Jalabert, "Micro-raman characterization of in_xga_{1-x}n/gan/al₂o₃ heterostructures," *Phys. Rev. B*, vol. 72, p. 155336, Oct. 2005.
- [241] X. Kong, S. Albert, A. Bengoechea-Encabo, M. A. Sanchez-Garcia, E. Calleja, and A. Trampert, "Plasmon excitation in electron energy-loss spectroscopy for determination of indium concentration in (in,ga)n/gan nanowires," *Nanotechnology*, vol. 23, no. 48, p. 485701, 2012.
- [242] T. Böttcher, S. Einfeldt, V. Kirchner, S. Figge, H. Heinke, D. Hommel, H. Selke, and P. L. Ryder, "Incorporation of indium during molecular beam epitaxy of ingan," *Appl. Phys. Lett.*, vol. 73, pp. 3232–3234, Nov. 1998.
- [243] A. Dussaigne, B. Damilano, N. Grandjean, and J. Massies, "In surface segregation in ingan/gan quantum wells," *J. Cryst. Growth*, vol. 251, pp. 471–475, Apr. 2003.
- [244] C. Adelmann, R. Langer, G. Feuillet, and B. Daudin, "Indium incorporation during the growth of ingan by molecular-beam epitaxy studied by reflection high-energy electron diffraction intensity oscillations," *Appl. Phys. Lett.*, vol. 75, pp. 3518–3520, Nov. 1999.
- [245] E. Dimakis, E. Iliopoulos, K. Tsagaraki, T. Kehagias, P. Komninou, and A. Georgakilas, "Heteroepitaxial growth of in-face inn on gan (0001) by plasma-assisted molecular-beam epitaxy," *J. Appl. Phys.*, vol. 97, p. 113520, June 2005.
- [246] D. N. Nath, E. Gur, S. A. Ringel, and S. Rajan, "Molecular beam epitaxy of n-polar ingan," *Appl. Phys. Lett.*, vol. 97, p. 071903, Aug. 2010.

- [247] H. Turski, M. Siekacz, M. Sawicka, G. Cywiński, M. Kryśko, S. Grzanka, J. Smalc-Koziorowska, I. Grzegory, S. Porowski, Z. R. Wasilewski, and C. Skierbiszewski, "Growth mechanism of ingan by plasma assisted molecular beam epitaxy," *J. Vac. Sci. Technol., B*, vol. 29, p. 03C136, May 2011.
- [248] G. Koblmüller, C. S. Gallinat, and J. S. Speck, "Surface kinetics and thermal instability of n-face inn grown by plasma-assisted molecular beam epitaxy," *J. Appl. Phys.*, vol. 101, no. 8, p. 083516, 2007.
- [249] H. Sekiguchi, K. Kishino, and A. Kikuchi, "Emission color control from blue to red with nanocolumn diameter of ingan/gan nanocolumn arrays grown on same substrate," *Appl. Phys. Lett.*, vol. 96, no. 23, p. 231104, 2010.
- [250] L. Chen, A. J. Yin, J. S. Im, A. V. Nurmikko, J. M. Xu, and J. Han, "Fabrication of 50-100 nm patterned ingan blue light emitting heterostructures," *Phys. Status Solidi A*, vol. 188, pp. 135–138, Nov. 2001.
- [251] C. H. Chiu, T. C. Lu, H. W. Huang, C. F. Lai, C. C. Kao, J. T. Chu, C. C. Yu, H. C. Kuo, S. C. Wang, C. F. Lin, and T. H. Hsueh, "Fabrication of ingan/gan nanorod light-emitting diodes with self-assembled ni metal islands," *Nanotechnology*, vol. 18, p. 445201, Nov. 2007.
- [252] C. Böcklin, R. G. Veprek, S. Steiger, and B. Witzigmann, "Computational study of an ingan/gan nanocolumn light-emitting diode," *Phys. Rev. B*, vol. 81, pp. 155306–, Apr. 2010.
- [253] Y. S. Park, "Quantum confined stark effect of ingan/gan multi-quantum disks grown on top of gan nanorods," *Nanotechnology*, vol. 21, no. 11, p. 115401, 2010.
- [254] M. A. Reshchikov and H. Morkoç, "Luminescence properties of defects in GaN," *J. Appl. Phys.*, vol. 97, p. 061301, Mar. 2005.
- [255] M. J. Holmes, Y. S. Park, X. Wang, C. C. S. Chan, A. F. Jarjour, R. A. Taylor, J. H. Warner, J. Luo, H. A. R. El-Ella, and R. A. Oliver, "Carrier dynamics of in[sub x]ga[sub 1 -][sub x]n quantum disks embedded in gan nanocolumns," *J. Appl. Phys.*, vol. 109, no. 6, p. 063515, 2011.
- [256] B. Wilsch, "Composition and strain variations in (in,ga)n/gan epitaxial layers," Master's thesis, Freie Universität Berlin, November 2011.
- [257] L. F. Zagonel, L. Rigutti, M. Tchernycheva, G. Jacopin, R. Songmuang, and M. Kociak, "Visualizing highly localized luminescence in gan/aln heterostructures in nanowires," *Nanotechnology*, vol. 23, no. 45, p. 455205, 2012.
- [258] G. Snider, "1D Poisson freeware." University of Notre Dame, 1990.
- [259] P. D. C. King, T. D. Veal, C. E. Kendrick, L. R. Bailey, S. M. Durbin, and C. F. McConville, "InN/GaN valence band offset: High-resolution x-ray photoemission spectroscopy measurements," *Phys. Rev. B*, vol. 78, p. 033308, July 2008.
- [260] V. Fiorentini, F. Bernardini, and O. Ambacher, "Evidence for nonlinear macroscopic polarization in III-V nitride alloy heterostructures," *Appl. Phys. Lett.*, vol. 80, no. 7, pp. 1204–1206, 2002.

Bibliography

- [261] O. Brandt, Y. J. Sun, H.-P. Schönherr, K. H. Ploog, P. Waltereit, S.-H. Lim, and J. S. Speck, "Improved synthesis of (in,ga)n/gan multiple quantum wells by plasma-assisted molecular-beam epitaxy," *Appl. Phys. Lett.*, vol. 83, no. 1, pp. 90–92, 2003.
- [262] A. Kikuchi, M. Tada, K. Miwa, and K. Kishino, "Growth and characterization of ingan/gan nanocolumn led," in *Proc. SPIE* (K. G. Eyink and D. L. Huffaker, eds.), vol. 6129, p. 612905, SPIE, 2006.
- [263] V. Cardin, L. I. Dion-Bertrand, P. Grégoire, H. P. T. Nguyen, M. Sakowicz, Z. Mi, C. Silva, and R. Leonelli, "Recombination dynamics in ingan/gan nanowire heterostructures on si(111)," *Nanotechnology*, vol. 24, no. 4, p. 045702, 2013.
- [264] D. J. Huntley, "An explanation of the power-law decay of luminescence," *J. Phys.: Condens. Matter*, vol. 18, no. 4, p. 1359, 2006.
- [265] A. Morel, P. Lefebvre, S. Kalliakos, T. Taliercio, T. Bretagnon, and B. Gil, "Donor-acceptor-like behavior of electron-hole pair recombinations in low-dimensional (ga,in)n/gan systems," *Phys. Rev. B*, vol. 68, p. 045331, July 2003.
- [266] C. Rivera, U. Jahn, T. Flissikowski, J. L. Pau, E. Muñoz, and H. T. Grahn, "Strain-confinement mechanism in mesoscopic quantum disks based on piezoelectric materials," *Phys. Rev. B*, vol. 75, p. 045316, Jan. 2007.
- [267] L. Rigutti, J. Teubert, G. Jacopin, F. Fortuna, M. Tchernycheva, A. D. Bugallo, F. H. Julien, F. Furtmayr, M. Stutzmann, and M. Eickhoff, "Origin of energy dispersion in alxga1-xn/gan nanowire quantum discs with low al content," *Phys. Rev. B*, vol. 82, p. 235308, Dec. 2010.
- [268] L. Geelhaar, O. Brandt, V. Kaganer, and M. Wölz, "Herstellung einer Halbleitereinrichtung mit mindestens einem säulen- oder wandförmigen Halbleiter-Element." Patent applications DE 10 2011 118 273.3 of 11.11.2011, and PCT/EP2012/004667 of 9.11.2012, 2012.
- [269] C. Bougerol, R. Songmuang, D. Camacho, Y. M. Niquet, R. Mata, A. Cros, and B. Daudin, "The structural properties of gan insertions in gan/aln nanocolumn heterostructures rid b-9005-2008," *Nanotechnology*, vol. 20, p. 295706, July 2009.
- [270] N. Tschirner, H. Lange, A. Schliwa, A. Biermann, C. Thomsen, K. Lambert, R. Gomes, and Z. Hens, "Interfacial alloying in cdse/cds heteronanocrystals: A raman spectroscopy analysis," *Chem. Mater.*, vol. 24, pp. 311–318, Jan. 2011.
- [271] T. Gotschke, *Untersuchungen zum geordneten Wachstum von III-Nitrid Nanodrähten. Analyse der Nukleations-, Dekompositions- und Diffusionsmechanismen.* PhD thesis, Humboldt-Universität, 2012.
- [272] B. Heying, R. Aeverbeck, L. F. Chen, E. Haus, H. Riechert, and J. S. Speck, "Control of gan surface morphologies using plasma-assisted molecular beam epitaxy," *J. Appl. Phys.*, vol. 88, no. 4, pp. 1855–1860, 2000.

List of Figures

2.1	Electron–hole recombination in the energy band model of semiconductors. Reprinted with permission from Ref. 1. Copyright 2006, Cambridge University Press.	6
2.2	Illustration of electron and hole dispersion relations for a direct-bandgap semiconductor. Reprinted with permission from Ref. 1. Copyright 2006, Cambridge University Press.	6
2.3	Illustration of LED active regions embedded in a p-n junction. Reprinted with permission from Ref. 1. Copyright 2006, Cambridge University Press.	7
2.4	Illustration of the carrier capture in a QW as a function of the barrier height. Reprinted with permission from Ref. 1. Copyright 2006, Cambridge University Press.	8
2.5	Vertical structure of a simple GaN-based LED, and band profile of the single QW and EBL. Reprinted with kind permission of Springer Science+Business Media: Ref. 3, copyright 2000.	8
2.6	Bandgap and lattice parameter of III-V semiconductors. Reproduced from Degreen, Wikimedia Commons, licensed under Creative Commons-License by-sa-2.0-de.	10
2.7	GaN unit cells of two polytypes differing in stacking sequence. Reprinted from Ref. 24	12
2.8	Planes in the hexagonal unit cell. Reprinted with permission from Ref. 25. Copyright 2009, IOP Publishing Ltd.	12
2.9	Illustration of the quantum-confined Stark effect (QCSE). Reprinted by permission from Macmillan Publishers Ltd: Ref. 39, copyright 2006.	13
2.10	Effect of the QCSE on the radiative decay time of $\text{In}_x\text{Ga}_{1-x}\text{N}/\text{GaN}$ QWs with increasing width. Reprinted with permission from Ref. 40. Copyright 2001, American Institute of Physics.	13
2.11	Relaxation of axial $\text{In}_x\text{Ga}_{1-x}\text{N}/\text{GaN}$ MQWs in a nanowire.	16
2.12	Steps in NW LED device planarization and n-contact fabrication. Published in Ref. 57.	17
3.1	MBE8 growth chamber cross sections. With kind permission based on scale drawings from Createc Fischer GmbH.	20
3.2	Ewald construction and RHEED geometry. From Ref. 73.	21
3.3	Typical RHEED patterns. Adapted from Ref. 74.	21
3.4	RHEED patterns of GaN grown on Si(111). 7×7 reconstruction observed during experiment M81002. h-GaN and c-GaN observed during growth of sample M81023.	23
3.5	Quadrupole mass spectrometer: principle of operation. Reprinted from Ref. 86, Copyright 1987, with permission from Elsevier.	24
3.6	<i>In-situ</i> protocol of routine pyrometer test. Data acquired prior to sample growth M8979.	26

List of Figures

3.7	GaN growth diagram delimiting the compact and nanowire growth regimes. Adapted with permission from Ref. 96. Copyright 2009, American Institute of Physics.	28
3.8	Shapes of GaN islands on Si_xN_y . Reprinted from Ref. 97. Copyright 2011 by The American Physical Society.	29
3.9	Wulff-plot for GaN nanostructures. Reprinted with permission from Ref. 114. Copyright 2009, American Institute of Physics.	29
3.10	SEM images of GaN nanocrystals on <i>A</i> -plane GaN substrates. Adapted with permission from (a) Ref. 114, Copyright 2009, American Institute of Physics and (b) Ref. 119, Copyright 2012, Elsevier.	31
3.11	RHEED patterns of GaN grown on sputtered Ti layers. Ti on Al_2O_3 , sample M81295. Ti on Si(111) with 100 nm thermal oxide, sample M81321.	34
3.12	SEM images of GaN NWs grown on sputtered Ti layers: Ti on Al_2O_3 , sample M81295. Ti on silica glass, sample M81389. Ti on Si(111) with 100 nm thermal oxide, sample M81321.	36
3.13	XRD profiles of Ti films. As sputtered on glass, sample M81389, and after GaN NW growth and reaction of Ti film with two different substrates: Al_2O_3 , sample M81295. Thermal Si oxide, sample M81321.	37
3.14	Comparison of PL data from GaN NWs grown on Ti (sample M81295), and GaN NWs grown on Si.	41
4.1	STEM HAADF image of sample M8934, and a sketch showing the principal fluctuations in structure, published in Ref. 154.	44
4.2	Room temperature photoluminescence micrograph of $\text{In}_x\text{Ga}_{1-x}\text{N}/\text{GaN}$ NWs as-grown on sample M81113. (Image 3 in Fig. 6.5)	45
4.3	Symmetric Bragg XRD scans of $\text{In}_x\text{Ga}_{1-x}\text{N}/\text{GaN}$ MQWs: planar sample M81256, and nanowire sample M81089.	47
4.4	Simulated XRD profiles for an $\text{In}_x\text{Ga}_{1-x}\text{N}/\text{GaN}$ MQW in a planar film and in nanowire ensembles, with comparison to data from NW sample M8995 grown directly on Si(111) and M81016 grown on an AlN buffer. Published in Ref. 154.	48
4.5	Strain states of lattice-mismatched crystal heterostructures: Pseudomorphic epitaxial QW growth, NW superlattice with non-uniform strain profile, and lateral relaxation estimate.	50
4.6	Strain $\varepsilon_{xx}/x_{\text{well}}$ in axial $\text{In}_x\text{Ga}_{1-x}\text{N}$ QWs as a function of $d_{\text{barrier}}/d_{\text{SL}}$	54
4.7	Relaxation factor describing the strain state of NW heterostructures. In the limit for thin NWs, the Poisson effect vanishes on average. Reprinted from Ref. 174. Copyright 2012 by The American Physical Society.	56
4.8	Raman spectra of GaN NW sample M9257 and planar GaN buffer layer sample NAE_02042 (Osram Opto Semiconductors GmbH), reprinted from Ref. 182.	57
4.9	Phonon frequency shift in $\text{In}_x\text{Ga}_{1-x}\text{N}$ as a function of composition and strain. Adapted from (a) Ref. 188, Copyright 2000 by The American Physical Society, and (b) Ref. 175, Copyright 2002 by The American Physical Society.	58
4.10	Literature values for the $A_1(\text{LO})$ phonon frequency shift under biaxial strain in GaN, InN, and the ternary alloy.	59

4.11	Calculated Raman shift for GaN NW with $\text{In}_x\text{Ga}_{1-x}\text{N}$ quantum disks containing different structural fluctuations.	61
5.1	SEM images of sample M81089 in cross-section and plan view. Published in Ref. 202.	67
5.2	STEM images of sample M8934 in bright field and z-contrast.	68
5.3	TEM images of $\text{In}_x\text{Ga}_{1-x}\text{N}/\text{GaN}$ NW samples. (a) M8939, (b) M81011 . . .	69
5.4	Idealized shapes of $\text{In}_x\text{Ga}_{1-x}\text{N}$ insertions in GaN NWs.	70
5.5	Evolution of RHEED pattern during growth of sample M81016, showing h-GaN in the GaN NW base and additional c-GaN in the active region. Published in Ref. 220.	71
5.6	HRTEM images of sample M8939 showing cubic GaN segments of different thickness.	72
5.7	SEM cross section of sample M8997, showing the $\text{In}_x\text{Ga}_{1-x}\text{N}/\text{GaN}$ MQW contrast in the NW. Published in Ref. 169.	73
5.8	SEM cross section of NW LED sample M81325, showing branches on the base NW due to In droplet contamination.	74
5.9	SEM cross section and in-situ QMS data from sample M8957, with a simple model of the diameter increase in the MQW region.	75
5.10	XRD ω -2 θ scans across the GaN(0002) reflection of $\text{In}_x\text{Ga}_{1-x}\text{N}/\text{GaN}$ NW superlattices, (a) sample series 18, published in Ref. 169, and (b) series 27.	80
5.11	Axial growth rate determination in plot of superlattice periods d_{SL} vs. growth time t_{barrier} . (a) Series 18, published in Ref. 169, (b) series 27.	81
5.12	Graphical determination of x_{well} from growth data for t_{barrier} and x-ray data for d_{SL} . Sample series 18.	82
5.13	SEM plan view images of $\text{In}_x\text{Ga}_{1-x}\text{N}/\text{GaN}$ NW samples M8994, M8995, and M8997, series 18.	85
5.14	SEM plan view images of $\text{In}_x\text{Ga}_{1-x}\text{N}/\text{GaN}$ NW samples M81260, M81258, and M81261, series 27.	85
5.15	Experimental and simulated ω -2 θ scans. Samples M81005, M81011, M81017, M81013, M81014. Published in Ref. 220.	87
5.16	TEM images and GPA of axial $\text{In}_x\text{Ga}_{1-x}\text{N}$ QWs in GaN NWs. Sample M81011. Published in Ref. 220.	88
5.17	In content of $\text{In}_x\text{Ga}_{1-x}\text{N}/\text{GaN}$ NW samples with variation in T_a , series 19. Published in Ref. 220.	89
5.18	Raman spectra of $\text{In}_x\text{Ga}_{1-x}\text{N}/\text{GaN}$ nanowire axial superlattices grown at different temperatures T_a . Samples M81005, M81011, M81017, M81013, M81014. Published in Ref. 220.	89
5.19	Raman spectrum of sample M8994, with simulated spectra using non-uniform strain distribution and constant strain approximation.	92
5.20	Atomic processes occurring during $\text{In}_x\text{Ga}_{1-x}\text{N}$ growth. Published in Ref. 202.	94
5.21	QMS calibration and measurement of In desorption from the sample surface during the growth of $\text{In}_x\text{Ga}_{1-x}\text{N}/\text{GaN}$ NWs by MBE. Samples M81096, M81113, M81089, M81105, M81095. Published in Ref. 202.	96
5.22	$\text{In}_x\text{Ga}_{1-x}\text{N}$ QW composition x as predicted from desorbing In flux, and Arrhenius-like plot of the experimental $\Phi_{\text{In,des}}$ from line-of-sight QMS. Published in Ref. 202.	97

List of Figures

5.23	Symmetric Bragg XRD scans of $\text{In}_x\text{Ga}_{1-x}\text{N}/\text{GaN}$ NW superlattice samples. Samples M81096, M81113, M81089, M81105, M81095 (series 23). Published in Ref. 202.	99
5.24	Estimates of x from XRD for $\text{In}_x\text{Ga}_{1-x}\text{N}/\text{GaN}$ NW samples from series 23. Published in Ref. 202.	100
6.1	Room temperature photoluminescence for a variation in QW composition (series 19, samples '05, '11, '17, '13, '14, '15) and thickness (series 11, samples '34, '37, '38, '44).	105
6.2	Raman spectra and room temperature photoluminescence for barrier thickness series 27.	106
6.3	Comparison of ensemble photoluminescence and cross-section cathodoluminescence from sample M8997.	108
6.4	Cathodoluminescence at different heights in an $\text{In}_x\text{Ga}_{1-x}\text{N}/\text{GaN}$ NW ensemble, sample M81310.	109
6.5	Room temperature photoluminescence micrographs of $\text{In}_x\text{Ga}_{1-x}\text{N}/\text{GaN}$ NW ensembles as-grown on sample M81113. The false-color PL images are taken at positions with different growth temperatures.	109
6.6	Cathodoluminescence of $\text{In}_x\text{Ga}_{1-x}\text{N}/\text{GaN}$ NW ensemble in plan view. Sample M81310.	110
6.7	Room temperature PL spectra of $\text{In}_x\text{Ga}_{1-x}\text{N}/\text{GaN}$ NW axial superlattices. Series 19, samples M81005, M81011, M81017, M81013, M81014. Published in Ref. 220.	111
6.8	Experimental PL peak positions from NW samples, and calculated planar QW transition energies. Published in Ref. 220.	112
6.9	Electroluminescence from $\text{In}_x\text{Ga}_{1-x}\text{N}$ NW LEDs. Samples M81274 and M81275. Published in Ref. 202. Grayscale camera image of sample M81274.	114
6.10	Principle of strain engineering in an axial NW superlattice.	116
6.11	Resonant Raman spectra of $\text{In}_x\text{Ga}_{1-x}\text{N}/\text{GaN}$ NW samples with different degrees of relaxation but constant x . Series 18, samples M8994, M8995, M8997.	117
6.12	Relative strain in $\text{In}_x\text{Ga}_{1-x}\text{N}/\text{GaN}$ NW samples with a variation in the barrier thickness (series 18 and 27). SEM images of samples M8994 and M81257.	119
B.1	SEM cross section of sample M81258 and histograms combining all samples of series 27, showing typical diameter and lengths of self-induced GaN NWs on Si(111).	134
B.2	SEM of samples M8995 in cross section and plan view showing the tilt and twist angles. XRD rocking curves of GaN NWs on Si(111) (samples M8995) and on AlN buffer layer on (Si(111) (sample M81016).	135
C.1	BEP measurement and growth rate calibration for the Ga,1 effusion cell in MBE 8. BEP data from 10.06.10. Calibration sample M8970.	137

List of Tables

2.1	Lattice parameters and thermal characteristics of III-nitrides and substrates for heteroepitaxy.	11
2.2	Strategies for LED devices based on GaN-nanowires.	15
3.1	Preparation of samples with self-induced GaN NWs on Ti interlayer (series 30).	33
4.1	Typical magnitudes of structural fluctuations in self-induced NWs.	46
5.1	Step-by-step description of typical $\text{In}_x\text{Ga}_{1-x}\text{N}/\text{GaN}$ NW heterostructure and NW LED growth experiments.	65
5.2	Source fluxes for the growth of $\text{In}_x\text{Ga}_{1-x}\text{N}/\text{GaN}$ NWs with a tapered active region, sample M8957.	74
5.3	Growth parameters for barrier thickness series 18 and 27.	79
5.4	Structural parameters for samples from series 18 and 27, determined by XRD.	81
A.1	List of all $\text{In}_x\text{Ga}_{1-x}\text{N}/\text{GaN}$ NW samples used in this work.	128

Danksagung

Meine Arbeit am *Paul-Drude-Institut für Festkörperelektronik* in Berlin (PDI) ist von kenntnis- und ideenreichen, interessierten und hilfsbereiten Kollegen begleitet worden, die mich auf jedem Schritt unterstützt haben und die Anfertigung dieser Dissertation ermöglicht haben. Ich habe hier, sowie bei Konferenzreisen und am *Indian Institute of Technology Bombay* (IITB), sehr viel gelernt und wertvolle Freundschaften gewonnen, und möchte einigen besonders danken.

Herrn Prof. Dr. Henning Riechert danke ich für die Themenstellung und die Finanzierung dieser Arbeit, sowie für die Freiheit, soviel Arbeitskraft für die Dissertation verwenden zu können, wie auf jeder Etappe nötig war.

Bei Herrn Prof. Dr. W. Ted Masselink bedanke ich mich sehr für die Bereitschaft zur Übernahme des zweiten Gutachtens.

Herrn Dr. Bruno Daudin danke ich für das Interesse an technischen Details meiner experimentellen Arbeit, die spannende Möglichkeit des Vergleichs mit den Ergebnissen seiner Gruppe, und für die Zusage des externen Gutachtens.

Ganz besonders möchte ich mich bei Herrn Dr. Lutz Geelhaar für die vorbildliche Betreuung bedanken, die mit der Aufnahme in die „Nanowire“ Arbeitsgruppe im PDI und seinem Interesse an meiner Industrieerfahrung begann. Die wissenschaftliche Leistung dieser Arbeit fußt, mehr noch als auf dem Experiment, auf seiner geschickten Fragestellung. Ich bin ihm sehr dankbar für die intensive inhaltliche und strategische Beratung, in der er die Veröffentlichungen und die Konferenzbeiträge, aber auch den Stipendienantrag und die Patentanmeldung, und schließlich die Dissertation, angestoßen und begleitet hat.

Herrn Prof. Dr. Subhabrata Dhar und seiner Arbeitsgruppe möchte ich für die Gastfreundschaft am IITB danken, die mir einen weiteren Blick auf experimentelle Methoden ermöglicht hat.

Ich hatte das Glück, weitere wissenschaftliche Lehrer im PDI zu finden, die diese Arbeit mit ständiger Hilfsbereitschaft maßgeblich gefördert haben:

Herrn Dr. Oliver Brandt habe ich elementare und weiterführende Einsichten in das Wesen der Nitride aus vielen humorigen Lehrveranstaltungen zu verdanken. Ich danke ihm auch sehr für das Vertrauen, mich Prof. Dhar zu empfehlen.

Herrn Dr. Vladimir M. Kaganer danke ich für das große Interesse an dieser Arbeit, und für die mit intensivem Einsatz beigesteuerten Spannungsberechnungen.

Große Hilfe verdanke ich Herrn Dr. Manfred Ramsteiner, aus dessen ursprünglichem Interesse für eine Meßmethode nun ein Kapitel über Halbleiterherstellung entstanden ist. Ich danke ihm auch für die ganz praktische Durchführung der Simulation resonanter Raman-Spektren.

Herrn Dr. Sergio Fernández-Garrido danke ich für die unermüdliche Anleitung zur Bewertung von Wachstumsmodellen in analytischer Klarheit.

Weiteren Kollegen schulde ich Dank für Messungen und Rechnungen, sowie deren Interpretation und lehrreiche Diskussionen in diesen Jahren angenehmer Zusammenarbeit. Ich danke im besonderen Dr. Carsten Pfüller für die erste Erfolgsmeldung über eine

leuchtende Probe, Jonas Lähnemann für die Berechnung der Übergangsenergie, Christian Hauswald für umfassende PL-Messungen, Dr. Friederich Limbach für den Aufbau der hauseigenen LED-Produktion, Dr. Michael Hanke für erste Einsichten in ungleichförmige Verspannung, Dr. Tore Niermann für das freundliche Interesse und HRTEM Ergebnisse, Dr. Suman De für Sonderschichten in der PL-Mikroskopie, Dr. Tobias Gotschke für AlN Pufferschichten, Dr. Caroline Chèze für die Eichung der Plasmaquellen und Dr. Timur Flissikowski für die Besprechung zeitaufgelöster PL-Messungen. Auch danke ich Dr. Achim Trampert und Dr. Chang Ning Huang für TEM Bilder.

Viele Kollegen waren mit hohem Zeitaufwand direkt an der Probenherstellung beteiligt oder haben ganze Prozesse dafür entwickelt. Ich danke Claudia Herrmann, Gert Jaschke und Hans-Peter Schönherr für die Instandhaltung der MBE, Anne-Kathrin Bluhm für sehr zahlreiche SEM Aufnahmen, Walid Anders, Bernd Drescher und Angela Riedel für die Prozessierung der Nanowire-LEDs auf Silizium, Doreen Steffen für die TEM-Probenpräparation, und Werner Seidel und Jacob Dinner für die konzentrierte Arbeit an der Herstellung einer Nanowire-LED auf Titan und Glas. Viele Ausgangsdaten lagen gedruckt vor, deshalb gilt ein weiterer Dank Sylvia Räther und Dagmar Dormeyer für die umgehende Literaturbeschaffung.

Die wichtigste Unterstützung habe ich abseits von Nanowires durch Gesine Heyden erhalten. Sie hat meine Arbeit mit Liebe und Geduld begleitet, für die ich sehr dankbar bin.

Diese Arbeit wurde zum Teil finanziert unter dem Verbundprojekt MONALISA des Bundesministeriums für Bildung und Forschung, Förderkennzeichen 01BL0810, sowie durch ein Kurzstipendium des Deutschen Akademischen Austauschdienstes, Kennziffer D/10/50443.

Selbständigkeitserklärung

Hiermit erkläre ich die Kenntnis der Promotionsordnung der Mathematisch-Naturwissenschaftlichen Fakultät I der Humboldt-Universität zu Berlin vom 6. Juli 2009.

Ich versichere, dass die vorliegende Arbeit „Control of the emission wavelength of gallium nitride-based nanowire light-emitting diodes“ selbständig und nur unter Verwendung der gemäß § 7 Absatz 3 der Promotionsordnung angegebenen Hilfen und Hilfsmittel angefertigt worden ist.

Ich habe mich nicht anderwärts um einen Doktorgrad beworben und besitze auch keinen entsprechenden Doktorgrad.

Berlin, den 7. Februar 2013

Martin Wölz